DEVELOPMENT AND APPLICATION OF COUPLED HURRICANE WAVE AND SURGE MODELS FOR SOUTHERN LOUISIANA

A Dissertation

Submitted to the Graduate School
of the University of Notre Dame
in Partial Fulfillment of the Requirements
for the Degree of

Doctor of Philosophy

by

Joel Casey Dietrich

Joannes Westerink, Director

Graduate Program in Civil Engineering and Geological Sciences
Notre Dame, Indiana
October 2010

DEVELOPMENT AND APPLICATION OF COUPLED HURRICANE WAVE AND SURGE MODELS FOR SOUTHERN LOUISIANA

Abstract

by

Joel Casey Dietrich

Coastal Louisiana and Mississippi are especially prone to large hurricanes due to their geographic location in the north-central Gulf of Mexico. Several recent hurricanes have devastated the region, creating complicated environments of waves and storm surge. Katrina (2005) and Gustav (2008) made landfall in southeastern Louisiana, and their counter-clockwise winds pushed surge onto the Louisiana-Mississippi continental shelf, into the low-lying wetlands surrounding the Mississippi River, and over and through the levee system that protects metropolitan New Orleans. Rita (2005) and Ike (2008) passed farther to the west, moved across the Texas-Louisiana continental shelf, and created surge that flooded large portions of southwestern Louisiana.

These hurricanes demand detailed hindcasts that depict the evolution of waves and surge during these storm events. These hindcasts can be used to map the likely floodplains for insurance purposes, to understand how the current protection system responded during each storm, and to design a new protection system that will resist better the waves and surge. In addition, the resulting computational model can be used to forecast the system's response to future storm events.

The work described herein represents a significant step forward in the modeling of hurricane waves and surge in complicated nearshore environments. The

system is resolved with unprecedented levels of detail, including mesh sizes of 1km on the continental shelf, less than 200m in the wave breaking zones and inland, and down to 20-30m in the fine-scale rivers and channels. The resulting hindcasts are incredibly accurate, with close matches between the modeled results and the measured high-water marks and hydrograph data. They can be trusted to provide a faithful representation of the evolution of waves and surge during all four hurricanes.

This work also describes advancements in the coupling of wave and surge models. This coupling has been implemented typically with heterogeneous meshes, which is disadvantageous because it requires intra-model interpolation at the boundaries of the nested, structured wave meshes and inter-model interpolation between the wave and circulation meshes. The recent introduction of unstructured wave models makes nesting unnecessary. The unstructured-mesh SWAN wave and ADCIRC circulation models are coupled in this work so that they run on the same unstructured mesh. This identical, homogeneous mesh allows the physics of wave-circulation interactions to be resolved correctly in both models. The unstructured mesh can be applied on a large domain to follow seamlessly all energy from deep to shallow water. There is no nesting or overlapping of structured wave meshes, and there is no inter-model interpolation. Variables and forces reside at identical, vertex-based locations. Information can be passed without interpolation, thus reducing significantly the communication costs.

The coupled SWAN+ADCIRC model is highly scalable and integrates seamlessly the physics and numerics from deep ocean to shelf to floodplain. Waves, water levels and currents are allowed to interact in complex problems and in a way that is accurate and efficient to thousands of computational cores. The coupled

model is validated against extensive measurements of waves and surge during the four recent Gulf hurricanes. Furthermore, the coupling paradigm employed by SWAN+ADCIRC does not interfere with the already-excellent scalability of the component models, and the coupled model maintains its scalability to 7,168 computational cores. SWAN+ADCIRC is well-suited for the simulation of hurricane waves and surge.

CONTENTS

FIGURES

TABLES

ACKNOWLEDGMENTS

I have learned so much during my time at Notre Dame, almost entirely though my interaction with a great group of people, both here and elsewhere, all of whom are working together toward common goals.

A lifetime of thanks to my adviser, Joannes Westerink, for everything. Your support, direction and never-ending patience made this work possible. From you, I have learned a great deal about the connections between the physics, numerics and computational science that form the foundation of what we do; the necessity of poring over even the most minute details of our work; and the proper conduct of a teacher, researcher and engineer. I will always be your student.

This work also benefited significantly from the contributions of my committee members: Andrew Kennedy, Harindra Fernando and Clint Dawson. Thank you for your guidance and shared expertise over the past few years. I hope this work meets your expectations.

I continue to learn from and be supported by the greater ADCIRC community, specifically Randall Kolar and Rick Luettich, but also the many researchers and scientists who continue to develop and use the model. I hope the work represented in this dissertation will somehow make your work easier.

I have also benefited from collaborations with some of the world's best wave modelers, including Robert Jensen, Jane Smith, Leo Holthuijsen and Marcel Zijlema. Every phone call and e-mail exchange was a joy, because I always learned

something new. I hope you will continue to share your expertise with this novice wave modeler.

My fellow students at Notre Dame have shared the burden of this work, thus making it both possible and better. I will treasure the long hours I shared in the lab with Ethan Kubatko, Shintaro Bunya, Seizo Tanaka, Rose Martyr, Mark Hope and many others.

My parents continue to support me with a strong foundation, even as it is projected all the way from Oklahoma to Indiana. Thank you for your support and your love.

And my fiancé, Lindsay, is much too nice to me!

CHAPTER 1

A BRIEF INTRODUCTION TO HURRICANE WAVES AND SURGE IN SOUTHERN LOUISIANA

1.1 Overview

Coastal Louisiana and Mississippi are especially prone to large hurricanes due to their geographic location in the north-central Gulf of Mexico. Between 1941 and 2008, the central Gulf was impacted by 16 major hurricanes including storms in 1941, 1957 (Audrey), 1964 (Hilda), 1965 (Betsy), 1969 (Camille), 1974 (Carmen), 1979 (Frederic), 1992 (Andrew), 1995 (Opal), 2002 (Lili), 2004 (Ivan), 2005 (Dennis, Katrina and Rita) and most recently in 2008 (Gustav and Ike). It is estimated that this region is more than twice as likely to see a major Gulf hurricane compared to the adjacent coasts of Texas and Florida (Resio, 2007). Wind-driven coastal surge from these large hurricanes was the most important contributor to devastating regional flooding, although maximum high-water levels were also influenced by atmospheric pressure, tides, riverine currents, waves and rainfall.

The central Gulf is not only statistically susceptible to more frequent hurricanes, but portions of this varied geographic system are vulnerable to developing especially large storm surge for a given set of storm characteristics due to the local geographic configuration. In particular, the east bank of the Mississippi River in southeastern Louisiana is characterized by a protruding delta on the Mississippi-Alabama shelf; the river itself; barrier islands; extensive levee, raised road and

railroad systems; low-lying topography; and large interconnected shallow lakes. Many of these features tend to amplify surge as water is blown from both the east and the south onto the shelf and then blocked by the delta, river banks, levees, and railroad beds. The regional surge in the lower Mississippi River is often propagated up the river, reaching New Orleans within hours. While the state of Mississippi is topographically more varied than Louisiana, with shallow estuaries and low-lying riverine basins interspersed with higher areas including a system of barrier islands lying to the south, Mississippi is also dramatically affected by the Mississippi River's protrusion onto the shallow continental shelf. Finally, western Louisiana is characterized by an east-west coastline, large inland lakes and extensive low-lying wetlands. These features tend to diminish surge heights because the southerly winds in the right center quadrant of the storm are the most effective in pushing water against the coast, and the extensive low-lying wetlands may attenuate transient surges in this area.

This geographical region has been devastated by several recent hurricanes. In 2005, Katrina caused devastating flooding within the city of New Orleans and created storm surge along the Mississippi-Alabama coastline that was the largest ever measured in the continental United States (Ebersole *et al.*, 2007), while Rita made landfall in southwestern Louisiana and flooded large portions of the marshes and bayous in the region. In 2008, Gustav made landfall in southeastern Louisiana and threatened New Orleans with wave overtopping of its levee protection system, while Ike made landfall in Galveston, Texas, but created currents and extensive flooding along the coastlines of all of Louisiana and eastern Texas.

These hurricanes created complex environments of waves, currents and storm surge throughout the region. In the deep water of the Gulf of Mexico, large, long

waves were developed that propagated as swell in all directions. These waves have been measured at buoys to have significant heights up to 17.5m and peak periods up to 25s, but their significant heights are likely 20-25m closer to the hurricane track. In regions where the continental shelf is narrow, such as at the bird's foot of the Mississippi River, these large waves approach closely to the shoreline before breaking due to rapid changes in bathymetry. Behind the breaking zones and inside the marshes and bayous of southern Louisiana, the wave environment is completely different, with wind-sea waves generated locally but limited by depth and bottom friction to significant heights of 1-2m and periods of 0.5-4s.

The storm surge also varies widely from its generation on the continental shelf to its interaction with the nearshore estuaries, floodplains and channels. Currents of 2 m s^{-1} or greater can exist on the shelf, around the delta and the barrier islands, and within the natural and man-made passes and channels that connect New Orleans to the Gulf. Water levels reached 4-5m along the coastline of southwest Louisiana during Rita, 3-4m along the Mississippi River levees during several storms, and up to 10m along the Mississippi-Alabama coastline during Katrina.

In order to model coastal waves and surge in this complex region, we must include all significant flow processes, define accurately the physical system, resolve numerically the system and the energetic flows, and apply accurate algorithms to solve the resulting mathematical model. The goal is to implement a modeling capability that represents the basic physics of the system as it is observed and does not require *ad hoc* model tuning of sub-mesh-scale coefficients, forcing functions and/or boundary conditions.

A broad energy spectrum exists in oceans, with wave periods ranging from seconds to months. Short waves, such as wind-driven waves and swell, have pe-

riods that range from 0.5-25 s. Longer waves, such as seiches, tsunamis, storm surges and tides, have periods that range from minutes to months. These short and long waves are well-separated in the energy spectrum and have well-defined spatial scales. This separation leads to distinct modeling approaches, depending on whether the associated scales can be resolved. For oceanic scales, short-wave models cannot resolve spatially or temporally the individual wind-driven waves or swell, and thus they treat the wave field as an energy spectrum and apply the conservation of wave action density to account for wave-current interactions. Long-wave models apply forms of conservation of mass and momentum, in two or three spatial dimensions, to resolve the circulation associated with processes such as tsunamis, storm surges or tides.

Although wind-driven waves and circulation are separated in the spectrum, they can interact. Water levels and currents affect the propagation of waves and the location of wave-breaking zones. Wave transformation generates radiation stress gradients that drive set-up and currents. Wind-driven waves affect the vertical momentum mixing and bottom friction, which in turn affect the circulation. Water levels can be increased by 5-20 percent in regions across a broad continental shelf, and by as much as 35 percent in regions of steep slope (Funakoski *et al.*, 2008; Dietrich *et al.*, 2010a). Thus, in many coastal applications, waves and circulation processes should be coupled.

Hurricanes also act over a wide range of spatial scales. Waves and storm surge are generated in the deep waters of the Gulf of Mexico, propagate and then transform on the continental shelf and in the complex nearshore environment due to rapid changes in bathymetry and bottom friction. Wave dissipation can be spread over large, smoothly-varying shelfs, or it can be focused near the barrier islands

or other breaking zones. Storm surge is pushed over the sounds and marshes and then interacts with the levees and channels in the region.

Wave and circulation models have been limited by their spectral, spatial and temporal resolution. This limitation can be overcome by nesting structured meshes, to enhance resolution in specific regions by employing meshes with progressively finer scales. In a wave application, nesting also allows the use of models with different physics and numerics. Relatively fine nearshore wave models, such as STWAVE and SWAN, can be nested inside relatively coarse deep-water wave models, such as WAM and WaveWatch III (WAMDI Group, 1988; Komen *et al.*, 1994; Booij *et al.*, 1999; Smith *et al.*, 2001; Thompson *et al.*, 2004; Gunther 2005; Tolman 2009). The nearshore wave models may not be efficient if applied to large domains, and the deep-water wave models may not contain the necessary physics or resolution for nearshore wave simulation. Until recently, wave models required nesting in order to vary resolution from basin to shelf to nearshore applications. These structured wave models can be coupled to structured circulation models that run on the same nested meshes (Kim *et al.*, 2008).

Unstructured circulation models have emerged to provide localized resolution of gradients in geometry, bathymetry/topography, and flow processes. Resolution varies over a range of scales within the same mesh from deep water to the continental shelf to the channels, marshes and floodplains near shore (Westerink *et al.*, 2008). Unstructured meshes allow for localized resolution where solution gradients are large and correspondingly coarser resolution where solution gradients are small, thus minimizing the computational cost relative to structured meshes with similar minimum mesh spacings.

The coupling of wave and circulation models has been implemented typically with heterogeneous meshes. A coupling application may have one unstructured circulation mesh and several structured wave meshes, and the models may pass information via external files (Weaver and Slinn, 2004; Ebersole *et al.*, 2007; Chen *et al.*, 2008; Funakoshi *et al.*, 2008; Pandoe and Edge, 2008). Chapters 2 and 3 describe an example of this 'loose' coupling as applied to Katrina and Rita (Bunya *et al.*, 2010; Dietrich *et al.*, 2010a). This loose coupling is disadvantageous because it requires intra-model interpolation at the boundaries of the nested, structured wave meshes and inter-model interpolation between the wave and circulation meshes. This interpolation creates problems with respect to both accuracy and efficiency. Overlapping nested or adjacent wave meshes often have different solutions, and inter-mesh interpolation can smooth or enhance the integrated wave forcing. Furthermore, even if a component model is locally conservative, its interpolated solution will not necessarily be conservative. Finally, inter-model interpolation must be performed at all vertices of the meshes. This interpolation is problematic in a parallel computing environment, where the communication between sub-meshes is inter-model and semi-global. The sub-meshes must communicate on an area basis (*i.e.*, the information at all vertices on a sub-mesh must be shared). Global communication is costly and can prevent models from being scalable in high-performance computing environments.

An emerging practice is to couple models through a generic framework, such as the Earth System Modeling Framework (ESMF) (Hill *et al.*, 2004; Collins *et al.*, 2005), the Open Modeling Interface (OpenMI) Environment (Moore and Tindall, 2005; Gregersen *et al.*, 2005) or the Modeling Coupling Toolkit (MCT) (Warner *et al.*, 2008). These frameworks manage when and how the individual models are

run, interpolate information between models if necessary, and make transparent the coupling to developers and users. However, these frameworks do not eliminate the fundamental problems of coupling when using heterogeneous meshes. Boundary conditions must be interpolated between nested, structured wave meshes, and water levels, currents and wave properties must be interpolated between the unstructured circulation and structured wave meshes. This interpolation is costly, destroys the scalability of the coupled model, and thus limits the resolution that can be employed and the corresponding physics that can be simulated.

The recent introduction of unstructured wave models makes nesting unnecessary. Resolution can be enhanced nearshore and relaxed in deep water, allowing the model to simulate efficiently the wave evolution. SWAN has been used extensively to simulate waves in shallow water (Booij *et al.*, 1999; Ris *et al.*, 1999; Gorman and Neilson, 1999; Rogers *et al.*, 2003), and it has been converted recently to run on unstructured meshes (Zijlema, 2010). This version of SWAN employs the unstructured-mesh analog to the solution technique from the structured version. It retains the physics and numerics of SWAN, but it runs on unstructured meshes, and it is both accurate and efficient in the nearshore and in deep water.

Chapter 4 describes a 'tight' coupling of the SWAN wave model and the ADCIRC circulation model (Dietrich *et al.*, 2010b). SWAN and ADCIRC are run on the same unstructured mesh. This identical, homogeneous mesh allows the physics of wave-circulation interactions to be resolved correctly in both models. The unstructured mesh can be applied on a large domain to follow seamlessly all energy from deep to shallow water. There is no nesting or overlapping of structured wave meshes, and there is no inter-model interpolation. Variables and forces reside at identical, vertex-based locations. Information can be passed through lo-

cal cache without interpolation, thus reducing significantly the communication costs between models.

In parallel computing applications, identical sub-meshes and communication infrastructure are used for both SWAN and ADCIRC, which run as the same program on the same computational core. All inter-model communication on a sub-mesh is done through local cache. Communication between sub-meshes is intra-model. Information is passed only to the edges of neighboring sub-meshes, and thus the coupled model does not require global communication over areas. Domain decomposition places neighboring sub-meshes on neighboring cores, so communication costs are minimized. The coupled model is highly scalable and integrates seamlessly the physics and numerics from ocean to shelf to floodplain. Large domains and high levels of local resolution can be employed for both models, allowing the accurate depiction of the generation, propagation and dissipation of waves and surge. The resulting SWAN+ADCIRC model is suited ideally to simulate waves and circulation and their propagation from deep water to complicated nearshore systems. Chapter 5 describes the application of SWAN+ADCIRC to a hindcast of Gustav, and it makes use of the next generation of unstructured meshes and measured data (Dietrich *et al.*, 2010c).

Hurricane forecasting applications demand both accuracy and efficiency. Model results must be reliable for a wide range of storm characteristics, and thus a high-resolution mesh should be employed to resolve the complex geometry throughout the region. But model results must also be timely, often on the order of less than 1hr, so that they can be useful to emergency management officials to aid with decision-making. Chapter 6 validates the accuracy and efficiency of SWAN+ADCIRC on the SL16 unstructured mesh, which employs 5M vertices and

10M finite elements to provide a high-resolution description of southern Louisiana (Dietrich *et al.*, 2010d). The model is validated against measured waves and storm surge during the four recent hurricanes to impact the region, namely Katrina and Rita (2005), and Gustav and Ike (2008).

Benchmarking results show SWAN+ADCIRC is efficient to thousands of computational cores. As meshes continue to grow in size and complexity, it is imperative that models make good use of the expanding computational resources. The coupling paradigm employed by SWAN+ADCIRC does not interfere with the already-excellent scalability of the component models, and the coupled model also manages well its file output through the use of dedicated writer cores. The coupled model maintains its scalability to 7,168 computational cores. The tight coupling of SWAN+ADCIRC enables waves, water levels and currents to interact in complex problems and in a way that is accurate and efficient.

1.2 Layout of the Dissertation

Thus, the work herein describes an evolution of wave model coupling to the unstructured-mesh, ADCIRC circulation model.

Chapters 2 and 3 describe the hindcasts of Katrina and Rita that were performed with a loosely-coupled system of wave and circulation models. WAM and STWAVE are employed to simulate the evolution of waves from deepwater to the nearshore, respectively, while ADCIRC is employed to simulate the circulation on the unstructured SL15 mesh. The model components are validated independently, showing a high level of model skill in representing riverine flows, tides, wind-waves and hurricane storm surge. Then the storms are examined synoptically, with a focus on how the storm surge developed and impacted the region. These chap-

ters have been published in *Monthly Weather Review* as Bunya *et al.* (2010) and Dietrich *et al.* (2010a).

Chapter 4 describes the tight coupling of SWAN+ADCIRC. It discusses the different types of model coupling and their drawbacks, with an emphasis on how the use of heterogeneous meshes limits the performance of a coupled model in a high-performance computing environment. SWAN+ADCIRC is coupled tightly so that the models run on the same unstructured meshes and on the same computational cores, thus ensuring good performance because information can be passed through local cache without the need for interpolation. The coupled model is validated via hindcasts of Katrina and Rita, with a focus on how its results compare to the solutions obtained from WAM and STWAVE. The tightly-coupled SWAN+ADCIRC is shown to be as accurate as the structured-mesh wave models, but better positioned to increase mesh resolution in regions with large gradients in bathymetry and/or the computed solution. This chapter is in press in *Coastal Engineering* as Dietrich *et al.* (2010b).

Chapter 5 employs SWAN+ADCIRC in a next-generation hindcast of Gustav. It utilizes the unstructured SL16 mesh, which contains twice the resolution of previous meshes, with mesh spacing of 4-6 km in the deeper Gulf that varies downward to 30-50 m in the fine-scale channels of southern Louisiana. It makes good use of the coupling to improve the model physics; a storm-sector-based wind drag scheme is shared between SWAN and ADCIRC, and the bottom friction in SWAN is updated to use roughness lengths derived from the Manning's n values used by ADCIRC. Furthermore, SWAN employs a larger range of discretized frequencies, to better model the short-period waves in the marshes, and a stronger set of convergence criteria, to better model the propagation of swell on the fine mesh.

A careful comparison to extensive measurement data shows that SWAN+ADCIRC captures well the evolution of wave and surge from the deep water, to the continental shelf, and into the complex nearshore environment. This chapter has been submitted to *Monthly Weather Review* as Dietrich *et al.* (2010c).

Chapter 6 examines the performance of SWAN+ADCIRC. The coupled model is validated comprehensively through hindcasts of all four recent Gulf hurricanes, which offer coverage of the entire domain of interest, and thus require a consistent, physics-based modeling approach. Then the coupling is tested via benchmarking of SWAN+ADCIRC on the TACC Ranger and NICS Kraken machines. The coupling adds no overhead to the simulation, and the coupled model shows linear scaling through 7,168 computational cores. This chapter will be submitted to the *Journal of Scientific Computing* as Dietrich *et al.* (2010d).

1.3 Acknowledgments

This work would not have been possible without support from the DOD National Defense Science and Engineering Graduate Fellowship; the Office of Naval Research (N00014-06-1-0285); the National Science Foundation (DMS06-20696, DMS06-20697, DMS06-20791, OCI-0746232, OCI-0749015); and the Department of Homeland Security (2008-ST-061-ND-0001). Computational resources and support were provided by the US Army Engineering Research and Development Center; the DOD Supercomputing Resource Center; and the UT-Austin Texas Advanced Computing Center (TG-DMS08-0016N).

CHAPTER 2

A HIGH-RESOLUTION COUPLED RIVERINE FLOW, TIDE, WIND, WIND WAVE AND STORM SURGE MODEL FOR SOUTHERN LOUISIANA AND MISSISSIPPI: PART I - MODEL DEVELOPMENT AND VALIDATION

2.1 Overview

This chapter describes the hindcasts of Katrina and Rita that were performed with a loosely-coupled system of wave and circulation models. WAM and STWAVE are employed to simulate the evolution of waves from deepwater to the nearshore, respectively, while ADCIRC is employed to simulate the circulation on the unstructured SL15 mesh. The model components are validated independently, showing a high level of model skill in representing riverine flows, tides, wind-waves and hurricane storm surge. This chapter has been published in *Monthly Weather Review* as Bunya *et al.* (2010).

A coupled system of wind, wind-wave and coastal circulation models has been implemented for Southern Louisiana and Mississippi to simulate riverine flows, tides, wind-waves and hurricane storm surge in the region. The system combines the H*WIND and IOKA kinematic wind analyses, the WAM offshore and STWAVE nearshore wind-wave models, and the ADCIRC basin- to channel-scale unstructured-mesh circulation model. The system emphasizes a high-resolution (down to 50 m) representation of the geometry, bathymetry and topography;

nonlinear coupling of all processes including wind-wave radiation-stress-induced set up; and objective specification of frictional parameters based on land-cover databases and commonly used parameters. Riverine flows and tides are validated for no storm conditions, while winds, wind-waves, hydrographs and high-water marks are validated for Hurricanes Katrina and Rita.

2.2 Introduction

Coastal Louisiana and Mississippi are especially prone to large hurricanes due to their geographic location in the north-central Gulf of Mexico. Between 1941 and 2008, the central Gulf was impacted by 16 major hurricanes including storms in 1941, 1957 (Audrey), 1964 (Hilda), 1965 (Betsy), 1969 (Camille), 1974 (Carmen), 1979 (Frederic), 1992 (Andrew), 1995 (Opal), 2002 (Lili), 2004 (Ivan), 2005 (Dennis, Katrina and Rita) and most recently in 2008 (Gustav and Ike). It is estimated that this region is more than twice as likely to see a major Gulf hurricane compared to the adjacent coasts of Texas and Florida (Resio, 2007). Wind-driven coastal surge from these large hurricanes was the most important contributor to devastating regional flooding, although maximum high-water levels were also influenced by atmospheric pressure, tides, riverine currents, waves and rainfall.

The central Gulf is not only statistically susceptible to more frequent hurricanes, but portions of this varied geographic system are vulnerable to developing especially large storm surge for a given set of storm characteristics due to the local geographic configuration. In particular, the east bank of the Mississippi River in southeastern Louisiana is characterized by a protruding delta on the Mississippi-Alabama shelf; the river itself; barrier islands; extensive levee, raised road and railroad systems; low-lying topography; and large interconnected shallow lakes.

Many of these features tend to amplify surge as water is blown from both the east and the south onto the shelf and then blocked by the delta, river banks, levees, and railroad beds. The regional surge in the lower Mississippi River is often propagated up the river, reaching New Orleans within hours. While the state of Mississippi is topographically more varied than Louisiana, with shallow estuaries and low-lying riverine basins interspersed with higher areas including a system of barrier islands lying to the south, Mississippi is also dramatically affected by the Mississippi River's protrusion onto the shallow continental shelf. In fact, Pass Christian, MS, experienced the largest storm surge ever recorded in the United States during Hurricane Katrina (Ebersole *et al.*, 2007). Finally, western Louisiana is characterized by an east-west coastline, large inland lakes and extensive low-lying wetlands. These features tend to diminish surge heights because the southerly winds in the right center quadrant of the storm are the most effective in pushing water against the coast, and the extensive low-lying wetlands may attenuate transient surges in this area.

In order to model coastal surge in this complex region, we must include all significant flow processes, define accurately the physical system, resolve numerically the system and the energetic flows, and apply accurate algorithms to solve the resulting mathematical model. The goal is to implement a modeling capability that represents the basic physics of the system as it is observed and does not require *ad hoc* model tuning of sub-mesh-scale coefficients, forcing functions and/or boundary conditions.

The processes that affect storm surge inundation include winds, air-sea momentum transfer, atmospheric pressure, wind-driven waves, riverine flows, tides, and friction. Wind is the driving force of both wind-waves and surge, and the

characterization of the marine winds is paramount to obtaining accurate surge predictions. Wind-wave generation and propagation, subsequent depth-limited breaking and dissipation by vegetation in the nearshore or floodplain, and the associated transfer of the wind-wave momentum through wave radiation stress gradient forcing, influence storm surge elevations and currents and modify the peak surge, the time of arrival of the peak surge, and drawdown. Water levels, currents, and wind-waves affect the atmospheric boundary layer and the air-sea momentum transfer while water levels and currents affect the generation and transformation of waves. Riverine flows not only affect overall water levels, but can also affect the propagation of wind waves, tides, and surge up the rivers. Although tides are modest in the region and dominated by less energetic diurnal tides, they modify water levels and can do so nonlinearly. We consider the full nonlinear interaction of these processes to simulate wave and water level conditions throughout the domain.

Tides, waves, and surge are influenced by both basin-scale and local-scale geometric features and flow gradients. Astronomical tides in the Gulf of Mexico are affected by basin-wide generation and shelf dissipation processes, while inland propagation of these tides is affected by the details of the connecting channels and marshes. Storm surge in Lake Pontchartrain depends not only on local setup but also on the high-volume inflows from Lake Borgne through the Rigolets and Chef Menteur passes, and over the inter-lake marshes. In turn, the Lake Pontchartrain - Lake Borgne storm surge flow exchange depends on the water pushed onto the Mississippi-Alabama shelf, wind-wave breaking induced set up, the level of attenuation of surge into inland Mississippi, and local geometry and bathymetry.

The complexity of the entire system must be defined accurately and resolved computationally in the numerical models in order for the growth, propagation, and attenuation of waves, surge, tides, and riverine flows to be modeled correctly. High mesh resolution is necessary when high spatial gradients exist in the geometric and topographic features as well as in the waves, surface elevations, and currents. The emergence of high-density observational data such as LiDAR and satellite photography has significantly improved the accurate characterization of topography, raised features, and surface roughness. In addition, dense soundings have improved the accurate characterization of the bathymetry.

In this chapter, we describe the "SL15" storm surge model for Louisiana and Mississippi, which couples a sequence of well-verified and validated wind, short-period wind-wave, and coastal circulation models as an atmospheric-hydrodynamic modeling system. We validate independently each process with the available observational data, quantify differences between the component modeled and observational data and when possible estimate the uncertainty in the observational data itself. We stress that the validity of the coupled system relies on its ability to represent accurately the individual components and to then couple nonlinearly these components. We derive error estimates for the modeled river flows, tides, and Hurricane Katrina and Rita winds, waves and surge levels. In the following chapter, we describe the detailed evolution and physics of winds, waves, surface elevation, and currents during Hurricanes Katrina and Rita (Dietrich *et al.*, 2010a).

2.3 Coupled Wind, Wind-Wave, Tide, Riverine Flow Model System

2.3.1 Kinematic Winds

For hindcasting historical storms, we define wind fields using objectively-analyzed measurements. Observational data comes from anemometers, airborne and land-based Doppler radar, airborne stepped-frequency microwave radiometer, buoys, ships, aircraft, coastal stations, and satellite measurements. For Katrina, the measured winds in the inner core are assimilated using NOAA's Hurricane Research Division Wind Analysis System (H*WIND) (Powell *et al.*, 1996; Powell *et al.*, 1998) and are then blended with Gulf-scale winds using an Interactive Objective Kinematic Analysis (IOKA) System (Cox *et al.*, 1995; Cardone *et al.*, 2007). H*WIND composites observations of wind velocity relative to the storm's center and transforms them to a common reference condition of 10m height, peak 1min-averaged "sustained" wind speed, and marine exposure. A special set of H*WIND reanalyzed snapshots are available for Katrina (Powell *et al.*, 2008). Peripheral winds are derived from the NOAA National Centers for Environmental Prediction/National Center for Atmospheric Research Reanalysis Project (Kalnay *et al.*, 1996). Before inner-core and peripheral wind fields are blended, the inner-core peak "sustained" winds are transformed to 30min-averaged wind speeds using a gust model consistent with the H*WIND system. A final step is to inject local marine data, adjusted to a consistent 10m elevation and neutral stability using the IOKA System. Lagrangian-based interpolation is used to produce the final wind fields on a regular 0.05° x 0.05° mesh with snapshots every 15 min. Hurricane Rita inner-core wind fields are based mainly on the TC96 mesoscale model (Thompson and Cardone, 1996) solutions blended as described above into peripheral fields using IOKA (Cardone and Cox, 2007; Cardone *et al.*, 2007). Both

hurricanes' pressure fields used to drive the atmospheric pressure term in the circulation model are derived using a widely-adopted parametric relationship (Holland, 1980).

2.3.2 Deep-water Wave Model WAM

The WAM model is run to generate deepwater wave fields and directional spectra in a Gulf of Mexico domain. WAM is a third-generation discrete spectral wave model that solves the wave action balance equation and includes source-sink terms, atmospheric input, nonlinear wave-wave interactions, white-capping, bottom friction, and depth-limited wave breaking. The spatial and temporal variation of wave-action in frequency and direction is solved over a fixed spatial mesh (Komen *et al.*, 1994). WAM has recently undergone major revisions to source term specification, multi-mesh nesting, and depth-limited breaking (Gunther, 2005). The model computes directional wave spectra for 28 discrete frequency bands and 24 directional bands centered every 15°.

The WAM model domain, shown in Figure 2.1, extends over the entire Gulf of Mexico with a mesh at 0.05° resolution. It is assumed that the wind waves are generated in the Gulf and that wave energy entering the Gulf and reaching the area of interest through the Florida and Yucatan Straits is minimal. Wave data within and outside of the Gulf indicates that the dominant wave energy is generated within the Gulf, along with the hurricane. The WAM model allows wave energy to propagate out of the Gulf through the Yucatan and Florida straits. The water depth is derived from the General Bathymetric Chart of the Oceans (GEBCO, 2003). The H*WIND/IOKA 30min-averaged wind fields are linearly interpolated in time and space onto the WAM mesh.

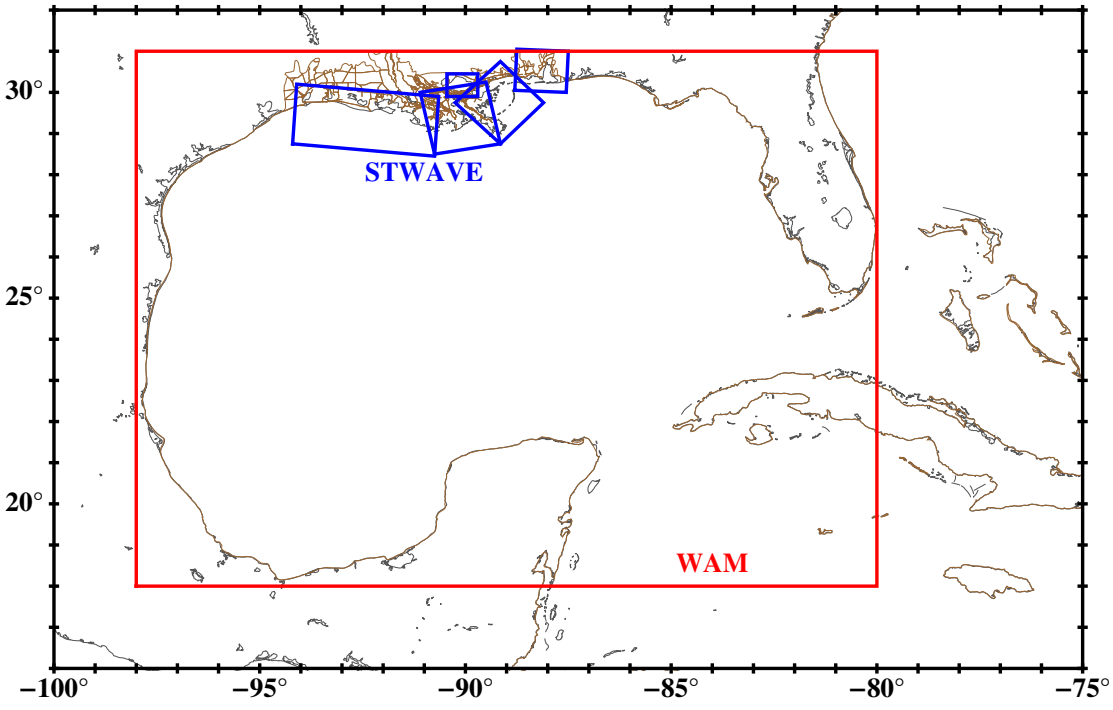

Figure 2.1. WAM model domain shown in red and nested STWAVE model domains shown in blue. In order from west to east, the five STWAVE domains are W, S, LP, SE and MS-AL, as described in Table 2.1.

2.3.3 Nearshore Wave Model STWAVE

The nearshore wind-wave model STWAVE (Smith, 2000; Smith *et al.*, 2001; Smith and Smith, 2001; Thompson *et al.*, 2004) is used to generate and transform waves to the shore. STWAVE solves the steady-state conservation of spectral action balance along backward-traced wave rays. The source terms include wind input, nonlinear wave-wave interactions, dissipation within the wave field, and surf-zone breaking. The computed terms include wave propagation and source terms representing energy growth and decay in the spectrum. The assumptions made in STWAVE include a mild bottom slope; negligible wave reflection; steady

waves, currents, and winds; linear refraction and shoaling, and a depth-uniform current. STWAVE can be implemented as either a half-plane model, where only waves propagating toward the coast are represented, or a full-plane model, allowing generation and propagation in all directions. Wave breaking in the surf zone limits the maximum wave height based on the local water depth and wave steepness.

Four or five STWAVE meshes are used to simulate nearshore and coastal floodplain wind-wave propagation and attenuation. These meshes, also shown in Figure 2.1 and summarized in Table 2.1, extend across coastal Louisiana, Mississippi, and Alabama. The spatial resolution of each STWAVE mesh is 200m. Bathymetry for all meshes is interpolated from the ADCIRC mesh.

Open-water boundary conditions are obtained by extracting the wave energy spectra from the WAM solutions at the STWAVE boundary vertices. The wind fields are interpolated from the ADCIRC wind fields, which apply land effects to the H*WIND/ IOKA marine wind fields. STWAVE is run at 30 min intervals for 2 days. The STWAVE computations include preliminary water levels interpolated from ADCIRC simulations forced only with wind, atmospheric pressure, riverine flows, and tides. Radiation stresses computed with STWAVE are added as input to a subsequent ADCIRC simulation.

TABLE 2.1

SUMMARY OF STWAVE MESHES

Mesh	Origin	Orientation	x Cells	y Cells	STWAVE Version	Storm Usage
Lake Pontchartrain (LP)	-90.4668°, 30.4301°	270°	284	352	Full plane	Katrina, Rita
Louisiana southeast (SE)	-88.1354°, 29.9731°	141°	683	744	Half plane	Katrina, Rita
Louisiana south (S)	-89.0945°, 28.9617°	108°	825	839	Half plane	Katrina, Rita
Mississippi and Alabama (MS-AL)	-87.6000°, 30.0000°	90°	563	605	Half plane	Katrina, Rita
Louisiana west (W)	-90.7332°, 28.4633°	86°	980	1740	Half plane	Rita

2.3.4 ADCIRC Circulation Model

The last component of the system is the ADCIRC unstructured coastal ocean circulation model, which is applied to compute surface water elevation and currents. The ADCIRC model solves the depth-integrated barotropic shallow-water equations in spherical coordinates using a finite-element solution (Luettich and Westerink, 2004; Atkinson *et al.*, 2004a; Dawson *et al.*, 2006; Westerink *et al.*, 2008). The solution maintains both accuracy and robustness when applied to the wide range of scales of motion and wide range of hydrodynamic balances that exist when computing flows in the deep ocean transitioning to flows in inlets, floodplains, and rivers. The use of an unstructured mesh allows for high localized mesh resolution where solution gradients are large, and low mesh resolution where solution gradients are small, minimizing both local and global error norms for a given computational cost.

2.3.5 SL15 Domain and Mesh

The ADCIRC SL15 model domain, shown in Figure 2.2, is an evolution of the earlier EC2001 U.S. East Coast and Gulf of Mexico astronomical tide model and the S08 Southern Louisiana storm surge model (Blain *et al.*, 1994; Mukai *et al.*, 2002; Westerink *et al.*, 2008). These models incorporate the western North Atlantic Ocean, the Gulf of Mexico, and the Caribbean Sea to allow for full dynamic coupling between oceans, continental shelves, and the coastal floodplain without necessitating that these complicated couplings be defined in the boundary conditions. The SL15 model extends the coverage of these earlier models to include all the floodplains of Southern Louisiana and Mississippi. In addition, improved definitions of features, surface roughness, wave radiation stress, and mesh resolution

are incorporated. The highly-resolved floodplain in the SL15 model extends from Beaumont, TX, to Mobile Bay. Areas in Texas and Alabama are included to allow storm surge that affects Louisiana and Mississippi to attenuate realistically and spread laterally into the adjacent states. In Southern Louisiana and Mississippi, the northern land boundary extends along the 10-20 m elevation contours or major hydraulic controls. Details of the domain with bathymetry and topography as well as levees and raised roadways across Southern Louisiana can be seen in Figures 2.3 - 2.5 with geographic places of interest listed in Table 2.2.

The computational mesh resolves the tidal, wind, atmospheric pressure, and riverine-flow forcing functions and flow processes from the ocean basins to the coastal floodplain. Effective resolution of tidal and hurricane response within the basins and on the shelf is determined by tidal wavelength, topographic length scale criteria, and hurricane size criteria (Westerink *et al.*, 1994; Blain *et al.*, 1998; Hagen *et al.*, 2001). The mesh applies localized refinement of the coastal floodplains and of the important hydraulic features, down to 50 m in critical channels and conveyances, as shown in Figure 2.6. We accommodate the STWAVE forcing function by adding a swath of 50-200 m mesh resolution along the coast, over barrier islands, and around Lake Pontchartrain where there are significant gradients in the wave radiation stresses and where forcing of surge through wave transformation is the largest. Barrier islands also need high mesh refinement to resolve the very high currents that develop when these features are overtopped.

The SL15 mesh contains 2,409,635 vertices and 4,721,496 elements. Resolution varies from 24 km in the Atlantic Ocean to about 50 m in Louisiana and Mississippi. Unstructured meshes can resolve the critical features and the associated local flow processes with fewer computational vertices than a structured mesh.

TABLE 2.2

GEOGRAPHIC LOCATION BY TYPE AND NUMBER

Type	Number	Geographic Location
Rivers and channels	1	Sabine Pass
	2	Calcasieu Shipping Channel
	3	Atchafalaya River
	4	Mississippi River
	5	Southwest Pass
	6	Pass Manchac
	7	Inner Harbor Navigation Canal (IHNC)
	8	Gulf Intracoastal Waterway (GIWW)
	9	Mississippi River Gulf Outlet
	10	Chef Menteur Pass
	11	Rigolets
	12	Pearl River
	13	Yucatan Strait
	14	Florida Strait
Bays, lakes and sounds	15	Sabine Lake
	16	Calcasieu Lake
	17	Grand Lake
	18	White Lake
	19	Vermilion Bay
	20	Atchafalaya Bay

TABLE 2.2

Continued

Type	Number	Geographic Location
	21	Terrebonne Bay
	22	Timbalier Bay
	23	Barataria Bay
	24	Lake Maurepas
	25	Bayou Labranche
	26	Lake Pontchartrain
	27	Lake Borgne
	28	Breton Sound
	29	Chandeleur Sound
	30	Mississippi Sound
	31	St. Louis Bay
	32	Biloxi Bay
	33	Pascagoula Bay
	34	Mobile Bay
Islands	35	Marsh Island
	36	Point au Fer Island
	37	Isle Dernieres
	38	Timbalier Island
	39	Grand Isle
	40	Chandeleur Islands

TABLE 2.2

Continued

Type	Number	Geographic Location
	41	Half Moon Island
	42	Deer Island
	43	Singing River Island
	44	Dauphin Island
	45	Florida Keys
Places	46	Port Isabel, TX
	47	Beaumont, TX
	48	Lake Charles, LA
	49	Simmesport, LA
	50	Tarbert Landing
	51	Baton Rouge, LA
	52	Tiger Shoal, Trinity Shoal
	53	Port Fourchon, LA
	54	Venice, LA
	55	Socola, LA
	56	Pointe a la Hache, LA
	57	New Orleans, LA
	58	St. Bernard
	59	New Orleans East
	60	English Turn

TABLE 2.2

Continued

Type	Number	Geographic Location
	61	Caernarvon Marsh
	62	CSX Railroad
	63	Biloxi Marsh
	64	Pass Christian, MS
	65	Mississippi-Alabama Shelf
	66	Panama City Beach, FL
	67	Apalachicola, FLA

2.3.6 SL15 Bathymetry and Topography

Geometry, topography, and bathymetry in the SL15 model are defined to replicate the prevailing conditions in August 2005 prior to Hurricane Katrina, with the exception of some of the barrier islands and the area between Lake Pontchartrain and Lake Borgne, which are included as post-Katrina September 2005 configurations. Open ocean and shelf bathymetric depths are interpolated in order of preference from NOAA's bathymetric sounding database, the Digital Nautical Charts database, and the ETOPO5 database (NOS, 1997; USDOD, 1999; NGDC, 1988; Mukai *et al.*, 2002). Inland bathymetry is taken from regional bathymetric surveys from the U.S. Army Corps of Engineers New Orleans District (USACE-MVN).

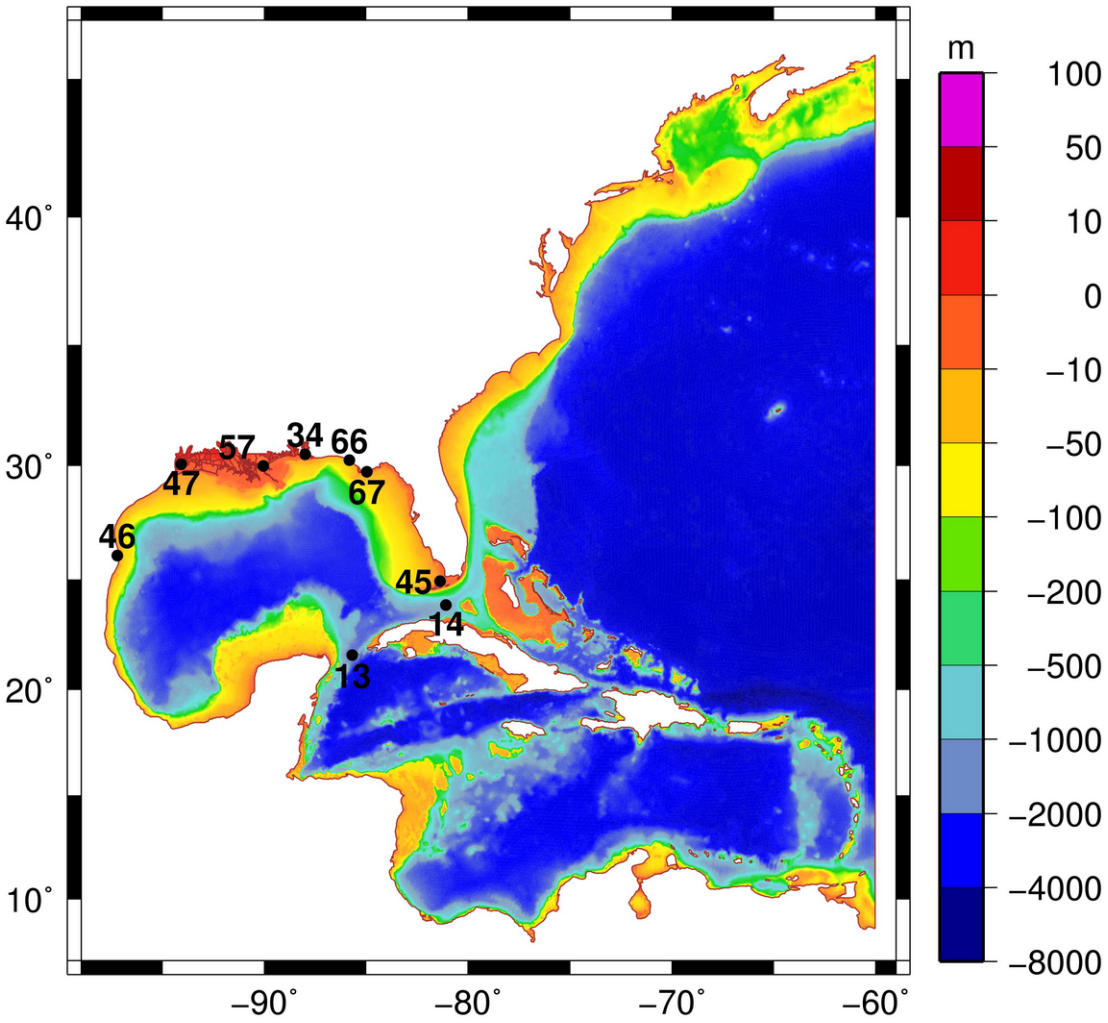

Figure 2.2. ADCIRC SL15 model domain with bathymetry (m). Geographic locations of interest are indicated by numbers identified in Table 2.2.

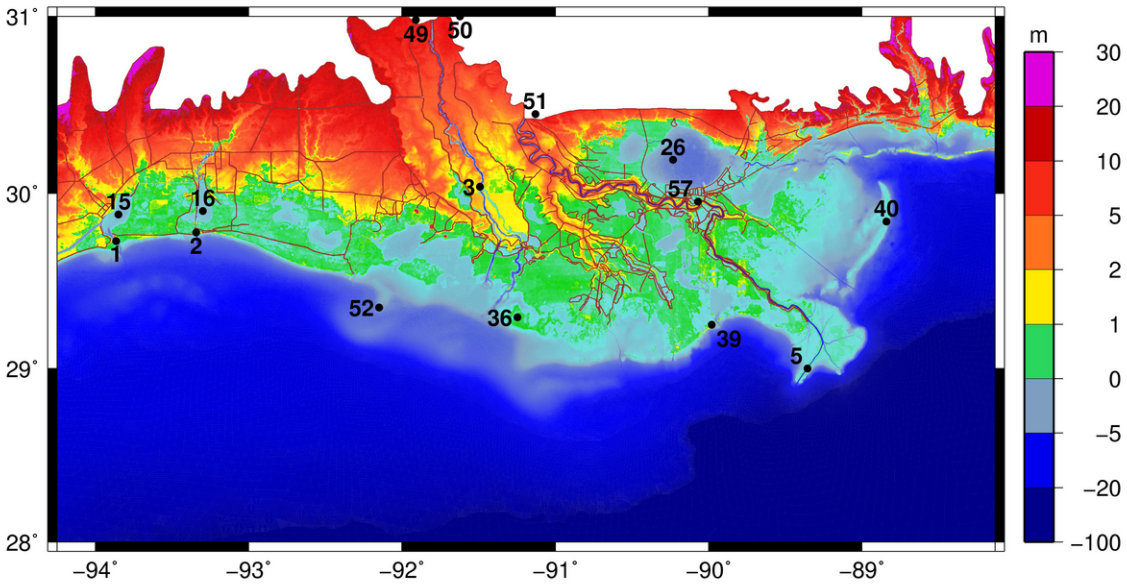

Figure 2.3. Detail of the SL15 domain across southern Louisiana and Mississippi with bathymetry and topography (m, relative to NAVD88 (2004.65)) with raised features such as levees, railroads, and highways shown in brown. Geographic locations of interest are indicated by numbers identified Table 2.2.

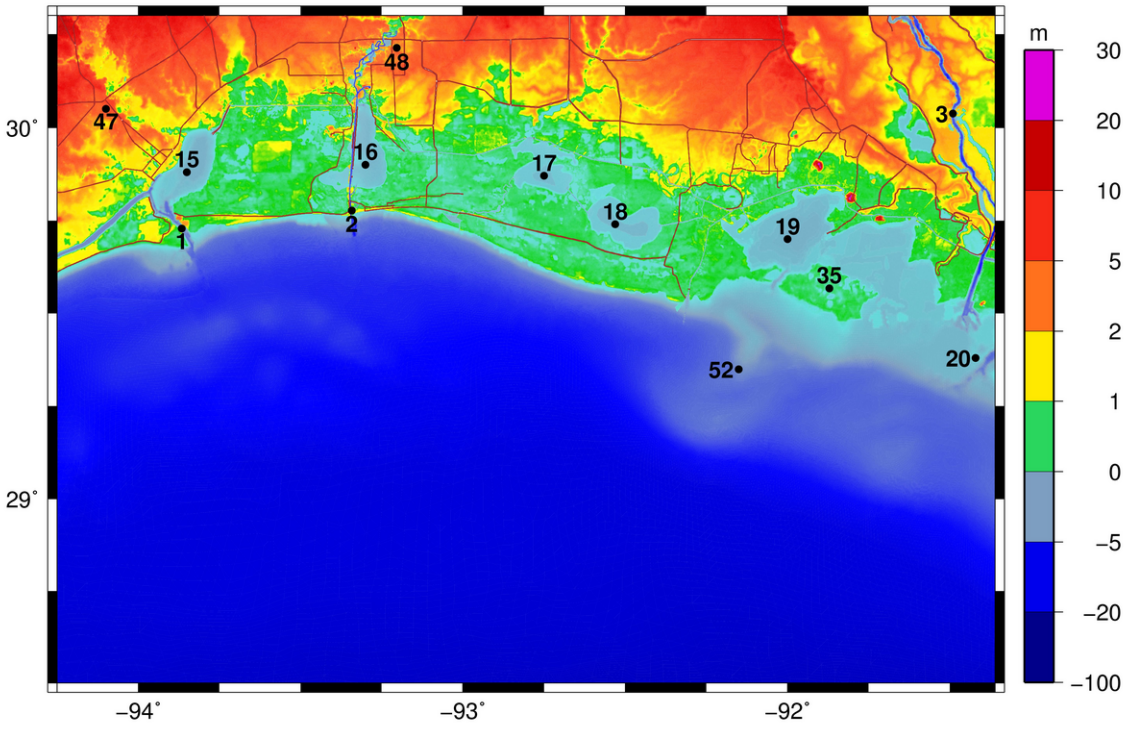

Figure 2.4. Detail of the SL15 domain with bathymetry and topography (m, relative to NAVD88 (2004.65)) across Southwestern Louisiana with raised features, such as levees, railroads, and highways, shown in brown. Geographic locations of interest are indicated by numbers identified in Table 2.2.

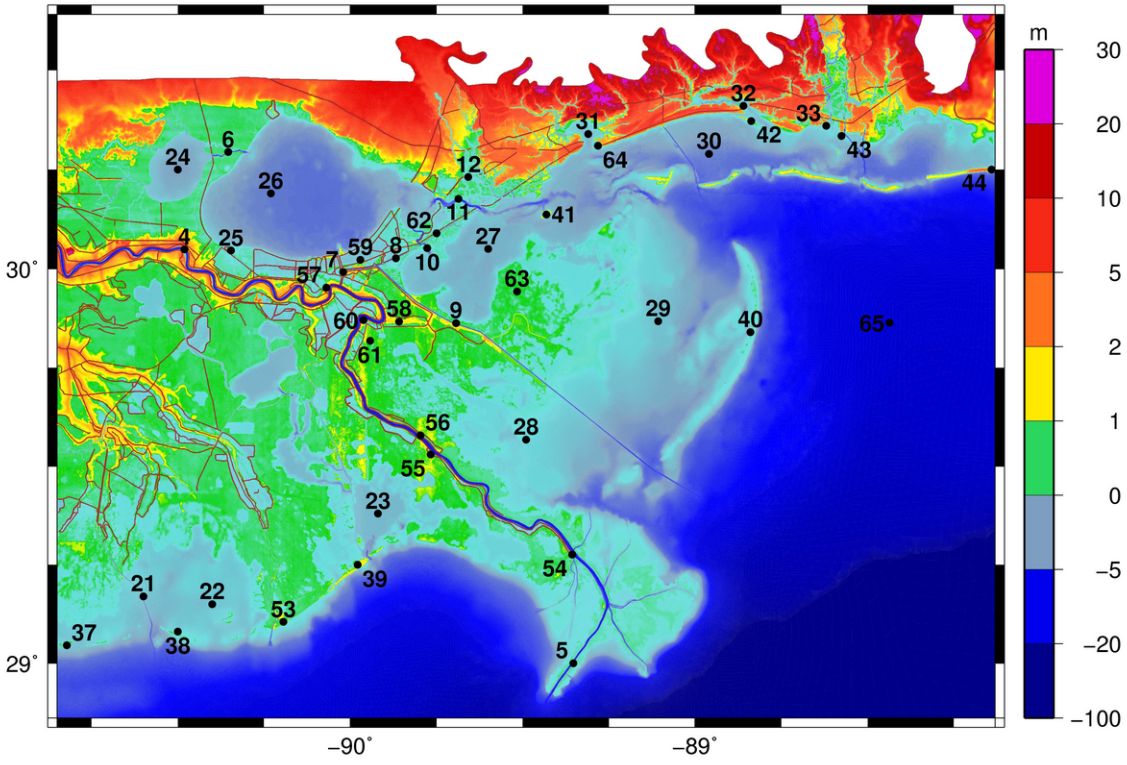

Figure 2.5. Detail of the SL15 domain with bathymetry and topography (m, relative to NAVD88 (2004.65)) across Southeastern Louisiana and Mississippi with raised features, such as levees, railroads, and highways, shown in brown. Geographic locations of interest are indicated by numbers identified in Table 2.2.

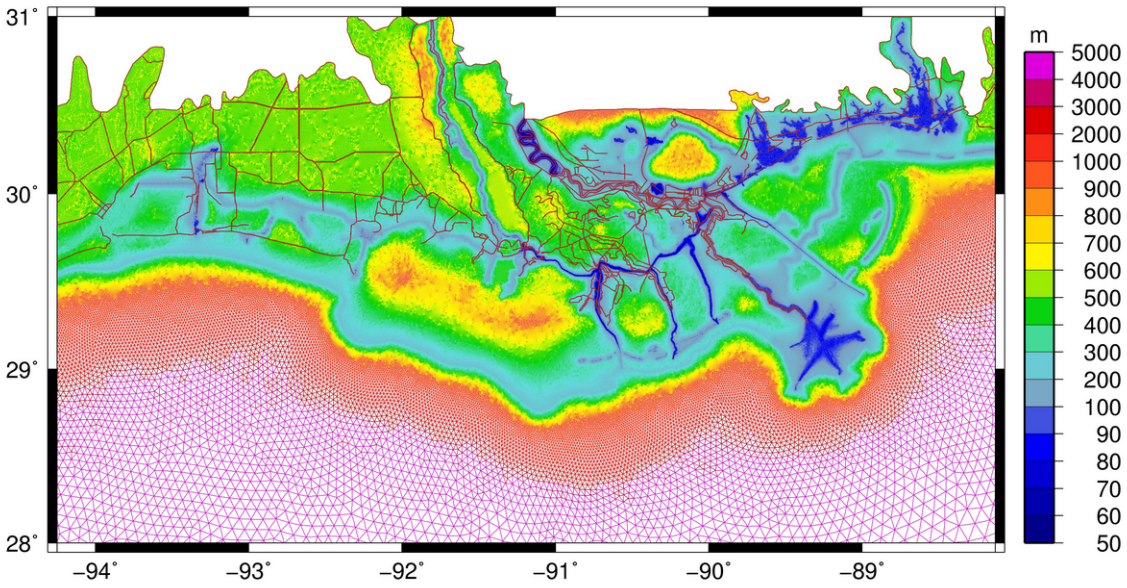

Figure 2.6. Detail of the SL15 grid across Southern Louisiana and Mississippi with finite element sizes shown in m.

Topography in the floodplain is obtained predominantly from the Atlas and the Mississippi Coastal Analysis LiDAR Projects (LSU, 2004; URS, 2006a). Where no data is available in the wetlands, the LA-GAP land cover data (Hartley *et al.*, 2000) is applied with estimated topographic heights of 0.8 m for marshland and -0.4 m for water. USGS post-Katrina LiDAR data is applied to the Chandeleur Islands, and U.S. Army Corps of Engineers (USACE) post-Katrina LiDAR data is used for the Mississippi Sound Islands with the exception of Half Moon Island, Deer Island, and Singing River Island, where MARIS data is used (MARIS, 2006). Levee and road systems that are barriers to flood propagation are features that fall below the defined mesh scale, and represent a non-hydrostatic flow handled as a sub-mesh scale weir (Westerink *et al.*, 2008). All federal levees, many local and private levees and road heights are defined using the USACE- MVN surveys. Road

and railroad crown heights in Louisiana are generally taken from the Atlas LiDAR surveys. Note that the CSX railway between the Rigolets and Chef Menteur Pass in particular is important as a control in the flow between Lake Borgne and Lake Pontchartrain. According to the Atlas LiDAR surveys, the railway has a height of about 3.5m. However, CSX railway personnel involved in the reconstruction indicated that the gravel bed was washed out during the storm and that the remaining compacted bed was at no more than 2m, the elevation incorporated into the model. In addition, US 90 sustained some damage and estimates of the lowered values are made.

2.3.7 Vertical Datum, LMSL and Steric Water Level Adjustments

The North American Vertical Datum of 1988 updated to the 2004.65 epoch, NAVD88 (2004.65) is used as the vertical reference. Topography is available relative to the original epoch, NAVD88, while federal levees and high-water mark (HWM) data are available relative to NAVD88 (2004.65). Garster *et al.* (2007) computed the adjustment from Local Mean Sea Level (LMSL) to NAVD88 (2004.65) at 12 stations throughout southern Louisiana. The average adjustment at the 11 reliable stations is 0.134 m. Additionally, an examination of the datums at NOAA stations in the region reveals that LMSL regionally lies above Mean Lower Low Water (MLLW) by 0.152 m. Thus, bathymetric data, referenced to MLLW, has been regionally adjusted to NAVD88 (2004.65) by adding 0.018 m.

The computations themselves are referenced to NAVD88 (2004.65) by adding 0.134 m to the baseline LMSL reference of the model. Because the computations are barotropic, it is also necessary to account for the annual fluctuation in sea level due to thermal expansion of the upper layers of the Gulf of Mexico and by

other effects. NOAA long-term stations at Dauphin Island, MS, Grand Isle, LA, and Sabine Pass, TX indicate that the increase in surface elevations is bi-modal with station averaged maximum mid- September water levels increasing to 0.158 m above the annual average (`http://tidesandcurrents.noaa.gov/sltrends/sltrends.html`). This expansion is also captured in harmonically decomposed tidal records by the long-term S_a and S_{sa} constituents, which show an average regional combined amplitude of 0.15 m with a standard deviation of 0.03 m. To make the seasonal sea surface adjustment for a specific storm, the regional long-term sea level station data is used at the date of landfall. Thus for Katrina, which occurred in late August, sea surface level increase above the annual average is regionally estimated as 0.10 m above LMSL, while for Rita, which made landfall on September 24, the estimated increase is 0.15 m. Initial water levels in the model are therefore raised at the start of the computation with the combined average regional difference between LMSL and NAVD88 (2004.65) in addition to the steric increase. For Katrina, this adjustment equals 0.13 m + 0.10 m = 0.23 m. For Rita, the adjustment equals 0.13 m + 0.15 m = 0.28 m.

2.3.8 Hydraulic Friction

Bottom friction is computed by the standard quadratic parameterization of bottom stress using a Manning's n formulation. Nodal Manning's n coefficients are spatially assigned using land cover definitions from the USGS LA-GAP in Louisiana, USGS MS- GAP in Mississippi, and the USGS National Land Cover Data (NLCD) in Texas and Alabama (Hartley *et al.*, 2000; Villea, 2005; Vogelmann *et al.*, 2001). The GAP data are preferred because the classification system, particularly in wetlands, is more detailed than the NLCD data. The Manning's

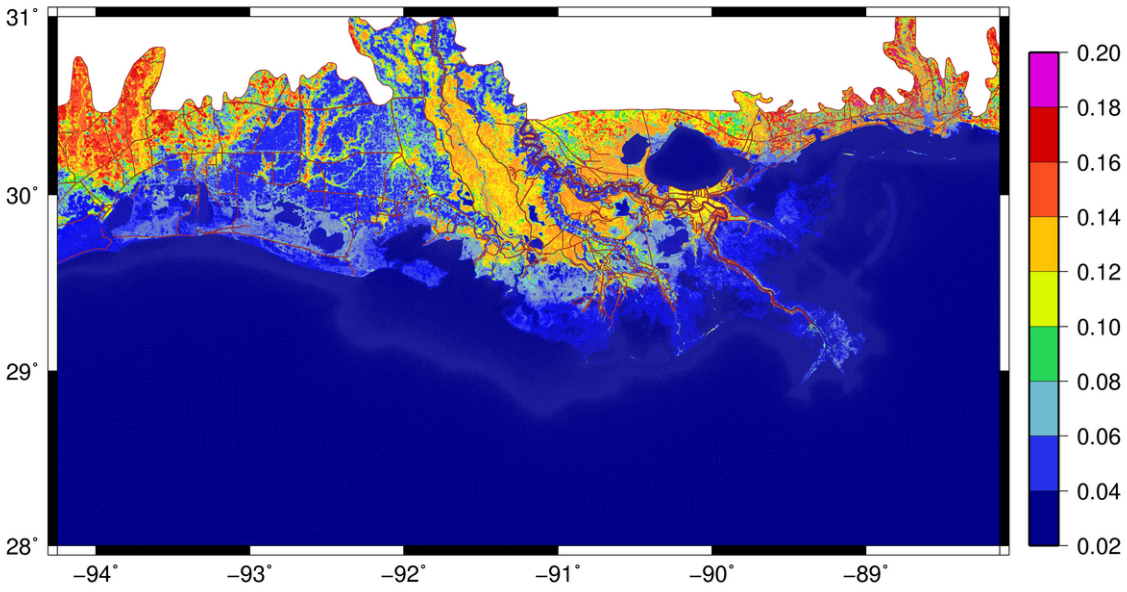

Figure 2.7. Detail of the applied Manning's n roughness coefficients for Southern Louisiana.

n associated with these land classifications, presented in Tables 2.3 - 2.5, are selected or interpolated from standard hydraulic literature (Chow, 1959; Barnes, 1967; Arcement and Schneider, 1989). For the open ocean, large inland lakes, sheltered estuaries, deep straight inlet channels, deep meandering rivers, and shallow meandering channels, n is assigned 0.02, 0.02, 0.025, 0.025, 0.025, 0.045, respectively. Figure 2.7 shows the applied Manning's n values in Southern Louisiana. The bottom friction coefficient C_f has a defined lower limit equal to 0.003 in ocean and shelf waters in order to be consistent with Mukai *et al.* (2002). Lateral eddy viscosity is uniformly set to 5 m^2 s^{-1} in water and 50 m^2 s^{-1} on land.

TABLE 2.3

MANNING'S n VALUES FOR LA-GAP CLASSIFICATION

LA-GAP Class	Description	Manning's n
1	Fresh marsh	0.055
2	Intermediate marsh	0.050
3	Brackish marsh	0.045
4	Saline marsh	0.035
5	Wetland forest - deciduous	0.140
6	Wetland forest - evergreen	0.160
7	Wetland forest - mixed	0.150
8	Upland forest - deciduous	0.160
9	Upland forest - evergreen	0.180
10	Upland forest - mixed	0.170
11	Dense pine thicket	0.180
12	Wetland scrub/shrub - deciduous	0.060
13	Wetland scrub/shrub - evergreen	0.080
14	Wetland scrub/shrub - mixed	0.070
15	Upland scrub/shrub - deciduous	0.070
16	Upland scrub/shrub - evergreen	0.090
17	Upland scrub/shrub - mixed	0.080
18	Agriculture - crops - grass	0.040
19	Vegetated urban	0.120
20	Nonvegetated urban	0.120

TABLE 2.3

Continued

LA-GAP Class	Description	Manning's n
21	Wetland barren	0.030
22	Upland barren	0.030
23	Water	0.020-0.045

TABLE 2.4

MANNING's n VALUES FOR MS-GAP CLASSIFICATION

MS-GAP Class	Description	Manning's n
1	Agriculture	0.060
2	Freshwater	0.025
3	Aquaculture	0.045
4	Estuarine water	0.025
6	Farmed wetlands	0.035
7	Estuarine emergent	0.050
8	Estuarine woody	0.060
9	Palustrine emergent	0.055
10	Bottomland hardwood	0.140
11	Riverine swamp	0.060

TABLE 2.4

Continued

MS-GAP Class	Description	Manning's n
12	Pine savannah	0.160
13	Freshwater shrub/scrub	0.070
14	Palustrine nonvegetated	0.030
15	Transportation	0.032
16	High density urban	0.150
24	Urban freshwater	0.025
25	Wet soil / water / shadow	0.040
26	Urban pine	0.180
27	Urban hardwood	0.160
28	Urban low herbaceous	0.070
29	Urban grassy / pasture	0.035
30	Bare urban I	0.120
31	Bare urban II	0.120
32	Clear cuts	0.036
50	Low-density pine	0.160
51	Medium-density pine	0.180
52	High-density pine	0.200
53	Medium-density hardwood	0.170
54	High-density hardwood	0.170
55	Mixed forest	0.160

TABLE 2.4

Continued

MS-GAP Class	Description	Manning's n
56	Recent harvest	0.052
57	Cypress / tupelo	0.180
60	Agriculture	0.060
61	Grassy / pasture / range	0.042
62	Low herbaceous wetland	0.047
63	Evergreen shrub	0.080
71	Wetland	0.045
80	Bare	0.030
81	Sand bar / beach	0.030

TABLE 2.5

MANNING's n AND LAND ROUGHNESS VALUES FOR 1992 NLCD CLASSIFICATION

NLCD Class	Description	Manning's n	z_{0-land}
11	Open water	0.022	0.001
12	Ice / snow	0.022	0.012
21	Low residential	0.120	0.330

TABLE 2.5

Continued

NLCD Class	Description	Manning's n	z_{0-land}
22	High residential	0.121	0.500
23	Commercial	0.050	0.390
31	Bare rock / sand	0.040	0.090
32	Gravel pit	0.060	0.180
33	Transitional	0.100	0.180
41	Deciduous forest	0.160	0.650
42	Evergreen forest	0.180	0.720
43	Mixed forest	0.170	0.710
51	Shrub land	0.070	0.120
61	Orchard / vineyard	0.100	0.270
71	Grassland	0.035	0.040
81	Pasture	0.033	0.060
82	Row crops	0.040	0.060
83	Small grains	0.035	0.050
84	Fallow	0.032	0.050
85	Recreational grass	0.030	0.050
91	Woody wetland	0.140	0.550
92	Herbaceous wetland	0.035	0.110

TABLE 2.6

RIVER FLOW RATES (m^2 s^{-1}) FOR THE VARIOUS SIMULATIONS

Simulation	Mississippi River	Atchafalaya River
River validation	4,730 - 33,110	1,980 - 13,860
Tidal validation	4,730	1,980
Hurricane Katrina	4,730	1,980
Hurricane Rita	5,125	2,240

2.3.9 Riverine Forcing

At the Mississippi River at Baton Rouge and at the Atchafalaya River at Simmesport, inflows are specified with a wave radiation boundary condition that ensures that neither surges nor tides artificially reflect back into the computational domain (Westerink *et al.*, 2008). The river condition is spun up specifying a steady flow with no other forcings in the model, using a 0.5-day hyperbolic ramp, and running to 2.0 days to reach a dynamic steady state. After this, the river radiation boundary condition is applied and other forcings are spun up. The river validation simulation ended at 5.0 days. River flow rates for the simulations are specified in Table 2.6.

2.3.10 Tidal Forcing

After the rivers have reached equilibrium, tides are spun up in the circulation model. Tides are forced on the Atlantic open-ocean boundary along the 60°W meridian with the seven dominant astronomical tidal constituents and include the

diurnal O_1, K_1, and Q_1 constituents and the semi-diurnal M_2, N_2, S_2, and K_2 constituents, using data from Le Provost's FES95.2 global model (Le Provost *et al.*, 1998; Mukai *et al.*, 2002). In addition, tidal potential functions are forced within the model domain for the same constituents. Periods, tidal potential constants, and Earth elasticity factors, which reduce the magnitude of the tidal potential forcing due to Earth tides, are listed in Table 2.7 (Hendershott, 1981). Finally, the nodal factor and equilibrium argument for boundary and interior domain forcing tidal constituents are based on the starting time of the simulation. The resonant characteristics of the Gulf of Mexico and Caribbean Sea require a period of model simulation or spin-up in order for the initial transients to dissipate physically and correct tides to be generated. For the tidal validation simulation, the river ramp was applied from 0.0 to 0.5 days, the river equilibrium occurred from 0.5 to 2.0 days, the tidal forcing ramp was applied from 2.0 to 20.0 days, the tidal forcing equilibrium occurred from 20.0 to 45.0 days, and then the harmonic constituents were analyzed from 45.0 to 105.0 days.

TABLE 2.7

PRINCIPAL TIDAL CONSTITUENTS

Species, j	n	Constituent	Name	Period, T_{jn} (h)	Tidal potential constituents, C_{jn} (m)	Effective earth elasticity factors, α_{jn}
1	1	K_1	Luni-solar	23.934470	0.141565	0.736
	2	O_1	Principal lunar	25.819342	0.100514	0.695
	3	Q_1	Elliptical lunar	26.868357	0.019256	0.695
2	1	M_2	Principal lunar	12.420601	0.242334	0.693
	2	S_2	Principal solar	12.000000	0.112841	0.693
	3	N_2	Elliptical lunar	12.658348	0.046398	0.693
	4	K_2	Luni-solar	11.967235	0.030704	0.693

2.3.11 Atmospheric and Wave Forcing

The IOKA/H*WIND wind field analyses provide marine wind exposure at 10m height and 30min-averaged winds. The wind surface stress is computed by a standard quadratic air-sea drag law. The air-sea drag coefficient is defined by Garratt's drag formula which is based largely on 10min-averaged wind data (Garratt, 1977). The IOKA/ H*WIND winds are therefore adjusted to 10min-averages by noting that shorter sampling periods lead to higher averaged winds and increasing them by a factor of 1.09 as recommended by Cardone. Cardone's factor leads to almost identical 10min winds as would be obtained by converting H*WIND peak 1-min winds to 10-min winds using Powell's recommended conversion factor of 0.89 (Powell *et al.*, 1996). The drag coefficient is limited to 0.0035 to represent sheeting processes. Powell *et al.* (2003) found upper limit values based on GPS dropwindsondes as low as 0.0025 although there appears to be strong quadrantal variation; the limit may be higher in outer portions of the storm and values in shallow shelf waters are only now being obtained.

The ADCIRC model corrects the IOKA/H*WIND marine winds to account for land roughness by making directional adjustments to the marine winds depending on upwind roughness, level of local inundation, and the presence of tree canopies (Westerink *et al.*, 2008). The directional wind reduction is based on USGS NLCD supplemented with GAP Land Cover Classification raster maps for areas identified as cypress forest, combined with land roughness lengths in Table 2.5. In addition, a class for cypress forest was constructed by merging the GAP datasets onto the NLCD data; the $z_{0-land} = 0.550$ for cypress forest. Wind boundary layer re-adjustments depend upon roughness conditions upwind of the location. Figure 2.8 shows sample directional roughness coefficients for steady

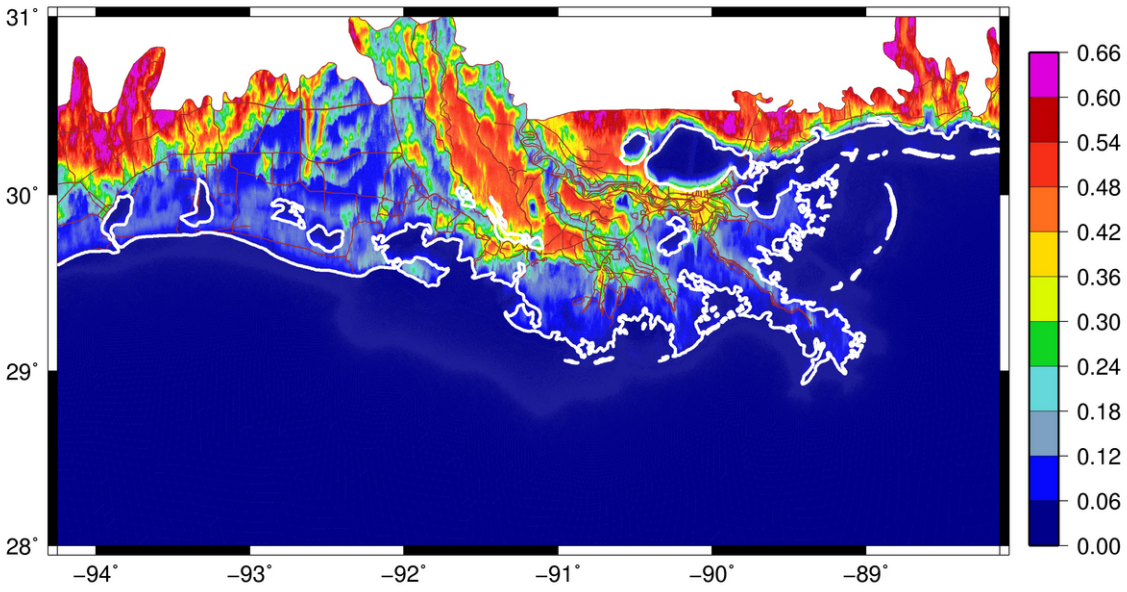

Figure 2.8. Sample of the applied directional wind reduction factor for uniform steady southerly winds for Southern Louisiana. The coastline is outlined in white.

uniform southerly winds. Furthermore, as inundation takes place, the land roughness elements are submerged and the drag is reduced. Finally, canopied areas are defined where there are deciduous forests, evergreen forests, mixed forests, woody wetlands, or cypress forests. Canopies are assumed to be so high that no water overtops them and thick enough for wind not to penetrate them.

For the hurricane simulations, the wind forcings were preceded by a 0.5-day river ramp, a river equilibrium to 2.0 days, and then a tidal forcing and equilibrium to 18.0 days. The wind and pressure fields snapshots are applied every 15 min and are linearly interpolated in time between snaps. For the Hurricane Katrina simulation, the wind forcing was applied from 0000 UTC 25 August 2005 to 0000 UTC 31 August 2005. For the Hurricane Rita simulation, the wind forcing was

applied from 0000 UTC 18 September 2005 to 0000 UTC 25 September 2005. The STWAVE wave radiation stress fields are read every 30min and are linearly interpolated in time and space. For the Hurricane Katrina simulation, the wave forcing was applied from 1215 UTC 28 August 2005 to 1145 UTC 30 August 2005. For the Hurricane Rita simulation, the wave forcing was applied from 1830 UTC 22 September 2005 to 1800 UTC 24 September 2005.

2.3.12 System Performance

The five STWAVE meshes and the ADCIRC SL15 mesh were run on a CRAY XT3 with 2.6 GHz Opteron processors (Sapphire; www.erdc.hpc.mil). The five STWAVE meshes were run with a relatively large time interval of 1800 s, and they required 2484 s per day of simulation on 96 computational cores. The ADCIRC SL15 mesh was run with a relatively small time step of 1 s, and it required 4380 s per day of simulation on 256 computational cores. The ADCIRC model wall-clock times reduce linearly as the number of cores is increased (Kubatko *et al.*, 2009).

2.4 River Validation

The representation of the Mississippi River in the SL15 model was validated by comparing measured and predicted stages at stations from Baton Rouge to Venice, LA, shown in Figure 2.9. At each station, the USACE-MVN has measured stage-flow data, where water level is matched with the flow rate upriver at Tarbert Landing. Using data from multiple years, a best-fit stage-flow curve can be derived at each station, as shown in Figure 2.10.

SL15 model stage-flow curves, obtained by running a variety of steady flow rates on the Mississippi River, are also shown in Figure 2.10. The model-predicted

TABLE 2.8

SUMMARY OF AVERAGE ABSOLUTE DIFFERENCES (m) FOR THE STAGE-FLOW RELATIONSHIPS SHOWN IN FIGURE 2.10

Station name	Station ID	Average absolute difference, SL15 to best-fit curve	Average absolute difference, measured data to best-fit curve
Baton Rouge	01160	0.583413	0.343085
Donaldsonville	01220	0.377853	0.216160
New Orleans	01300	0.120856	0.142391
Alliance	01390	0.181827	0.180448
Empire	01440	0.043808	0.112920
Venice	01480	0.181197	0.112920

stages fall within the scatter of the measured data. It is only at the large flow rates that the SL15 model begins to over- or under-predict the stages. Table 2.8 summarizes the absolute average differences between the SL15 model stages and the measured data derived best fit curve. Table 2.8 also includes the uncertainty in the measured data by computing the absolute differences between the measured data and the measured-data-derived best-fit curve. The differences between the SL15 stages and measured-data-derived best-fit curve are on the same order as the estimated uncertainties in the measured data.

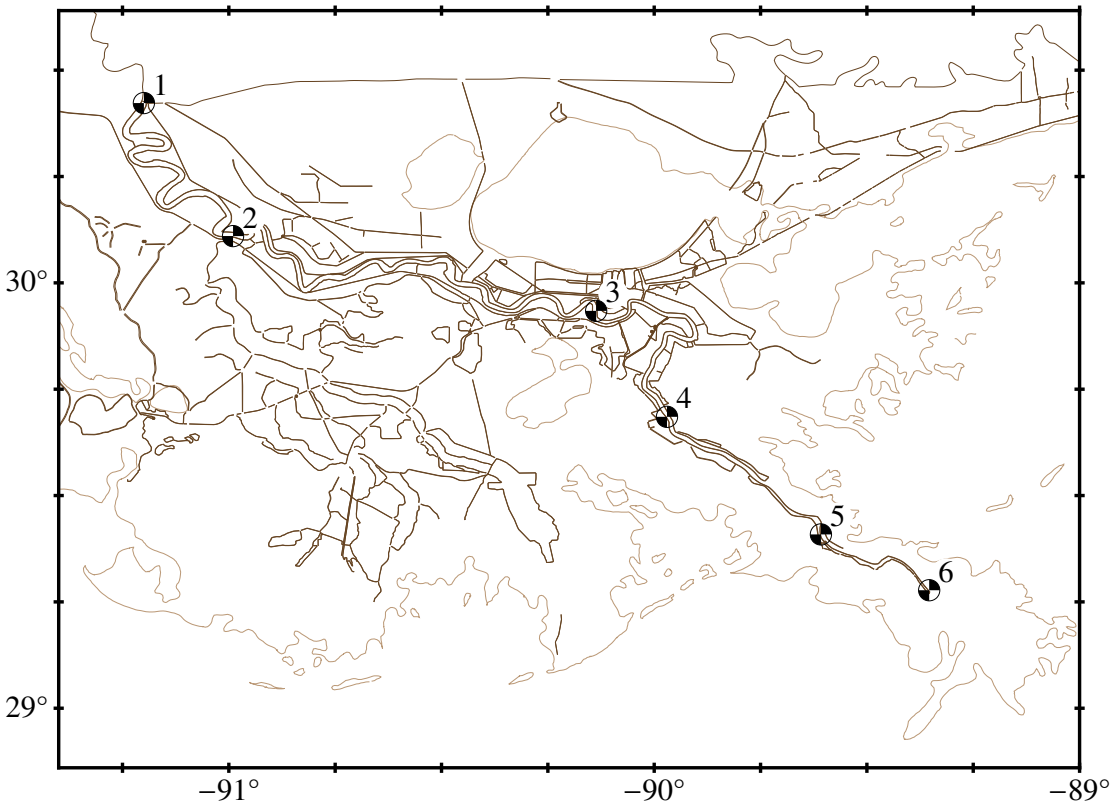

Figure 2.9. Locations of the six USACE stations with stage-flow relationships that were compared to the computed water levels in Figure 2.10. In numerical order, the six stations are: Baton Rouge, Donaldsonville, New Orleans, Alliance, Empire and Venice.

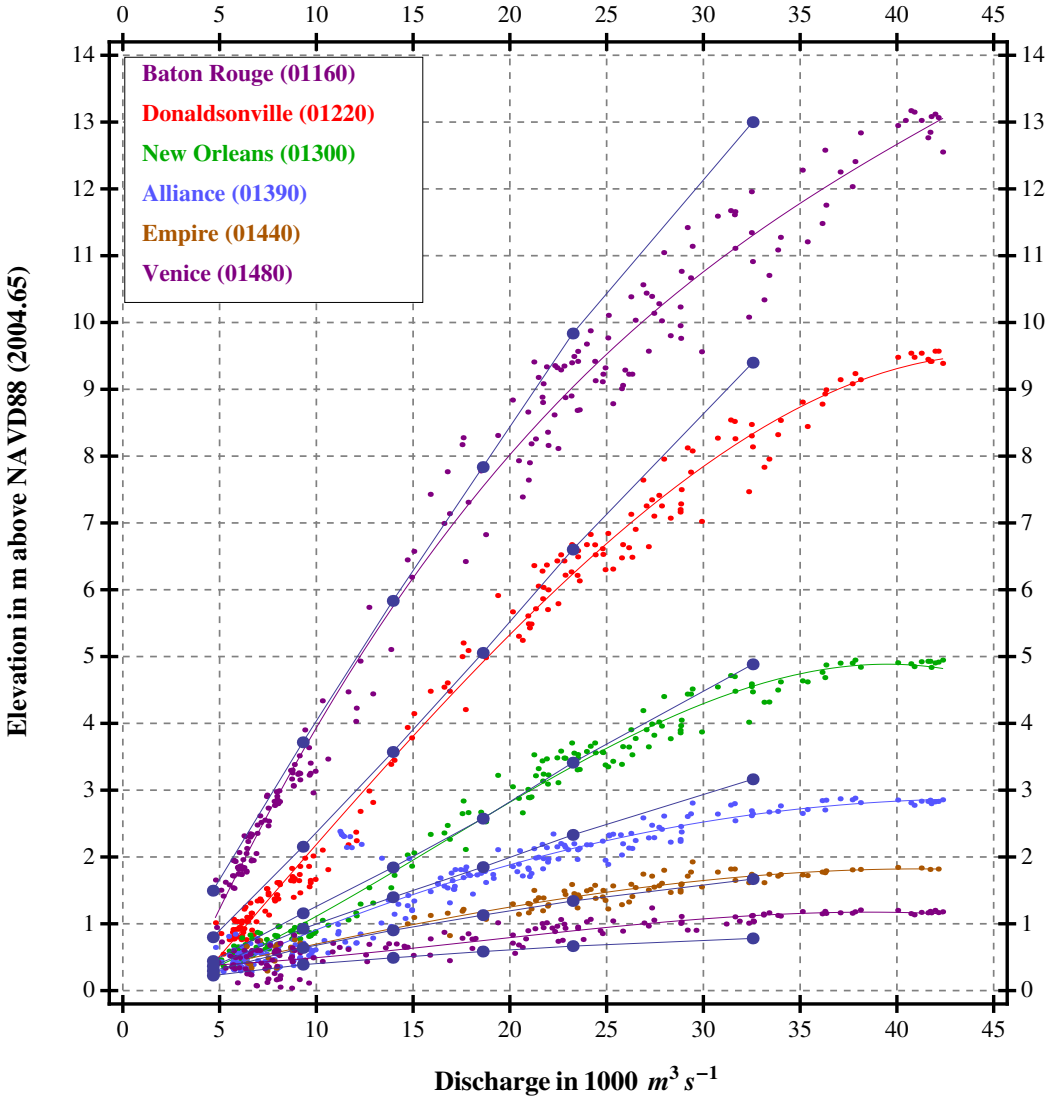

Figure 2.10. Stage-flow relationships at six USACE stations along the Mississippi River. Measured data is shown as scatter points with associated best-fit curves. The predicted data is shown as connected blue dots.

2.5 Tidal Validation

The tides are weak in the Gulf of Mexico, with mixed semi-diurnal and diurnal tides on the Florida shelf up to Apalachicola, FL; diurnally dominated tides between Panama City Beach, FL and Port Fourchon, LA; and mixed tides again being prevalent between Point au Fer Island, LA and Port Isabel, TX. Along all three coastlines, the dominant constituents have amplitudes that are less than 0.2-0.4 m.

SL15 modeled tides are validated by comparing them to measurement-derived data at NOAA tidal harmonic constituent stations. These stations are listed in Table 2.9 and span the Florida Keys to Port Isabel, TX. In Florida and Texas, where the SL15 domain does not include inland waters, stations are selected in open water. In the regions where the SL15 model does resolve inland water bodies, stations are selected in both open water and inland. The station IDs marked with asterisks (*) in Table!2.9 indicate stations whose longitude and latitude were shifted slightly in the ADCIRC SL15 model. Model time histories at the selected stations are analyzed harmonically over 60 days using the 23 constituents defined in Table 2.10.

A comparison is made between the NOAA measured and the SL15 computed amplitudes and phases for the seven dominant constituents in Figure 2.11. Difference bands are defined at 0.025 m and 0.05 m for the amplitude plots and 10° and 20° for the phases. For the 10 stations in Florida, the constituents fall very near or inside the difference bands. For the stations in the other regions, the constituents group together and only the phases of the K_2 constituent show significant differences.

TABLE 2.9

NOAA STATIONS USED IN THE ANALYSIS FOR TIDAL CONSTITUENTS

State	Station ID	Station Name	Longitude (°)	Latitude (°)
FL	8723962*	Key Colony Beach	-81.016667	24.710000
	8724580	Key West	-81.808333	24.553333
	8724698	Loggerhead Key	-82.820000	24.631667
	8725110	Naples	-81.806667	26.130000
	8726724	Clearwater Beach	-82.831667	27.978333
	8727520	Cedar Key	-83.031667	29.135000
	8728130	St. Marks Lighthouse	-84.178333	30.078333
	8728360	Turkey Point	-84.511667	29.915000
	8729210	Panama City Beach	-85.878333	30.213333
	8729678	Navarre Beach	-86.865000	30.376667
MS-AL	8735180*	Dauphin Island	-88.068000	30.250000
	8735181*	Dauphin Island Hydro	-88.068000	30.250000
	8737048	Mobile	-88.043333	30.708333
	8741196	Pascagoula Point	-88.533333	30.340000
	8741533*	Pascagoula NOAA Lab	-88.565263	30.358333
	8742221*	Horn Island	-88.666667	30.240000
	8743281	Ocean Springs	-88.798333	30.391667
	8744117*	Biloxi	-88.903333	30.412408
	8745557	Gulfport Harbor	-89.081667	30.260000

TABLE 2.9

Continued

State	Station ID	Station Name	Longitude (°)	Latitude (°)
	8747437	Bay Waveland Yacht Club	-89.325000	30.325000
	8747766	Waveland	-89.366667	30.281667
LA	8760551	South Pass	-89.140000	28.990000
	8760922	Pilots Station East, SW Pass	-89.406667	28.931667
	8760943	SW Pass	-89.418333	28.925000
	8761720*	Grand Isle	-89.962380	29.269130
	8761724*	Grand Isle East Point	-89.962380	29.269130
	8761927*	New Canal Station	-90.110150	30.027630
	8762075*	Port Fourchon	-90.209420	29.114220
	8762372	East Bank	-90.368333	30.050000
	8762482	West Bank	-90.418333	29.776667
	8764227	Lawma, Amerada Pass	-91.338333	29.448333
	8764311	Eugene Island	-91.385000	29.371667
	8765251	Cypremort Point	-91.880000	29.713333
	8766072	Freshwater Canal Locks	-92.305000	29.713333
	8767816*	Lake Charles	-93.224430	30.223510
	8768094	Calcasieu Pass	-93.343333	29.765000
TX	8770475	Port Arthur	-93.930000	28.866667
	8771510	Galveston Pleasure Pier	-94.788333	29.285000
	8775870	Corpus Christi	-97.216667	27.580000

TABLE 2.9

Continued

State	Station ID	Station Name	Longitude (°)	Latitude (°)
	8779770	Port Isabel	-97.215000	26.060000

TABLE 2.10

HARMONIC CONSTITUENTS USED TO DECOMPOSE MODEL TIME SERIES

Tidal constituent	Tidal description	T_{jn} (h)
Steady	Overtide	
MN	Compound	661.309205
SM	Compound	354.367052
KO	Compound	327.858999
O_1	Principal lunar	25.819342
K_1	Luni-solar	23.934470
Q_1	Elliptical lunar	26.868357
MNS_2	Compound	13.127267
$2MS_2$	Compound	11.606952
N_2	Elliptical lunar	12.658348
K_2	Luni-solar	11.967235

TABLE 2.10

Continued

Tidal constituent	Tidal description	T_{jn} (h)
M_2	Principal lunar	12.420601
$2MN_2$	Compound	12.191620
S_2	Principal solar	12.000000
$2SM_2$	Compound	11.355899
MN_4	Compound	6.269174
M_4	Overtide	6.210301
MS_4	Compound	6.103339
2MN6	Compound	4.166284
M_6	Overtide	4.140200
MSN_6	Compound	4.117870
M_8	Overtide	3.105150
M_10	Overtide	2.484120

Table 2.11 lists the correlation coefficients, R^2, for the four groups of NOAA stations. The R^2 coefficients are greater than 0.942, indicating an excellent match, with the exception of the non-Florida phases. When the K_2 constituent is removed from the analysis, these values increase to greater than 0.937. Note that the K_2 constituent is small and difficult to separate from the larger S_2 constituent in a harmonic analysis of 60 days.

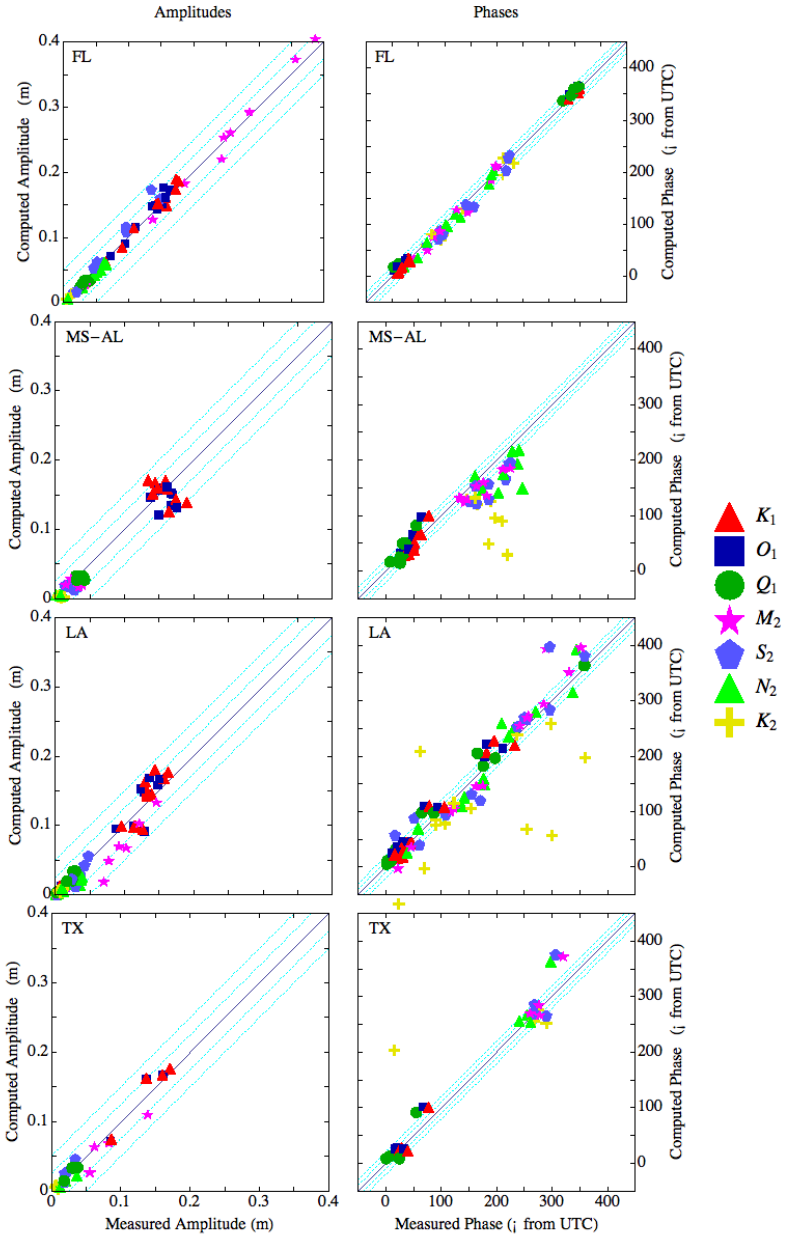

Figure 2.11. Comparison of amplitudes and phases as measured by NOAA and predicted by the SL15 model. Amplitudes are in the left column, while phases are in the right column. Each row of figures represents a region as indicated in Table 2.9 with difference estimates given in Table 2.11.

TABLE 2.11

CORRELATION COEFFICIENTS R^2 OF COMPUTED HARMONIC CONSTITUENTS

		FL	MS-AL	LA	TX
Amplitude	Seven constituents	0.991	0.953	0.947	0.962
	Six constituents (without K_2)	0.990	0.948	0.942	0.957
Phase	Seven constituents	0.993	0.768	0.839	0.896
	Six constituents (without K_2)	0.995	0.937	0.960	0.971

Table 2.12 shows the difference statistics between the NOAA measured and the SL15 computed tidal data for the four groups of NOAA stations. These difference values include measurement uncertainties. Average difference, average absolute difference, and the standard deviation are shown for the amplitudes and phases. In addition, the dimensionless normalized root-mean-square (rms) difference is computed for the amplitudes and is defined as:

$$E_{j-amp}^{c-m} = \sqrt{\frac{\sum_{l=1}^{L}[\hat{\eta}_j^{computed}(x_l, y_l) - \hat{\eta}_j^{meas}(x_l, y_l)]^2}{\sum_{l=1}^{L}[\hat{\eta}_j^{meas}(x_l, y_l)]^2}} \tag{2.1}$$

where L is the number of elevation stations within a region, $(x_l,\ y_l)$ is the station location, $\hat{\eta}_j^{computed}$ is the computed model elevation amplitude for constituent j, and $\hat{\eta}_j^{meas}$ is the NOAA measured elevation amplitude for constituent j. In Table 2.12, the dimensional amplitude differences range from 0.002-0.010 m, and the

TABLE 2.12

DIFFERENCE STATISTICS FOR THE FOUR GROUPS OF NOAA STATIONS

			FL	MS-AL	LA	TX
Amplitude	Seven constituents	Avg (m)	-0.002	0.005	0.002	0.002
		Avg abs (m)	0.006	0.010	0.009	0.009
		Std dev (m)	0.009	0.014	0.013	0.012
		E_{j-amp}^{c-m}	0.023	0.049	0.057	0.044
	Six constituents (without K_2)	Avg (m)	-0.003	0.005	0.002	0.002
		Avg abs (m)	0.007	0.011	0.010	0.010
		Std dev (m)	0.010	0.015	0.014	0.013
		E_{jamp}^{c-m}	0.023	0.049	0.057	0.043
Phase	Seven constituents	Avg (°)	0.810	19.640	0.970	-15.700
		Avg abs (°)	8.540	26.190	26.200	24.970
		Std dev (°)	10.330	38.630	46.720	42.040
	Six constituents (without K_2)	Avg (°)	-0.360	10.540	-7.480	-12.380
		Avg abs (°)	7.960	17.970	18.110	19.270
		Std dev (°)	9.610	23.620	24.500	24.670

dimensionless amplitude differences range from 0.023-0.057. The phase differences range from 1° to 26°. The phase behavior improves when the K_2 constituent is excluded from the analysis.

We note that these quantities reflect the differences between the NOAA measured and the SL15 model harmonic constituents and therefore include the uncertainties in the NOAA measured data itself. In order to estimate the uncertainties in the NOAA measured data, we compare the current (as of March 2007) NOAA published harmonic data to previously measured and published NOAA harmonic constituent data. The normalized rms amplitude and absolute average phase differences in the NOAA data at stations with multiple measured values are listed in Table 2.13. Overall, the normalized rms amplitude differences range between 0.013 and 0.041, the average phase differences range between 5.8° and 18.4°. The measurement data uncertainties estimated by the differences between the two NOAA data sets can be explained by the shifting geometry/bathymetry of coastal regions and the occurrences of non-tidal events including wind-driven events, radiational heating cycles, and riverine discharges. The measurement uncertainties represent 35-60 percent of the model-to-measurement amplitude differences for the majority of the constituents. For the model-to-measurement phase differences, the measurement uncertainties account for 50-80 percent. The results in Table 2.13 indicate that a significant portion of the difference between the model and the measurement data can be attributed to uncertainties in the measurements themselves.

2.6 Hurricane Katrina

Hurricane Katrina is incomparable in U.S. recorded events in terms of surge levels and the quality and quantity of recorded data. Wind, wave, and water level

TABLE 2.13

SL15-COMPUTED AND NOAA-MEASURED DIFFERENCES FOR EACH HARMONIC CONSTITUENT

	Constituent	SL15-computed and NOAA-measured /analyzed difference	Estimated NOAA-measured/analyzed data uncertainties
Normalized rms constituent amplitude difference	K_1	0.041	0.019
	O_1	0.038	0.020
	Q_1	0.045	0.032
	M_2	0.036	0.013
	S_2	0.064	0.015
	N_2	0.076	0.031
	K_2	0.084	0.041
Avg absolute constituent phase difference	K_1	7.620	5.810
	O_1	11.840	9.380
	Q_1	10.320	6.370
	M_2	18.640	16.640
	S_2	24.190	11.750
	N_2	22.460	18.370
	K_2	60.160	11.060

data were collected during the event, and extensive post-event surveys of HWMs were made and referenced to NAVD88 (2004.65).

Wind speed and direction data collected during Hurricane Katrina at 12 NDBC buoys, shown in Figure 2.12, are used to validate the H*WIND/IOKA wind fields. It should be noted that the NDBC buoy data are assimilated into the H*WIND/IOKA analysis, but that many other sources of data also influenced the analysis. Differences between the H*WIND/IOKA wind and that measured at the buoys is indicative of the analysis' fidelity to all the input data. Comparisons at buoys close to the storm track are shown in Figure 2.13. The H*WIND/IOKA winds match the oscillations in the wind speeds before the storm, the magnitude of the peak winds, and the rate at which the winds die down after the storm passes the buoys. A one-to-one comparison of available peak wind speeds at 11 buoys shows a best-fit slope of 0.99 and an R^2 value of 0.93, indicating a good match between measured and predicted data.

At the same buoys, significant wave heights and peak wave periods are used to validate the WAM model as shown in Figure 2.14. WAM matches the timing and magnitude of the peaks at the selected buoys, and a one-to-one comparison of peak significant wave heights at all 12 deep-water buoys shows a best-fit slope of 0.93 and an R^2 value of 0.90. Station 42040 misses the quick peak at this buoy as do other wave models. It is unclear if the wind fields are regionally missing features, the models are unable to achieve the maximum wave heights or if the buoy data is biased for the two peak data points at this station. The results of the frequency spectra and the mean wave direction as a function of frequency comparisons have similar trends. Matching energy levels and mean wave directions across the entire frequency range for all NDBC sites show differences that are consistent with the

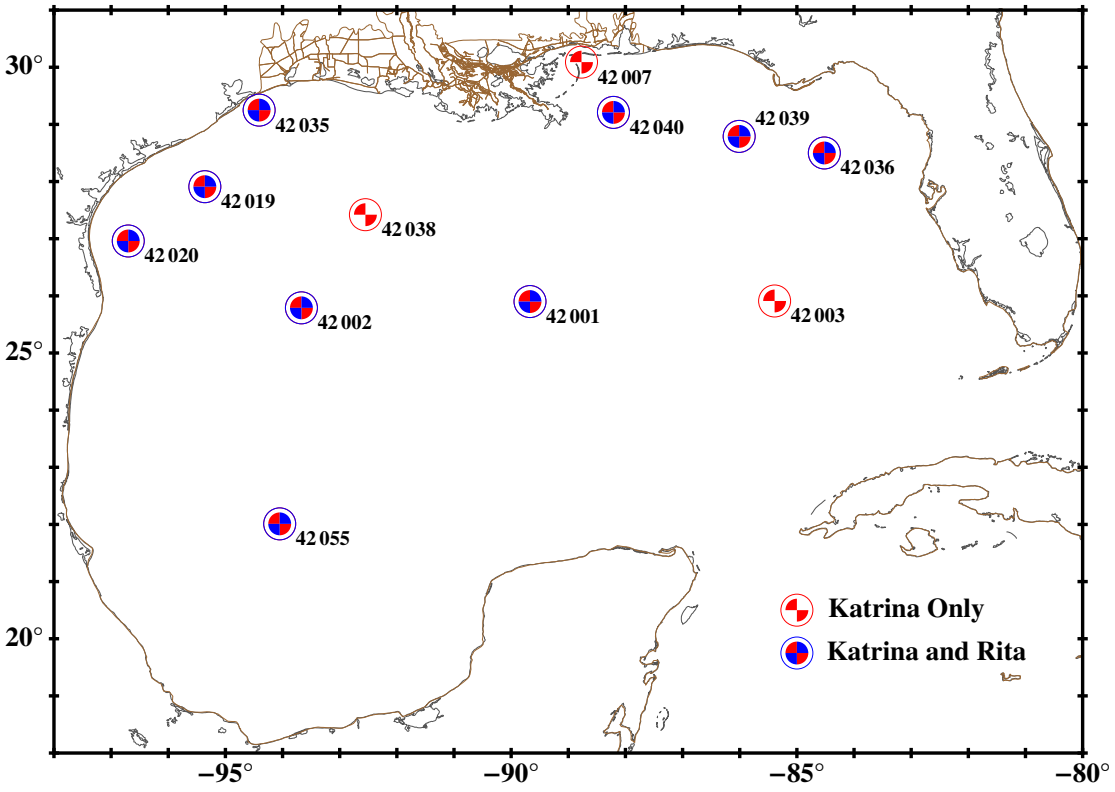

Figure 2.12. Locations of the deep water NDBC buoys used in the analysis of Hurricanes Katrina and Rita with offshore buoy identifier numbers.

peak data as well as with other third- generation wave models. We note that the peak significant wave height is the square root of the integrated energy spectrum.

STWAVE is validated by comparing computed significant wave heights and peak wave periods to limited measured data at two open water Louisiana State University (LSU) Coastal Studies Institute (CSI) stations: CSI05, located south of Isle Dernieres; and CSI06, located south of Timbalier Island. Comparisons at these two coastal stations are also presented in Figure 2.14. At CSI05, the computed wave heights and periods match the qualitative behavior of the storm, and their

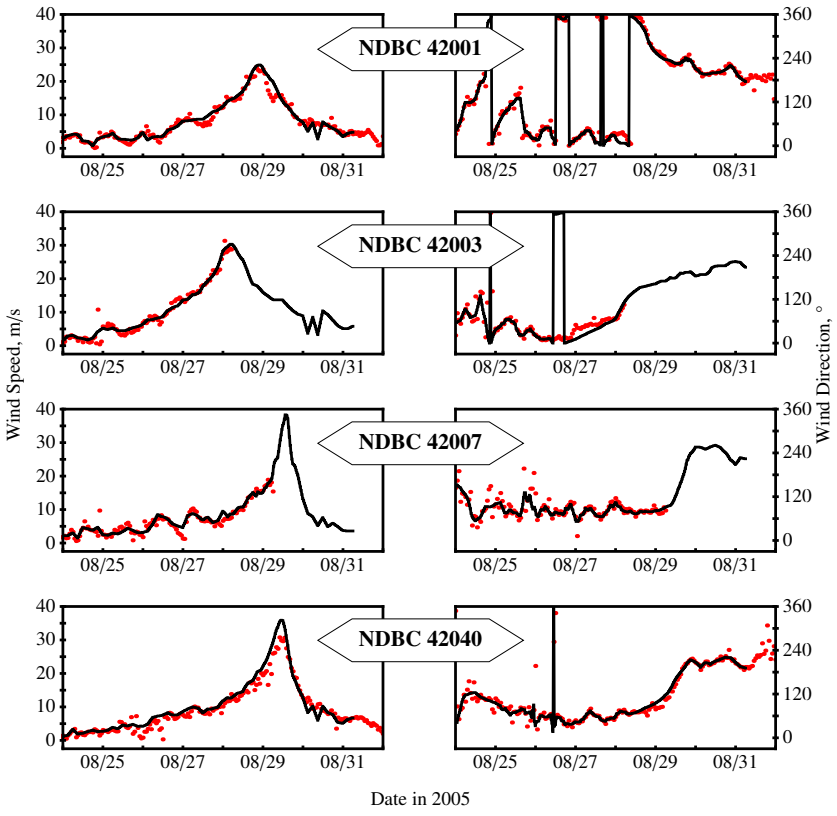

Figure 2.13. Wind speeds and directions during Hurricane Katrina at four offshore NDBC buoys with buoy identifiers. The measured data is shown with red dots, while the predicted results are shown with black lines.

values lie within the scatter of the recordings. At CSI06, where the station failed during the peak of the storm, the computed wave heights and periods match the run-up to the storm.

During Katrina, the USACE-MVN, NOS, and NWS collected hydrograph data at nine stations shown in Figure 2.15. This figure also shows the differences between ADCIRC computed and measured peak surge values at these stations. Figure 2.16 compares ADCIRC computed water levels against the measured time histories. Water levels at Pass Manchac on the west side of the lake compare to within 0.37 m of the measured values, showing excellent agreement in terms of timing and hydrograph features. The comparison at Bayou LaBranche shows good agreement in the timing of peaks and rising and drainage rates. The discrepancy, which is consistent in time, is attributed to a discrepancy in datum levels. Model results at Midlake in Lake Pontchartrain show two peaks occurring in the lake. The first peak is caused by winds from the north and northeast that pile water against the lake's south shore, and the second peak is caused by the westerly winds pushing water towards the east side of the lake coupled with the massive intrusion of water from Lake Borgne during the storm's second landfall. The comparison at the 17th Street Canal indicates that the model is under-predicting peak surge by about 0.6 m, but local Boussinesq models have indicated that there is more wave-driven setup, as much as 0.5 m, which cannot be captured with the current horizontal resolution. The model results at Little Irish Bayou on Lake Pontchartrain show rising water levels that match the recorded levels. Model and measured data at the Inner Harbor Navigation Canal (IHNC) lock staff gauge at the south end of the IHNC are well-matched in terms of peak water levels and drawdown rates. The model does show a temporary drawdown prior to a second

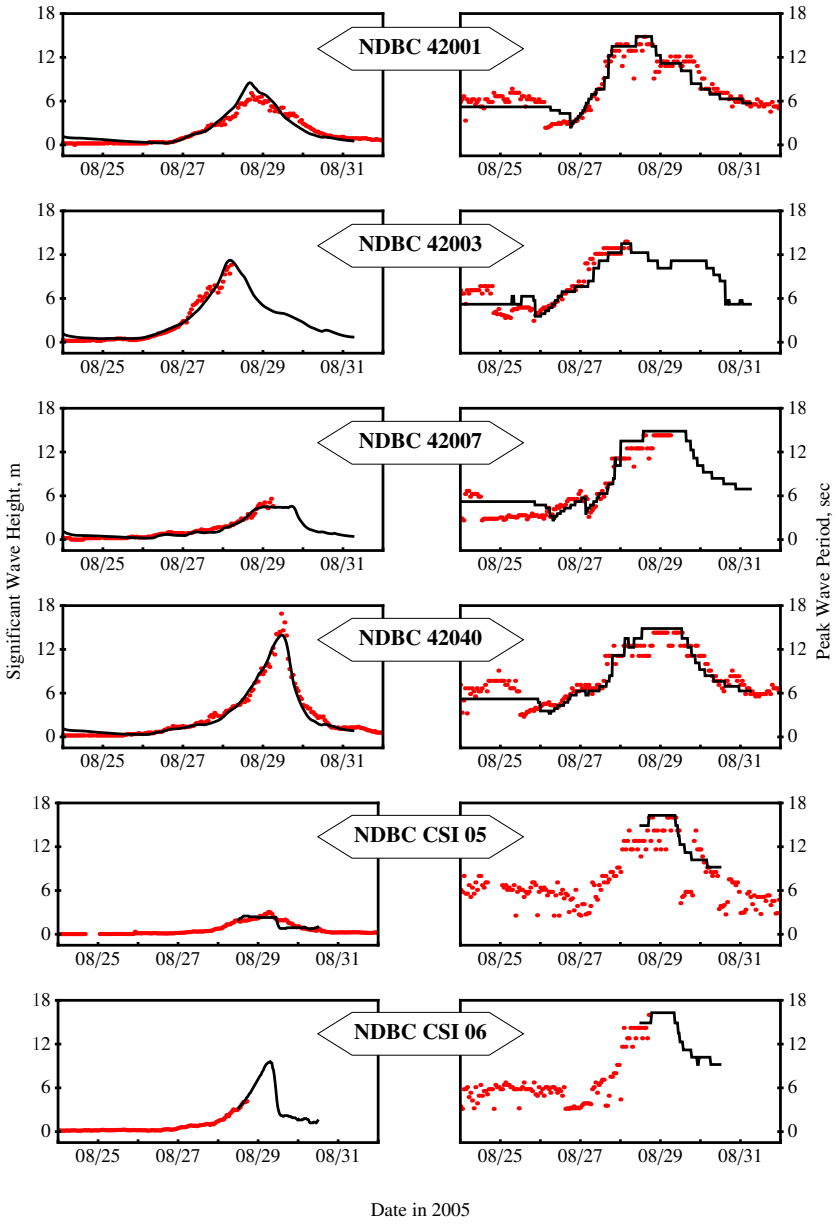

Figure 2.14. Wave heights and periods during Hurricane Katrina at six NDBC buoys with identifiers. The measured data is shown with red dots, while the predicted results are shown with black lines. The first four rows show comparisons to WAM results at selected offshore buoys, while the last two rows show comparison to STWAVE results at available coastal stations.

peak that is not fully matched in the data. This relates to localized drawdown on the west end of Lake Borgne that occurs as the storm passes, coupled with the model under-prediction seen on the south side of Lake Pontchartrain. The comparison at Southwest Pass indicates that the modeled tides are well represented in the region and that the peak storm surge is over-predicted by about 0.4 m. The gauge at Carrollton adjacent to New Orleans indicates that the model captures the propagation of tides and surge up the Mississippi River. Finally, the comparison at Grand Isle shows good agreement. We note the excellent comparison of modeled and measured recession rates for stations in the Lake Pontchartrain - Lake Maurepas region, suggesting that the non-forced, but frictionally dominated recession process is well represented as water is withdrawn from these bodies through the Rigolets, Chef Menteur and through Lake Borgne and off the shelf past the barrier islands.

The USACE collected 206 reliable HWMs and URS/FEMA collected 193 reliable HWMs during post-storm surveys with the locations and model to measurement differences shown in Figures 2.17 - 2.18, respectively (Ebersole *et al.*, 2007; URS 2006b). The HWMs were collected as indicators of the "still-water levels" and thus did not include the active motion of wind waves but did include the effects of wave setup. The two sets of HWMs offer wide coverage of the impacted region. The overall match is good, with 70 percent of the USACE HWMs and 73 percent of the URS/FEMA HWMs matching the model results to within 0.5 m. Missing features, processes, and/or poor mesh resolution are associated with the larger differences. For example, along the west bank of the Mississippi River within Plaquemines Parish at Socola, LA, as well as up and down river from this location, numerous HWMs within the levee system are substantially

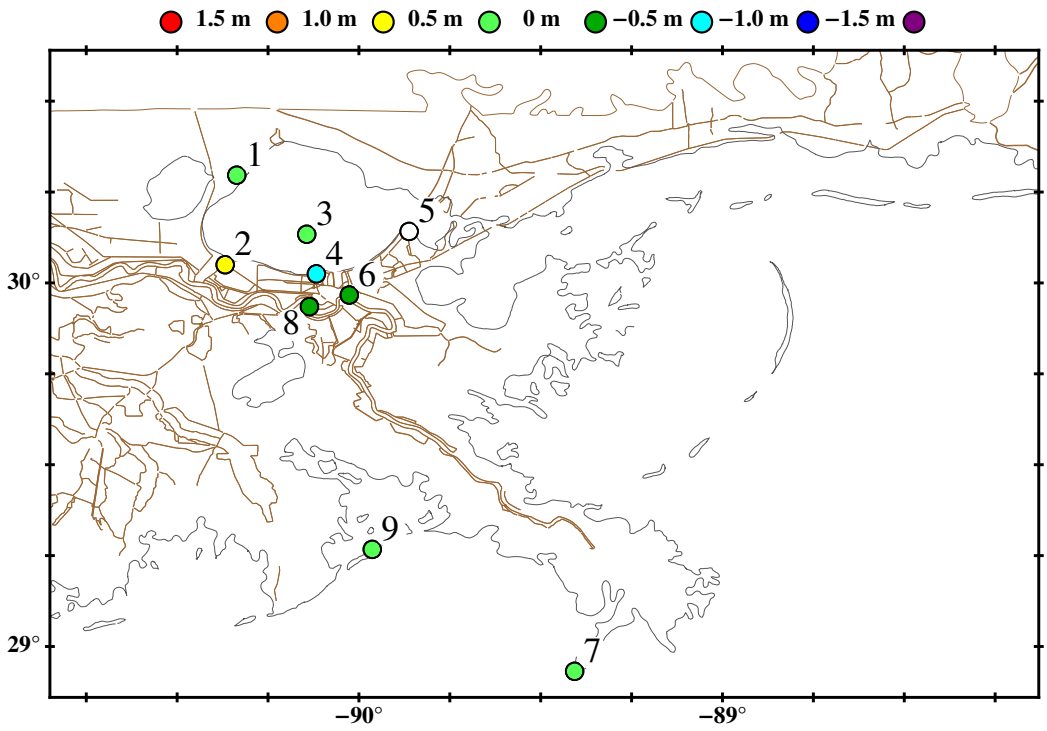

Figure 2.15. Locations of the nine USACE, NOS and NWS stations with hydrograph data for Hurricane Katrina. The nine stations are: (1) Pass Manchac, (2) Bayou LaBranche, (3) Lake Pontchartrain Midlake Causeway, (4) 17th Street Canal, (5) Little Irish Bayou, (6) the IHNC Lock Staff Gauge, (7) Southwest Pass, (8) Mississippi River at Carrollton, and (9) Grand Isle. Colors indicate the differences between the modeled and measured peak surge. Green points indicate a match within 0.5 m. Red, orange and light green circles indicate over-predictions by the model; green, blue and dark blue circles indicate under- predictions. The clear circle at station 5 indicates an incomplete hydrograph that does not allow for a peak point comparison.

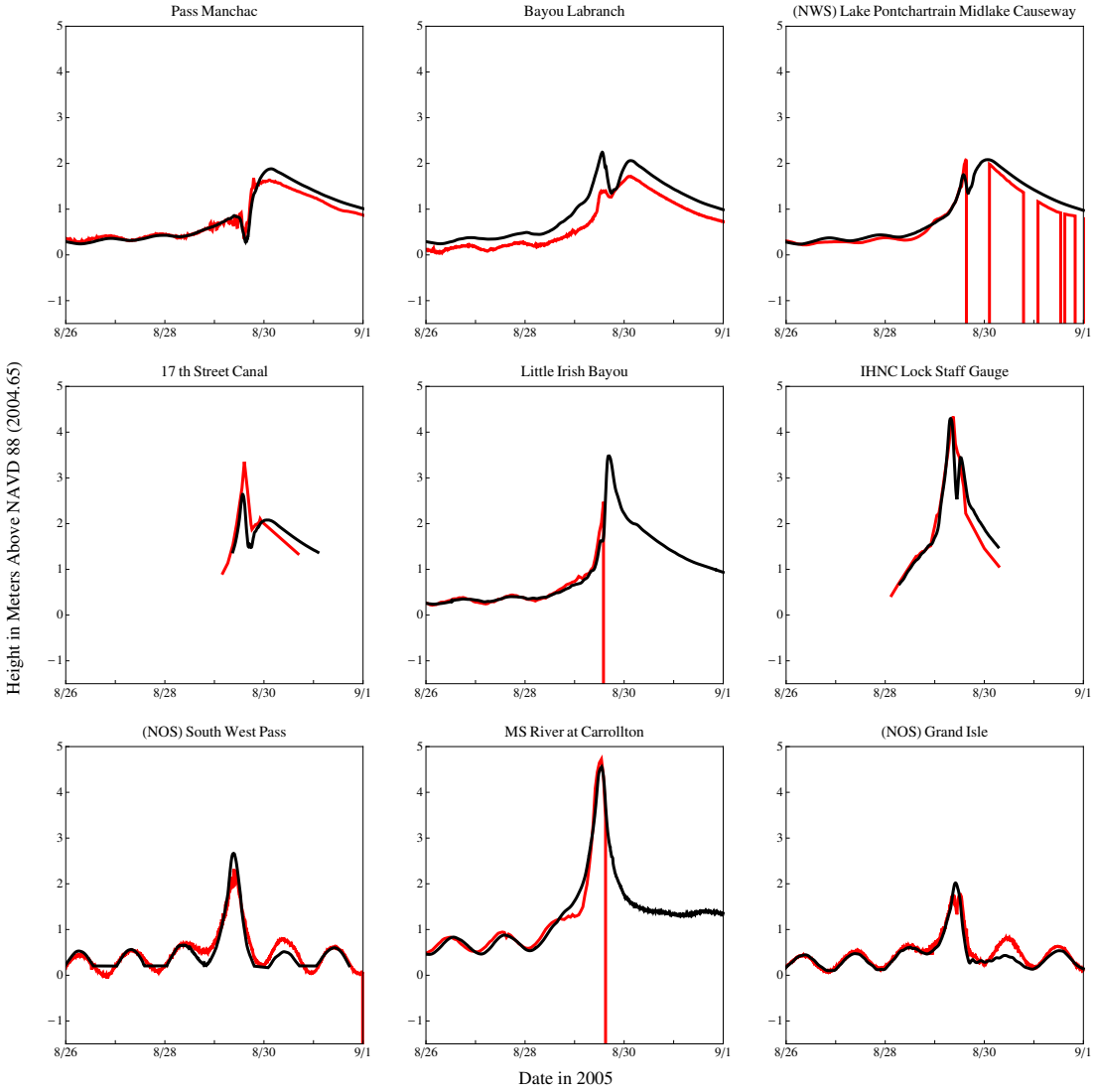

Figure 2.16. Hydrographs for the nine USACE, NOS and NWS stations during Hurricane Katrina. The black lines are the computed water levels from the ADCIRC SL15 model, while the red lines are the measured data.

under-predicted due to the fact that we do not model levee breaching. Inadequate resolution in the circulation and wave models leads to the under-prediction of wave induced setup on the south shore of Lake Pontchartrain as well as other locations with levees and raised roads. Further inland, the model over- or under-predicts surge unless the area is connected to well-defined inland waterways, which allow surge to flow past or to the HWM locations. For far inland locations adjacent to steep topography, such as up the Pearl River basin, rainfall runoff may have significantly added to the surge levels.

Scatter plots of measured versus predicted HWMs are presented in Figures 2.19 - 2.20. For the USACE marks, the slope of the best-fit line is 0.99 and the correlation coefficient, R^2, is 0.92. For the URS marks, the slope of the best-fit line is 1.02 and R^2 equals 0.94. Error statistics for Katrina are summarized in Table 2.14. For both data sets, the average absolute difference between modeled and measured HWMs is 0.36-0.4 m, and the standard deviation is 0.44-0.48 m. A portion of these differences can be attributed to uncertainties in the measured HWMs themselves. If two or more measured HWMs are hydraulically connected (defined as being within 500 m horizontally, having no barrier in between them and, having computed water levels within 0.1 m), then HWM uncertainties are estimated by examining the differences in these adjacent HWMs. Table 2.14 indicates that the estimated uncertainties in the measured HWMs are 20-30 percent of the differences between the modeled and measured HWMs. When the HWM uncertainties are removed from the predicted to measured differences, then the estimated average absolute model error range is between 0.27-0.28 m, and the standard deviation is 0.42-0.44 m.

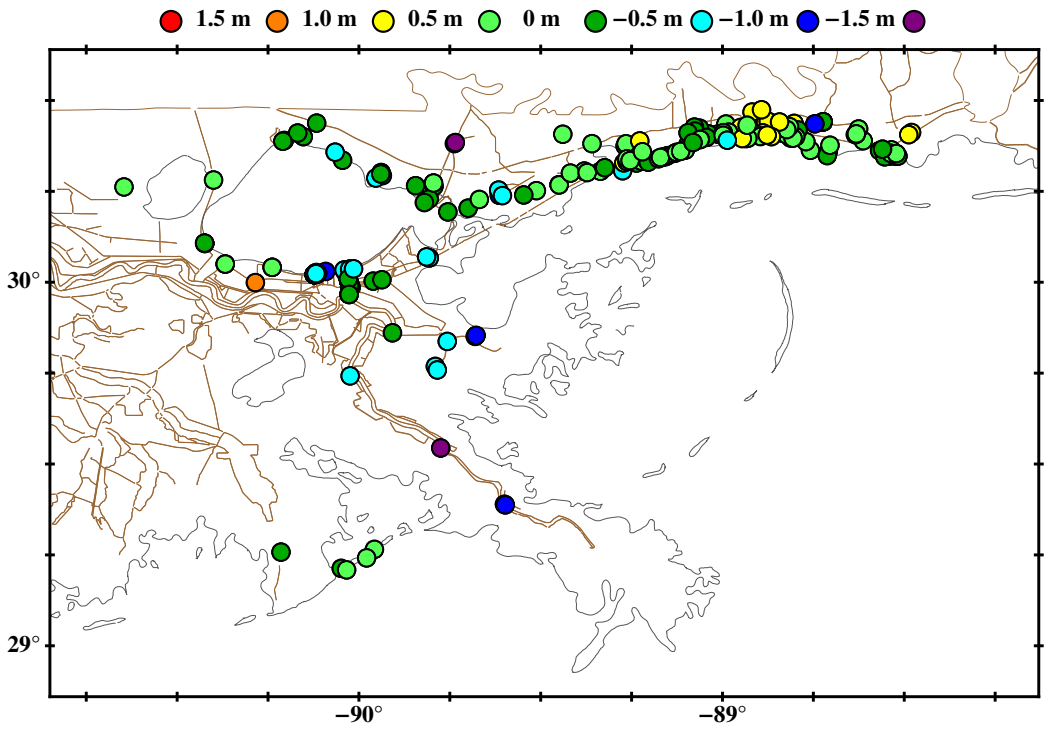

Figure 2.17. Locations of USACE HWMs for Hurricane Katrina. Colors indicate the difference between the maximum computed water elevation from the ADCIRC SL15 hindcast and the measured high water mark. Green points indicate a match within 0.5m. Red, orange and light green circles indicate over-predictions by the model; green, blue and dark blue circles indicate under-predictions.

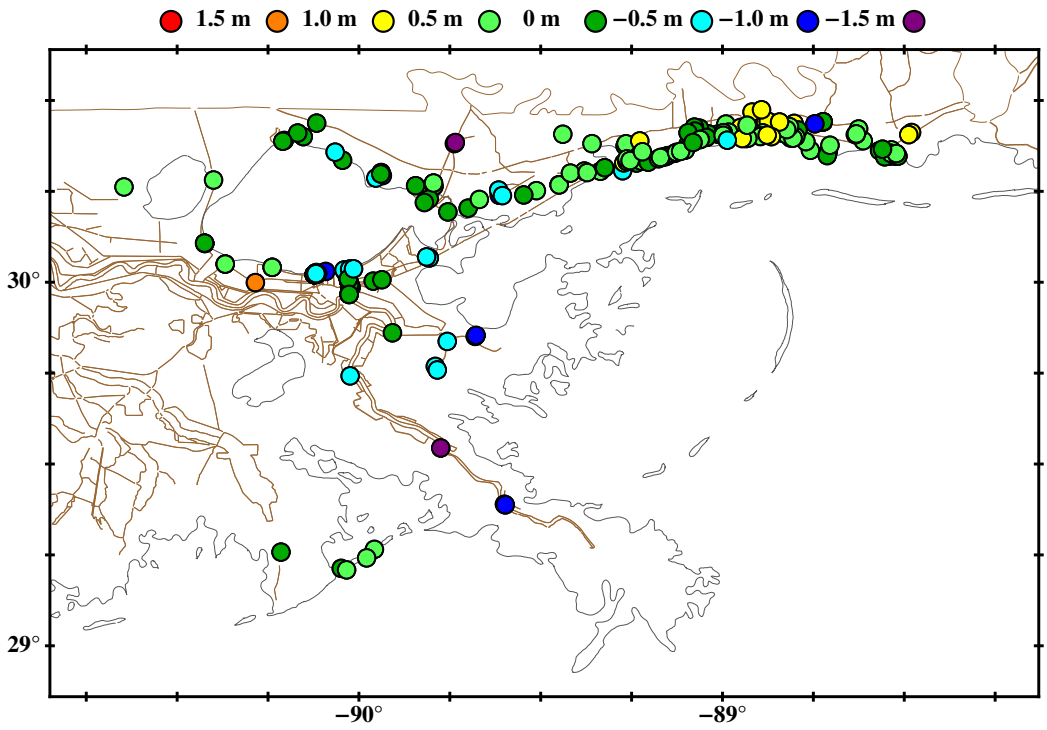

Figure 2.18. Locations of URS HWMs for Hurricane Katrina. Colors indicate the difference between the maximum computed water elevation from the ADCIRC SL15 hindcast and the measured high water mark. Green points indicate a match within 0.5m. Red, orange and light green circles indicate over-predictions by the model; green, blue and dark blue circles indicate under-predictions.

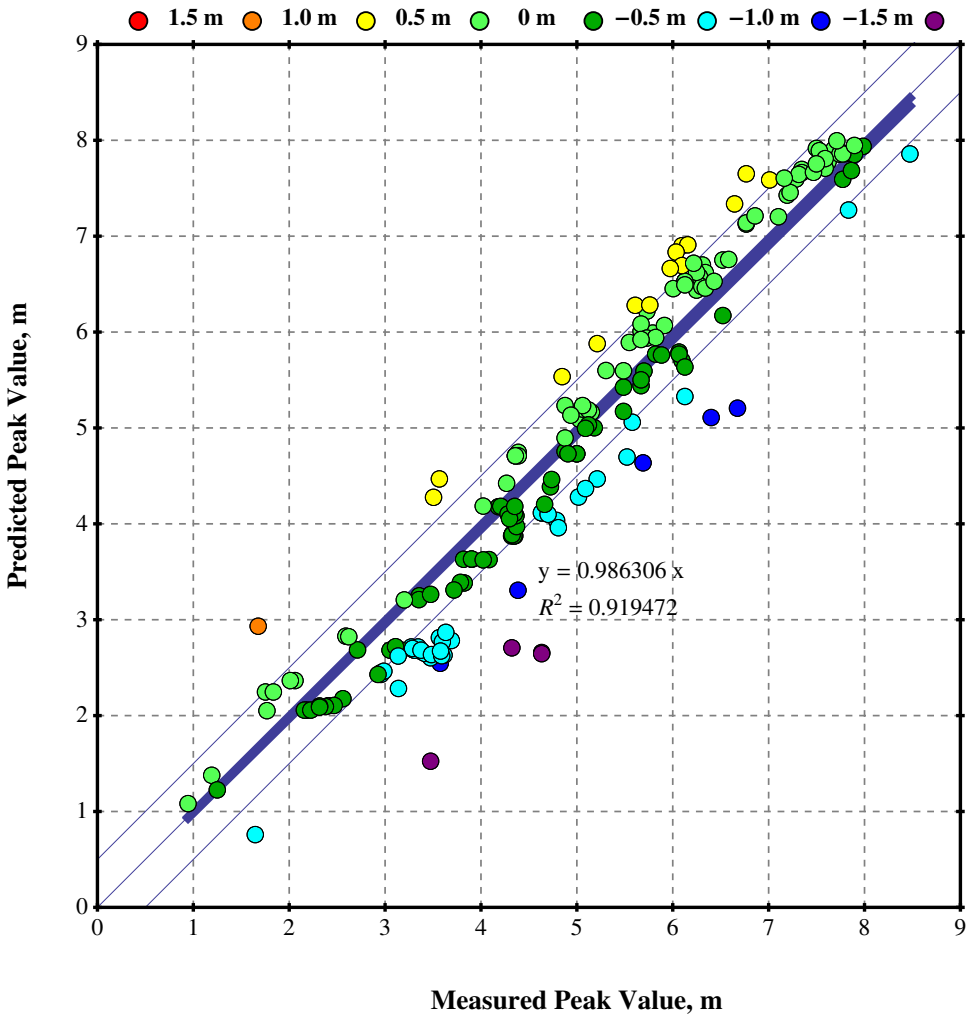

Figure 2.19. Comparisons between observed USACE high water marks and ADCIRC maximum surges during Hurricane Katrina at 206 locations shown in Figure 2.17. Green points indicate a match within 0.5 m. Red, orange and light green circles indicate over- predictions by the model; green, blue and dark blue circles indicate under-predictions. The slope of the best-fit line through all points is 0.99 and R^2 value is 0.92.

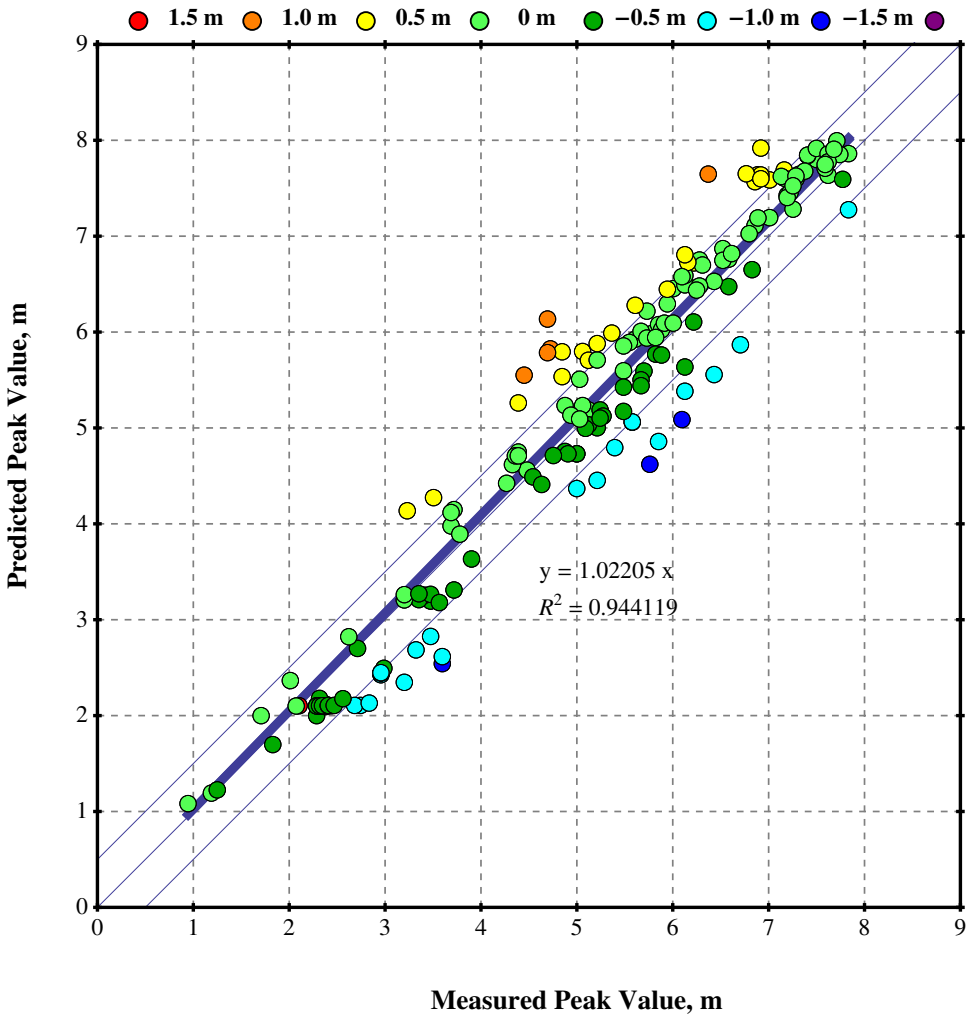

Figure 2.20. Comparisons between observed URS high water marks and ADCIRC maximum surges during Hurricane Katrina at 193 locations shown in Figure 2.18. Green points indicate a match within 0.5 m. Red, orange and light green circles indicate over- predictions by the model; green, blue and dark blue circles indicate under-predictions. The slope of the best-fit line through all points is 1.02 and R^2 value is 0.94.

TABLE 2.14

SUMMARY OF DIFFERENCE / ERROR STATISTICS FOR HWM DATASETS

Storm	Dataset	ADCIRC to measured HWMs		Measured HWMs		Estimated ADCIRC Errors	
		Avg abs diff (m)	Std dev (m)	Avg abs diff (m)	Std dev (m)	Avg abs diff (m)	Std dev (m)
Katrina	USACE	0.40	0.48	0.12	0.18	0.28	0.44
	URS	0.36	0.44	0.09	0.15	0.27	0.42
Rita	URS	0.31	0.40	0.10	0.18	0.21	0.35
	URS (without Vermilion data)	0.27	0.34	0.11	0.19	0.16	0.28

2.7 Hurricane Rita

Hurricane Rita was a large storm that made landfall at the western edge of Louisiana, with extensive inland penetration. Rita was also rich in both the quality and quantity of recorded data.

Wind data was collected at nine NDBC buoys shown in Figure 2.12. Comparisons of wind speeds and directions at selected buoys are shown in Figure 2.21. The IOKA winds match the oscillations in the wind speeds before the storm, the magnitude of the peak winds, and the rate at which the winds die down after the storm passes the buoy. The IOKA winds performed similarly at the other buoys, and a one-to-one comparison of peak wind speeds shows a best-fit slope of 0.97 and an R^2 equal to 0.96.

At those same deep water buoys, the significant wave heights and peak wave periods are used to validate WAM, and time series plots at selected stations are shown in Figure 2.22. WAM matches the timing and magnitude of the peaks at the buoys, and a comparison of measured and predicted peak significant wave heights at the available nine stations shows a best-fit slope of 0.96 and an R^2 value of 0.87.

STWAVE is validated by comparing its computed significant wave heights and peak periods to measured data at coastal station CSI05. As shown in Figure 2.22, the model-predicted wave heights and periods lie within the scatter of the recordings. STWAVE computes a "double peak" in the wave heights and periods, because the winds shifted from southeasterly to southwesterly as Rita passed this station.

The USGS collected hydrograph data from 23 water-level sensors positioned as shown in Figure 2.23 (McGee *et al.*, 2006). This figure also shows the differ-

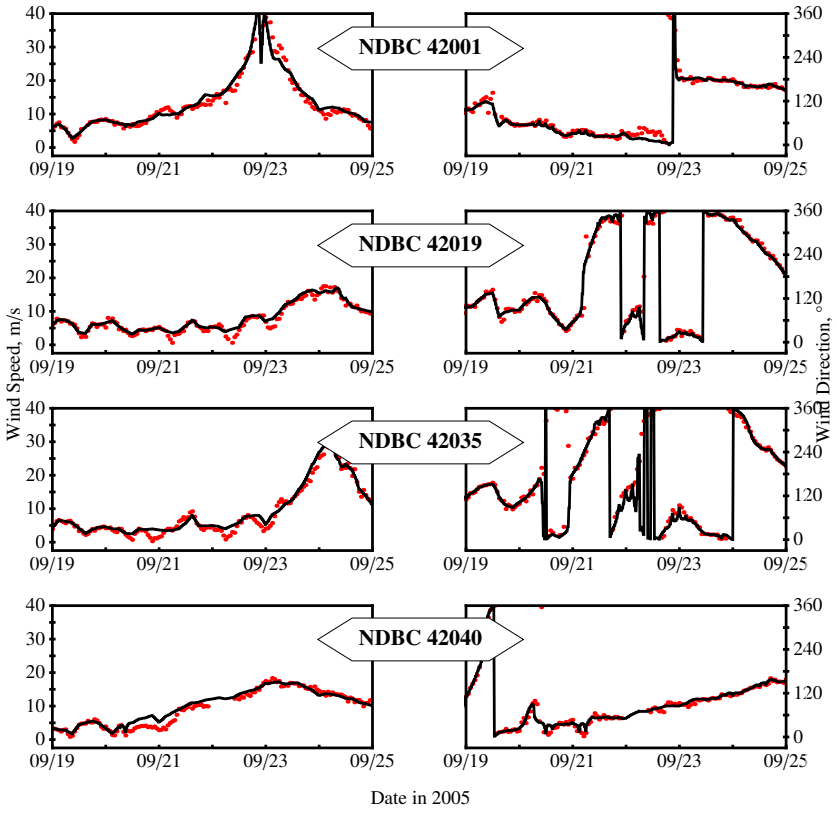

Figure 2.21. Wind speeds and directions during Hurricane Rita at four offshore NDBC buoys with buoy identifiers. The measured data is shown with red dots, while the predicted results are shown with black lines.

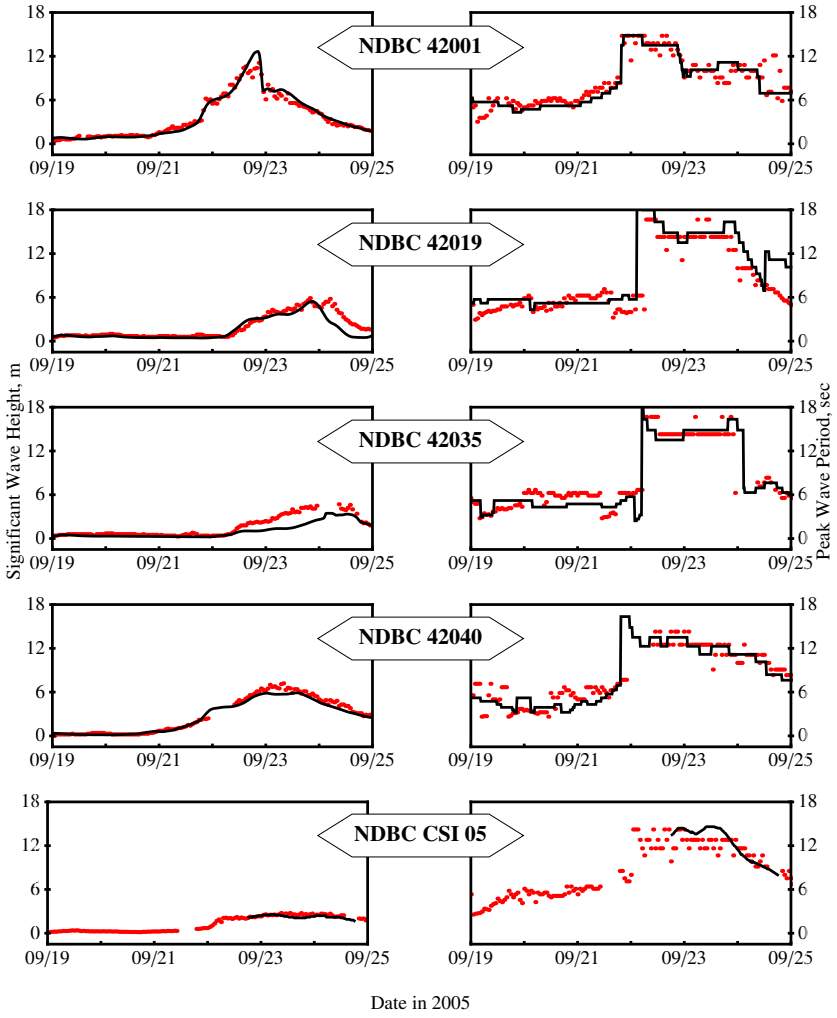

Figure 2.22. Wave heights and periods during Hurricane Rita at five NDBC buoys with identifiers. The measured data is shown with red dots, while the predicted results are shown with black lines. The first four rows show WAM results at selected offshore buoys, while the last row shows STWAVE results at the available coastal station.

ences between measured and modeled peak still water levels at these sensors. The model's ability to represent the drawdown, maximum water levels, and recession is shown in the hydrographs in Figures 2.24 - 2.25. Some stations, such as LA11, LA12, LC7, LC8a, LC11 and LC12, were located in regions that are normally dry, and thus only measured water levels above the vertical position at which they were placed. At most stations the features of the measured data are modeled well. At the stations where the recession curve was recorded, the modeled rate of dewatering, which is dominated by a balance between friction and water elevation gradients, is consistent with the observed rates. This indicates that bottom friction within the model provides an accurate representation of the actual role of bottom friction across these complex series of lakes and marshes. This is of critical importance to the accurate representation of inland surge decay in hurricanes such as Hurricane Rita.

At the few stations where the match is poor between the measured and predicted water levels, a lack of resolution is almost always the cause. The inlet into Sabine Pass, near Station B15b, lacks the same level of horizontal resolution found elsewhere in the SL15 model. In addition, there are vertical referencing uncertainties at this station. Stations LA2 and LA3 do not wet in the simulation and stations LA7 and LA8 flooded too early and by too much, because they are located along small tributaries that can not be resolved at the 50m resolution used typically in the model. Station LF3 also has narrow channel scale connectivity/resolution problems. The model performs well around channels when sufficient resolution is included, such as for stations LC2a and LC2b along the wider Calcasieu Shipping Channel. These stations highlight the importance of resolution, topography, and vertical datum.

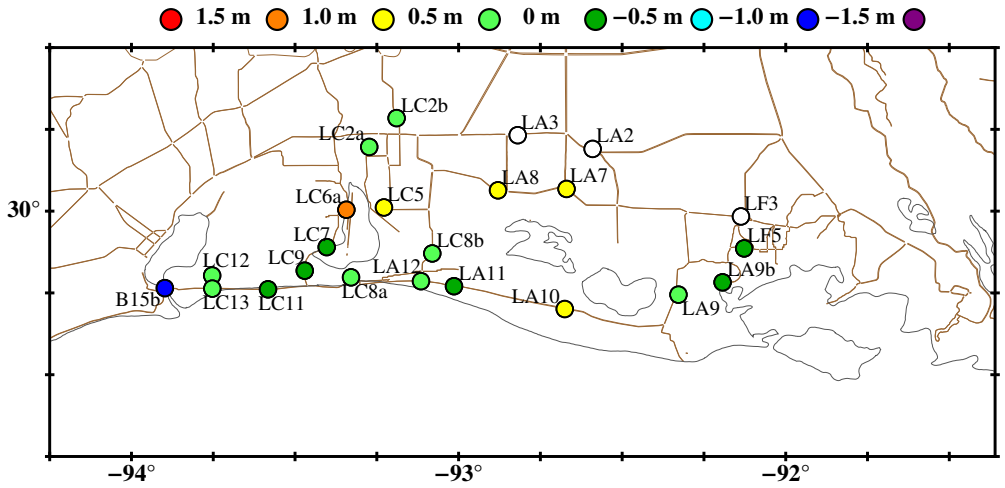

Figure 2.23. Locations of the 23 USGS stations for Hurricane Rita. Colors indicate the difference between the maximum water elevation from the ADCIRC SL15 hindcast and the maximum water level from the USGS hydrograph data. Green points indicate a match within 0.5 m. Red, orange and light green circles indicate over-predictions by the model; green, blue and dark blue circles indicate under-predictions. White points indicate stations where ADCIRC did not simulate storm surge.

The maximum water levels can also be compared to FEMA/URS HWMs (URS, 2006c). This analysis uses the 80 HWMs that were due only to storm surge with wave-induced setup and deemed by URS to be of good quality. The locations and model-to-measurement differences of these HWMs are shown in Figure 2.26. The differences are within 0.5 m at 77 percent of the comparison locations across the state. A scatter plot of the HWMs is shown in Figure 2.27. Overall, the slope of the best-fit line through all of the scatter points is 0.97, and the R^2 is 0.77. The worst HWM comparisons are a cluster concentrated inside Vermilion Bay and are consistently under-predicted. Vermilion Bay may have problems related to

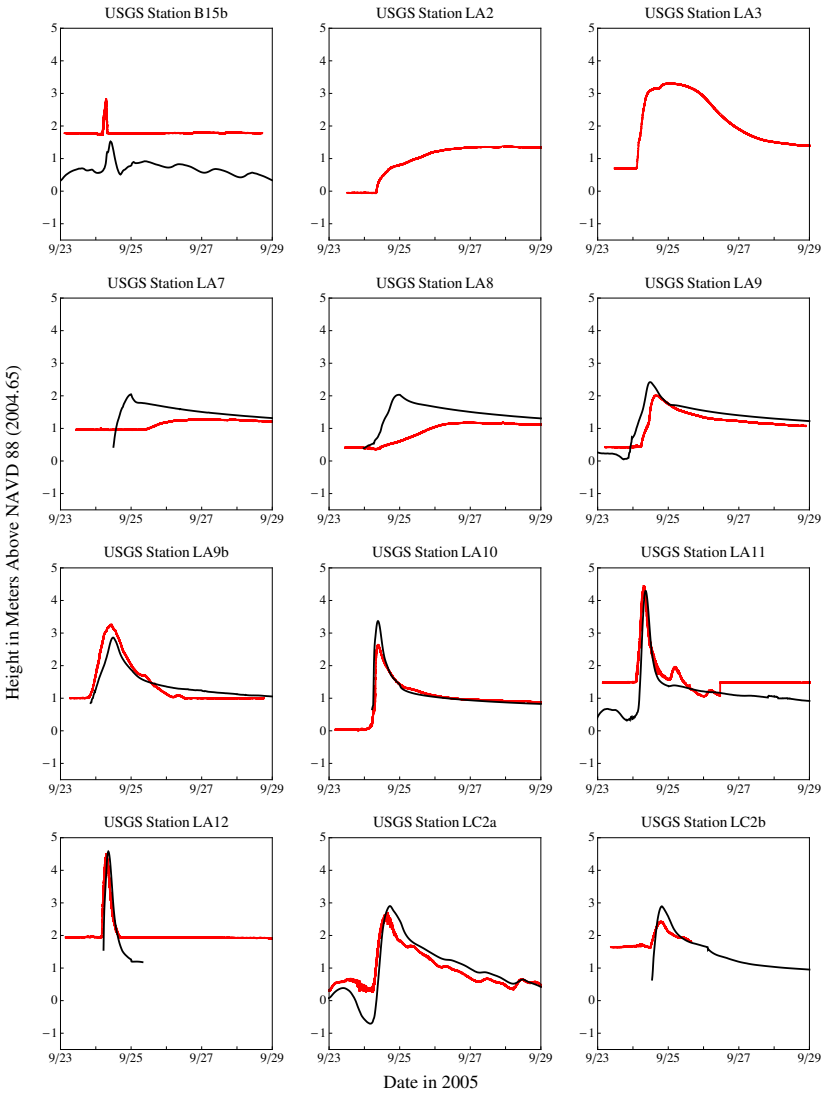

Figure 2.24. Hydrographs at the first 12 USGS stations for Hurricane Rita. The black lines are the computed water levels from the ADCIRC SL15 model, while the red dots are the measured data.

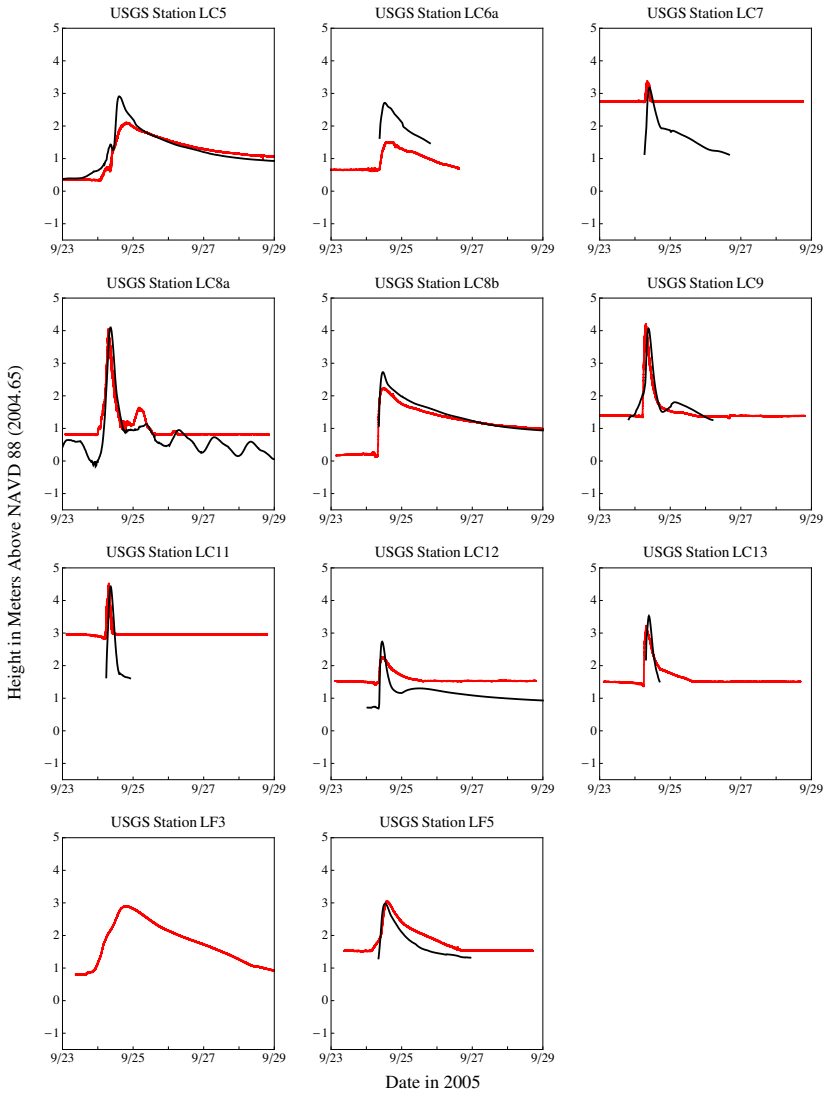

Figure 2.25. Hydrographs at the last 11 USGS stations for Hurricane Rita. The black lines are the computed water levels from the ADCIRC SL15 model, while the red dots are the measured data.

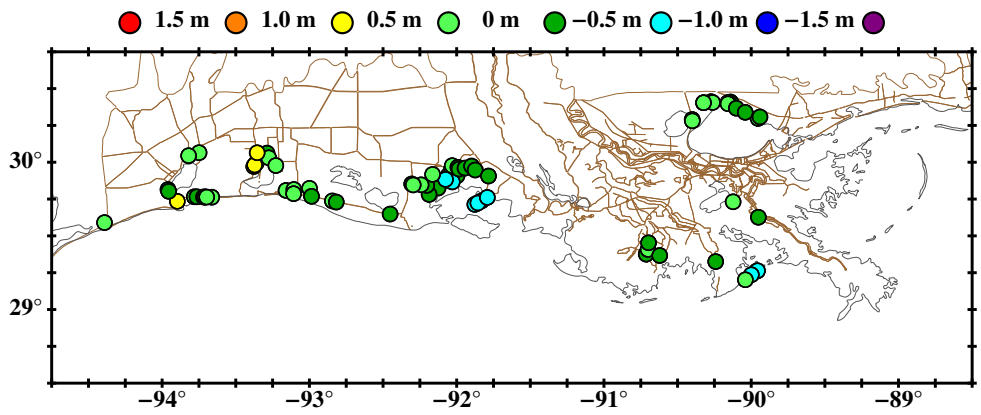

Figure 2.26. Locations of the 80 high water marks obtained from URS for Hurricane Rita. Colors at each location indicate the difference between the maximum elevation from the ADCIRC SL15 hindcast and the URS high water mark. Green points indicate a match within 0.5 m. Red, orange and light green circles indicate over-predictions by the model; green, blue and dark blue circles indicate under-predictions.

the relatively low mesh resolution in the region and/or its viscous muddy bottom (Sheremet *et al.*, 2005; Stone *et al.*, 2003), which may affect surge propagation, wind wave development and attenuation, and/or air-sea momentum transfer. A best-fit line for the 54 data points outside Vermilion Bay is presented in Figure 2.28, showing a slope of 1.04, and a much-improved R^2 of 0.87.

Table 2.14 gives the average absolute difference between modeled and measured HWMs as 0.31 m, and the standard deviation as 0.40 m. However, both quantities improve when the HWMs near Vermilion Bay are excluded. Accounting for the uncertainty in the HWMs themselves, the estimated model average absolute errors range from 0.16-0.21 m with a standard deviation of 0.28-0.35 m.

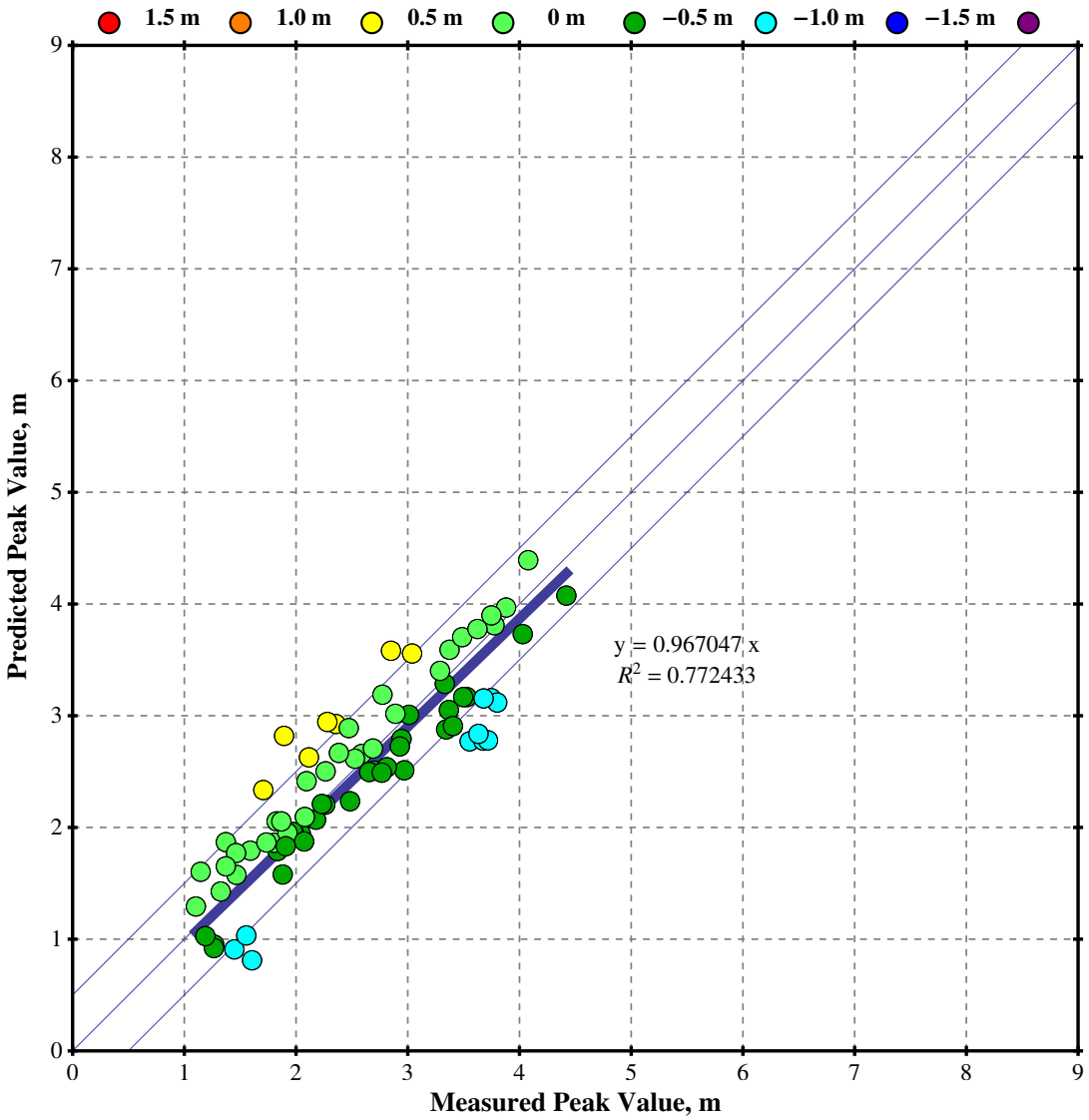

Figure 2.27. Scatter plot of high water marks for Hurricane Rita. Green points indicate a match within 0.5 m. Red, orange and light green circles indicate over-predictions by the model; green, blue and dark blue circles indicate under-predictions. The slope of the best- fit line through all points is 0.97 and the R^2 value is 0.77.

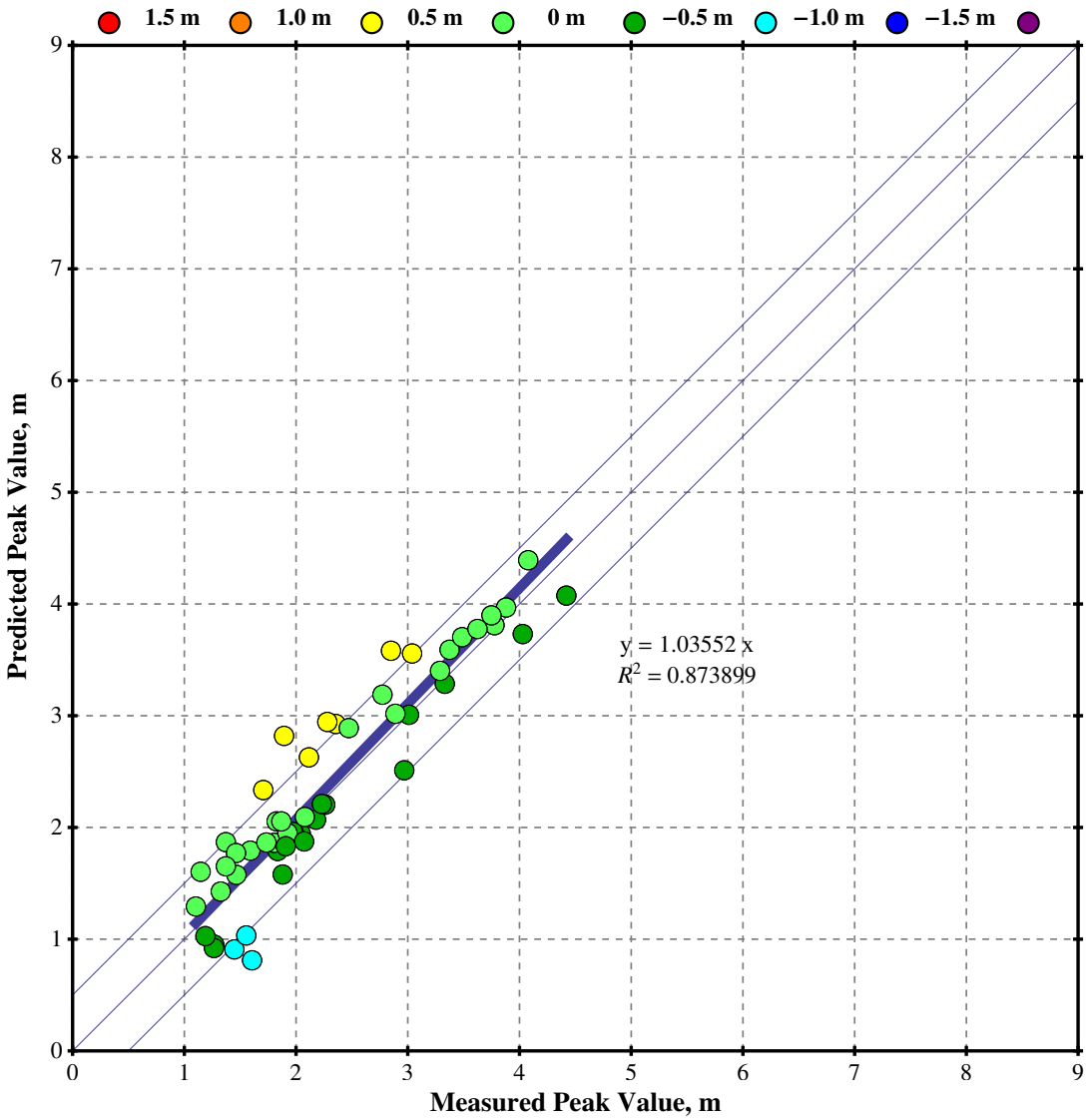

Figure 2.28. Scatter plot of high water marks for Hurricane Rita without data in Vermilion Bay. Green points indicate a match within 0.5 m. Red, orange and light green circles indicate over-predictions by the model; green, blue and dark blue circles indicate under- predictions. The slope of the best-fit line through all points is 1.04 and the R^2 value is 0.87.

2.8 Conclusions

Our coupled river, tide, wind, wind-wave, and circulation model for Southern Louisiana and Mississippi emphasizes: an accurate representation of the physical features with mesh resolution down to 50 m; the nonlinear coupling of the multiple processes that contribute to storm surge; an objective specification of frictional parameters that describe dissipation based on USGS GAP and NLCD land use data; wind adjustment based on upwind roughness; and robust and accurate boundary conditions achieved through nested model coupling in the case of the wave computations, and through a basin-scale unstructured-mesh model for the circulation computations. Forcing functions, boundary conditions, geometric, topographic, bathymetric, and surface friction descriptors are defined within the system as they are observed and are not tuned to optimize the model to match observational data for waves or water levels.

The processes are validated separately for riverine flow and tides and concurrently for the hurricane events, validating winds, waves, hydrographs, and HWMs. Flow-stage relationships in the Mississippi River match measured best-fit relationships to within an average of 0.24 m. Tides along the Gulf coast are also well-represented by the model with the dominant diurnal tides being captured with an average absolute difference equal to 0.01 m. During the hurricane events, the kinematic wind analyses accurately represent the measured wind fields with an R^2 of 0.93-0.96 while open water significant wave heights correlate to measured values with R^2 equal to 0.87-0.90. The HWMs during Katrina match measurements with an R^2 equal to 0.92-0.94 and, after accounting for measurement data uncertainties, with an estimated average absolute error of 0.27-0.28 m and a standard deviation of 0.42-0.44 m. Rita HWMs match measurements with R^2 equal

to 0.77-0.87 and, after accounting for uncertainties in the measurement data, with an estimated average absolute error of 0.16-0.21 m and a standard deviation of 0.28-0.35 m. Finally, the hydrographs demonstrate that the model captures both the forced water level rises, and flood recession process even at far inland stations, indicating that friction is correctly represented.

The ability to model waves and water levels correctly is very dependent on providing a high level of mesh resolution where gradients in topography, bathymetry, geometry, forcing functions, and elevation and current response functions are significant. Topography, inlets, channels, vertical structures, wave breaking zones and high current gradient zones all require high levels of mesh resolution. Most of the poor matches to data are attributable to poor mesh resolution. This includes the upper regions of the Mississippi River, wave transformation zones on the south shore of Lake Pontchartrain, Vermilion Bay, and narrow channels which penetrate roads. In addition to resolution, physical processes are critical. Riverine flows, tides, and wave-driven setup are vital contributors to overall surge. However, there are additional processes that should be added to further refine model skill. Upland locations in the vicinity of steep topography may be severely underpredicted due to the lack of rainfall-runoff processes. Interior portions of levee systems also require consideration of rainfall-runoff, wave overtopping flow rates and breaching. Vermilion Bay and other similar fine sediment deltaic regions will require a detailed examination of how muddy sea beds affect waves and surge propagation and attenuation. In addition, better descriptors of air-sea momentum transfer tied to wave conditions will be beneficial. Finally, vertical current structure can enhance or reduce water surface elevation.

The rapid advances in the observational systems such as LiDAR, satellite-based ocean vector winds and land cover analysis, land-based and airborne Doppler radar, airborne microwave radiometers, computational algorithms, and computing platforms will continue to allow improvements in our ability to model coastal storm environments. We envision future models focusing on higher resolution, more physics within dynamically coupled systems, and improved parameterizations based on objective analyses of micro- scale data. Furthermore, these high-resolution hurricane models will be applied as forecasting tools using high-performance parallel computing environments.

CHAPTER 3

A HIGH-RESOLUTION COUPLED RIVERINE FLOW, TIDE, WIND, WIND WAVE AND STORM SURGE MODEL FOR SOUTHERN LOUISIANA AND MISSISSIPPI: PART II - SYNOPTIC DESCRIPTION AND ANALYSIS OF HURRICANES KATRINA AND RITA

3.1 Overview

This chapter describes the hindcasts of Katrina and Rita that were performed with a loosely-coupled system of wave and circulation models. WAM and STWAVE are employed to simulate the evolution of waves from deepwater to the nearshore, respectively, while ADCIRC is employed to simulate the circulation on the unstructured SL15 mesh. The storms are examined synoptically, with a focus on how the storm surge developed and impacted the region. This chapter has been published in *Monthly Weather Review* as Dietrich *et al.* (2010a).

Hurricanes Katrina and Rita were powerful storms that impacted southern Louisiana and Mississippi during the 2005 hurricane season. In the previous chapter, we describe and validate a high-resolution coupled riverine flow, tide, wind, wave, and storm surge model for this region. Herein, the model is used to examine the evolution of these hurricanes in more detail. Synoptic histories show how storm tracks, winds and waves interacted with the topography, the protruding Mississippi River delta, east-west shorelines, manmade structures, and low-lying

marshes to develop and propagate storm surge. Perturbations of the model, in which the waves are not included, show the proportional importance of the wave radiation stress gradient induced setup.

3.2 Introduction

Hurricanes Katrina and Rita were powerful storms that impacted the central Gulf of Mexico. Katrina's winds reached Category 5 strength in the Gulf of Mexico, but weakened to Category 3 strength as the storm approached the continental shelf. Its southerly track placed it within 50 km of New Orleans and the infrastructure of southeastern Louisiana, and its storm surge of 8.8 m along the coastline of Mississippi was the largest ever recorded in the United States. In contrast, Rita's southeasterly track exposed large portions of southwestern Louisiana to hurricane-strength winds and southeastern Louisiana to tropical-storm-strength winds. Rita caused extensive inundation in the region. Its maximum storm surge reached 4.7 m along the coastline of Cameron Parish in southwestern Louisiana, but it also generated a surge of up to 3 m along portions of the New Orleans hurricane protection system, more than 300 km from the center of the storm.

The observed data for both storms is unprecedented in its coverage, detail and accuracy. Wind measurements were collected from a diverse set of observing platforms including Airborne Stepped Frequency Microwave Radiometer (SFMR), GPS dropwindsondes, Airborne and land-based Doppler radar, portable land-based mesonets, and instrumented platforms and buoys. National Oceanic and Atmospheric Administration (NOAA) and Louisiana State University Coastal Studies Institute stations recorded wave heights and periods (`http://www.ndbc.noaa.gov`). The Federal Emergency Management Agency (FEMA) and the U.S.

Army Corps of Engineers (USACE) surveyed high-water marks throughout the region (URS, 2006a; URS, 2006b; USACE, 2006), and the U.S. Geological Survey (USGS), NOAA, and the USACE recorded hydrographs at locations at the coast and far inland (McGee *et al.*, 2006; USACE, 2006).

Although Rita was a somewhat smaller and weaker storm compared to Katrina, especially on the continental shelf as it approached landfall, the differences in storm characteristics do not fully explain the significant differences in the resulting storm surges, which were influenced by the geography of their landfall locations. In southeastern Louisiana and Mississippi, where Katrina made landfall, the geography includes: a shallow continental shelf, which extends 100-120 km south of the Mississippi-Alabama coastline but only 10-15 km south of the so-called "bird's foot" of the Mississippi River delta; the Chandeleur and Mississippi Sound islands, which act as barriers; low-lying marshes near the delta, which can slow the propagation of storm surge; steep topography interspersed with low-lying bays and marshes along the Louisiana-Mississippi-Alabama coastline; natural river banks and levee protection systems that stop and build storm surge elevations; and the geographic "pocket" formed where the toe of Louisiana meets the Mississippi coast, which holds surge generated by winds blowing from the east and south. In southwestern Louisiana, where Rita made landfall, a different set of features exists: an east-west coastline without major protrusions that would stop flow or force wave breaking; a shallow, broad continental shelf, which extends 100-150 km into the Gulf of Mexico; an interconnected series of inland lakes and bays; and extensive low-lying marshes and topography, which extend 60-100 km inland with mild slopes less than 0.001. These geographic features helped to produce waves and surge that varied significantly throughout the region.

In the previous chapter, we present a hurricane modeling system of southern Louisiana and Mississippi that simulates coupled riverine flow, tides, winds, wind waves and storm surge (Bunya *et al.*, 2010). This system applies the H*WIND and IOKA wind analyses (Powell *et al.*, 1998; Cox *et al.*, 1995), the WAM ocean wave model (Komen *et al.*, 1994; Gunther, 2005), the STWAVE nearshore wave model (Smith and Smith 2001; Thompson *et al.*, 2004), and the ADCIRC circulation model (Luettich and Westerink, 2004; Westerink *et al.*, 2008). Riverine flows, tides, winds, wind waves and storm surges are validated independently. The resulting system is comprehensive, provides detail at a wide range of scales, and can be used to simulate hurricane storm surge and waves with a high level of confidence. However, although the observed data are useful to validate this system, they do not fully describe the evolution of the hurricanes or the interaction of the forcing mechanisms and their effects on winds, waves, surge and currents.

In this chapter, the coupled modeling system is used to examine the synoptic histories of Katrina and Rita. The components of wind (from the H*WIND/IOKA analysis) and storm surge (from ADCIRC) are presented at selected times during each storm, and maximum values are shown for all components of the coupled system. These histories allow an analysis of the evolution of storm surge, the mechanisms that drove the surge, and where that surge propagated.

3.3 Hurricane Katrina

Hurricane Katrina was a relatively fast moving storm characterized by its low pressure, its intensity, and especially its large size. Katrina approached the Mississippi shelf as a Category 5 storm on the Saffir-Simpson scale before degrading when it reached the continental shelf, as summarized in Figure 3.1 and Table 3.1

(Knabb *et al.*, 2005). The strongest 1-minute sustained wind speed estimated by the National Hurricane Center reached 77 m s^{-1} with 902 mb as the lowest atmospheric pressure. It made landfall as a strong Category 3 storm at about 1200 UTC 29 August 2005 along the southern reach of the Mississippi River in Plaquemines Parish. The storm then tracked north, passing over Lake Borgne and making a second Gulf landfall as a Category 3 hurricane at 1500 UTC 29 August 2005 near the Louisiana-Mississippi state line. NOAA recorded significant wave heights up to 16.9 m, the largest ever measured at their buoys (USACE, 2006, Vol. 4, Appendix 3). Note that the geographic landmarks discussed in this paper are shown in Figures 2.2 - 2.5.

TABLE 3.1

SUMMARY OF HURRICANE KATRINA

Date/Time (UTC)	Longitude	Latitude	Pressure (mb)	Maximum Wind Speed (m s^{-1})	Category on Saffir-Simpson
2005/08/23/1800	-75.1	23.1	1008	13.8	
2005/08/24/0000	-75.5	23.4	1007	13.8	
2005/08/24/0600	-76.2	23.8	1007	13.8	
2005/08/24/1200	-76.5	24.5	1006	16.1	
2005/08/24/1800	-76.9	25.4	1003	18.4	
2005/08/25/0000	-77.7	26.0	1000	20.7	
2005/08/25/0600	-78.4	26.1	997	22.9	
2005/08/25/1200	-79.0	26.1	994	25.3	

TABLE 3.1

Continued

Date/Time (UTC)	Longitude	Latitude	Pressure (mb)	Maximum Wind Speed (m s^{-1})	Category on Saffir-Simpson
2005/08/25/1800	-79.6	26.2	988	27.6	
2005/08/26/0000	-80.3	25.9	983	32.1	1
2005/08/26/0600	-81.3	25.4	987	29.8	1
2005/08/26/1200	-82.0	25.1	979	34.5	1
2005/08/26/1800	-82.6	24.9	968	39.0	2
2005/08/27/0000	-83.3	24.6	959	41.3	2
2005/08/27/0600	-84.0	24.4	950	43.7	2
2005/08/27/1200	-84.7	24.4	942	45.9	3
2005/08/27/1800	-85.3	24.5	948	45.9	3
2005/08/28/0000	-85.9	24.8	941	45.9	3
2005/08/28/0600	-86.7	25.2	930	57.4	4
2005/08/28/1200	-87.7	25.7	909	66.6	5
2005/08/28/1800	-88.6	26.3	902	68.9	5
2005/08/29/0000	-89.2	27.2	905	64.3	5
2005/08/29/0600	-89.6	28.2	913	57.4	4
2005/08/29/1200	-89.6	29.5	923	50.5	3
2005/08/29/1800	-89.6	31.1	948	36.8	1
2005/08/30/0000	-89.1	32.6	961	22.9	

TABLE 3.1

Continued

Date/Time (UTC)	Longitude	Latitude	Pressure (mb)	Maximum Wind Speed (m s^{-1})	Category on Saffir-Simpson
2005/08/30/0600	-88.6	34.1	978	18.4	
2005/08/30/1200	-88.0	35.6	985	13.8	
2005/08/30/1800	-87.0	37.0	990	13.8	
2005/08/31/0000	-85.3	38.6	994	13.8	
2005/08/31/0600	-82.9	40.1	996	11.5	

3.3.1 Synoptic History

At 0700 UTC 29 August 2005, shown in Figure 3.2, Katrina is downgraded to a Category 4 storm with the eye approximately 130 km south and 5 hr from the initial landfall. The easterly winds range from 20-40 m s^{-1} (10 minute averaged) and are blowing water into Breton and Chandeleur Sounds as well as Lake Borgne. Note the effect of the directional roughness wind boundary layer adjustment (Bunya *et al.*, 2010). In the Mississippi River delta and near Lake Pontchartrain, the winds are reduced in areas where the winds are blowing overland; however, nearshore regions experience the full marine winds directed onshore. Regions with extensive tree canopies, where the winds are not applied, are also shown in Figure 3.2(a). The hurricane pushes storm surge of 1.5-2.5 m from

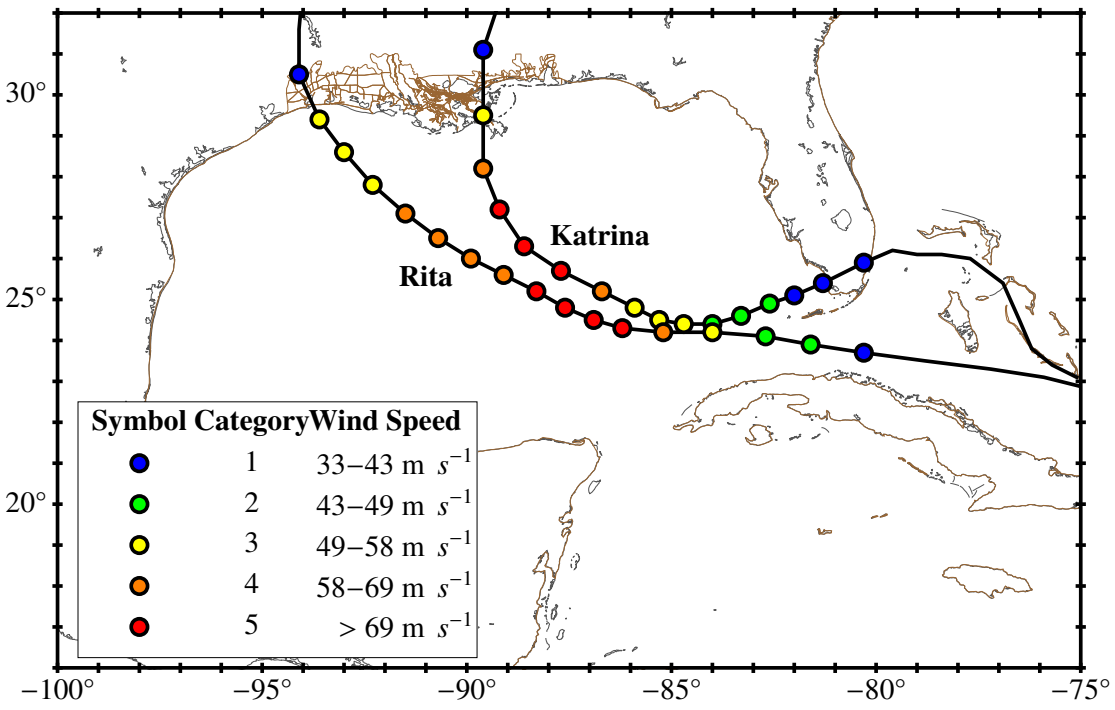

Figure 3.1. Storm tracks for Hurricanes Katrina and Rita.

the deeper Gulf of Mexico onto the Mississippi-Alabama shelf, which begins near the delta and extends east-northeast. Water is stopped by the Mississippi River banks and levees and by the St. Bernard/Chalmette protection levees, where surge is building to 2.5-3.5 m. Water levels are raised on the southwest end of Lake Pontchartrain, while water levels are suppressed in the eastern part of the lake. The water level rise in Lake Borgne and the drawdown of water in eastern Lake Pontchartrain cause a strong surface water gradient across the Chef Menteur Pass and the Rigolets Strait, which connect these two lakes. This gradient creates a current that drives water into Lake Pontchartrain, and this current is reinforced by the easterly winds. The currents in the Rigolets and Chef Menteur channels are already 1-2 m s^{-1}. This process initiates the critical rise of the mean water level within Lake Pontchartrain. Finally, the predominantly easterly and northerly winds to the west of the Mississippi River force a drawdown of water away from the west-facing levees and into northern Barataria, Timbalier and Terrebonne Bays.

At 1100 UTC 29 August 2005, shown in Figure 3.3, Katrina is within an hour of its initial landfall. The eye is west of the southern Plaquemines Parish levees, and the highest wind speeds are east from the bird's foot of the Mississippi River delta. Note the asymmetry in the wind field, which features 45 m s^{-1} southerly winds to the east and 30-40 m s^{-1} easterly winds north of the eye. The surge has been pushed onto the Mississippi- Alabama shelf to at least 2.5 m and builds to 5.8 m against the river banks and levees of lower Plaquemines Parish. The surge in this region has started to propagate up the Mississippi River and also extends broadly into Breton Sound. The currents over the Chandeleur Islands are 2-2.5 m s^{-1} as surge is pushed over these islands from the southeast. Further north, surge continues to build to 4 m against the St. Bernard/ Chalmette protection

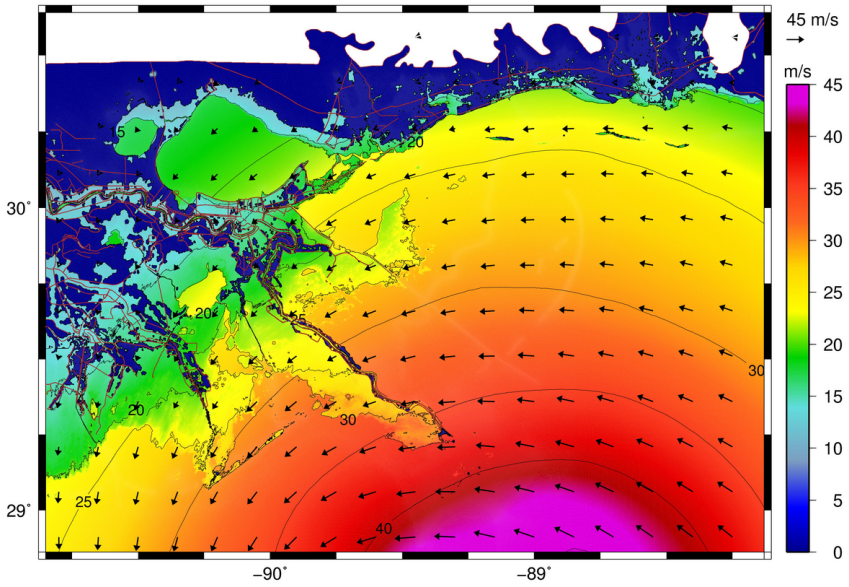

(a) Wind contours and vectors (m s^{-1}), shown with a 10 min averaging period and at 10 m elevation.

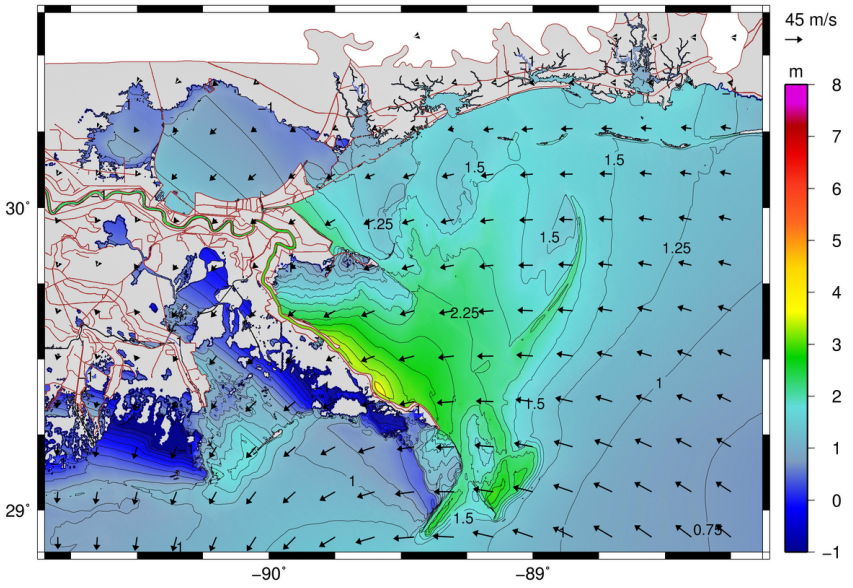

(b) Water elevation contours (m) relative to NAVD 88 (2004.65) and wind vectors (m s^{-1}).

Figure 3.2. Hurricane Katrina winds and water elevations at 0700 UTC 29 August 2005 in southeastern Louisiana.

levee due to the easterly and local northeasterly winds. A depression exists on the east side of Lake Borgne, as surge from the east is slow to replace the lake waters that have been blown to the west. A water surface slope is induced by local winds inside Lake Pontchartrain, creating a positive wind set-up on the southwest (downwind) side of the lake and set-down on the northeast (upwind) side. The difference in water level between Lakes Pontchartrain and Borgne has increased to 2.5 m, and in response, the currents in Chef Menteur Pass and the Rigolets Strait are increasing to 1.5-3 m s^{-1}. In the bird's foot of the Mississippi River delta, the surge levels are about 2-2.5 m, and, as later analysis will show, about 0.7-0.8 m of the surge there is due to wave breaking. Northerly winds build surge to a level of about 2.5 m on the north side of Grand Isle.

At 1400 UTC 29 August 2005, shown in Figure 3.4, Katrina is now centered over Lake Borgne. Across the Mississippi-Alabama shelf, winds are now southerly and southeasterly. Winds are blowing away from the east-facing levees near lower Plaquemines Parish and the bird's foot of the Mississippi River delta, English Turn, St. Bernard/Chalmette and New Orleans East. In Lake Pontchartrain, shifting winds are now northerly and northwesterly. Winds are pushing storm surge against the west-facing levees along the Mississippi River near Venice. On the east side of the river, surge builds broadly to more than 4 m on the shelf and intensifies along the Mississippi coast. The surge that built against the lower Mississippi River levees propagates northeastward toward Chandeleur Sound, while surge levels decrease along lower Plaquemines on the east side of the river. The peak surge propagating in the Mississippi River is 4 m and has reached metropolitan New Orleans. Although water levels have increased overall, the surge along the St. Bernard/Chalmette protection levee is decreasing. Water accumulates from

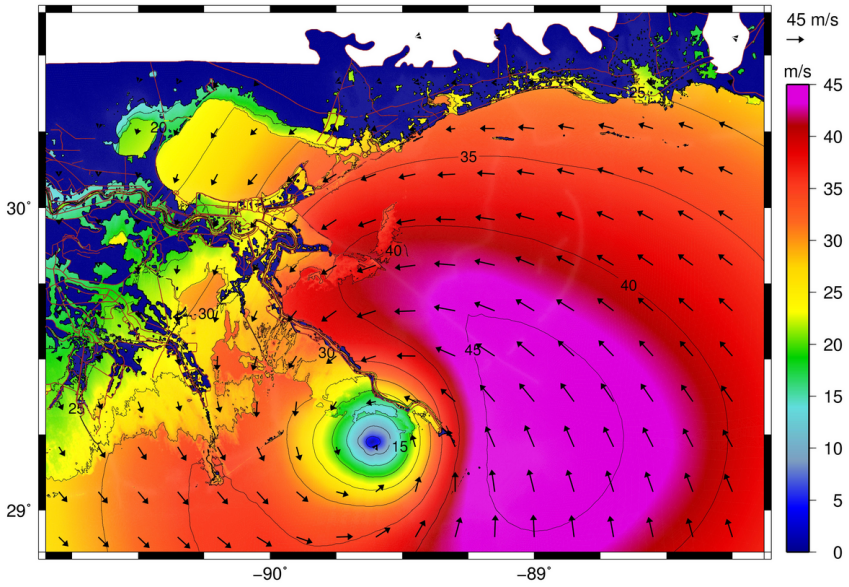

(a) Wind contours and vectors (m s^{-1}), shown with a 10 min averaging period and at 10 m elevation.

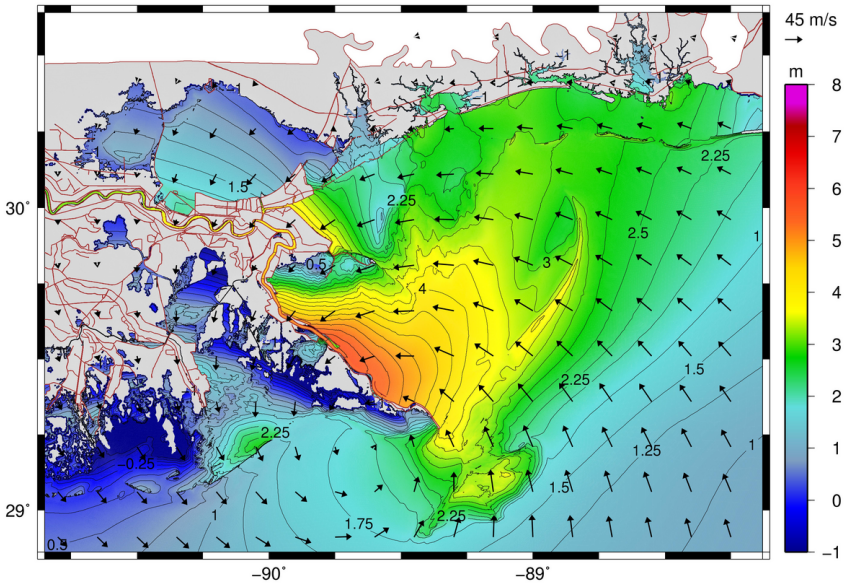

(b) Water elevation contours (m) relative to NAVD 88 (2004.65) and wind vectors (m s^{-1}).

Figure 3.3. Hurricane Katrina winds and water elevations at 1100 UTC 29 August 2005 in southeastern Louisiana.

the east and overtops the CSX railroad between Lakes Borgne and Pontchartrain, where the difference in water level is still increasing and causes high volumes of water to flow into Lake Pontchartrain. Water blows from the north of Lake Pontchartrain and builds to about 3 m along the southern shores, while a draw-down develops along the north shore. The highest surge along the south shore migrates from west to east as the winds shift. The currents over the Chandeleur Islands have decreased to 1.5-2 m s^{-1}, but the currents over the Mississippi Sound Islands have increased to 2-2.5 m s^{-1} as the water moves northward.

At 1600 UTC 29 August 2005, as shown in Figure 3.5, Katrina is now located about 40 km and an hour north of its second landfall. The wind speeds have decreased, but wind-field asymmetry has increased and the structure has broadened as the hurricane makes landfall. Wind speeds are 30-35 m s^{-1} over much of the continental shelf and are 25-30 m s^{-1} over Lake Pontchartrain. The surge from southern Plaquemines Parish has combined with the local surge forced by the southerly winds to increase water levels on the shelf along the Mississippi-Alabama coast to about 6 m. The surge spreads inland through the low-lying bays but is stopped by the relatively steep topography and builds to 8.8 m. Water blows eastward across Lake Pontchartrain while it flows from Lake Borgne due to the sustained 1.8-2.3 m water level differential between the two lakes. The currents in the Rigolets Strait range from 1.8-2.7 m s^{-1}. Water has started flowing from Chandeleur Sound back into the Gulf of Mexico.

At 1900 UTC 29 August 2005, shown in Figure 3.6, the winds are predominantly southwesterly and have decreased, but they still range from 20-30 m s^{-1} over much of the continental shelf. The surge from the Mississippi coast relaxes and spreads back into Mississippi, the Chandeleur and Breton Sounds, and Lake

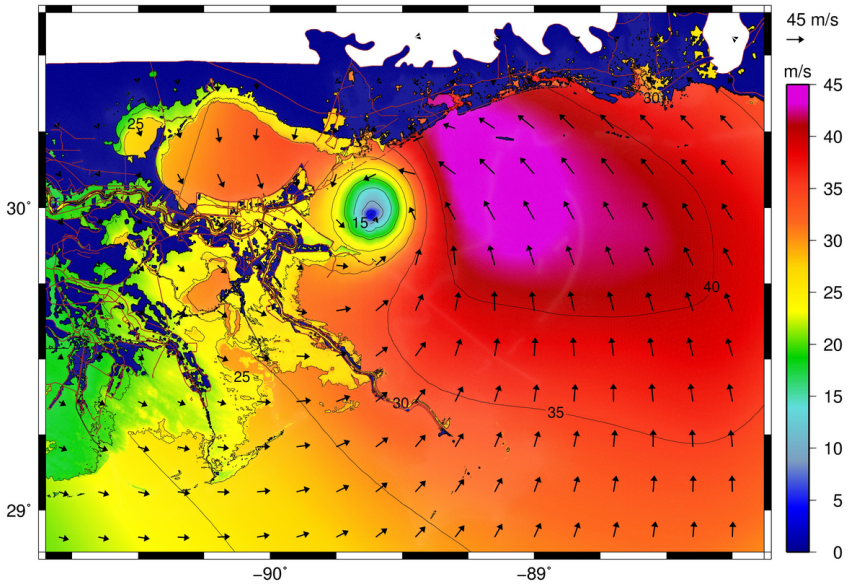

(a) Wind contours and vectors (m s^{-1}), shown with a 10 min averaging period and at 10 m elevation.

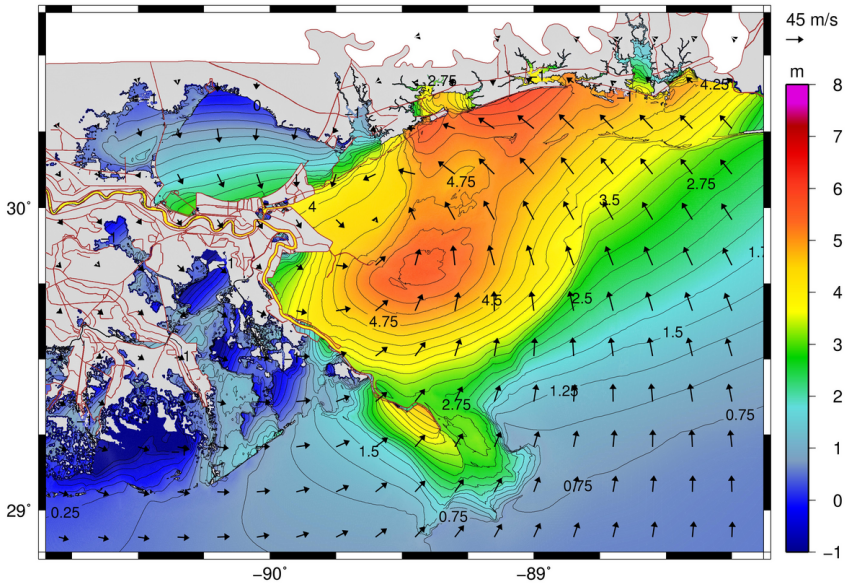

(b) Water elevation contours (m) relative to NAVD 88 (2004.65) and wind vectors (m s^{-1}).

Figure 3.4. Hurricane Katrina winds and water elevations at 1400 UTC 29 August 2005 in southeastern Louisiana.

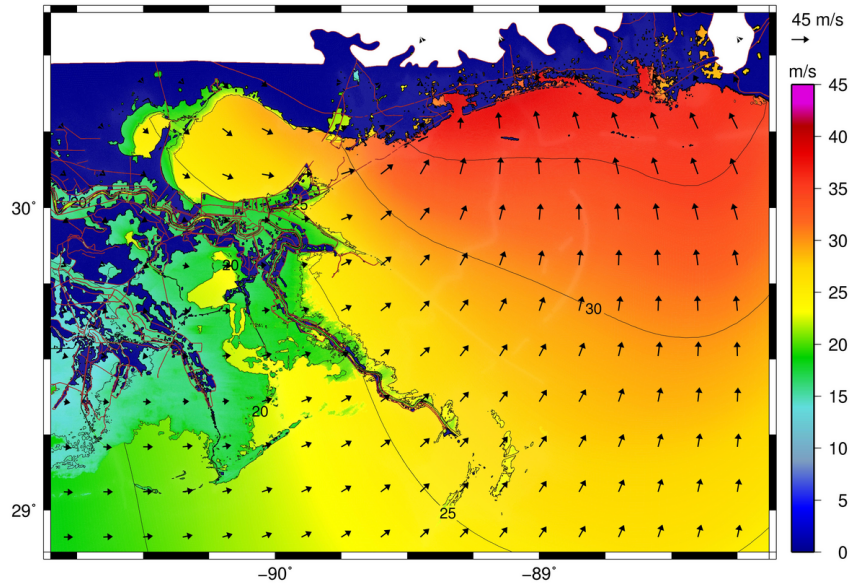

(a) Wind contours and vectors (m s^{-1}), shown with a 10 min averaging period and at 10 m elevation.

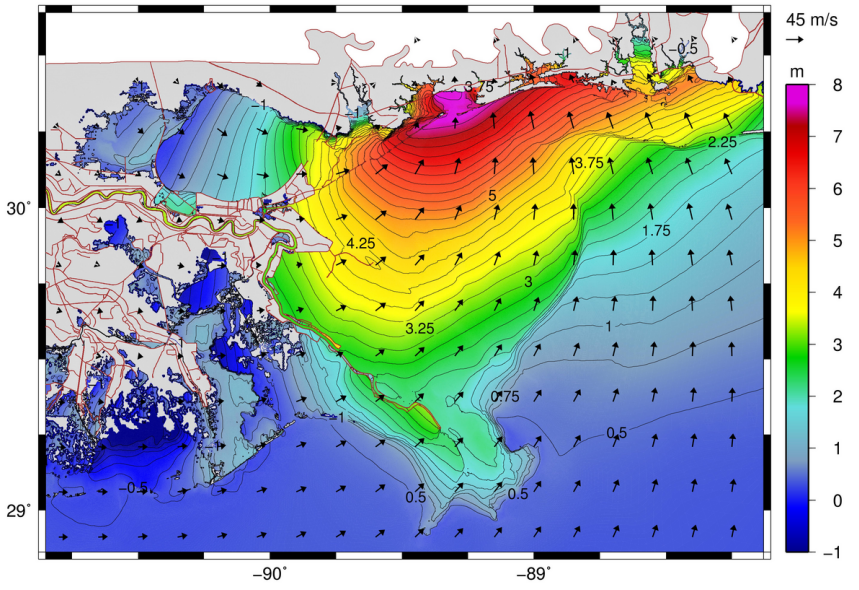

(b) Water elevation contours (m) relative to NAVD 88 (2004.65) and wind vectors (m s^{-1}).

Figure 3.5. Hurricane Katrina winds and water elevations at 1600 UTC 29 August 2005 in southeastern Louisiana.

Pontchartrain. Although winds are blowing westerly across Lake Pontchartrain and causing a drawdown in the west and increased surge in the east, the currents through Rigolets Strait are still easterly, due to the sustained water level differential between the two lakes. The currents in Chandeleur Sound and Mississippi Sound have turned toward the Gulf, with currents of 2-2.5 m s^{-1} over the barrier islands. The islands combined with the increased roughness of the marshes and shallow depths on the protected side of the islands slow the high waters from flowing back to the open Gulf and lead to significant water level differentials between the Gulf- and Sound-side of the islands.

At 2300 UTC 29 August 2005, shown in Figure 3.7, the wind speeds in southeastern Louisiana have decreased to 15 m s^{-1} or less, and the recession process continues. Surge in Lake Pontchartrain is at 2 m without a significant differential and has relaxed due to the slower wind speeds. Water still flows slowly from Lake Borgne into Lake Pontchartrain because of the surface water gradients between these lakes (although the gradient is decreasing). Note the slow withdrawal from the marshes and bays, where localized surge levels still range from 2-4 m or greater. The recession is resisted by the barrier islands and marshes.

3.3.2 Contours of Wave-Related Maxima

Figure 3.8 shows the maximum significant wave heights for Katrina. Wave heights up to 17 m are seen near the bird's foot of the Mississippi River delta coinciding with the passage of the most intense winds to the east of the storm track as well as refraction on the steep sided delta. Strong gradients in wave height are produced by wave breaking along the edge of the delta. Wave heights are reduced more gradually in the areas northeast and west of the delta, where

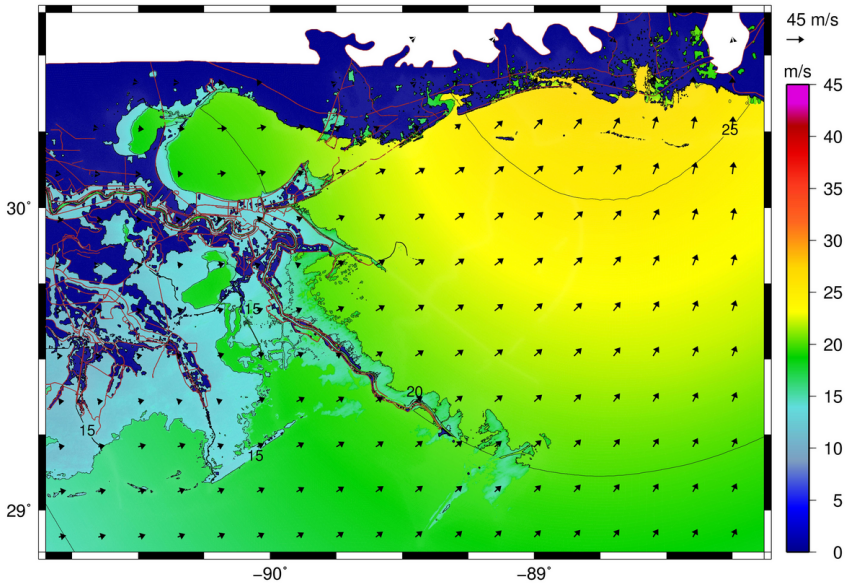

(a) Wind contours and vectors (m s^{-1}), shown with a 10 min averaging period and at 10 m elevation.

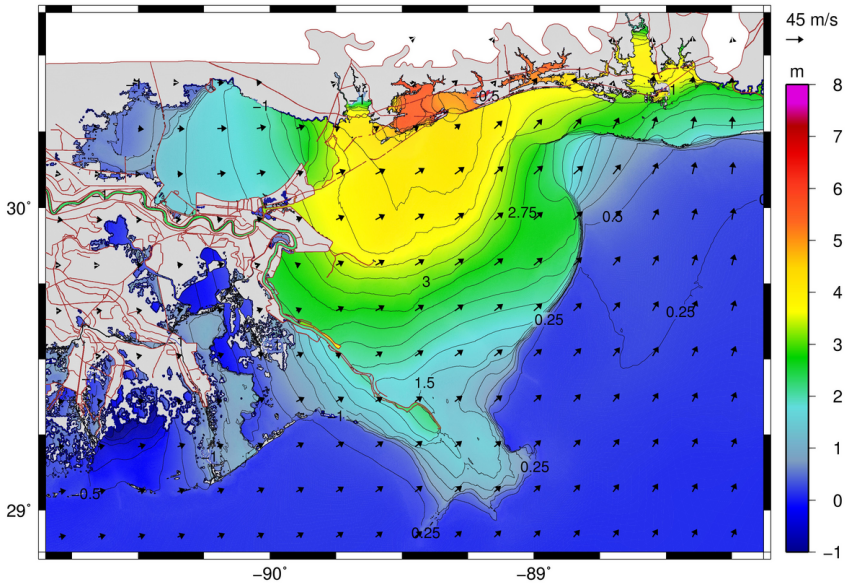

(b) Water elevation contours (m) relative to NAVD 88 (2004.65) and wind vectors (m s^{-1}).

Figure 3.6. Hurricane Katrina winds and water elevations at 1900 UTC 29 August 2005 in southeastern Louisiana.

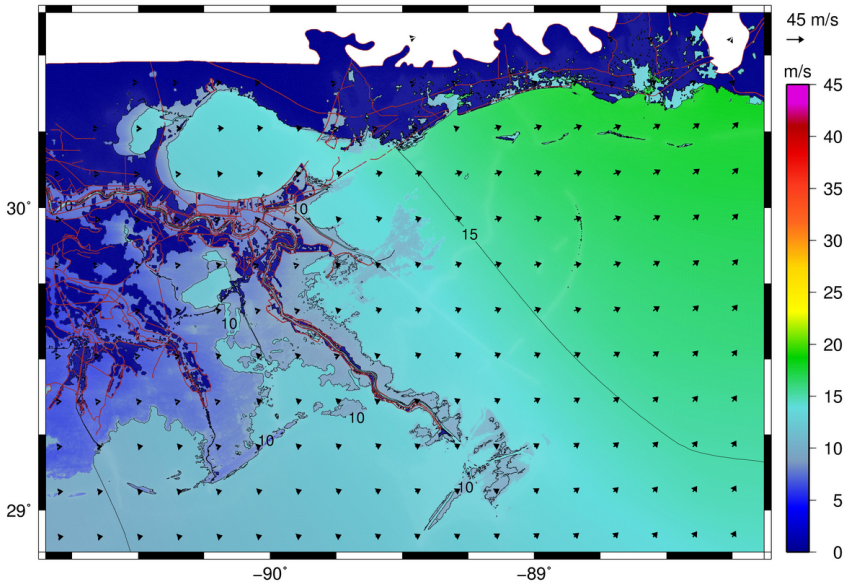

(a) Wind contours and vectors (m s^{-1}), shown with a 10 min averaging period and at 10 m elevation.

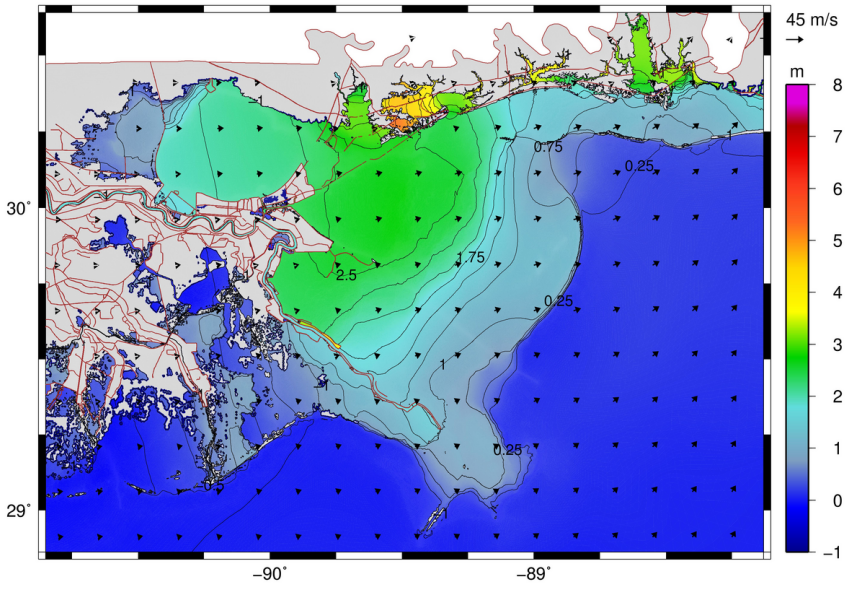

(b) Water elevation contours (m) relative to NAVD 88 (2004.65) and wind vectors (m s^{-1}).

Figure 3.7. Hurricane Katrina winds and water elevations at 2300 UTC 29 August 2005 in southeastern Louisiana.

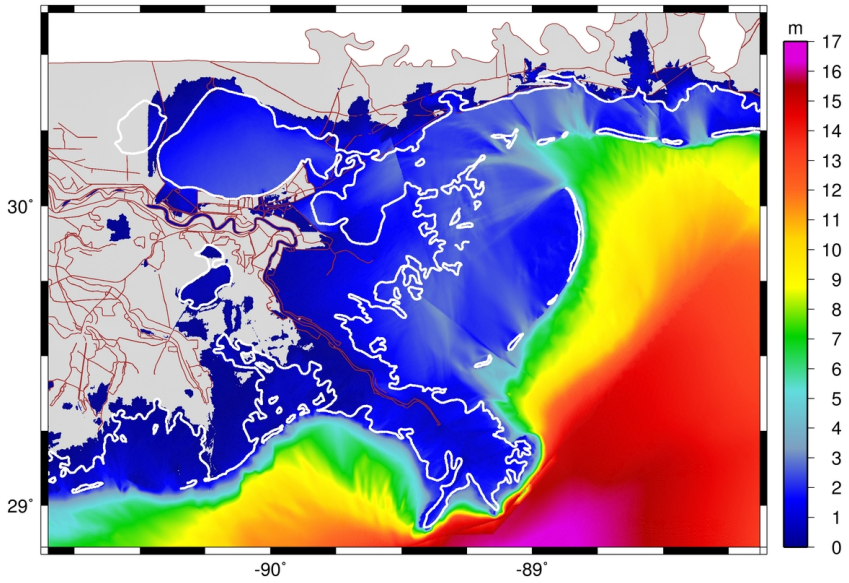

Figure 3.8. Maximum significant wave heights (m) for Hurricane Katrina in southeastern Louisiana.

wave breaking occurs on the shallow shelf. The barrier islands further reduce the nearshore wave height as waves break either on the seaward side or over the top of submerged islands. Wave energy also propagates through the gaps between the islands into the sounds. The Biloxi and Caenarvon Marshes east of the delta (shown within the white shoreline in Figure 3.8) also show reduced wave height due to their shallow depths and vegetation. Wave heights along the interior shorelines are typically in the range of 1-3 m.

Figure 3.9 shows the maximum storm event wave radiation stress gradients for Katrina. Wave radiation stress gradients are the forces applied to the water column as waves transform and are contributors to coastal circulation and surge levels. Forces are greatest where spatial changes in significant wave heights are greatest. The edges of the nearshore STWAVE domains are visible in Figure 3.9,

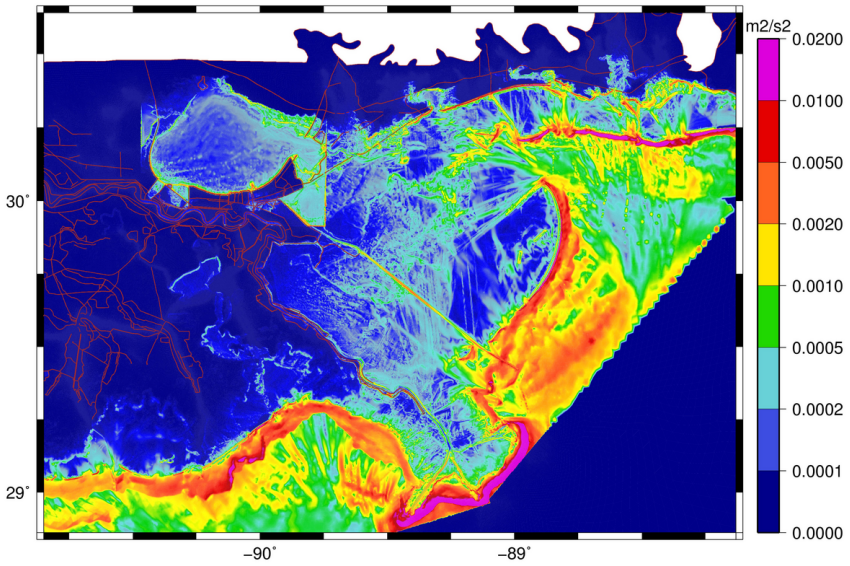

Figure 3.9. Maximum wave radiation stress gradient contours (m^2 s^{-2}) for Hurricane Katrina in southeastern Louisiana.

both along the southwest part of the figure and near Lake Pontchartrain. The regions with the largest radiation stress gradients occur at the bird's foot of the Mississippi River delta and over the barrier islands. Figure 3.10 shows the effect of waves on the maximum computed water levels for Katrina. The figure shows the differences between the maximum water levels for the fully coupled simulation and a simulation that did not include wave effects. The wave radiation stress gradients increase the water levels throughout much of the domain. The largest differences are located in the regions where significant depth-limited wave breaking occurs, such as the bird's foot of the Mississippi River delta, Grand Isle, and other barrier islands. Waves are focused on the delta by refraction, and wave radiation stress gradients increase the water levels by about 0.7-0.8 m, which is about 30-40 percent of the maximum water levels in that region. The continental shelf does not extend much farther than the delta itself, and thus the surge heights are limited,

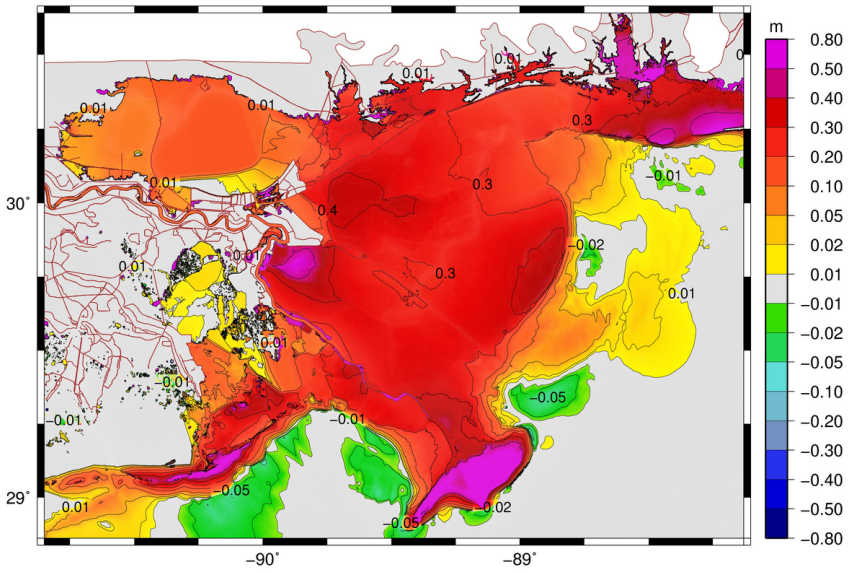

Figure 3.10. Effect of waves on the maximum water levels (m) during Hurricane Katrina.

and the relative contribution of wave-breaking induced set-up is significant (Resio and Westerink, 2008). The water levels are increased over large areas by at least 0.2-0.4 m inshore of the dominant wave breaking zones induced by the barrier islands, and localized maxima of about 0.5 m occur in Plaquemines Parish and the region near English Turn. Wave effects contribute about 5- 10 percent to overall surge levels, which is consistent with the broad continental shelf in this region. In Lake Pontchartrain, wave growth occurs from north to south, and radiation stresses act to push water to the north of the lake. Wave breaking on the south shore causes a focused increase of water levels on the south shore, which is not resolved fully in the modeling system.

3.4 Hurricane Rita

Hurricane Rita made landfall at the western edge of Louisiana, and did not directly threaten the New Orleans area. However, Rita was also an intense storm. Its minimum central pressure of 897 mb was the fourth-lowest ever recorded in the Atlantic basin (Knabb *et al.*, 2006). As summarized in Figure 3.1 and Table 3.2, Rita became a Category 5 storm by 1800 UTC 21 September 2005, and it retained its strength for the next 18 hr as it moved westward and north-westward across the Gulf of Mexico. The storm weakened on 23 September 2005 as it turned more to the northwest. Rita made landfall as a Category 3 storm at 0800 UTC 24 September 2005 near Sabine Pass and the border between Texas and Louisiana. Note that the geographic landmarks discussed in this paper are shown in Figures 2.2 - 2.5.

TABLE 3.2

SUMMARY OF HURRICANE RITA

Date/Time (UTC)	Longitude	Latitude	Pressure (mb)	Maximum Wind Speed ($m\ s^{-1}$)	Category on Saffir-Simpson
2005/09/18/0000	-69.9	21.3	1009	11.5	
2005/09/18/0600	-70.7	21.6	1009	11.5	
2005/09/18/1200	-71.5	21.9	1007	13.8	
2005/09/18/1800	-72.3	22.2	1005	16.1	
2005/09/19/0000	-73.0	22.4	1002	20.7	
2005/09/19/0600	-73.8	22.6	999	22.9	

TABLE 3.2

Continued

Date/Time (UTC)	Longitude	Latitude	Pressure (mb)	Maximum Wind Speed (m s^{-1})	Category on Saffir-Simpson
2005/09/19/1200	-74.7	22.8	997	25.2	
2005/09/19/1800	-75.9	23.1	994	27.6	
2005/09/20/0000	-77.2	23.3	992	27.6	
2005/09/20/0600	-78.8	23.5	990	27.6	
2005/09/20/1200	-80.3	23.7	985	32.1	1
2005/09/20/1800	-81.6	23.9	975	39.0	2
2005/09/21/0000	-82.7	24.1	967	43.7	2
2005/09/21/0600	-84.0	24.2	955	50.5	3
2005/09/21/1200	-85.2	24.2	941	55.1	4
2005/09/21/1800	-86.2	24.3	920	66.6	5
2005/09/22/0000	-86.9	24.5	897	68.9	5
2005/09/22/0600	-87.6	24.8	897	71.2	5
2005/09/22/1200	-88.3	25.2	908	64.3	4
2005/09/22/1800	-89.1	25.6	914	57.4	4
2005/09/23/0000	-89.9	26.0	915	54.8	4
2005/09/23/0600	-90.7	26.5	924	52.9	4
2005/09/23/1200	-91.5	27.1	927	52.9	4
2005/09/23/1800	-92.3	27.8	930	50.5	3

TABLE 3.2

Continued

Date/Time (UTC)	Longitude	Latitude	Pressure (mb)	Maximum Wind Speed (m s^{-1})	Category on Saffir-Simpson
2005/09/24/0000	-93.0	28.6	931	48.2	3
2005/09/24/0600	-93.6	29.4	935	45.9	3
2005/09/24/1200	-94.1	30.5	949	29.8	1
2005/09/24/1800	-94.1	31.6	974	20.8	
2005/09/25/0000	-94.0	32.7	982	16.1	
2005/09/25/0600	-93.6	33.7	989	13.8	
2005/09/25/1200	-92.5	34.7	995	11.5	
2005/09/25/1800	-91.4	35.8	1000	11.5	
2005/09/26/0000	-90.1	37.0	1003	9.2	
2005/09/26/0600	-88.0	39.5	1006	9.2	

3.4.1 Synoptic History in SW Louisiana

At 1200 UTC 23 September 2005, Rita was located about 350 km and 20 hr away from landfall, and had already weakened to a Category 4 storm (Knabb et al. 2006). In Figure 3.11(a), coastal winds over the shelf are predominantly northeasterly and range up to about 30 m s^{-1}. Note the effect of the directional land masking dominated by the low-lying marshes and the absence of extensive

canopied regions. The wind speeds range from about 15 m s^{-1} over the inland lakes to 5-10 m s^{-1} over the surrounding topography to zero in the heavily canopied Atchafalaya River basin.

These winds forced water out of many of the coastal water bodies, including Sabine, Calcasieu, Grand, and White Lakes, and Vermilion Bay in Figure 3.11(b). The four lakes and Vermilion Bay are connected to the Gulf of Mexico through a combination of natural waterways and shipping channels. However, there is additional hydraulic connectivity between the lakes themselves. Some is due to the low-lying, marshy character of the surrounding land and the man-made shipping channels, most notably the GIWW, which is depicted in Figure 3.11(b) as a thin line that runs along the north sides of these four lakes and Vermilion Bay. At this early stage of the hurricane, the area to the south of Grand Lake was inundated. The drawdown in northern Vermilion Bay leads to flooding of Marsh Island.

At 0300 UTC 24 September 2005, Rita was located about 95 km and 5 hr away from landfall, and had deteriorated to a strong Category 3 storm. In Figure 3.12(a), the largest wind speeds occur to the northeast of the eye and have magnitudes of about 44 m s^{-1}. The wind speeds in the coastal and inland water bodies are 30 m s^{-1} or higher, and the directional land masking reduces the wind speeds overland to 20-25 m s^{-1}. The hurricane winds do not blow away from the coastline, except for the region to the west of Sabine Lake, where significant drawdown exists. The winds are easterly and southeasterly, and they range from 30-35 m s^{-1} along the coastline from Vermilion Bay to Calcasieu Lake.

Because of these winds, the surface water elevation gradients have also intensified in Figure 3.12(b). The four lakes experience cross-lake water level differences of at least 2 m and extensive flooding of their western shores. The region around

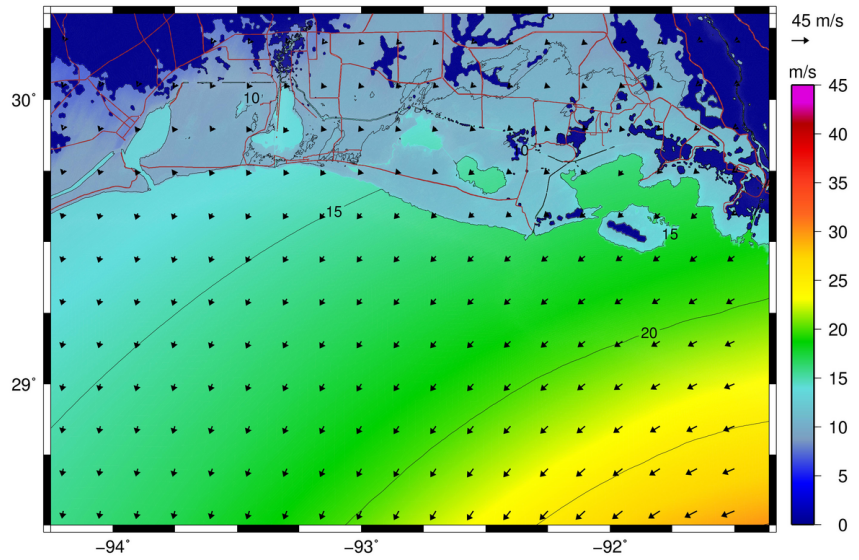

(a) Wind contours and vectors (m s^{-1}), shown with a 10 min averaging period and at 10 m elevation.

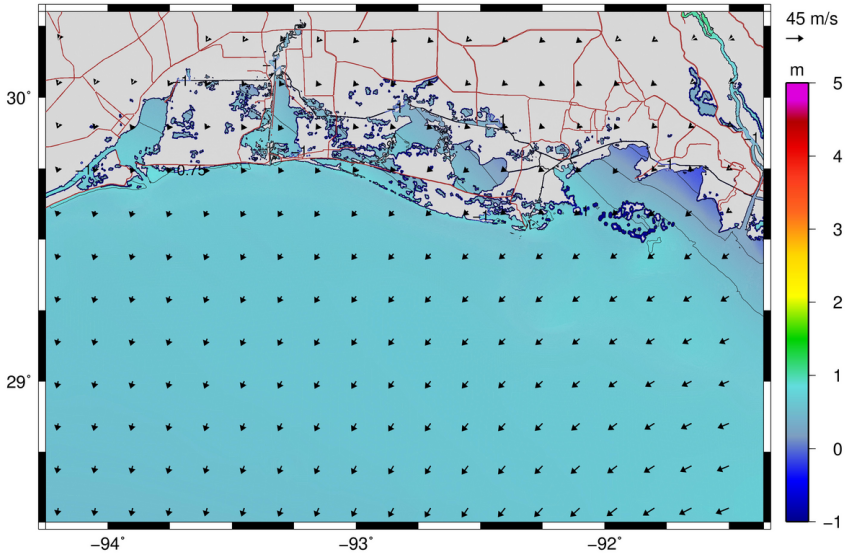

(b) Water elevation contours (m) relative to NAVD 88 (2004.65) and wind vectors (m s^{-1}).

Figure 3.11. Hurricane Rita winds and water elevations at 1200 UTC 23 September 2005 in southwestern Louisiana.

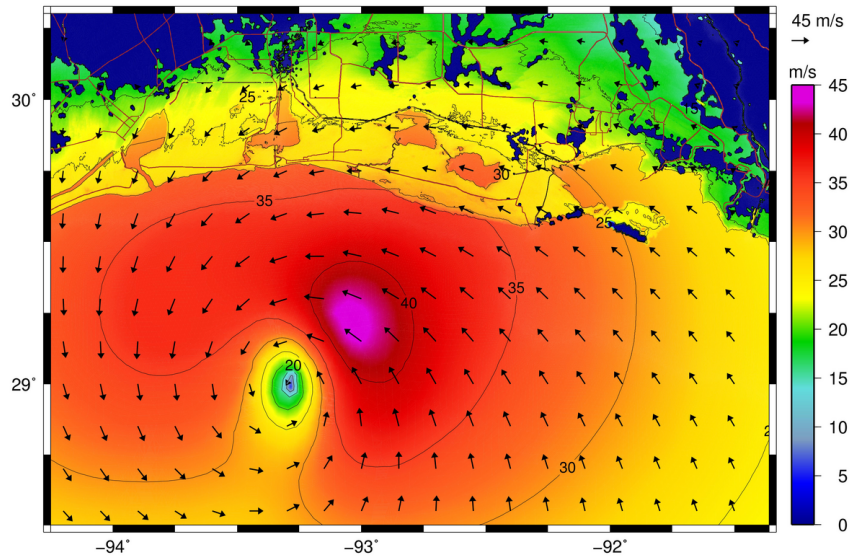

(a) Wind contours and vectors (m s^{-1}), shown with a 10 min averaging period and at 10 m elevation.

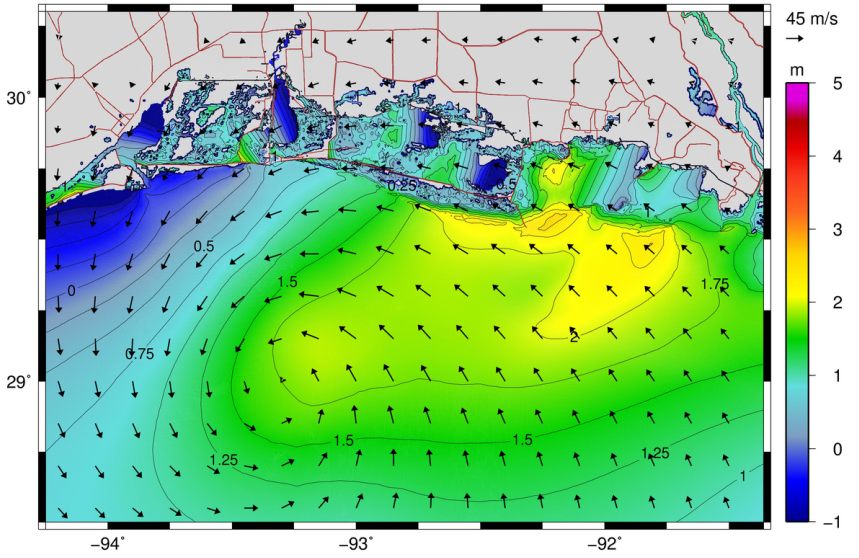

(b) Water elevation contours (m) relative to NAVD 88 (2004.65) and wind vectors (m s^{-1}).

Figure 3.12. Hurricane Rita winds and water elevations at 0300 UTC 24 September 2005 in southwestern Louisiana.

Grand Lake is flooded. Most of the water to the west is held by a local highway, but some of it is pushing through the GIWW to the region east of Calcasieu Lake. The water that began in Calcasieu Lake has pushed to the south and west, and it is now building against the north-facing side of a local highway. The water in Sabine Lake has also pushed to the south. Large portions of southwestern Louisiana are inundated. About 1-2 m of surge has built on the broad continental shelf, pushed by the southerly winds. The surge builds to 2.5 m on the protruding Tiger and Trinity shoals south of Marsh Island.

At 0600 UTC 24 September 2005, Rita was located about 35 km and 2 hr away from landfall. In Figure 3.13(a), the region of maximum winds of about 44 m s^{-1} is positioned just south of Calcasieu Lake. Over the inland lakes, the winds range from 25- 35 m s^{-1}. Even at this stage of the hurricane, the winds at the coast are directed along-shore and range from 30-40 m s^{-1} along the coastline itself, although strong southerly winds are blowing across a broad swath of the shelf.

Figure 3.13(b) shows the storm surge, which extends along the coast from Calcasieu Lake to Vermillion Bay. The region of southerly winds has moved closer to shore, and it has pushed 2-3 m of surge against the shore. This surge propagates inland but is slowed by the topography and marshes. To the east of the eye, the connectivity of Vermilion Bay allows the southeasterly winds to push water into the marshes to its west. To the west of the eye, northerly winds are causing significant drawdown in Sabine Lake and the Gulf outside Sabine Pass. Strong winds over all of the inland water bodies have created strong east-west water level gradients.

At 0800 UTC 24 September 2005, Rita has just made landfall near Sabine Pass, and the winds have begun to decrease (Figure 3.14(a)). The maximum

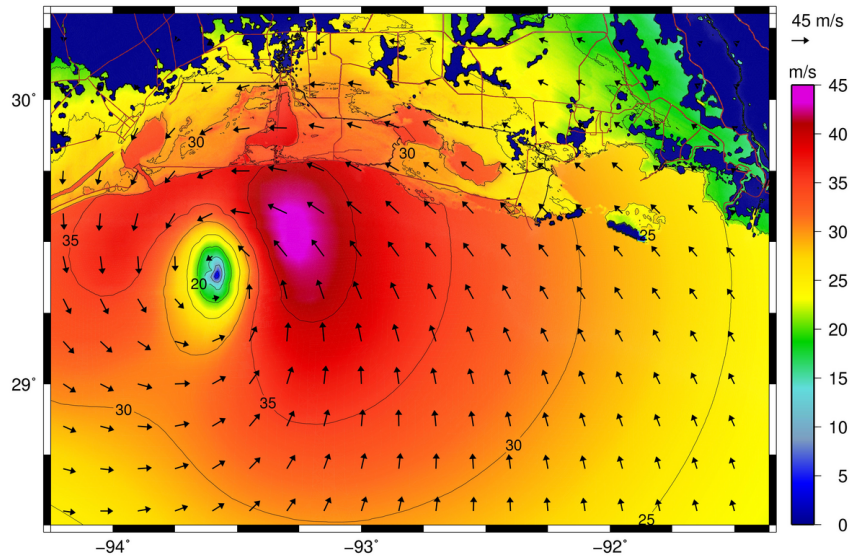

(a) Wind contours and vectors (m s^{-1}), shown with a 10 min averaging period and at 10 m elevation.

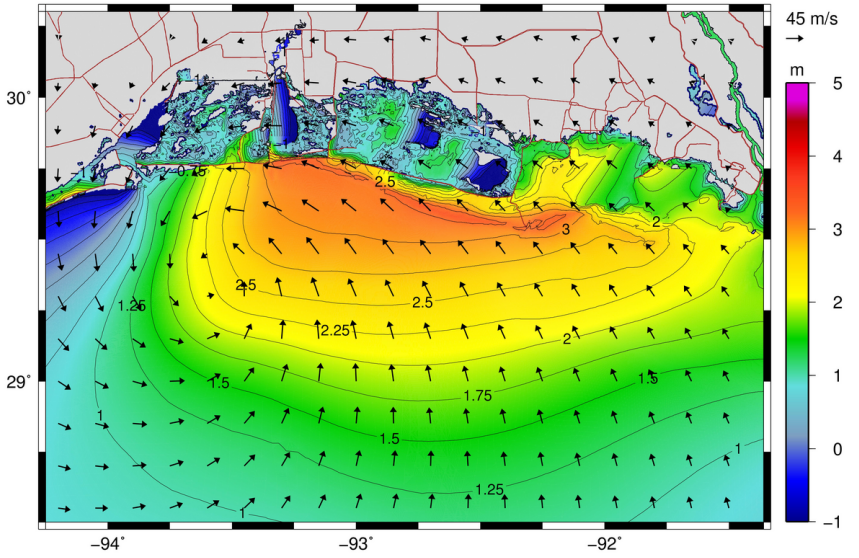

(b) Water elevation contours (m) relative to NAVD 88 (2004.65) and wind vectors (m s^{-1}).

Figure 3.13. Hurricane Rita winds and water elevations at 0600 UTC 24 September 2005 in southwestern Louisiana.

wind speed of 38 m s^{-1} occurs to the south of Calcasieu Lake. The wind speeds farther east, in the region north of Vermilion Bay, are about 25 m s^{-1}. However, the winds have shifted and are now southerly along the coastline. The maximum surge occurs at the coastline to the south of Calcasieu Lake, and these winds blow that surge inland. Figure 3.14(b) shows a broad swath of surge that is driven by the southerly winds and has built along the coast from Sabine Pass to Marsh Island. However, it faces resistance from the coastal highway and the increased friction of the marshes. In Vermilion Bay, where the surge can enter more freely around and over Marsh Island, the surge has reached 2-2.5 m and is building against the northwest shore. East-west water level gradients are still prevalent in most of the lakes.

At 1100 UTC 24 September 2005, Rita was located about 45 km inland. Figure 3.15(a) shows the winds are decreasing over Calcasieu Lake itself, where the maximum wind speed is now about 29 m s^{-1}. The directional land masking has less of an effect at this stage of the hurricane, when the marshes are inundated with significant surge. A large region of the system continues to experience southerly winds of 25 m s^{-1} or greater, and thus the storm surge continues to be pushed against the coastline south of Calcasieu Lake.

Figure 3.15(b) shows Calcasieu Lake has filled with surge, and its natural shoreline is indistinguishable from its inundated surroundings. The surge propagating through Calcasieu Lake causes a local depression in coastal surge levels and leads to high water at the north side of the lake. The overland surge has not reached this far north in adjacent regions, but surge is moving up this system of interconnected channels and lakes. Surge is able to propagate faster and more efficiently through Calcasieu Lake, and thus its water levels in the south are rel-

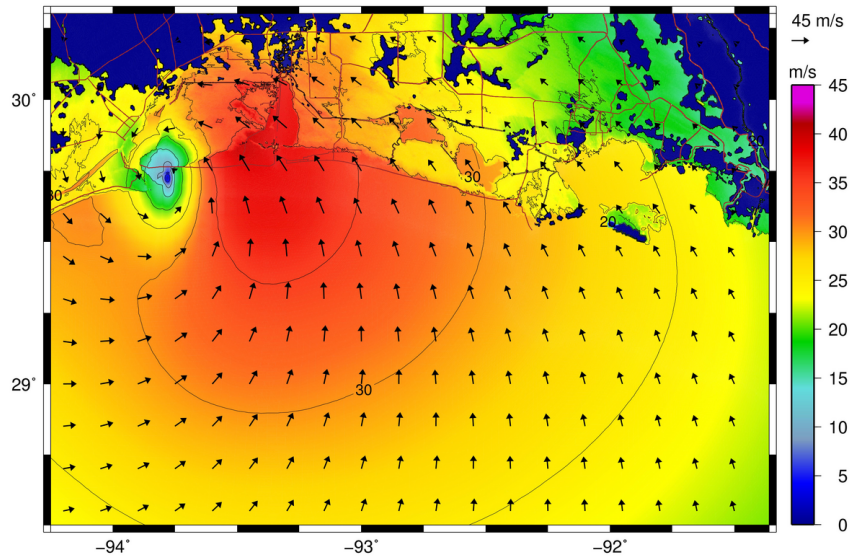

(a) Wind contours and vectors (m s^{-1}), shown with a 10 min averaging period and at 10 m elevation.

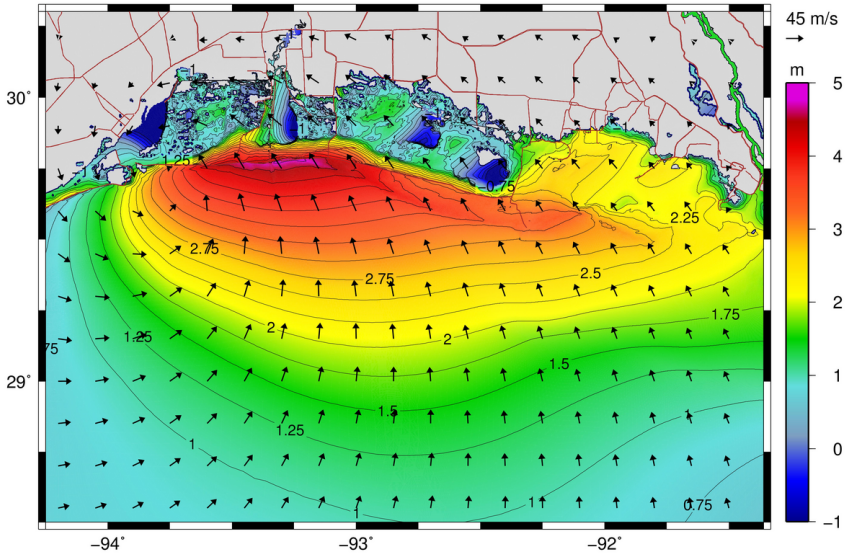

(b) Water elevation contours (m) relative to NAVD 88 (2004.65) and wind vectors (m s^{-1}).

Figure 3.14. Hurricane Rita winds and water elevations at 0800 UTC 24 September 2005 in southwestern Louisiana.

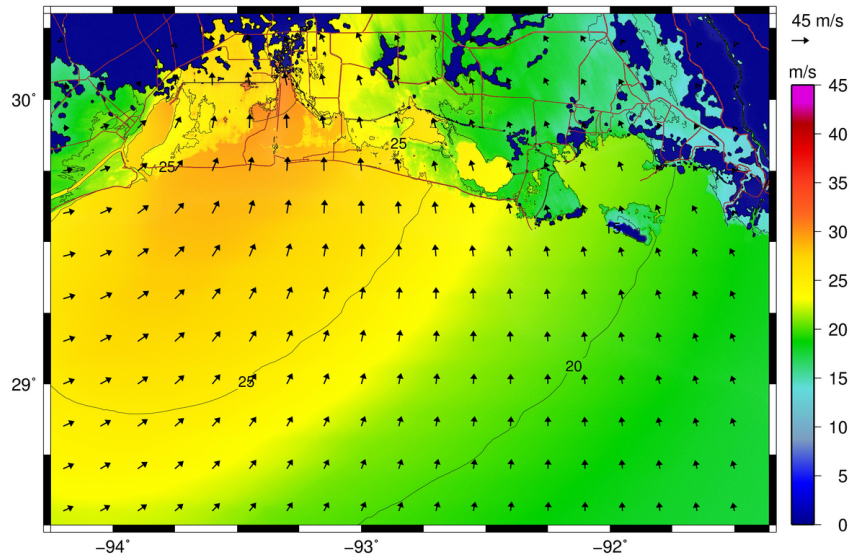

(a) Wind contours and vectors (m s^{-1}), shown with a 10 min averaging period and at 10 m elevation.

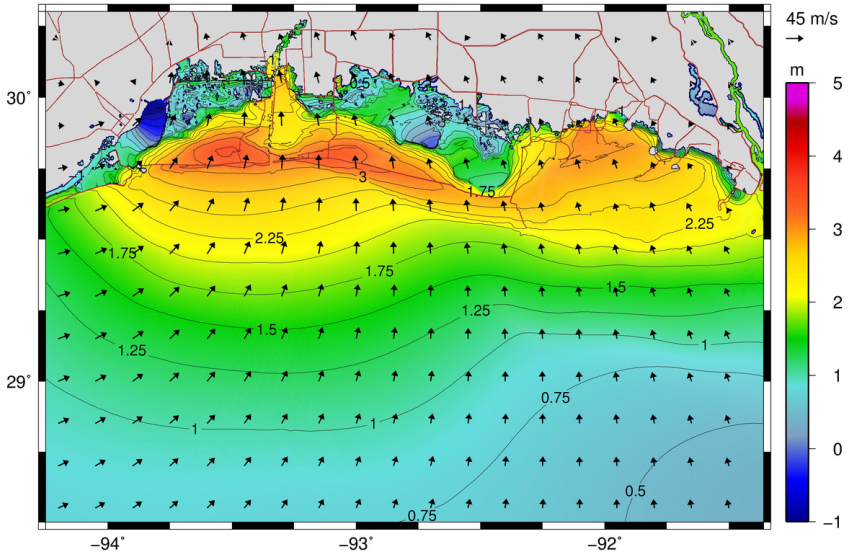

(b) Water elevation contours (m) relative to NAVD 88 (2004.65) and wind vectors (m s^{-1}).

Figure 3.15. Hurricane Rita winds and water elevations at 1100 UTC 24 September 2005 in southwestern Louisiana.

atively lower than those in the surrounding marshes, which are slowing the surge as it propagates northward. Sabine Lake is filling with surge moving from the Gulf through Sabine Pass, but overland surge from the east is also flowing into the lake. A gradient is visible on the south side of Grand Lake, where about 2 m of surge is flowing into the lake. Vermilion Bay and vicinity has filled with water levels reaching 3 m.

Finally, at 2100 UTC 24 September 2005, Rita was located about 225 km north of Sabine Pass. The maximum wind speeds of about 17 m s^{-1} now occur over Sabine and Calcasieu Lakes, as indicated in Figure 3.16(a). Over the marshes, the wind speeds range from 13 m s^{-1} in the west to 10 m s^{-1} in the east. Figure 3.16(b) shows the surge has propagated inland, water is held in the marshes, and water has receded rapidly from the shelf. The southwesterly winds are trying to push surge up the Calcasieu Shipping Channel toward Lake Charles, Louisiana, but the water elevations continue to decrease as water recedes back through Calcasieu Lake and into the Gulf. The high friction of the marshes now restrains the recession process, which continues for days after the storm (Bunya *et al.*, 2010).

3.4.2 Synoptic History in SE Louisiana

Figure 3.17(a) shows the winds across southeastern Louisiana at 1200 UTC 23 September 2005, when the eye of Rita is about 320 km from New Orleans. The tropical- storm-strength winds are easterly and already strong in this region, with 15-20 m s^{-1} winds extending over the Chandeleur and Mississippi Sound Islands and the shallow continental shelf. In Figure 3.17(b), significant surge is occurring in this region. The easterly winds push water against the western edge of Lake Pontchartrain, against the east side of metropolitan New Orleans, and against

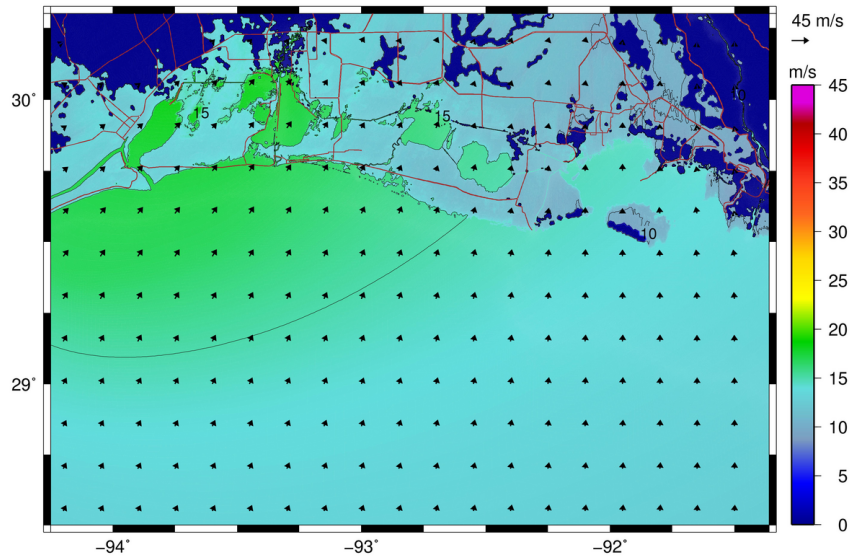

(a) Wind contours and vectors (m s^{-1}), shown with a 10 min averaging period and at 10 m elevation.

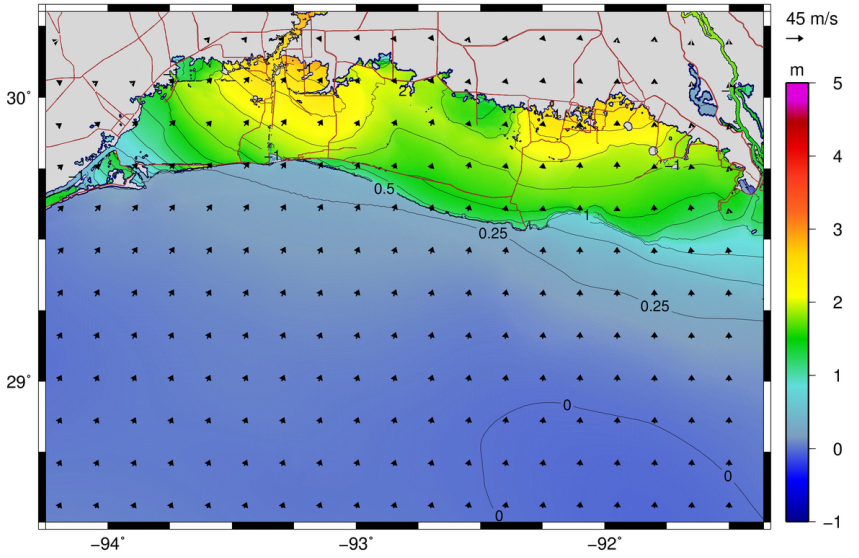

(b) Water elevation contours (m) relative to NAVD 88 (2004.65) and wind vectors (m s^{-1}).

Figure 3.16. Hurricane Rita winds and water elevations at 2100 UTC 24 September 2005 in southwestern Louisiana.

the levees along the lower Mississippi River. A depression exists in the eastern part of Lake Pontchartrain, where water is slow to flow in from Lake Borgne. The gradient in water levels between these two lakes, combined with the easterly winds, drives currents of 1.5-2 m s^{-1} through the passes into Lake Pontchartrain. The surge has reached 2 m in parts of Plaquemines Parish.

Figure 3.18 advance forward in time to 0300 UTC 24 September 2005. Rita is centered about 300 km southwest of New Orleans. In southeastern Louisiana, the winds have shifted to blow southeasterly at 15 m s^{-1}, pushing surge along the Mississippi River levees and toward New Orleans. Lake Pontchartrain has filled with 2 m of water, and 3 m of storm surge is built against the levees near English Turn. The winds and surge that have developed in the region remain steady for the next eight hours. In fact, a steady-state balance between the water surface gradient and the wind stress controls this region during this part of the storm.

Moving forward to 1100 UTC 24 September 2005, Rita was centered about 375 km from New Orleans. In Figure 3.19(a), the winds are very similar to the conditions of 8 hr earlier, but have begun to decrease slowly, allowing the storm surge to decrease slowly as well, as shown in Figure 3.19(b). The surge elevation has decreased to less than 2.75 m at English Turn to the southeast of New Orleans. Significant surge is driven into and held inside Lake Pontchartrain. The surge is smaller outside of the barrier islands, where the water levels are less than 0.75 m.

Finally, at 2100 UTC 24 September 2005, Rita was located more than 400 km from New Orleans, and the wind speeds have decreased in southeastern Louisiana (Figure 3.20(a)). In open water, the wind speed is 10 m s^{-1} or less throughout most of the region. The flood waters are slowly receding in a process that is dominated by the friction in the marshes and passes (Figure 3.20(b)), which are

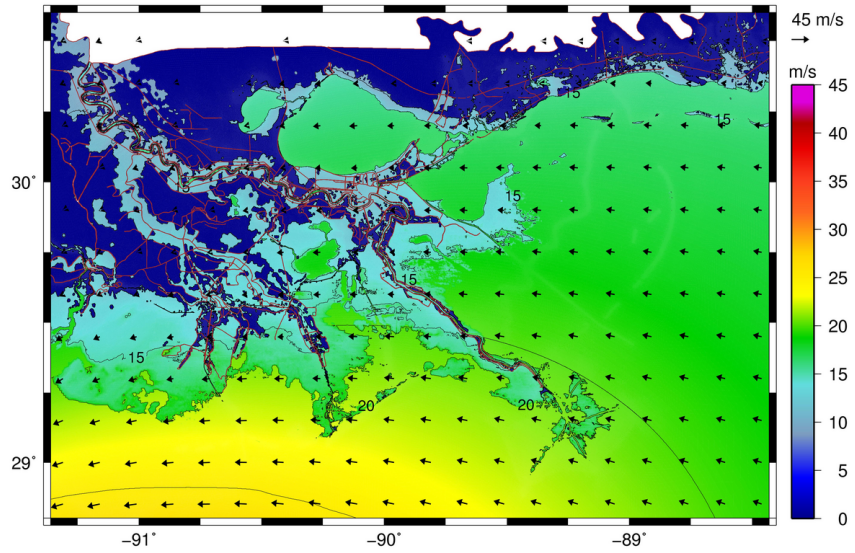

(a) Wind contours and vectors (m s^{-1}), shown with a 10 min averaging period and at 10 m elevation.

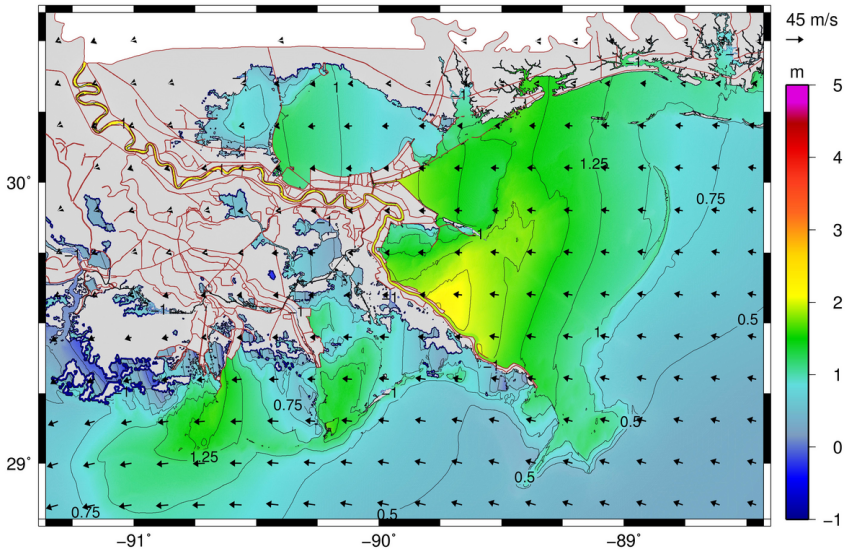

(b) Water elevation contours (m) relative to NAVD 88 (2004.65) and wind vectors (m s^{-1}).

Figure 3.17. Hurricane Rita winds and water elevations at 1200 UTC 23 September 2005 in southeastern Louisiana.

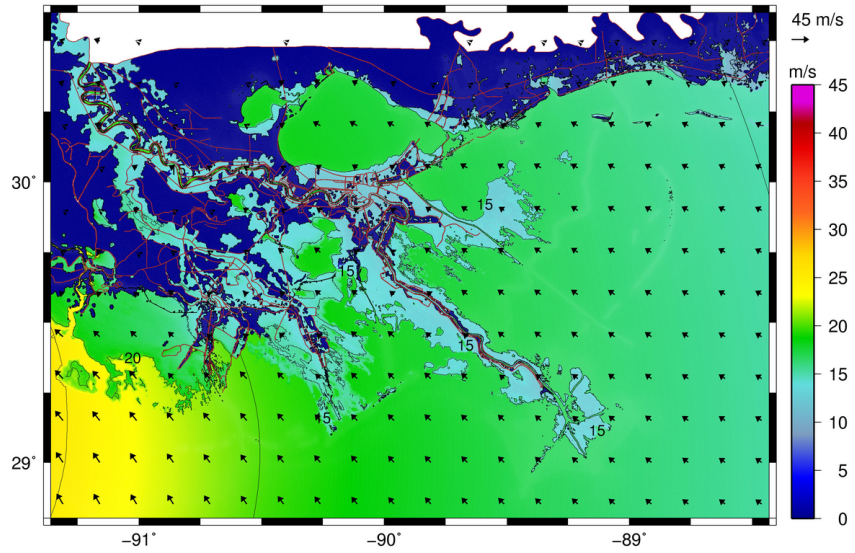

(a) Wind contours and vectors (m s^{-1}), shown with a 10 min averaging period and at 10 m elevation.

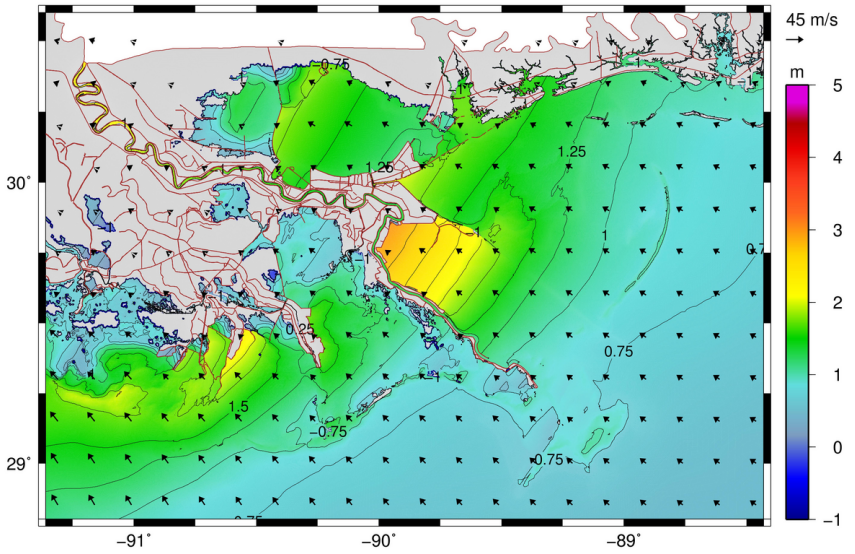

(b) Water elevation contours (m) relative to NAVD 88 (2004.65) and wind vectors (m s^{-1}).

Figure 3.18. Hurricane Rita winds and water elevations at 0300 UTC 24 September 2005 in southeastern Louisiana.

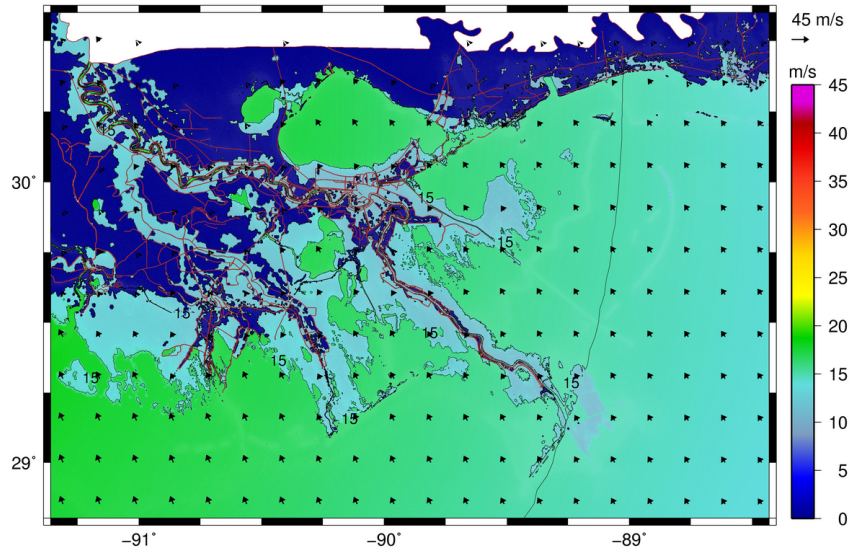

(a) Wind contours and vectors (m s^{-1}), shown with a 10 min averaging period and at 10 m elevation.

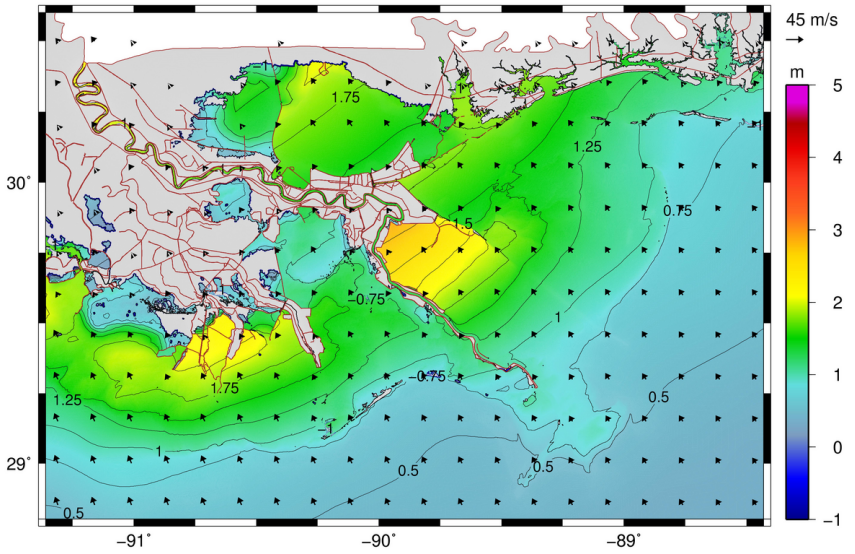

(b) Water elevation contours (m) relative to NAVD 88 (2004.65) and wind vectors (m s^{-1}).

Figure 3.19. Hurricane Rita winds and water elevations at 1100 UTC 24 September 2005 in southeastern Louisiana.

holding water on all sides of New Orleans. Lake Pontchartrain also holds its water efficiently.

3.4.3 Contours of Wave-Related Maxima

Figure 3.21 shows the maximum significant wave heights in south-western Louisiana. The wave heights are 10-12 m along the outer shelf and reduced to 3-5 m near the shore by breaking. Although the coastal marshes were inundated, wave height reduced dramatically due to depth limited breaking and friction. Figure 3.22 shows the maximum wave radiation stress gradients in southwestern Louisiana. The edge of the nearshore STWAVE domain is visible in the southern part of the figure, where the interpolation between the three models has caused large gradients at some nodes. However, the behavior becomes better near the shore, where the models contain high resolution to capture the wave breaking zones. The maximum wave radiation stress gradients occur along the shoreline and to the south of the Tiger and Trinity Shoals. Wave radiation stresses also appear in lakes that are farther inland, suggesting local wave generation and breaking along their shores.

Figure 3.23 shows the maximum significant wave heights in south-eastern Louisiana. The wave height trends were similar to those produced for Katrina (transformation and dissipation on the shelf, and further sheltering and breaking induced by the barrier islands), but the larger wave heights in this region are west of the delta due to the storm track. Higher water levels and on-shore winds in Barataria and Terrebonne Bays (west of the delta) produced larger wave heights in these inshore areas in Rita compared to Katrina, although the wave heights on the shelf west of the delta were lower for Rita (7-8 m) than Katrina (11-13 m).

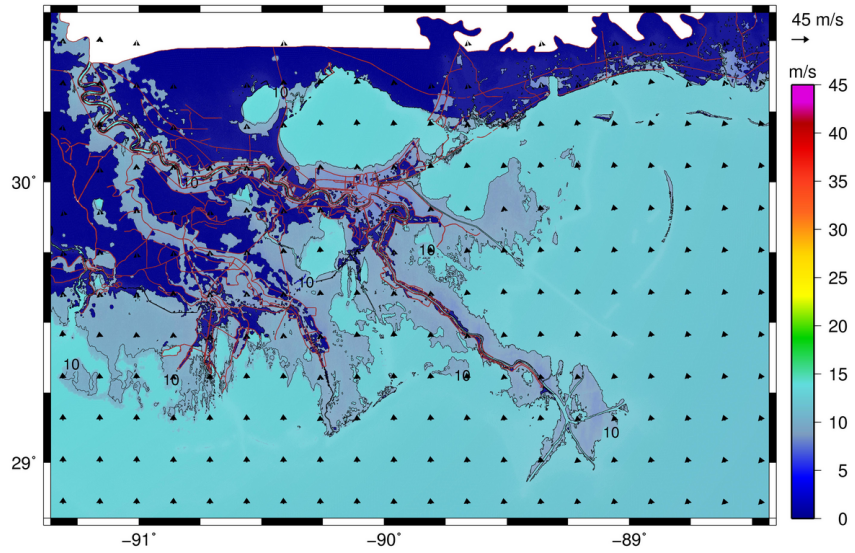

(a) Wind contours and vectors (m s^{-1}), shown with a 10 min averaging period and at 10 m elevation.

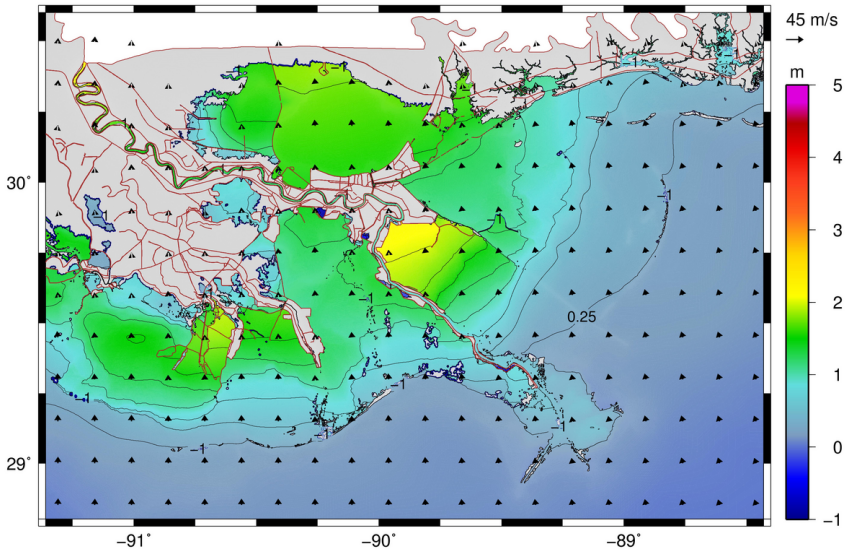

(b) Water elevation contours (m) relative to NAVD 88 (2004.65) and wind vectors (m s^{-1}).

Figure 3.20. Hurricane Rita winds and water elevations at 2100 UTC 24 September 2005 in southeastern Louisiana.

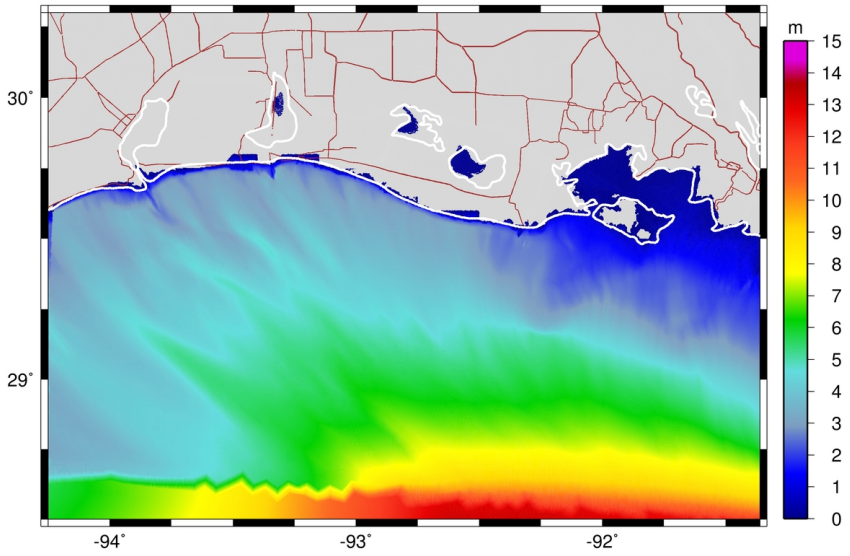

Figure 3.21. Maximum significant wave heights (m) for Hurricane Rita in southwestern Louisiana.

Figure 3.24 shows the maximum wave radiation stress gradients in the same region. Significant wave breaking occurs along the shoreline near Grand Isle in the southwestern part of the figure, throughout the Mississippi River delta, and along barrier islands at the periphery of the Chandeleur and Mississippi Sounds. Behind these features, though, the wave radiation stress gradients are insignificant.

Figure 3.25 shows the effect of waves as the difference between the fully coupled simulation and a simulation that did not include waves. As the waves break, they generate significant radiation stress gradients that push additional water inland. The maximum water levels are larger throughout much of the floodplain of southwestern Louisiana, by as much as 0.1-0.3 m or about 5-15 percent of the local surge. These modest increases in surge due to wave breaking are consistent with the broad continental shelf and expansive wetlands in southwestern Louisiana. The wave-induced set-up would be larger and more concentrated if the shelf was

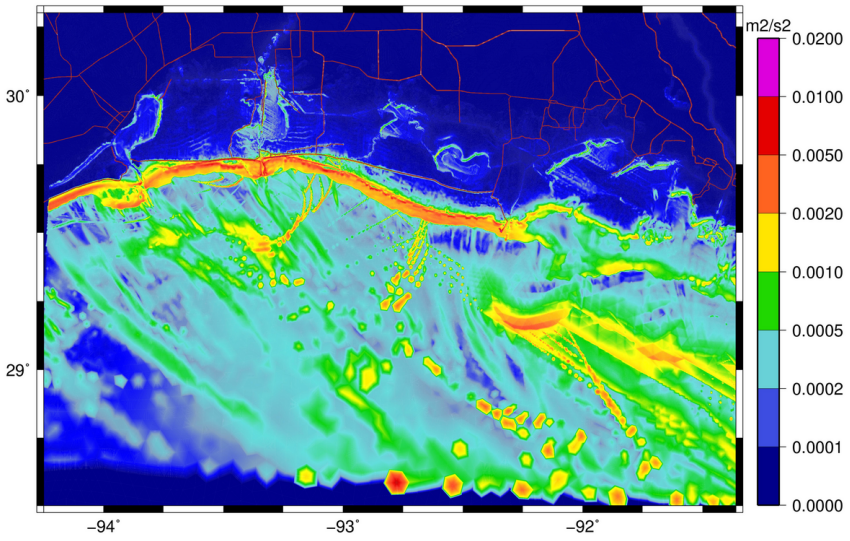

Figure 3.22. Maximum wave radiation stress gradient contours ($m^2\ s^{-2}$) for Hurricane Rita in southwestern Louisiana.

narrower or if the nearshore had a steeper slope. In southeastern Louisiana, the waves break at the barrier islands in the east and along the coastline in the south, and they increase the water levels by 0.05-0.2 m. Note the localized maxima of 0.4 m in Terrebonne Bay, Grand Isle and the Mississippi River delta. These contributions represent about 40 percent of the total surge in these regions.

3.5 Conclusions

The comprehensive synoptic histories of Hurricanes Katrina and Rita show that hurricane storm surge is a complex process that depends on the unique characteristics of the hurricanes and the geographical features of the regions they impact. The system's response to Katrina was markedly different east and west of the Mississippi River, highly localized, varied over even a few kilometers, and changed dramatically as the storm moved along its southerly track. In the early

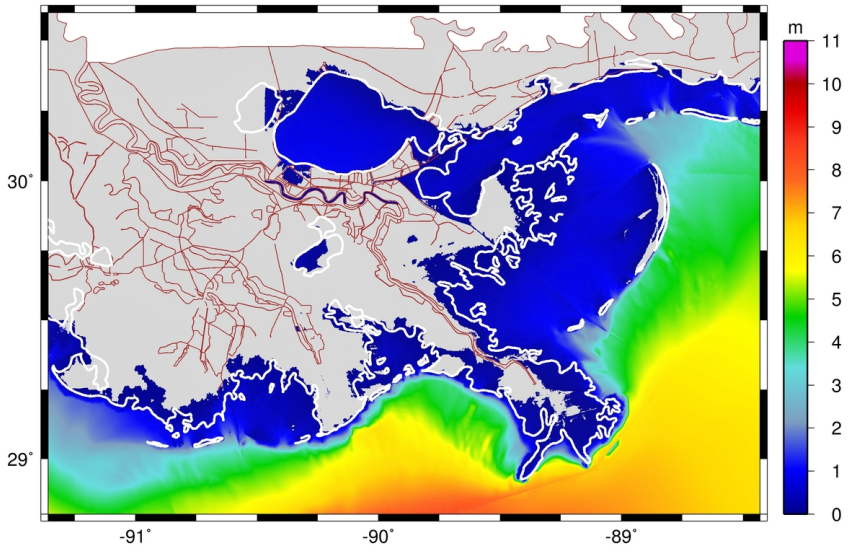

Figure 3.23. Maximum significant wave heights (m) for Hurricane Rita in southeastern Louisiana.

part of the storm, its asymmetry created strong easterly and southerly winds, which pushed 1.5-2.5 m of surge onto the broad, shallow shelf and into southeastern Louisiana. The shallower the water, the more effective the wind stress is at creating surge and piling it against obstructions. Currents were significant over the barrier islands and around the bird's foot of the Mississippi River delta. Surge collected against the east-facing banks and levees of the lower Mississippi River and delta. Instead of flowing past the river and into the marshes and bays to the southwest, this surge propagated partially up the river, eventually flowing past New Orleans and Baton Rouge. Another component propagated across Breton Sound toward Mississippi. The marshes did not play a significant role in this part of the storm, because the water levels became too large to be dominated by bottom friction. At least 2-3 m of storm surge formed behind the barrier islands and remained on the shelf throughout the storm. The exception was the Caernarvon

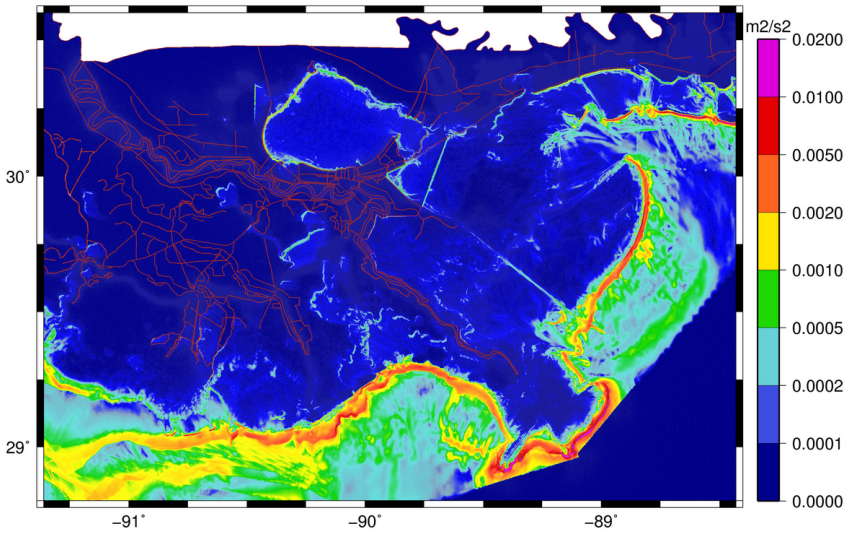

Figure 3.24. Maximum wave radiation stress gradient contours (m^2 s^{-2}) for Hurricane Rita in southeastern Louisiana.

Marsh southeast of English Turn, which controlled how fast water was able to propagate across the marsh and build against the Mississippi River levees at English Turn before the winds shifted. These shifting winds also limited the storm surge near the Chalmette extension levee. Water was forced into Lakes Borgne and Pontchartrain, and these lakes experienced significant gradients as surge was pushed toward their western and southern shores. In addition, water from Lake Borgne was not flowing into Lake Pontchartrain fast enough to replace the water being blown to the west and south, creating a strong inter-lake gradient.

As the storm made landfall in Mississippi, its winds shifted to blow southerly and westerly. Surge was pushed northward, where it built against the steep topography along the coastline of Mississippi and Alabama. This surge flooded the bays and coastline and pushed additional water into Lakes Borgne and Pontchartrain. The surge was held in the lakes and bays because of limited hydraulic

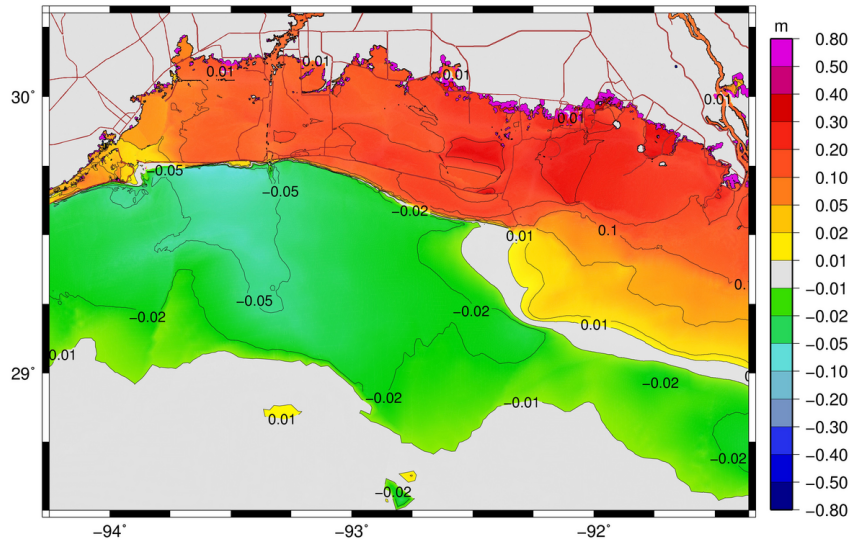

(a) Effect in southwestern Louisiana.

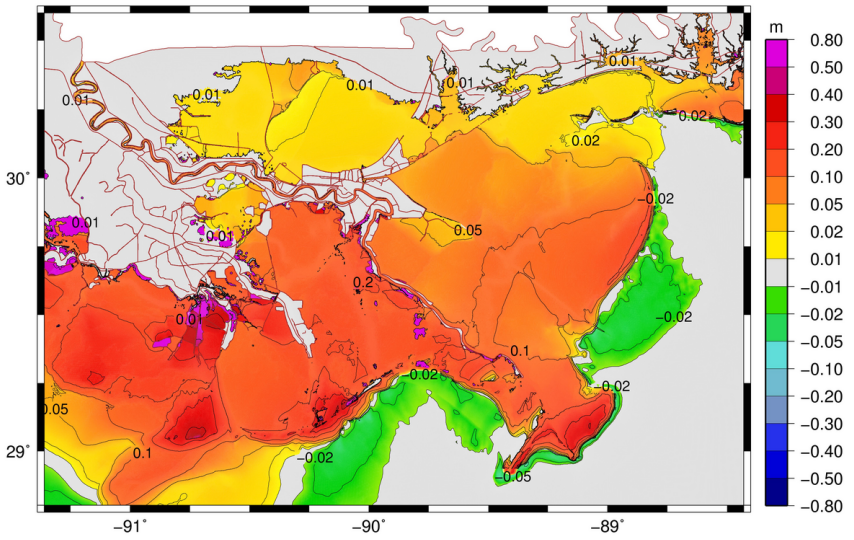

(b) Effect in southeastern Louisiana.

Figure 3.25. Effect of waves on the maximum water levels (m) during Hurricane Rita.

connectivity through the straits to the connecting water bodies, the locally steep topography, and the limited extent of the floodplain. The surge was held on the continental shelf because of the marshes and barrier islands, which greatly slowed the flood recession process. The wave-induced set-up was significant throughout the region, but especially in the bird's foot of the Mississippi River delta, where it was 30-40 percent of the overall water level. The delta's proximity to the edge of the continental shelf exposed it to large waves but little surge.

Rita caused extensive overland flooding in southwestern Louisiana. In the early part of the storm, its winds were easterly throughout much of the region, and they pushed water from lakes and bays onto the surrounding marshes, building within the low-lying land and against embankments and structures. However, storm surge did not form at the coastline, because the easterly winds were not directed toward shore, and the region does not contain natural protrusions that would collect surge, in contrast to the region impacted by Katrina. Instead, the winds pushed water along and even away from the shore. Significant drawdown was experienced along the coast of southwest Louisiana, but especially near Sabine Pass, west of the eventual landfall location.

The southerly winds prior to landfall built surge to 1-2 m on the continental shelf. When these southerly winds reached the coastline, the surge built to levels exceeding 4 m over a large area. The surge at the coast is dominated by the wind and relative hydraulic efficiencies of the ocean and land. The winds held the water at the coast and enabled its release into the low-lying marshes. This surge propagated quickly through Calcasieu Lake, but it also flowed over the marshes and low-lying topography. In the days after the storm, the recession process was relatively slow and dominated by the friction of the marshes. The

observed inland surge attenuation rates are consistent with those observed in previous storms in southwestern Louisiana (Resio and Westerink, 2008). Wave radiation stress gradients were strong along the coastline. The wave-induced set-up was significant; water levels were increased by about 0.1-0.3 m throughout the region. This set-up was proportionately less than for Katrina, but it is consistent with the broad continental shelf of southwest Louisiana.

Like Katrina, Rita created significant surge in complex southeastern Louisiana. Its eye was never closer than about 300 km to New Orleans, but its southeasterly track produced winds of tropical storm strength that were southeasterly and a relatively constant 15-20 m s^{-1}. A steady state was created in which the winds pushed significant surge against the banks and levees of the Mississippi River and the marshes and structures between Lakes Pontchartrain and Borgne, resulting in surge of about 2 m in Lake Pontchartrain and about 3m at the levees near English Turn. Once the surge had collected against these levees, it was held there by the near steady winds. Marsh friction did not play a role in the eventual surge level because a steady state balance between water surface gradients and wind stress was reached.

CHAPTER 4

MODELING HURRICANE WAVES AND STORM SURGE USING INTEGRALLY-COUPLED, SCALABLE COMPUTATIONS

4.1 Overview

This chapter describes the tight coupling of SWAN+ADCIRC. It discusses the different types of model coupling and their drawbacks, with an emphasis on how the use of heterogeneous meshes limits the performance of a coupled model in a high-performance computing environment. SWAN+ADCIRC is coupled tightly so that the models run on the same unstructured meshes and on the same computational cores, thus ensuring good performance because information can be passed through local cache without the need for interpolation. The coupled model is validated via hindcasts of Katrina and Rita, with a focus on how its results compare to the solutions obtained from WAM and STWAVE. The tightly-coupled SWAN+ADCIRC is shown to be as accurate as the structured-mesh wave models, but better positioned to increase mesh resolution in regions with large gradients in bathymetry and/or the computed solution. This chapter is in press in *Coastal Engineering* as Dietrich *et al.* (2010b).

The unstructured-mesh SWAN spectral wave model and the ADCIRC shallow-water circulation model have been integrated into a tightly-coupled SWAN+ADCIRC model. The model components are applied to an identical, unstructured

mesh; share parallel computing infrastructure; and run sequentially in time. Wind speeds, water levels, currents and radiation stress gradients are vertex-based, and therefore can be passed through cache to each model component. Parallel simulations based on domain decomposition utilize identical sub-meshes, and the communication is highly localized. Inter-model communication is intra-core, while intra-model communication is inter-core but is local and efficient because it is solely on adjacent sub-mesh edges. The resulting integrated SWAN+ADCIRC system is highly scalable and allows for localized increases in resolution without the complexity or cost of nested meshes or global interpolation between heterogeneous meshes. Hurricane waves and storm surge are validated for Hurricanes Katrina and Rita, demonstrating the importance of inclusion of the wave-circulation interactions, and efficient performance is demonstrated to 3,062 cores.

4.2 Introduction

A broad energy spectrum exists in oceans, with wave periods ranging from seconds to months. Short waves, such as wind-driven waves and swell, have periods that range from 0.5-25 s. Longer waves, such as seiches, tsunamis, storm surges and tides, have periods that range from minutes to months. These short and long waves are well-separated in the energy spectrum and have well-defined spatial scales. This separation leads to distinct modeling approaches, depending on whether the associated scales can be resolved. For oceanic scales, short-wave models cannot resolve spatially or temporally the individual wind-driven waves or swell, and thus they treat the wave field as an energy spectrum and apply the conservation of wave action density to account for wave-current interactions. Long-wave models apply forms of conservation of mass and momentum, in two or

three spatial dimensions, to resolve the circulation associated with processes such as tsunamis, storm surges or tides.

Although wind-driven waves and circulation are separated in the spectrum, they can interact. Water levels and currents affect the propagation of waves and the location of wave-breaking zones. Wave transformation generates radiation stress gradients that drive set-up and currents. Wind-driven waves affect the vertical momentum mixing and bottom friction, which in turn affect the circulation. Water levels can be increased by 5-20 percent in regions across a broad continental shelf, and by as much as 35 percent in regions of steep slope (Funakoski *et al.*, 2008; Dietrich *et al.*, 2010a). Thus, in many coastal applications, waves and circulation processes should be coupled.

Wave and circulation models have been limited by their spectral, spatial and temporal resolution. This limitation can be overcome by nesting structured meshes, to enhance resolution in specific regions by employing meshes with progressively finer scales. In a wave application, nesting also allows the use of models with different physics and numerics. Relatively fine nearshore wave models, such as STWAVE and SWAN, can be nested inside relatively coarse deep-water wave models, such as WAM and WaveWatch III (WAMDI Group, 1988; Komen *et al.*, 1994; Booij *et al.*, 1999; Smith *et al.*, 2001; Thompson *et al.*, 2004; Gunther 2005; Tolman 2009). The nearshore wave models may not be efficient if applied to large domains, and the deep-water wave models may not contain the necessary physics or resolution for nearshore wave simulation. Until recently, wave models required nesting in order to vary resolution from basin to shelf to nearshore applications. These structured wave models can be coupled to structured circulation models that run on the same nested meshes (Kim *et al.*, 2008).

Unstructured circulation models have emerged to provide localized resolution of gradients in geometry, bathymetry/topography, and flow processes. Resolution varies over a range of scales within the same mesh from deep water to the continental shelf to the channels, marshes and floodplains near shore (Westerink *et al.*, 2008). Unstructured meshes allow for localized resolution where solution gradients are large and correspondingly coarser resolution where solution gradients are small, thus minimizing the computational cost relative to structured meshes with similar minimum mesh spacings.

The coupling of wave and circulation models has been implemented typically with heterogeneous meshes. A coupling application may have one unstructured circulation mesh and several structured wave meshes, and the models may pass information via external files (Weaver and Slinn, 2004; Ebersole *et al.*, 2007; Chen *et al.*, 2008; Funakoshi *et al.*, 2008; Pandoe and Edge, 2008; Bunya *et al.*, 2010; Dietrich *et al.*, 2010a). This 'loose' coupling is disadvantageous because it requires intra-model interpolation at the boundaries of the nested, structured wave meshes and inter-model interpolation between the wave and circulation meshes. This interpolation creates problems with respect to both accuracy and efficiency. Overlapping nested or adjacent wave meshes often have different solutions, and inter-mesh interpolation can smooth or enhance the integrated wave forcing. Furthermore, even if a component model is locally conservative, its interpolated solution will not necessarily be conservative. Finally, inter-model interpolation must be performed at all vertices of the meshes. This interpolation is problematic in a parallel computing environment, where the communication between sub-meshes is inter-model and semi-global. The sub-meshes must communicate on an area basis (*i.e.*, the information at all vertices on a sub-mesh must be shared). Global

communication is costly and can prevent models from being scalable in high-performance computing environments.

An emerging practice is to couple models through a generic framework, such as the Earth System Modeling Framework (ESMF) (Hill *et al.*, 2004; Collins *et al.*, 2005), the Open Modeling Interface (OpenMI) Environment (Moore and Tindall, 2005; Gregersen *et al.*, 2005) or the Modeling Coupling Toolkit (MCT) (Warner *et al.*, 2008). These frameworks manage when and how the individual models are run, interpolate information between models if necessary, and make transparent the coupling to developers and users. However, these frameworks do not eliminate the fundamental problems of coupling when using heterogeneous meshes. Boundary conditions must be interpolated between nested, structured wave meshes, and water levels, currents and wave properties must be interpolated between the unstructured circulation and structured wave meshes. This interpolation is costly, destroys the scalability of the coupled model, and thus limits the resolution that can be employed and the corresponding physics that can be simulated.

The recent introduction of unstructured wave models makes nesting unnecessary. Resolution can be enhanced nearshore and relaxed in deep water, allowing the model to simulate efficiently the wave evolution. SWAN has been used extensively to simulate waves in shallow water (Booij *et al.*, 1999; Ris *et al.*, 1999; Gorman and Neilson, 1999; Rogers *et al.*, 2003), and it has been converted recently to run on unstructured meshes (Zijlema, 2010). This version of SWAN employs the unstructured-mesh analog to the solution technique from the structured version. It retains the physics and numerics of SWAN, but it runs on unstructured meshes, and it is both accurate and efficient in the nearshore and in deep water.

In this chapter, we describe a 'tight' coupling of the SWAN wave model and the ADCIRC circulation model. SWAN and ADCIRC are run on the same unstructured mesh. This identical, homogeneous mesh allows the physics of wave-circulation interactions to be resolved correctly in both models. The unstructured mesh can be applied on a large domain to follow seamlessly all energy from deep to shallow water. There is no nesting or overlapping of structured wave meshes, and there is no inter-model interpolation. Variables and forces reside at identical, vertex-based locations. Information can be passed without interpolation, thus reducing significantly the communication costs.

In parallel computing applications, identical sub-meshes and communication infrastructure are used for both SWAN and ADCIRC, which run as the same program on the same computational core. All inter-model communication on a sub-mesh is done through local cache. Communication between sub-meshes is intra-model. Information is passed only to the edges of neighboring sub-meshes, and thus the coupled model does not require global communication over areas. Domain decomposition places neighboring sub-meshes on neighboring cores, so communication costs are minimized. The coupled model is highly scalable and integrates seamlessly the physics and numerics from ocean to shelf to floodplain. Large domains and high levels of local resolution can be employed for both models, allowing the accurate depiction of the generation, propagation and dissipation of waves and surge. The resulting SWAN+ADCIRC model is suited ideally to simulate waves and circulation and their propagation from deep water to complicated nearshore systems.

In the sections that follow, the component SWAN and ADCIRC models are described, and the mechanics of their tight coupling is introduced. The coupled

model is then validated through its application to hindcasts of Hurricanes Katrina and Rita. Finally, a benchmarking study shows SWAN+ADCIRC is highly scalable.

4.3 Methods

4.3.1 SWAN Model

SWAN predicts the evolution in geographical space $\vec{x}$ and time t of the wave action density spectrum $N(\vec{x}, t, \sigma, \theta)$, with σ the relative frequency and θ the wave direction, as governed by the action balance equation (Booij et al., 1999):

$$\frac{\partial N}{\partial t} + \nabla_{\vec{x}} \cdot [(\vec{c}_g + \vec{U})N] + \frac{\partial}{\partial \theta} c_\theta N + \frac{\partial}{\partial \sigma} c_\sigma N = \frac{S_{tot}}{\sigma}. \tag{4.1}$$

The terms on the left-hand side represent, respectively, the change of wave action in time, the propagation of wave action in $\vec{x}$-space (with $\nabla_{\vec{x}}$ the gradient operator in geographic space, $\vec{c}_g$ the wave group velocity and $\vec{U}$ the ambient current vector), depth- and current-induced refraction and approximate diffraction (with propagation velocity or turning rate c_θ), and the shifting of σ due to variations in mean current and depth (with propagation velocity or shifting rate c_σ). The source term, S_{tot}, represents wave growth by wind; action lost to whitecapping, surf breaking and bottom friction; and action exchanged between spectral components in deep and shallow water due to nonlinear effects. The associated SWAN parameterizations are given by Booij *et al.* (1999), with all subsequent modifications as present in version 40.72, including the phase-decoupled refraction-diffraction (Holthuijsen *et al.*, 2003), although diffraction is disabled in the present simulations.

The unstructured-mesh version of SWAN implements an analog to the four-direction Gauss-Seidel iteration technique employed in the structured version, and it maintains SWAN's unconditional stability (Zijlema, 2010). SWAN computes the wave action density spectrum $N(\vec{x}, t, \sigma, \theta)$ at the vertices of an unstructured triangular mesh, and it orders the mesh vertices so it can sweep through them and update the action density using information from neighboring vertices. It then sweeps through the mesh in opposite directions until the wave energy has propagated sufficiently through geographical space in all directions. It should be noted that, as a spectral model, SWAN does not attempt to represent physical processes at scales less than a wave length even in regions with very fine-scale mesh resolution. Phase-resolving wave models should be employed at these scales if sub-wave length scale flow features need to be resolved. However, this fine-scale mesh resolution may be necessary for other reasons, such as representing the complex bathymetry and topography of the region, or to improve the numerical properties of the computed solution.

4.3.2 ADCIRC Model

ADCIRC is a continuous-Galerkin, finite-element, shallow-water model that solves for water levels and currents at a range of scales (Atkinson *et al.*, 2004; Luettich *et al.*, 2004; Dawson *et al.*, 2006; Westerink *et al.*, 2008). Water levels are obtained through solution of the Generalized Wave Continuity Equation (GWCE):

$$\frac{\partial^2 \zeta}{\partial t^2} + \tau_0 \frac{\partial \zeta}{\partial t} + \frac{\partial \tilde{J}_x}{\partial x} + \frac{\partial \tilde{J}_y}{\partial y} - UH \frac{\partial \tau_0}{\partial x} - VH \frac{\partial \tau_0}{\partial y} = 0, \tag{4.2}$$

where:

$$\tilde{J}_x = -Q_x\frac{\partial U}{\partial x} - Q_y\frac{\partial U}{\partial y} + fQ_y - \frac{g}{2}\frac{\partial \zeta^2}{\partial x} - gH\frac{\partial}{\partial x}\left[\frac{P_s}{g\rho_0} - \alpha\eta\right] + \frac{\tau_{sx,winds} + \tau_{sx,waves} - \tau_{bx}}{\rho_0} + (M_x - D_x) + U\frac{\partial \zeta}{\partial t} + \tau_0 Q_x - gH\frac{\partial \zeta}{\partial x}, \tag{4.3}$$

$$\tilde{J}_y = -Q_x\frac{\partial V}{\partial x} - Q_y\frac{\partial V}{\partial y} - fQ_x - \frac{g}{2}\frac{\partial \zeta^2}{\partial y} - gH\frac{\partial}{\partial y}\left[\frac{P_s}{g\rho_0} - \alpha\eta\right] + \frac{\tau_{sy,winds} + \tau_{sy,waves} - \tau_{by}}{\rho_0} + (M_y - D_y) + V\frac{\partial \zeta}{\partial t} + \tau_0 Q_y - gH\frac{\partial \zeta}{\partial y}, \tag{4.4}$$

and the currents are obtained from the vertically-integrated momentum equations:

$$\frac{\partial U}{\partial t} + U\frac{\partial U}{\partial x} + V\frac{\partial U}{\partial y} - fV = -g\frac{\partial}{\partial x}\left[\zeta + \frac{P_s}{g\rho_0} - \alpha\eta\right] + \frac{\tau_{sx,winds} + \tau_{sx,waves} - \tau_{bx}}{\rho_0 H} + \frac{M_x - D_x}{H}, \tag{4.5}$$

and:

$$\frac{\partial V}{\partial t} + U\frac{\partial V}{\partial x} + V\frac{\partial V}{\partial y} + fU = -g\frac{\partial}{\partial y}\left[\zeta + \frac{P_s}{g\rho_0} - \alpha\eta\right] + \frac{\tau_{sy,winds} + \tau_{sy,waves} - \tau_{by}}{\rho_0 H} + \frac{M_y - D_y}{H}, \tag{4.6}$$

where $H = \zeta + h$ is total water depth; ζ is the deviation of the water surface from the mean; h is bathymetric depth; U and V are depth-integrated currents in the x- and y-directions, respectively; $Q_x = UH$ and $Q_y = VH$ are fluxes per unit width; f is the Coriolis parameter; g is gravitational acceleration; P_s is atmospheric pressure at the surface; ρ_0 is the reference density of water; η is the

Newtonian equilibrium tidal potential and α is the effective earth elasticity factor; $\tau_{s,winds}$ and $\tau_{s,waves}$ are surface stresses due to winds and waves, respectively; τ_b is bottom stress; M are lateral stress gradients; D are momentum dispersion terms; and τ_0 is a numerical parameter that optimizes the phase propagation properties (Kolar *et al.*, 1994; Atkinson *et al.*, 2004). ADCIRC computes water levels ζ and currents U and V on an unstructured, triangular mesh by applying a linear Lagrange interpolation and solving for three degrees of freedom at every mesh vertex.

4.3.3 Sharing Information

SWAN is driven by wind speeds, water levels and currents computed at the vertices by ADCIRC. Marine winds can be input to ADCIRC in a variety of formats, and these winds are adjusted directionally to account for surface roughness (Bunya *et al.*, 2010). ADCIRC interpolates spatially and temporally to project these winds to the computational vertices, and then it passes them to SWAN. The water levels and ambient currents are computed in ADCIRC before being passed to SWAN, where they are used to recalculate the water depth and all related wave processes (wave propagation, depth- induced breaking, etc.).

The ADCIRC model is driven partly by radiation stress gradients that are computed using information from SWAN. These gradients $\tau_{s,waves}$ are computed by:

$$\tau_{sx,waves} = -\frac{\partial S_{xx}}{\partial y} - \frac{\partial S_{xy}}{\partial y}, \tag{4.7}$$

and:

$$\tau_{sy,waves} = -\frac{\partial S_{xy}}{\partial y} - \frac{\partial S_{yy}}{\partial y}, \tag{4.8}$$

where S_{xx}, S_{xy} and S_{yy} are the wave radiation stresses (Longuet-Higgins and Stewart, 1964; Battjes, 1972):

$$S_{xx} = \rho_0 g \int \int \Big(\Big(n \cos^2 \theta + n - \frac{1}{2} \Big) \sigma N \Big) \mathrm{d}\sigma \mathrm{d}\theta, \tag{4.9}$$

$$S_{xy} = \rho_0 g \int \int \Big(n \sin \theta \cos \theta \sigma N \Big) \mathrm{d}\sigma \mathrm{d}\theta, \tag{4.10}$$

and:

$$S_{yy} = \rho_0 g \int \int \Big(\Big(n \sin^2 \theta + n - \frac{1}{2} \Big) \sigma N \Big) \mathrm{d}\sigma \mathrm{d}\theta, \tag{4.11}$$

where n is the ratio of group velocity to phase velocity. The radiation stresses are computed at the mesh vertices using Equations 4.9 - 4.11. Then they are interpolated into the space of continuous, piecewise linear functions and differentiated to obtain the gradients in Equations 4.7 - 4.8, which are constant on each element. These element-based gradients are projected to the vertices by taking an area-weighted average of the gradients on the elements adjacent to each vertex.

4.3.4 Coupling Procedure

ADCIRC and SWAN run in series on the same local mesh and core. The two models "leap frog" through time, each being forced with information from the other model.

Because of the sweeping method used by SWAN to update the wave information at the computational vertices, it can take much larger time steps than ADCIRC, which is diffusion- and also Courant-time-step limited due to its semi-explicit formulation and its wetting-and-drying algorithm. For that reason, the coupling interval is taken to be the same as the SWAN time step. On each cou-

pling interval, ADCIRC is run first, because we assume that, in the nearshore and the coastal floodplain, wave properties are more dependent on circulation.

At the beginning of a coupling interval, ADCIRC can access the radiation stress gradients computed by SWAN at times corresponding to the beginning and end of the previous interval. ADCIRC uses that information to extrapolate the gradients at all of its time steps in the current interval. These extrapolated gradients are used to force the ADCIRC solution as described above. Once the ADCIRC stage is finished, SWAN is run for one time step, to bring it to the same moment in time as ADCIRC. SWAN can access the wind speeds, water levels and currents computed at the mesh vertices by ADCIRC, at times corresponding to the beginning and end of the current interval. SWAN applies the mean of those values to force its solution on its time step. In this way, the radiation stress gradients used by ADCIRC are always extrapolated forward in time, while the wind speeds, water levels and currents used by SWAN are always averaged over each of its time steps.

4.3.5 Parallel Coupling Framework

The METIS domain-decomposition algorithm is applied to distribute the global mesh over a number of computational cores (Karypis and Kumar, 1999). The decomposition minimizes inter-core communication by creating local sub-meshes with small ratios of the number of vertices within the domain to the number of shared vertices at sub-mesh interfaces. The decomposition also balances the computational load by creating local sub-meshes with a similar number of vertices; the local meshes decrease in geographical area as their average mesh size is decreased.

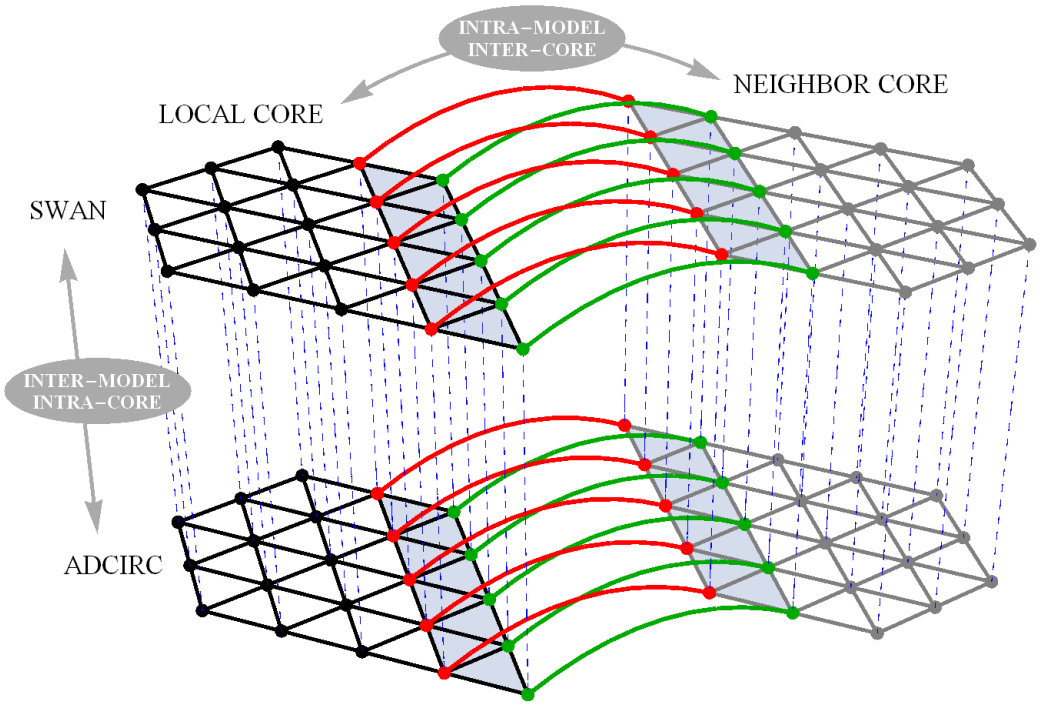

Figure 4.1. Schematic of parallel communication between models and cores. Dashed lines indicate communication for all vertices within a sub-mesh, and are inter-model and intra-core. Solid lines indicates communication for the edge-layer-based vertices between sub-meshes, and are intra-model and inter-core.

A schematic of the communication is shown in Figure 4.1. Each local core has a sub-mesh that shares a layer of boundary elements with the sub-meshes on its neighbor cores. To update the information at these boundaries in either model, information is passed at the shared vertices on each sub-mesh. This communication is local between adjacent sub-meshes. Furthermore, only a small fraction of the vertices on any sub-mesh are shared. Thus the parallel, inter-core communication is localized and efficient.

SWAN and ADCIRC utilize the same local sub-meshes. Information is stored at the vertices in both models, so it can be passed through local cache, without the need for any network-based, inter-core communication. In contrast to loose coupling paradigms, in which the model components run on different sub-meshes and different cores, SWAN+ADCIRC does not destroy its scalability by interpolating semi-globally. The inter-model communication is intra-core.

4.4 Hindcasts of Katrina and Rita

4.4.1 Parameters of Hindcasts

SWAN+ADCIRC will utilize the SL15 mesh that has been validated for applications in southern Louisiana (Bunya *et al.*, 2010; Dietrich *et al.*, 2010a). The complex bathymetry/topography and mesh resolution are shown in Figures 4.2 - 4.4. This mesh incorporates local resolution down to 50 m, but also extends to the Gulf of Mexico and the western North Atlantic Ocean. It includes a continental shelf that narrows near the protruding delta of the Mississippi River, sufficient resolution of the wave-transformation zones near the delta and over the barrier islands, and intricate representation of the various natural and man-made geographic features that collect and focus storm surge in this region. The SL15 mesh contains 2,409,635 vertices and 4,721,496 triangular elements. An example of the METIS domain decomposition of the SL15 mesh on 1014 cores is shown in Figure 4.5. Local sub-meshes are shown in separate colors, and the cores communicate via the layers of overlapping elements that connect these local meshes. Each parallel core utilizes the same unstructured local sub-mesh for both SWAN and ADCIRC. Notable geographic locations are summarized in Table 4.1 and shown in Figures 4.6 - 4.7.

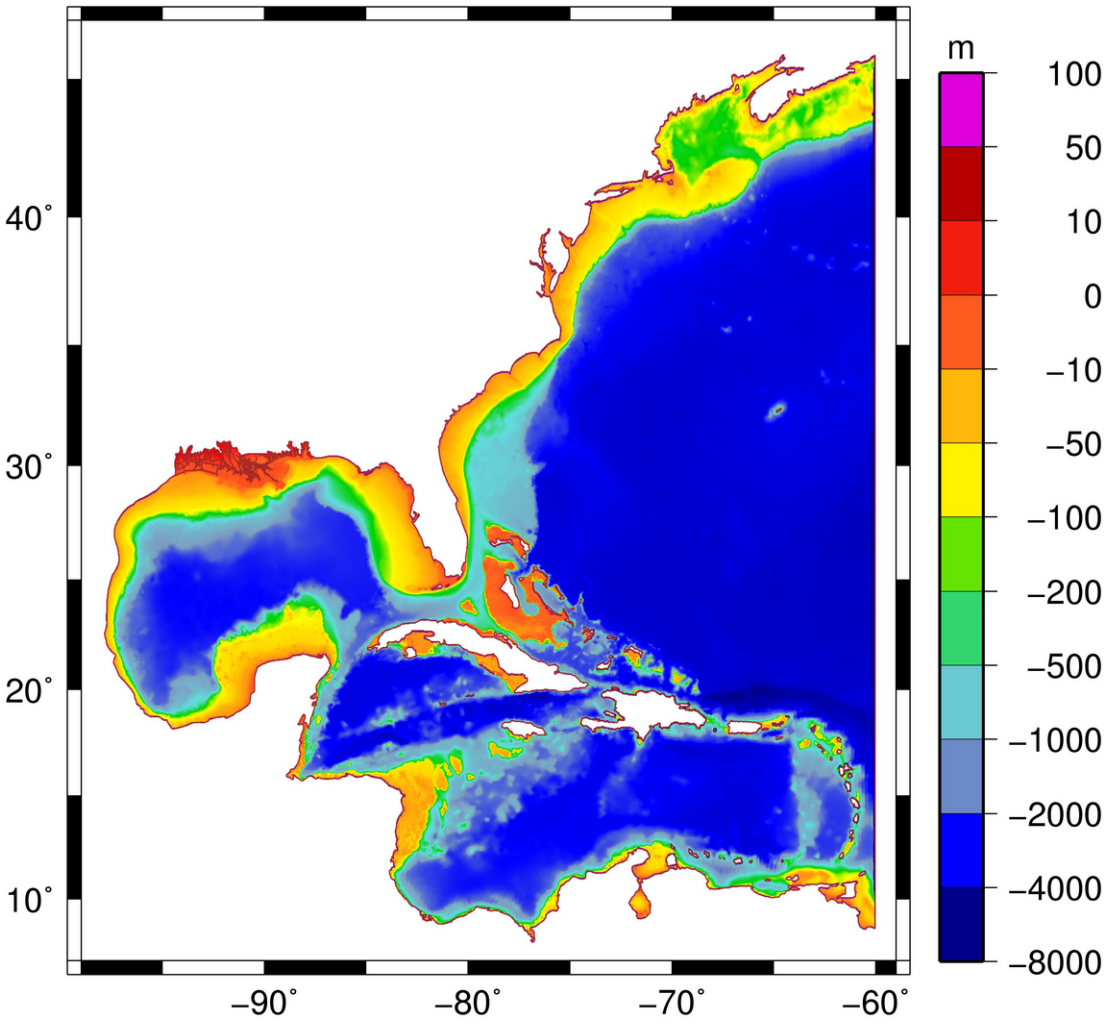

Figure 4.2. ADCIRC SL15 model domain with bathymetry (m).

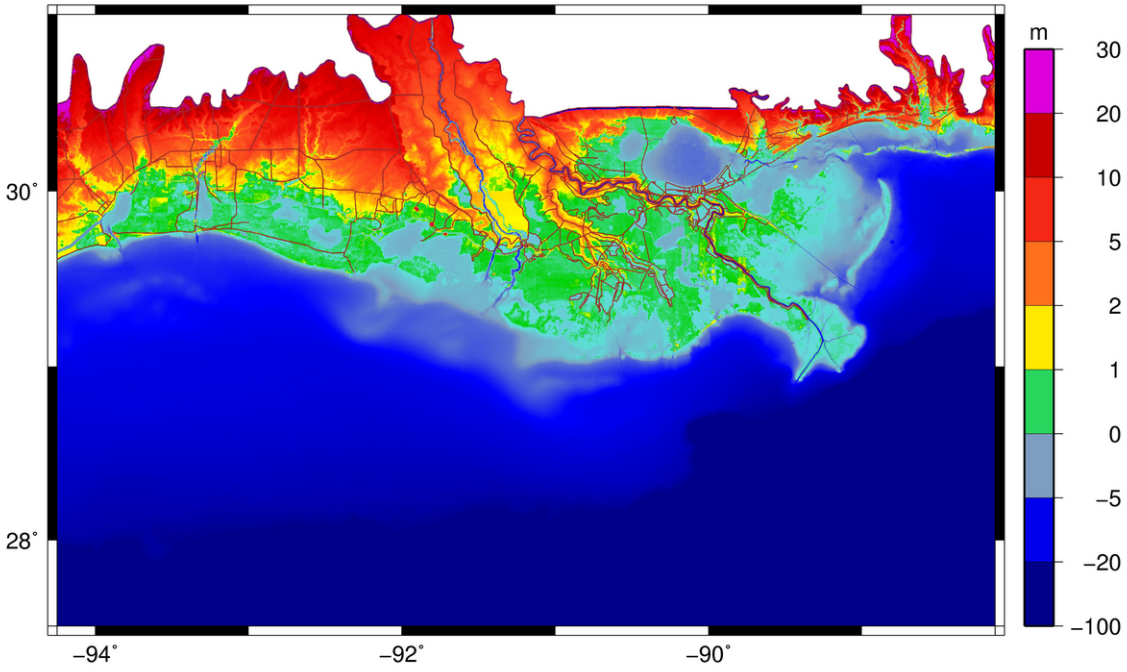

Figure 4.3. ADCIRC SL15 bathymetry and topography (m), relative to NAVD88 (2004.65), for southern Louisiana.

SWAN+ADCIRC has been validated via hindcasts of Katrina and Rita, which utilize optimized wind fields developed with an Interactive Objective Kinematic Analysis (IOKA) System (Cox *et al.*, 1995; Cardone *et al.*, 2007). The Katrina wind fields also have an inner core that is data-assimilated from NOAA's Hurricane Research Division Wind Analysis System (H*WIND) (Powell *et al.*, 1996; Powell *et al.*, 1998). The wind speeds are referenced to 10-m height, peak 30-min averaged "sustained" wind speed, and marine exposure. They contain snapshots at 15-min intervals on a regular 0.05° mesh. The wind fields are read by ADCIRC, and then each local core interpolates onto its local sub-mesh.

With the lone exception of the source of its radiation stress gradients, ADCIRC uses the same parameters as discussed in Bunya *et al.* (2010). The water levels

TABLE 4.1

GEOGRAPHIC LOCATION BY TYPE AND NUMBER

Rivers and channels	1	Calcasieu Shipping Channel
	2	Atchafalaya River
	3	Mississippi River
	4	Southwest Pass
Bays, lakes and sounds	5	Sabine Lake
	6	Calcasieu Lake
	7	White Lake
	8	Vermilion Bay
	9	Terrebonne Bay
	10	Timbalier Bay
	11	Lake Pontchartrain
	12	Lake Borgne
	13	Gulf of Mexico
Islands	14	Grand Isle
	15	Chandeleur Islands
Places	16	Galveston, TX
	17	Tiger and Trinity Shoals
	18	New Orleans, LA

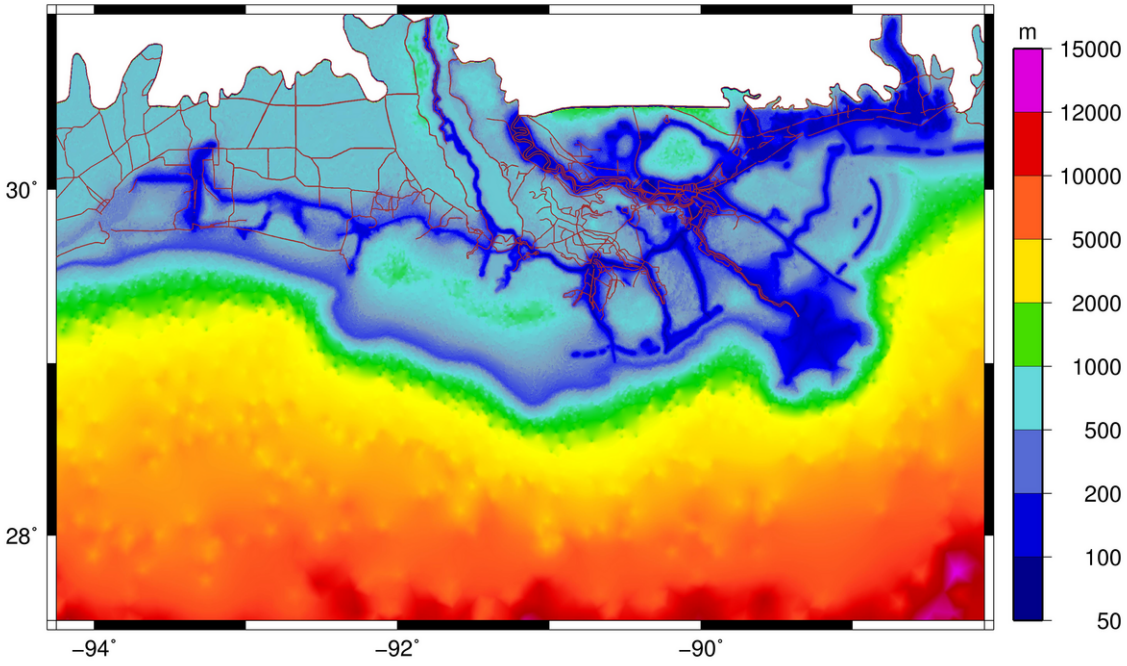

Figure 4.4. ADCIRC SL15 mesh resolution (m) in southern Louisiana.

are adjusted for the regional difference between LMSL and NAVD88 (2004.65) and the seasonal fluctuation in sea level in the Gulf of Mexico. Bottom friction is parameterized using a Manning's n formulation, with spatially-variable values based on land classification. The Mississippi and Atchafalaya Rivers are forced with flow rates that are representative of the conditions during the storms. In addition, seven tidal constituents are forced on the open boundary in the Atlantic Ocean. ADCIRC applies a wind drag coefficient due to Garratt (1977) with a cap of $C_d \leq 0.0035$.

The SWAN time step and the coupling interval are 600 s. The SWAN frequencies range from 0.031-0.548 Hz and are discretized into 30 bins on a logarithmic scale ($\Delta\sigma/\sigma \sim 0.1$). The wave directions are discretized into 36 sectors, each

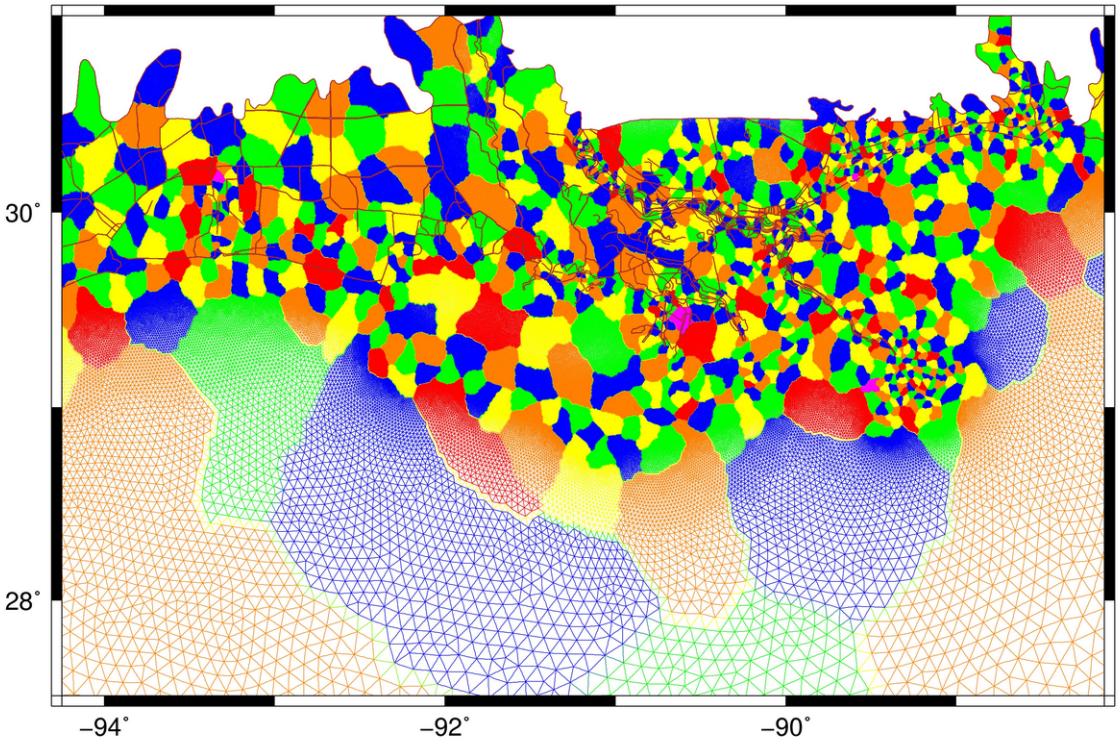

Figure 4.5. Example of the METIS domain decomposition of the ADCIRC SL15 mesh on 1014 computational cores. Colors indicate local sub-meshes and shared boundary layers.

sector representing 10°. The present simulations use the SWAN default for wind input based on Snyder *et al.* (1981) and the modified whitecapping expression of Rogers *et al.* (2003), which yields less dissipation in lower frequency components and better prediction of the wave periods compared to the default formulation of Hasselmann (1974). Quadruplet nonlinear interactions are computed with the Discrete Interaction Approximation (Hasselmann *et al.*, 1985). For the shallow-water source terms, depth-induced breaking is computed with a spectral version of the model due to Battjes and Janssen (1978) with the breaking index $\gamma = 0.73$, bottom friction is based on the JONSWAP formulation (Hasselmann *et al.*, 1973)

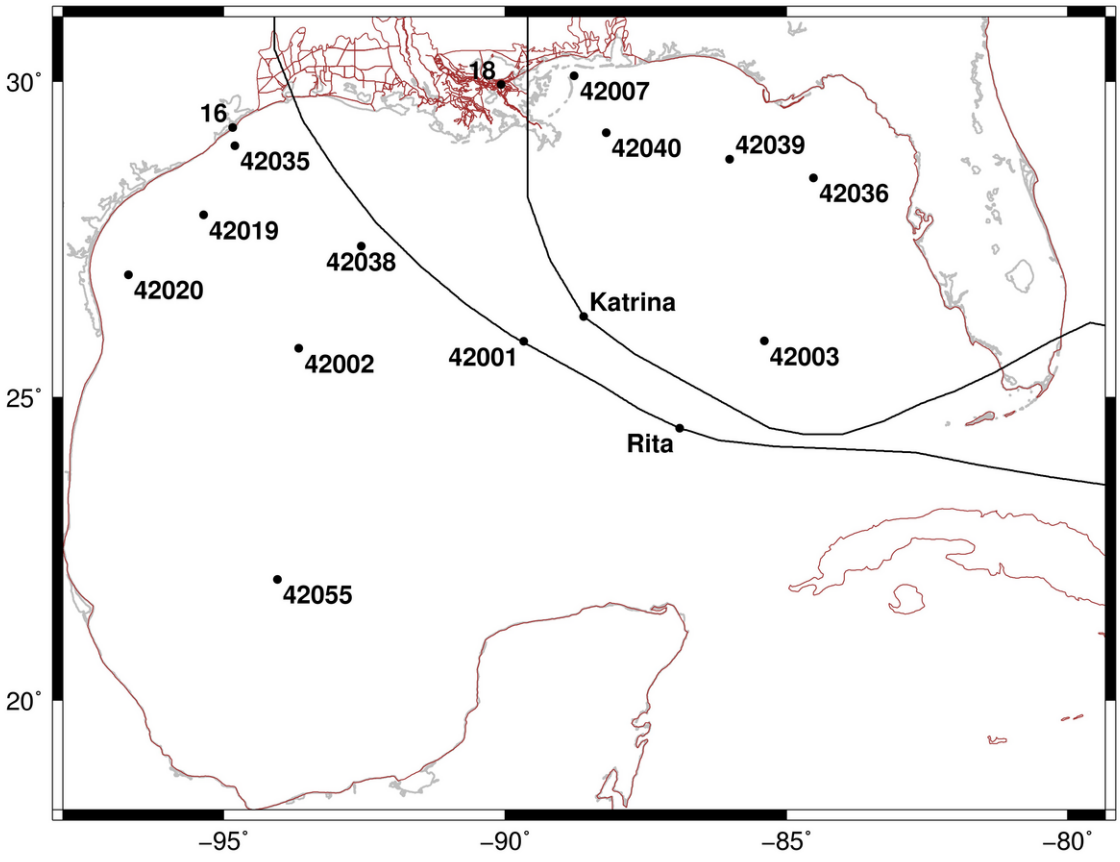

Figure 4.6. Schematic of the Gulf of Mexico with locations of the 12 NDBC buoy stations used for the deep-water validation of SWAN during both Katrina and Rita. The hurricane tracks are also shown.

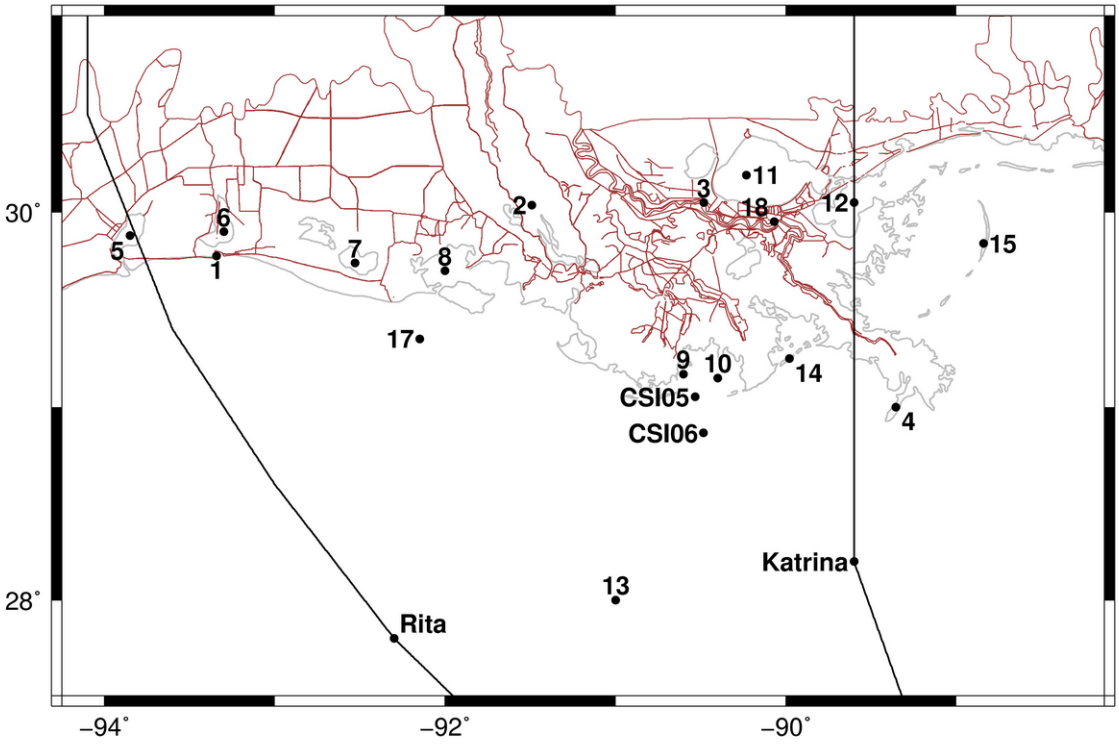

Figure 4.7. Schematic of southern Louisiana with numbered markers of the locations listed in Table 4.1. Locations of the two CSI nearshore wave gauges and the hurricane tracks are also shown.

with friction coefficient $C_b = 0.067$ m^2 s^{-3}, and the triad nonlinear interactions are computed with the Lumped Triad Approximation of Eldeberky (1996). Although the resolution in the SL15 mesh is well-suited to simulate waves and surge along the coastlines of Louisiana, Mississippi and Alabama, its relatively coarse resolution in the Caribbean Sea and Atlantic Ocean can create spurious wave refraction over one spatial element. Thus, wave refraction is enabled only in the computational sub-meshes in which the resolution of the bathymetry is sufficient, specifically in the northern Gulf of Mexico. SWAN applies a wind drag coefficient due to Wu (1982) with a cap of $C_d \leq 0.0035$.

In the validation sections that follow, the SWAN wave quantities will be compared to measured data and also to the solution from a loose coupling to structured versions of WAM and STWAVE. WAM was run on a regular 0.05° mesh with coverage of the entire Gulf of Mexico, while STWAVE was run on four or five nested sub-meshes with resolution of 200 m and coverage of southern Louisiana, Mississippi and Alabama. The details of this loose coupling can be found in Bunya *et al.* (2010) and Dietrich *et al.* (2010a). For the validation herein, wave parameters from WAM and STWAVE were integrated to 0.41 Hz, while parameters from SWAN were integrated to 0.55 Hz.

4.4.2 Hurricane Katrina

Katrina is a good validation case because of its size and scope. It was a large hurricane, with waves of 16.5 m measured off the continental shelf and storm surge of 8.8 m measured along the Mississippi coastline. But it also generated waves and storm surge over multiple scales and impacted the complex topography and levee protection system of southeastern Louisiana. To simulate the evolution of this hurricane, the coupled model must describe the system in rich detail and integrate seamlessly all of its components.

4.4.2.1 Evolution of Waves in Deep Water

Because SWAN has not been used traditionally in deep water, we examine the behavior of its solution as Katrina moved through the Gulf of Mexico. Figure 4.8 depicts the computed significant wave heights at 12-hr intervals as Katrina enters the Gulf, generates waves throughout the majority of the basin, and then makes landfall in southern Louisiana. In its early stages, Katrina generated significant

wave heights of 6-9 m in the eastern half of the Gulf. However, as the storm strengthened on 28 August 2005, the significant wave heights increased to a peak of about 22 m at 2200 UTC, and waves of at least 3 m were generated throughout most of the Gulf. The impact of the hurricane on waves was widespread and dramatic.

The unstructured mesh used by SWAN+ADCIRC captures this evolution. Relatively coarse mesh resolution of 12-18 km is applied in the Gulf to capture the generation of waves in deep water and their propagation onto the continental shelf, and relatively fine (but locally still fairly coarse) resolution of 200-500 m is applied in the wave breaking zones. It is unnecessary to change meshes or interpolate boundary conditions or solutions as would be required for nesting structured meshes.

4.4.2.2 Interaction of Processes at Landfall

We examine the system at 1000 UTC 29 August 2005, shortly before Katrina's landfall along the southern reach of the Mississippi River. Katrina is pushing its largest waves onto the continental shelf. Figure 4.9a shows the wind field in southeastern Louisiana. The eye is located less than 50 km and 90 min from landfall, and it is just west of Southwest Pass. The highest wind speeds of 45-50 m s^{-1} are located over the bird's foot of the Mississippi River delta, but winds of 25-40 m s^{-1} are blowing easterly and southeasterly over much of the continental shelf.

As shown in Figure 4.9b, the largest waves are generated in the Gulf and experience depth-limited breaking on the continental shelf. In regions where the shelf is narrow, the waves transform over short distances. To the south of the

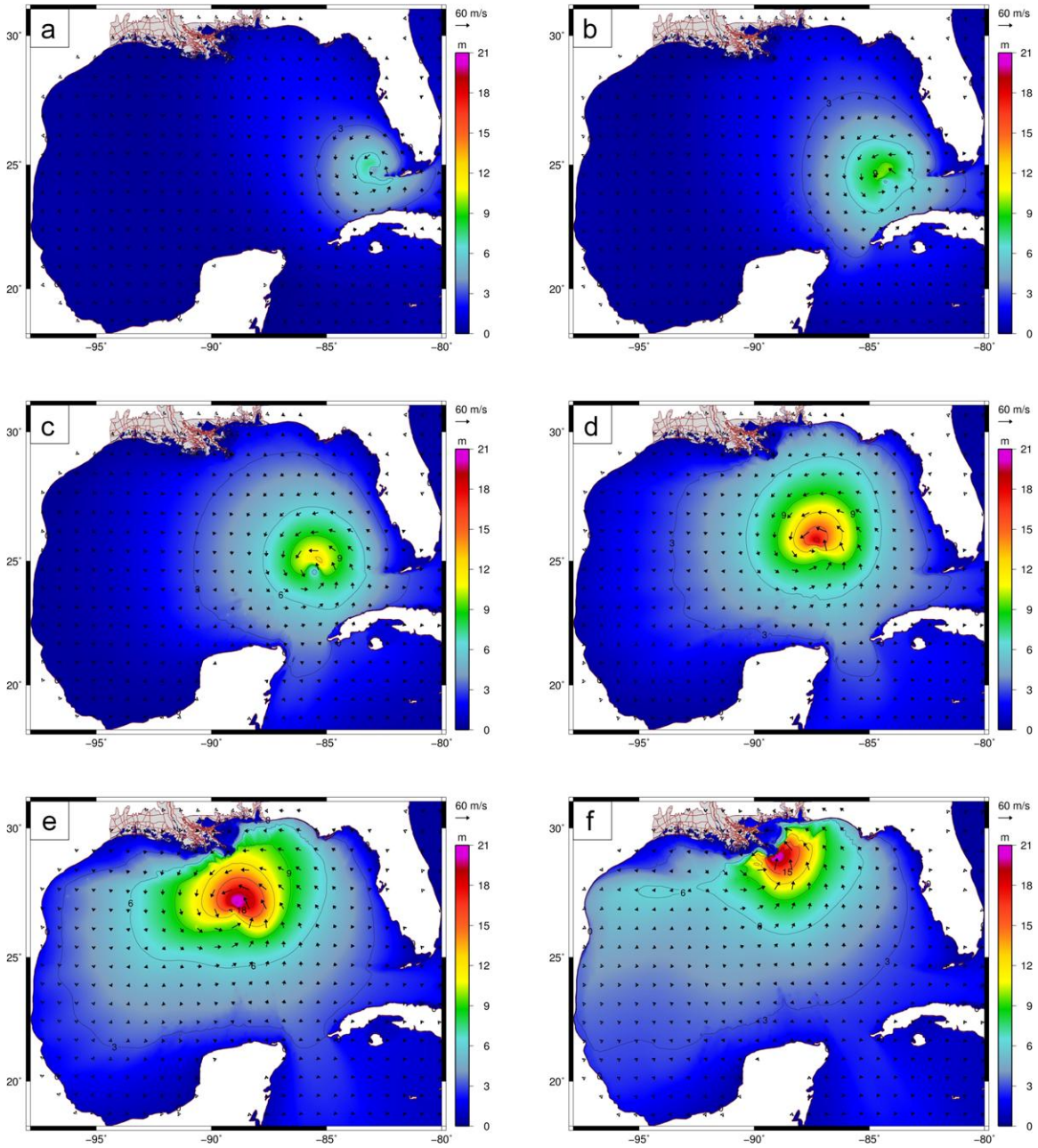

Figure 4.8. Hurricane Katrina significant wave height contours (m) and wind speed vectors (m s^{-1}) at 12-hr intervals in the Gulf of Mexico. The six panels correspond to the following times: (a) 2200 UTC 26 August 2005, (b) 1000 UTC 27 August 2005, (c) 2200 UTC 27 August 2005, (d) 1000 UTC 28 August 2005, (e) 2200 UTC 28 August 2005 and (f) 1000 UTC 29 August 2005.

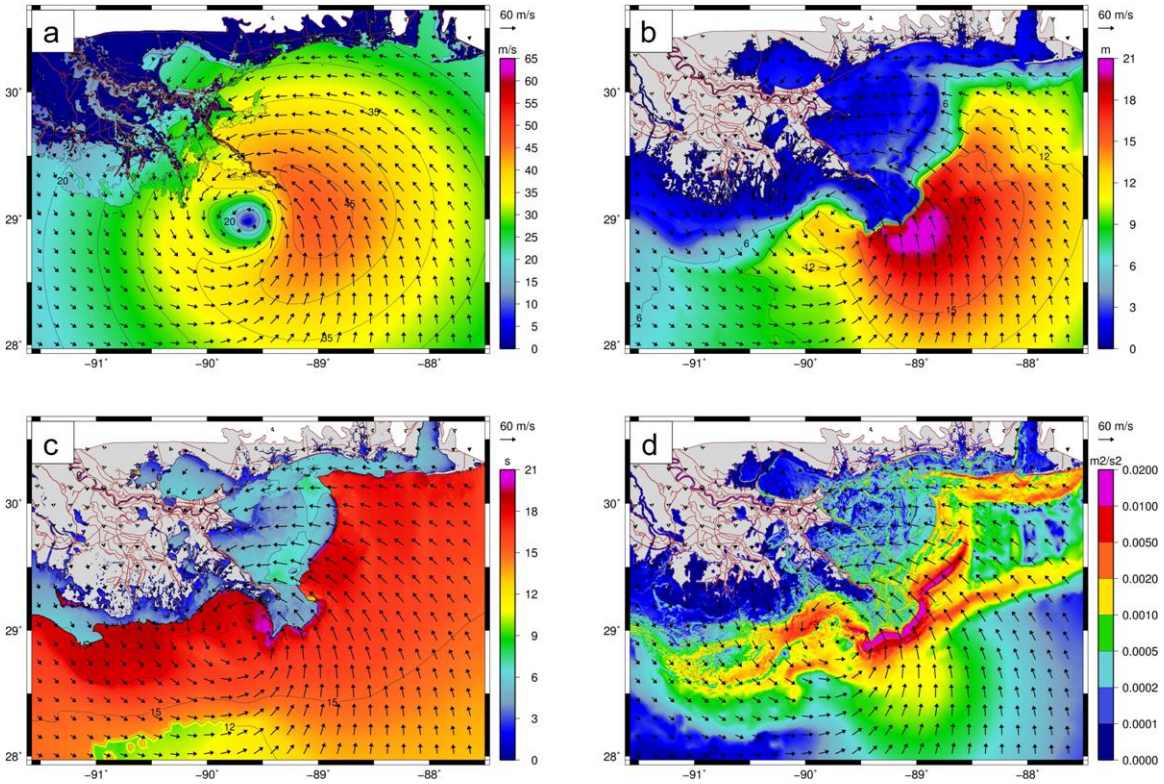

Figure 4.9. Hurricane Katrina winds and waves at 1000 UTC 29 August 2005 in southeastern Louisiana. The panels are: (a) wind contours and vectors (m s^{-1}), shown with a 10 min averaging period and at 10 m elevation; (b) significant wave height contours (m) and wind vectors (m s^{-1}); (c) mean wave period contours (s) and wind vectors (m s^{-1}); and (d) radiation stress gradient contours (m^2 s^{-2}) and wind vectors (m s^{-1}).

Mississippi River delta, waves of 18-19 m break where the bathymetry changes rapidly. To the east, near the Chandeleur Islands, the continental shelf is broader, and the wave heights decrease gradually on the shelf and over the barrier islands. Behind these initial breaking zones, smaller waves are generated and dissipated. In Lake Pontchartrain, northerly winds generate waves of 1.5-2 m that break along the northern edge of New Orleans. This behavior is mirrored in the mean periods shown in Figure 4.9c, in which there is a clear difference between the long-period

waves generated in deep water and the short-period waves generated behind the initial breaking zones.

As these waves break, they exert a stress on the water column that changes water levels and/or drives currents. As shown in Figure 4.9d, the largest radiation stress gradients of 0.02 m^2 s^{-2} are located at the south edge of the delta, where the largest waves are breaking. However, radiation stress gradients also exist on the continental shelf, over barrier islands, inside the marshes, and along coastlines. Because both models are running on the same local sub-mesh, the complexities of the SWAN solution are passed directly to ADCIRC.

The ADCIRC water levels are shown in Figure 4.10a. Easterly winds are pushing storm surge of 2-3 m onto the continental shelf, and 5 m of surge has built against the river levees. This surge will release northward as Katrina moves through the system and eventually makes landfall along the Mississippi coastline. However, significant flooding is occurring already in the marshes of southeast Louisiana. Some of this flooding is due to the wave set-up shown in Figure 4.10b. The stresses associated with wave breaking increased the overall water levels by 0.2-0.3 m over much of the region, and by as much as 0.8 m in the delta. These contributions range from 5-35 percent of the overall water level.

As shown in Figure 4.10c, the currents are significant throughout the region, with a range of 0.5-1.5 m s^{-1} on the continental shelf. As surge is pushed through Lake Borgne and into Lake Pontchartrain, the currents in the passes increase to 1.5-2.5 m s^{-1}. Similar currents are observed over the barrier islands and the delta, where waves are breaking. As shown in Figure 4.10d, the wave stresses increase the currents in these regions. In the bird's foot of the delta, the wave-driven currents are 0.1-0.3 m s^{-1}, or about 5-10 percent of the overall currents in this

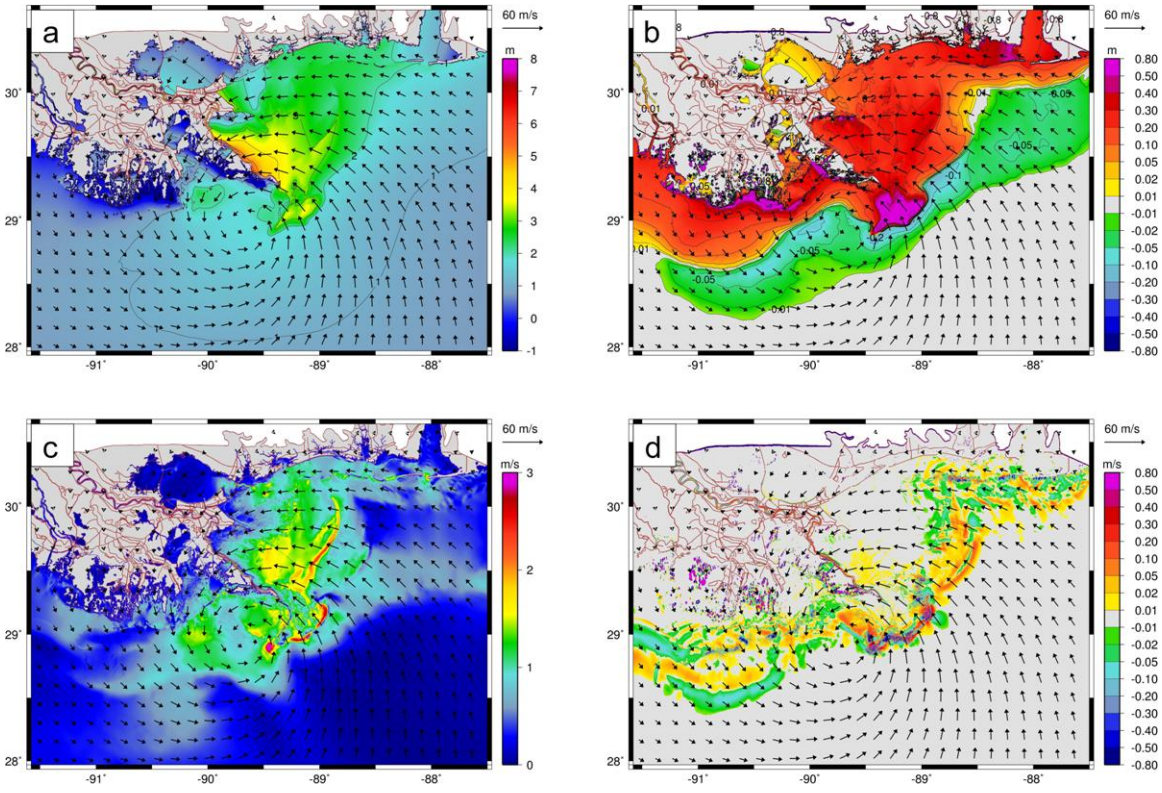

Figure 4.10. Hurricane Katrina water levels and currents at 1000 UTC 29 August 2005 in southeastern Louisiana. The panels are: (a) water level contours (m) and wind vectors (m s^{-1}); (b) wave-driven set up contours (m) and wind vectors (m s^{-1}); (c) currents contours (m s^{-1}) and wind vectors (m s^{-1}); and (d) wave-driven currents contours (m s^{-1}) and wind vectors (m s^{-1}).

region. The tightly-coupled SWAN+ADCIRC model does not have anomalies near boundaries, does not exhibit inconsistent solutions anywhere within the domain (as is possible with overlapping structured-mesh models), and the simulation increases dramatically in efficiency.

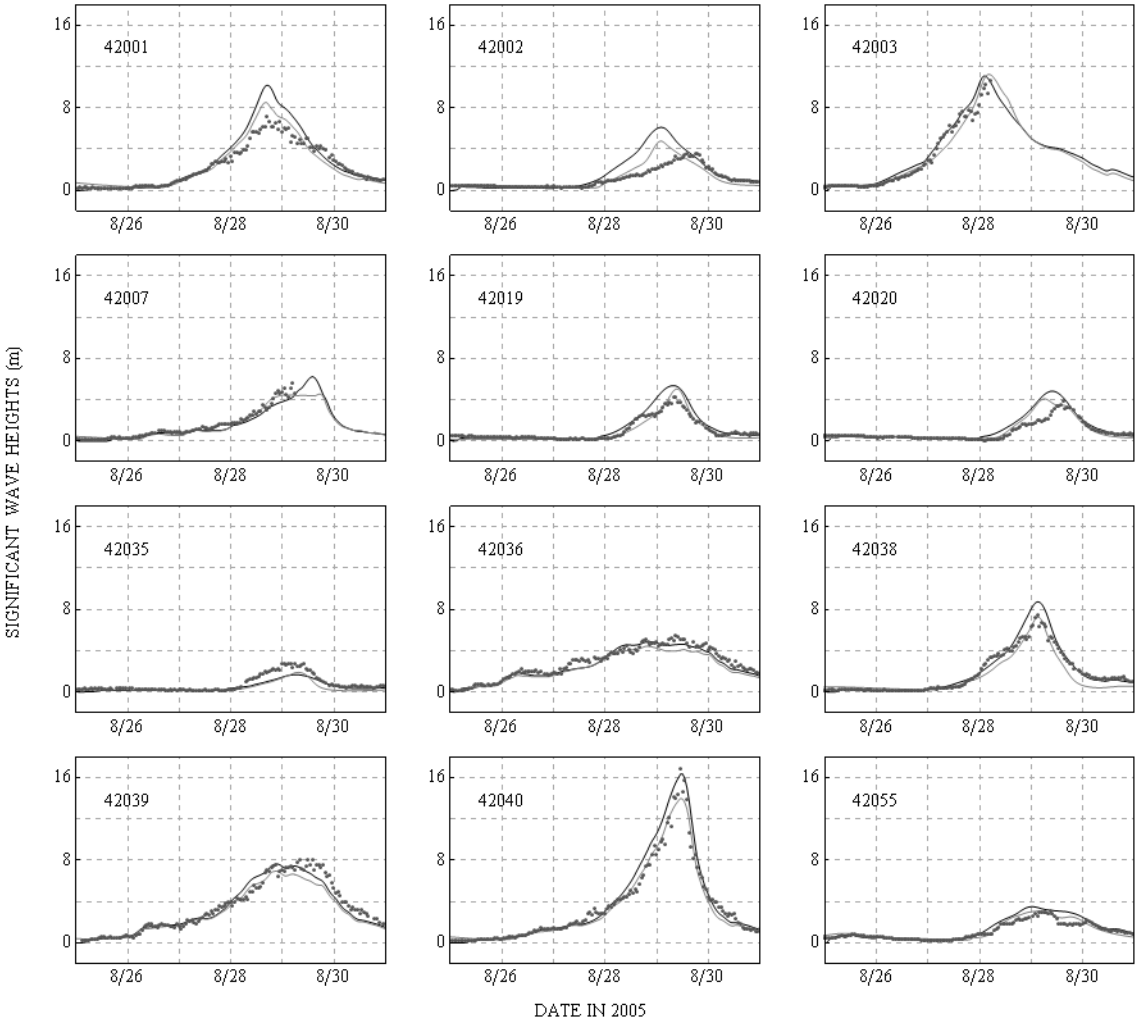

Figure 4.11. Significant wave heights (m) during Hurricane Katrina at 12 NDBC buoys. The measured data is shown with black dots, the modeled SWAN results are shown with black lines, and the modeled WAM results are shown with gray lines.

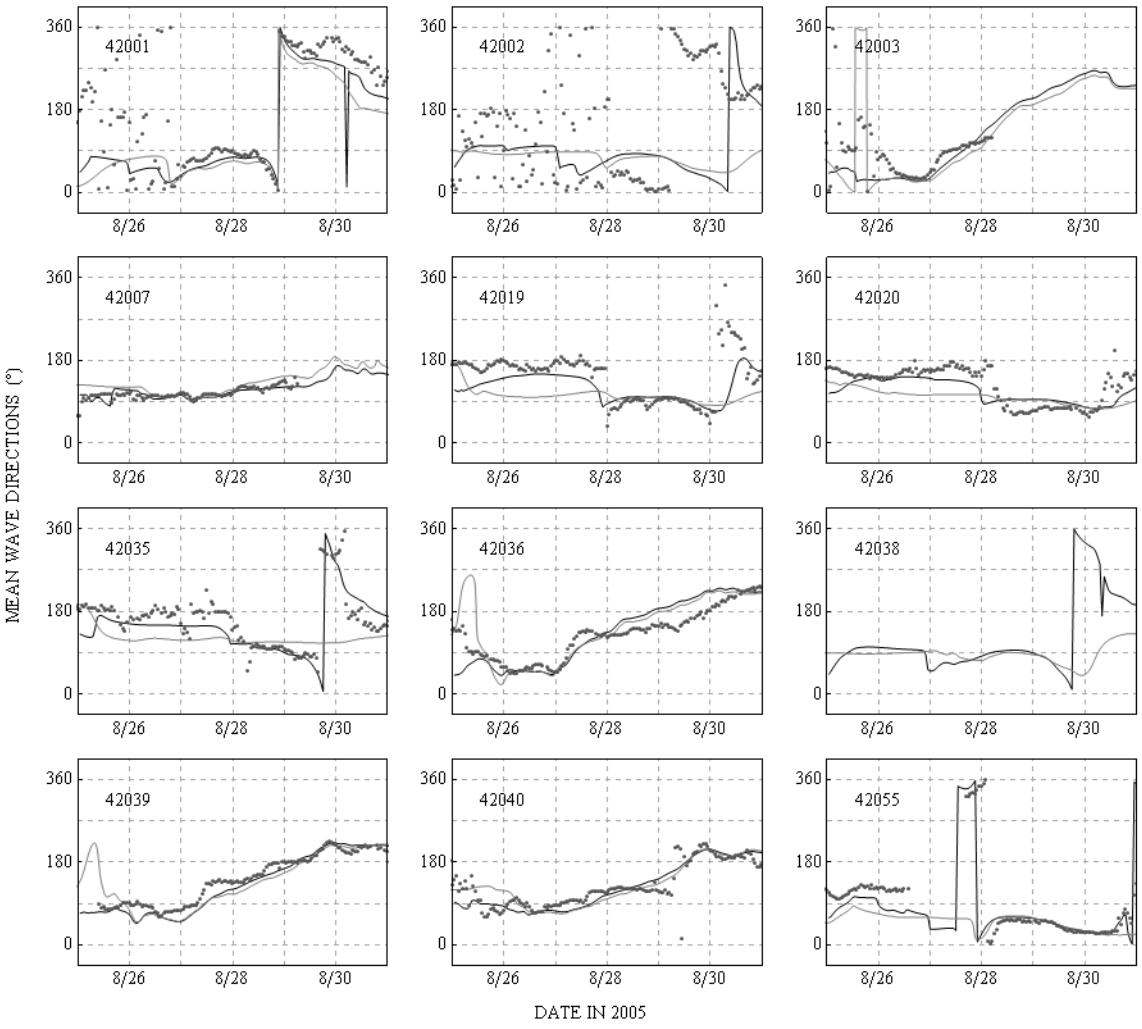

Figure 4.12. Mean wave directions (°), measured clockwise from geographic north, during Hurricane Katrina at 12 NDBC buoys. The measured data is shown with black dots, the modeled SWAN results are shown with black lines, and the modeled WAM results are shown with gray lines.

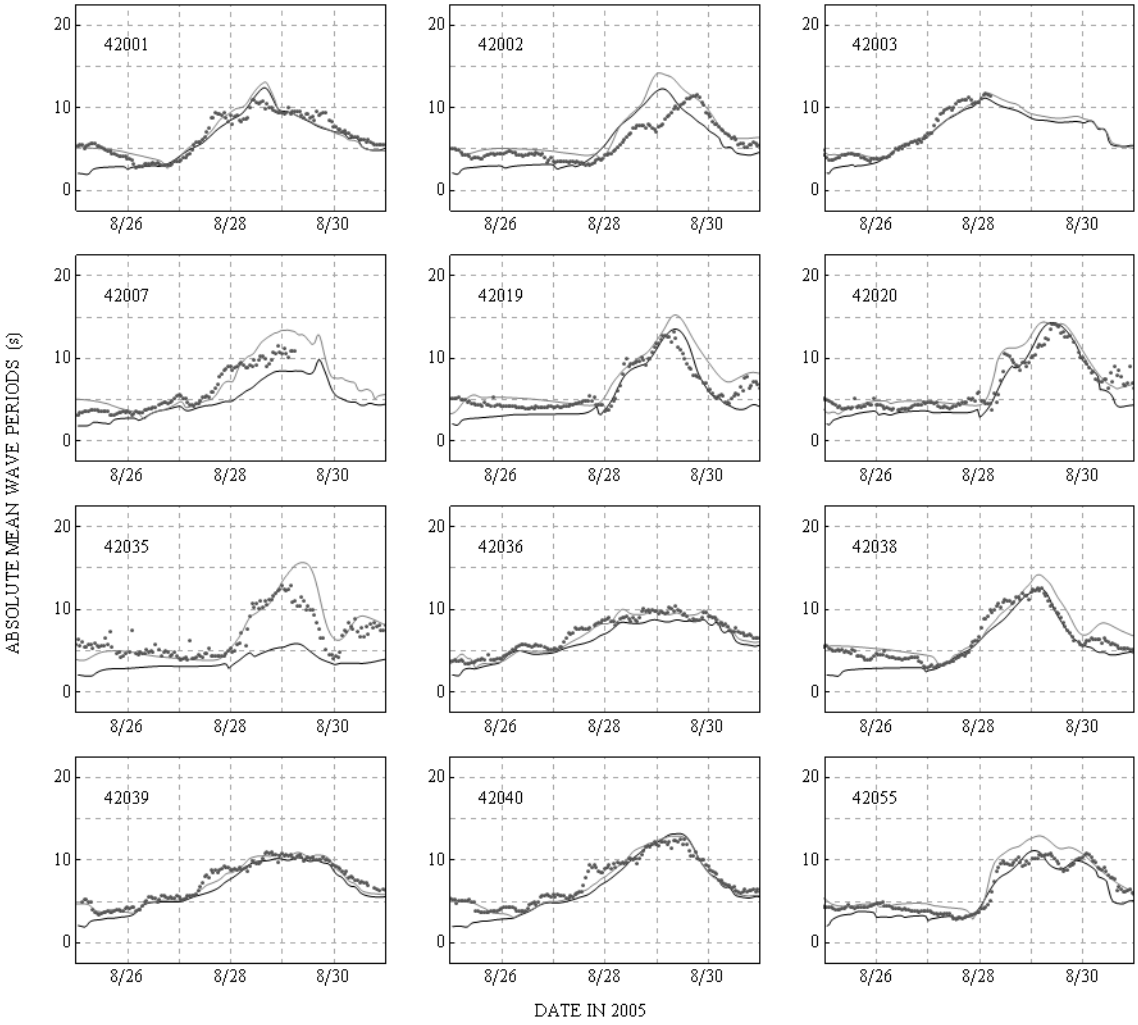

Figure 4.13. Mean wave periods (s) during Hurricane Katrina at 12 NDBC buoys. The measured data is shown with black dots, the modeled SWAN results are shown with black lines, and the modeled WAM results are shown with gray lines.

4.4.2.3 Validation of Coupled Model

SWAN+ADCIRC has been validated to several sets of measurement data. In deep water, the National Data Buoy Center (NDBC) collected and analyzed wave measurements at 12 buoys shown in Figure 4.6. Figures 4.11 - 4.13 compare measured significant heights, mean directions and mean periods to computed values from SWAN+ADCIRC as well as WAM. SWAN matches the magnitude and timing of the peaks at most buoys. For example, the modeled significant wave height of 16 m at buoy 42040 is very close to the measured peak height of 16.5 m. Similar behavior is seen with respect to directions and periods. At some buoys, errors are caused by a combination of missing physics and/or measurement error. At a few buoys to the west of the track, such as 42001, 42002, 42019 and 42020, the match is not as good as at other locations, possible reasons include the presence of a warm-core eddy (Wang and Oey, 2008), which is not included in the circulation model. Furthermore mesh resolution, especially the 12-18-km mesh sizes in the central Gulf, is also relatively coarse in these regions. When the waves were small in the days leading up to the storm (8/25-27), the measured mean directions tend to be noisy, which increases the model-to-measurement differences. A quantitative comparison was performed by computing the scatter index (SI):

$$SI = \frac{\sqrt{\frac{1}{N}\sum_{i=1}^{N}(S_i - O_i)^2}}{\frac{1}{N}\sum_{i-1}^{N} O_i}, \tag{4.12}$$

the relative bias parameter:

$$Relative\ Bias = \frac{\frac{1}{N}\sum_{i=1}^{N}(S_i - O_i)}{\frac{1}{N}\sum_{i-1}^{N} O_i}, \tag{4.13}$$

and the mean observation:

$$Mean\ Obs = \frac{1}{N}\sum_{i=1}^{N} O_i, \tag{4.14}$$

where N is the total number of data, O_i is the measured value and S_i is the modeled value. These metrics are summarized in Table 4.3, although the metrics for the mean directions are not normalized because the reference direction is arbitrary. The differences in the mean observations for each model reflect the differences in the time periods over which the errors were computed, as shown in Table 4.2. The relative bias in SWAN is caused mostly by a time shift between its results and the measured data; SWAN does not match exactly the timing of the peak. The *SI* errors are large compared to other wave studies (Cardone *et al.*, 1996; Janssen, 2004), but they reflect the complexities of modeling hurricane systems that change rapidly over multiple scales. In deep water, the errors in the SWAN results are only slightly larger than in the WAM results, even though the SWAN mesh spacing of 12-18 km is much larger than WAM's regular mesh spacing of 5 km.

TABLE 4.2

ANALYSIS TIMEFRAMES FOR THE THREE WAVE MODELS

Storm	Model	Beginning of Analysis	End of Analysis
Katrina	SWAN	2005/08/25/0100Z	2005/08/31/2300Z
	WAM	2005/08/24/0100Z	2005/08/31/0600Z
	WAM/STWAVE	2005/08/28/1215Z	2005/08/30/1145Z
Rita	SWAN	2005/09/18/0100Z	2005/09/24/2300Z
	WAM	2005/09/18/0015Z	2005/09/25/0000Z
	WAM/STWAVE	2005/09/22/1830Z	2005/09/24/1800Z

TABLE 4.3

SUMMARY OF AVERAGE ERRORS AT NDBC BUOYS

Storm	Model	Significant Heights			Mean Directions			Mean Periods		
		SI	Rel. Bias	Mean Obs. (m)	RMS (°)	Bias (°)	Mean Obs. (°)	*SI*	Rel. Bias	Mean Obs. (s)
Katrina	SWAN	0.44	0.077	1.87	37.8	-9.0	136.7	0.22	-0.140	6.53
	WAM	0.36	-0.038	1.71	49.7	-13.0	134.7	0.18	0.182	6.43
Rita	SWAN	0.35	0.094	1.98	36.5	0.9	126.5	0.21	-0.156	6.74
	WAM	0.32	-0.104	1.97	45.1	0.2	127.0	0.16	0.012	6.73

It is more difficult to validate SWAN in shallow water because of the scarcity of nearshore measurement data. The Coastal Studies Institute at Louisiana State University operates two gauges south of Terrebonne Bay, as shown in Figure 4.7 (`http://www.wavcis.lsu.edu`). Stations CSI05 and CSI06 are located in water depths of about 7 m and 20 m, respectively, so they experience the nearshore physics of bottom friction, triad wave-wave interactions and depth-induced breaking. As shown in Figure 4.14, SWAN matches well the wave parameters at these stations. As shown in Table 4.4, the average errors produced by WAM/STWAVE are somewhat smaller than those produced by SWAN, presumably because of the better estimate of the deep-water wave conditions.

The ADCIRC water levels have been validated to high-water marks (HWMs) collected at 206 stations by the USACE and 193 stations by URS/FEMA (Ebersole *et al.*, 2007; URS, 2006b). These HWMs include the effects of surge and wave set-up but not wind waves. ADCIRC predicts well the majority of the HWMs, with most locations having differences less than 0.5 m. Comparisons of measured-to-modeled HWMs have best-fit slopes of 0.98-1.02 and correlation coefficients R^2 of 0.92-0.94. Differences occur in places where the resolution is insufficient, such as on the south shore of Lake Pontchartrain, but the match to the HWMs is much better in regions near open water. Average magnitudes and standard deviations of the differences were computed, both with and without the errors in the measurement data, and those values are summarized in Table 4.5. When we account for the HWM uncertainties, the estimated average absolute model error is 0.26-0.27 m, and the standard deviation is 0.41-0.44 m.

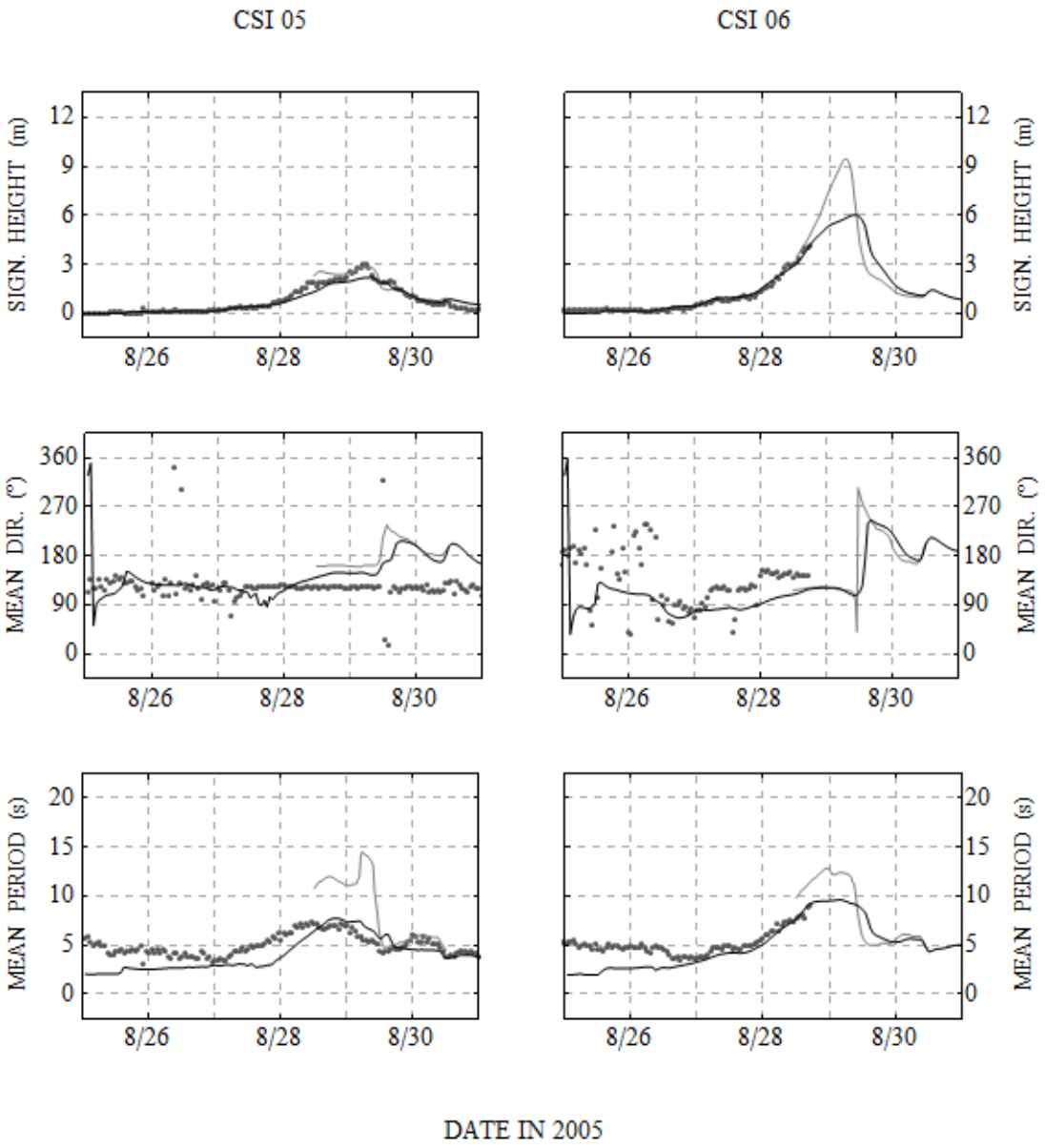

Figure 4.14. Hurricane Katrina significant wave heights (m); mean wave directions (°), measured clockwise from geographic north; and mean wave periods (s) at two CSI stations. The measured data is shown with black dots, the modeled SWAN results are shown with black lines, and the modeled WAM/STWAVE results are shown with gray lines. The CSI station data was collected by WAVCIS (`http://www.wavcis.lsu.edu`).

TABLE 4.4

SUMMARY OF AVERAGE ERRORS AT CSI STATIONS

Storm	Station	Model	Significant Heights			Mean Directions			Mean Periods		
			SI	Rel. Bias	Mean Obs. (m)	RMS (°)	Bias (°)	Mean Obs. (°)	*SI*	Rel. Bias	Mean Obs. (s)
Katrina	CSI05	SWAN	0.34	-0.029	0.73	52.7	21.0	123.9	0.29	-0.179	4.84
		WAM/ STWAVE	0.20	0.073	1.70	75.6	61.5	120.8	0.70	0.510	5.67
Katrina	CSI06	SWAN	0.16	-0.001	0.90	64.1	-34.4	132.9	0.32	-0.249	5.14
		WAM/ STWAVE	0.06	0.030	3.87	25.2	-23.3	143.8	0.29	0.291	8.25
Rita	CSI05	SWAN	0.18	-0.127	1.13	40.2	22.8	123.5	0.25	-0.084	5.03
		WAM/ STWAVE	0.10	-0.002	2.50	44.4	43.9	124.5	0.78	0.741	5.90

TABLE 4.5

DIFFERENCE/ERROR STATISTICS FOR THE HWM DATA SETS

Storm	Data Set	ADCIRC to Measured HWMs		Measured HWMs		Estimated ADCIRC Errors	
		Avg Abs Diff (m)	Std Dev (m)	Avg Abs Diff (m)	Std Dev (m)	Avg Abs Diff (m)	Std Dev (m)
Katrina	USACE	0.40	0.47	0.13	0.18	0.27	0.44
Katrina	URS	0.36	0.44	0.10	0.16	0.26	0.41
Rita	URS	0.34	0.43	0.10	0.18	0.24	0.39
Rita (No VB)	URS	0.28	0.38	0.11	0.19	0.18	0.33

These error statistics are similar to results obtained from the loose coupling of ADCIRC to the structured wave models WAM and STWAVE (Bunya *et al.*, 2010). In addition, a qualitative comparison to that study shows the SWAN+ADCIRC solution is remarkably similar. Because the wave set-up in Figure 4.10b is shown near the peak of the hurricane, it can be compared to the maximum wave set-up obtained from the loose coupling (Dietrich *et al.*, 2010a). Both coupled models create set-up of 0.8 m over the Mississippi River delta and 0.2-0.3 m over much of the region. WAM/STWAVE is slightly more focused, with higher wave set-up behind the barrier islands, whereas SWAN wave breaking is spread farther onto the continental shelf.

4.4.3 Hurricane Rita

Like Katrina, Rita was a powerful and destructive hurricane during the 2005 season. However, it pushed farther to the west and made landfall near the Louisiana-Texas border. In southwest Louisiana, a broad continental shelf distributed the wave breaking over a larger distance, while the lack of protruding geographic features prevented the early build-up of storm surge. These distinctions caused waves to develop and propagate differently during Rita, thus making it a good test of SWAN+ADCIRC.

4.4.3.1 Evolution of Waves in Deep Water

Rita created large waves throughout the Gulf of Mexico. As shown in Figure 4.15a, 60 hr before landfall, the storm was well into the Gulf and was generating waves with significant heights very near their maximum of about 19 m. In addition, waves of 3- 6 m propagate throughout most of the Gulf. Rita moved

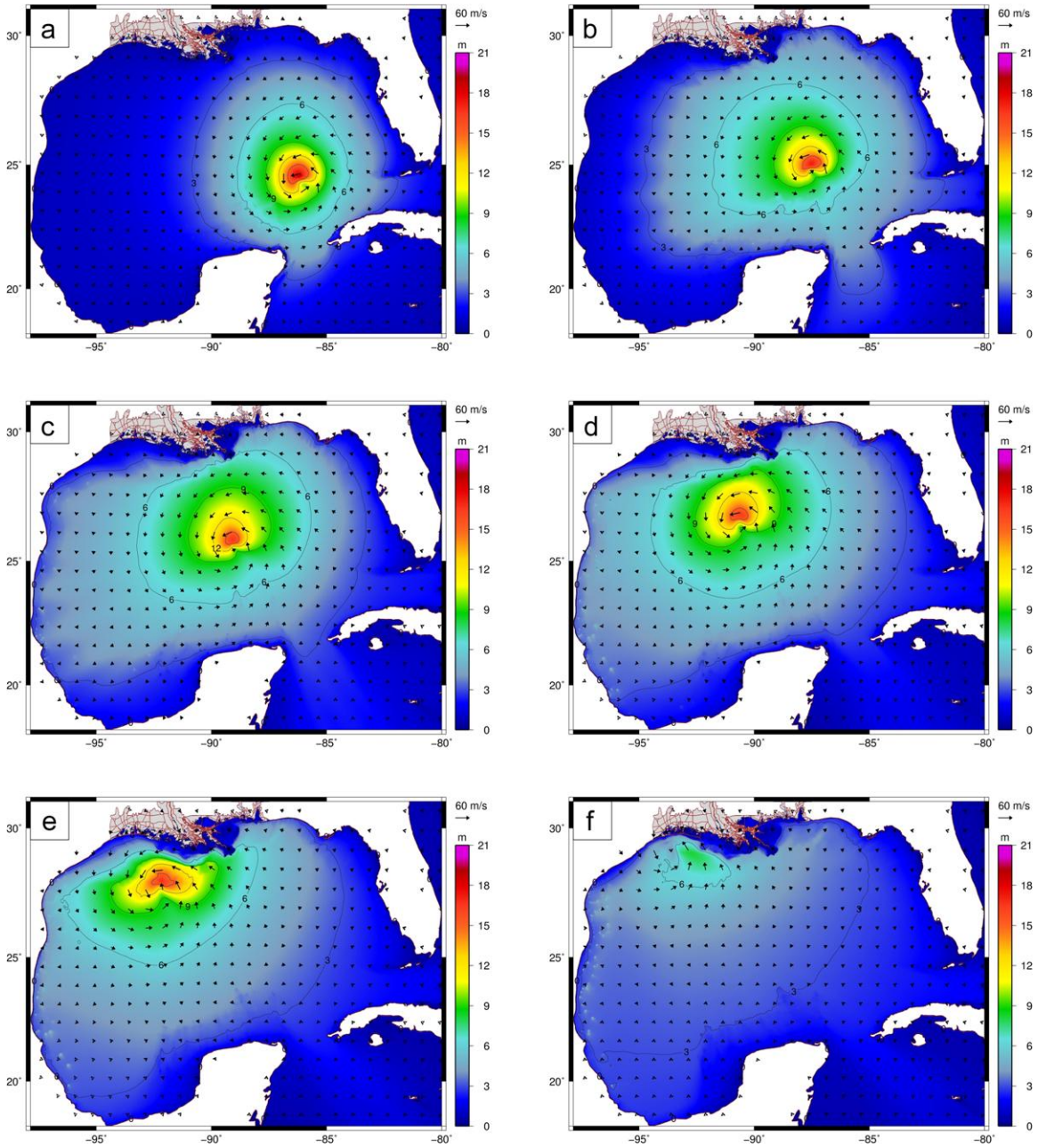

Figure 4.15. Hurricane Rita significant wave height contours (m) and wind speed vectors (m s^{-1}) at 12-hr intervals in the Gulf of Mexico. The six panels correspond to the following times: (a) 1800 UTC 21 September 2005, (b) 0600 UTC 22 September 2005, (c) 1800 UTC 22 September 2005, (d) 0600 UTC 23 September 2005, (e) 1800 UTC 23 September 2005 and (f) 0600 UTC 24 September 2005.

northwestward through the region, threatening Galveston and the Texas coastline before turning northward to make landfall at Sabine Pass. On 23 September 2005, the storm reached the continental shelf break, and its largest waves began to spread and break. The symmetry of the wave field deteriorates as the largest waves reach the shelf, as shown in Figure 4.15d-e. Finally, as Rita moved over the shelf and made landfall, as shown in Figure 4.15f, the largest significant wave heights it generated were about 8 m. These waves broke near the coastline and created set-up and currents in southwest Louisiana.

4.4.3.2 Interaction of Processes at Landfall

We examine all aspects of the coupled system as they interact at 0600 UTC 24 September 2005, when Rita was located about 35 km and 2 hr from landfall. As shown in Figure 4.16a, its eye was located on the continental shelf, and its maximum wind speeds reduced to 40-45 m s^{-1}. Because of the storm's northwestward track, its winds blew parallel to the coastline in southwest Louisiana for hours before landfall. It is only at this relatively late stage in the hurricane that the winds are changing to blow inland.

The shelf has a dramatic effect on the SWAN wave solution. In Figure 4.16b, the significant wave heights decreased from their maximum of about 19 m in the Gulf; now the maximum wave heights are about 8 m. Note the depth-induced breaking as the waves approach the coastline, and especially near the Tiger and Trinity Shoals (shown in Figure 4.7). The wave heights decrease to 2.5-3 m over the shoals and less at the coastline. Waves of 1-1.5 m are generated inside Vermilion Bay, while waves of 1 m are generated inside Calcasieu and White Lakes. This behavior is also seen in Figure 4.16c, in which sharp gradients in the mean

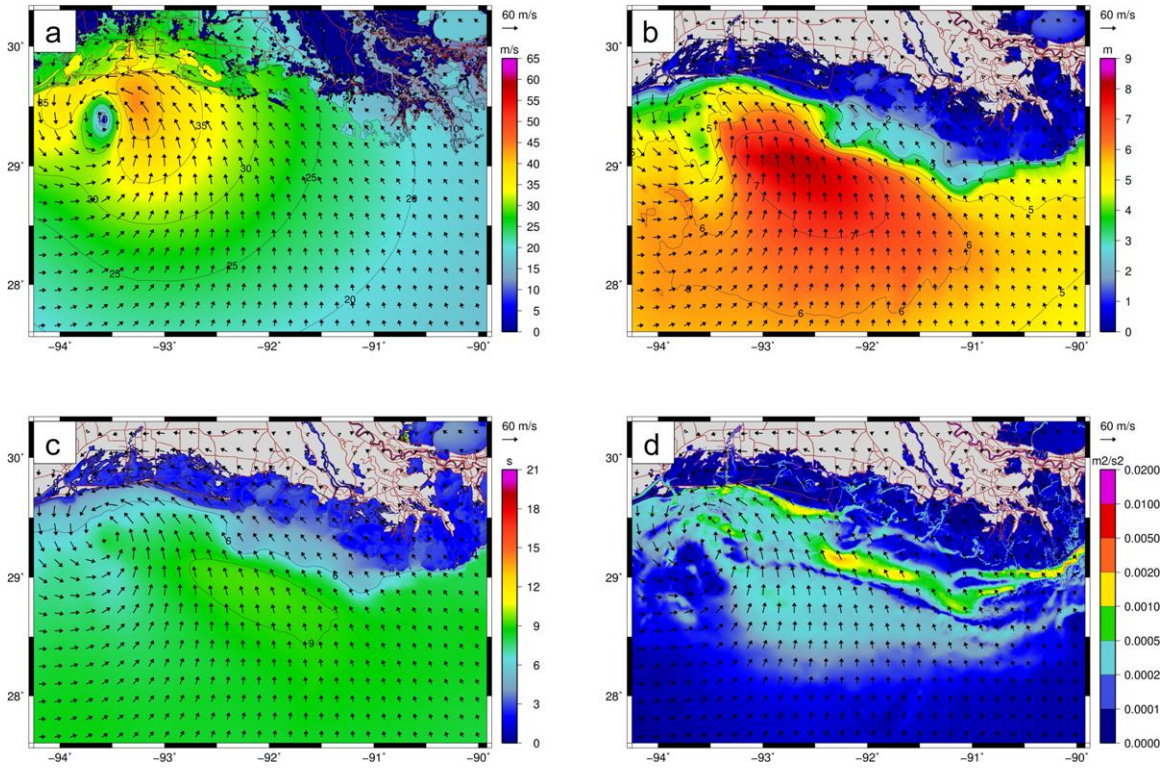

Figure 4.16. Hurricane Rita winds and waves at 0600 UTC 24 September 2005 in southeastern Louisiana. The panels are: (a) wind contours and vectors (m s^{-1}), shown with a 10 min averaging period and at 10 m elevation; (b) significant wave height contours (m) and wind vectors (m s^{-1}); (c) mean wave period contours (s) and wind vectors (m s^{-1}); and (d) radiation stress gradient contours (m^2 s^{-2}) and wind vectors (m s^{-1}).

wave periods are observed in the wave breaking zones, and smaller periods are seen in the bays and lakes. A broad swath of mean periods of 7-9 s exists on the continental shelf, but the periods decrease as the large waves break.

As shown in Figure 4.16d, the radiation stress gradients are near their maximum in regions with significant wave breaking, such as along the coastline and the shoals. The radiation stress gradients reach 0.005-0.02 m^2 s^{-2} in these regions. However, significant gradients are also located at the northeast shores of the inland

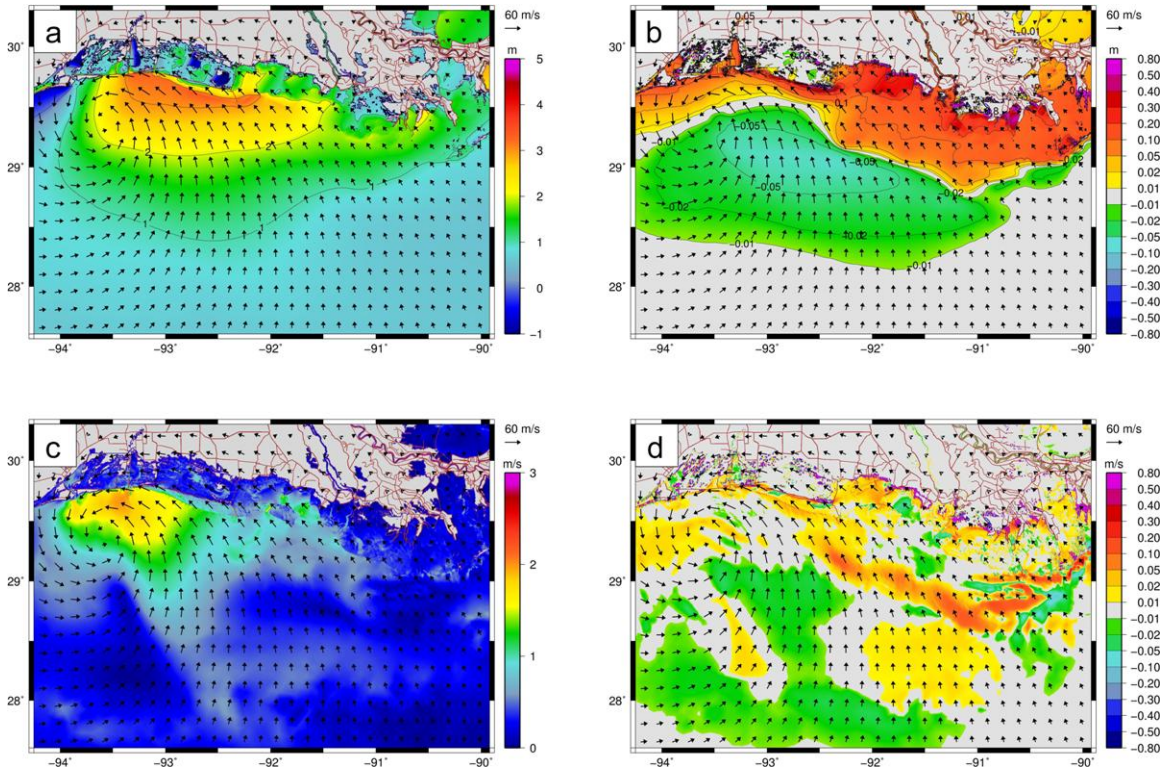

Figure 4.17. Hurricane Rita water levels and currents at 0600 UTC 24 September 2005 in southeastern Louisiana. The panels are: (a) water level contours (m) and wind vectors (m s^{-1}); (b) wave-driven set up contours (m) and wind vectors (m s^{-1}); (c) currents contours (m s^{-1}) and wind vectors (m s^{-1}); and (d) wave-driven currents contours (m s^{-1}) and wind vectors (m s^{-1}).

water bodies and channels, as waves break in these regions. The largest gradients occur to the east, nearer to Timbalier Bay, where the hurricane is pushing large waves onto the relatively narrow shelf, creating large radiation stress gradients and set-up.

As shown in Figure 4.17a, the storm surge has not yet pushed coastal water onshore, but the overland flooding due to the lakes and bays is evident. In the four lakes, strong east-west gradients are observed, with eastern drawdown and

western flooding. Easterly winds have pushed water from these lakes and into the surrounding marshes. Storm surge builds at the coastline as the winds change to blow onshore; the maximum storm surge of 4.7 m occurs near Calcasieu Pass as Rita makes landfall. As shown in Figure 4.17b, at the coastline near Sabine and Calcasieu Lakes, the wave set-up is about 0.05-0.1 m, while it is 0.1-0.2 m near Vermilion Bay. The difference is caused by the shoals, which reach farther onto the shelf, where the larger waves are breaking. This set- up represents 2-5 percent of the overall water levels near the coastline, and 10-20 percent of the overall water levels farther inland.

The winds and waves also drive currents, as shown in Figure 4.17c. In the region nearest the eye of the hurricane and its maximum-strength winds, the currents range from 1-2 m s^{-1}. The winds have developed surge on the continental shelf, and now they are pushing it into southwest Louisiana. There are also several localized instances of significant currents, such as the channel connecting Vermilion Bay to the Gulf, where the currents range from 1.5-2 m s^{-1} as water flows into the bay. Currents are caused by gradients in the water levels, but they are also caused by the wave-breaking, as shown in Figure 4.17d. The wave-driven currents are focused where the waves break, including in the channel near Vermilion Bay, along the coastline and near the shoals.

4.4.3.3 Validation of Coupled Model

The SWAN wave solution for Rita has been compared to measured results from NDBC buoys. The significant wave heights in Figure 4.18 match well in regions with sufficient resolution, including the buoys on the continental shelf on either side of the storm track. At some stations near the track, however, the match is

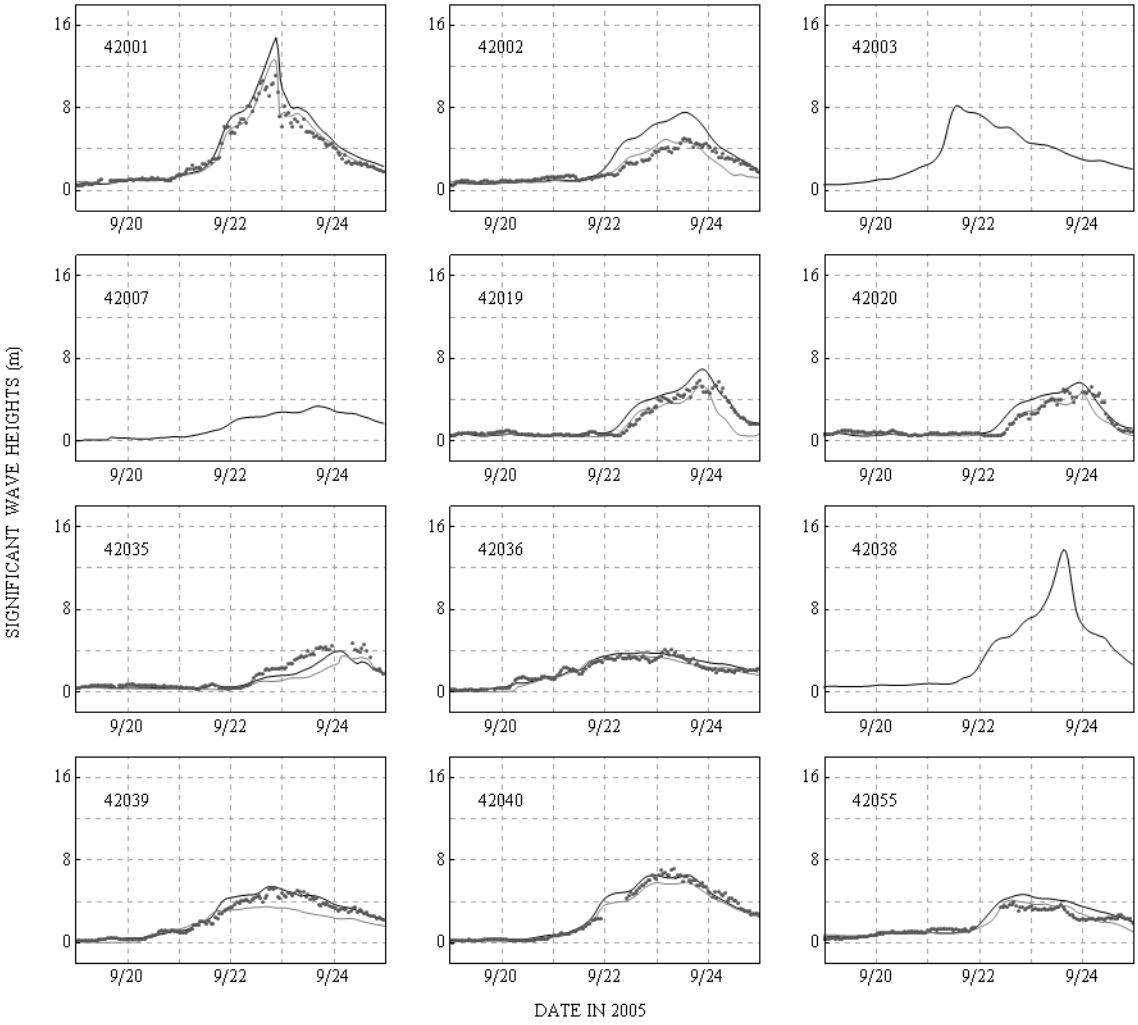

Figure 4.18. Significant wave heights (m) during Hurricane Rita at 12 NDBC buoys. The measured data is shown with black dots, the modeled SWAN results are shown with black lines, and the modeled WAM results are shown with gray lines.

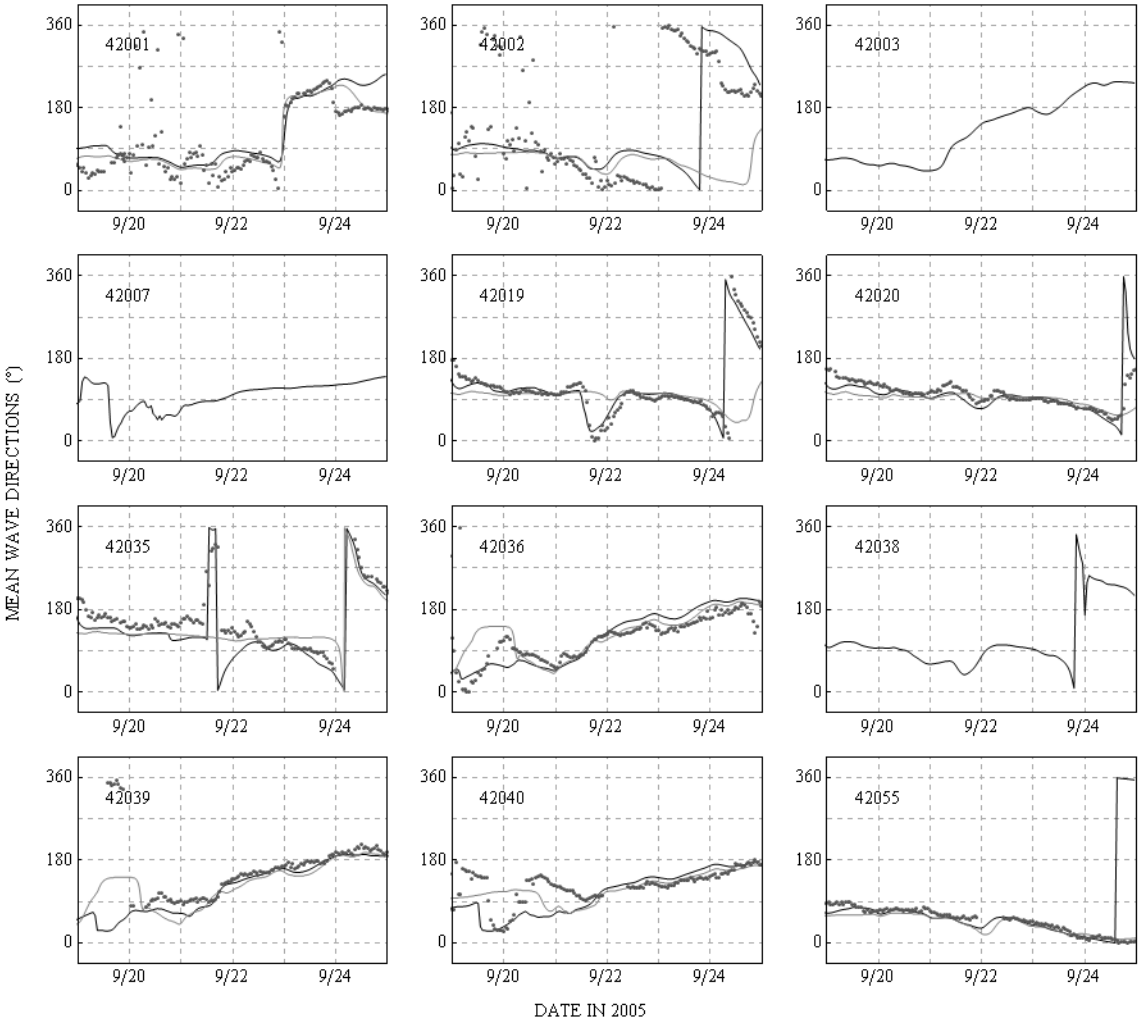

Figure 4.19. Mean wave directions (°), measured clockwise from geographic north, during Hurricane Rita at 12 NDBC buoys. The measured data is shown with black dots, the modeled SWAN results are black lines, and the modeled WAM results are gray lines.

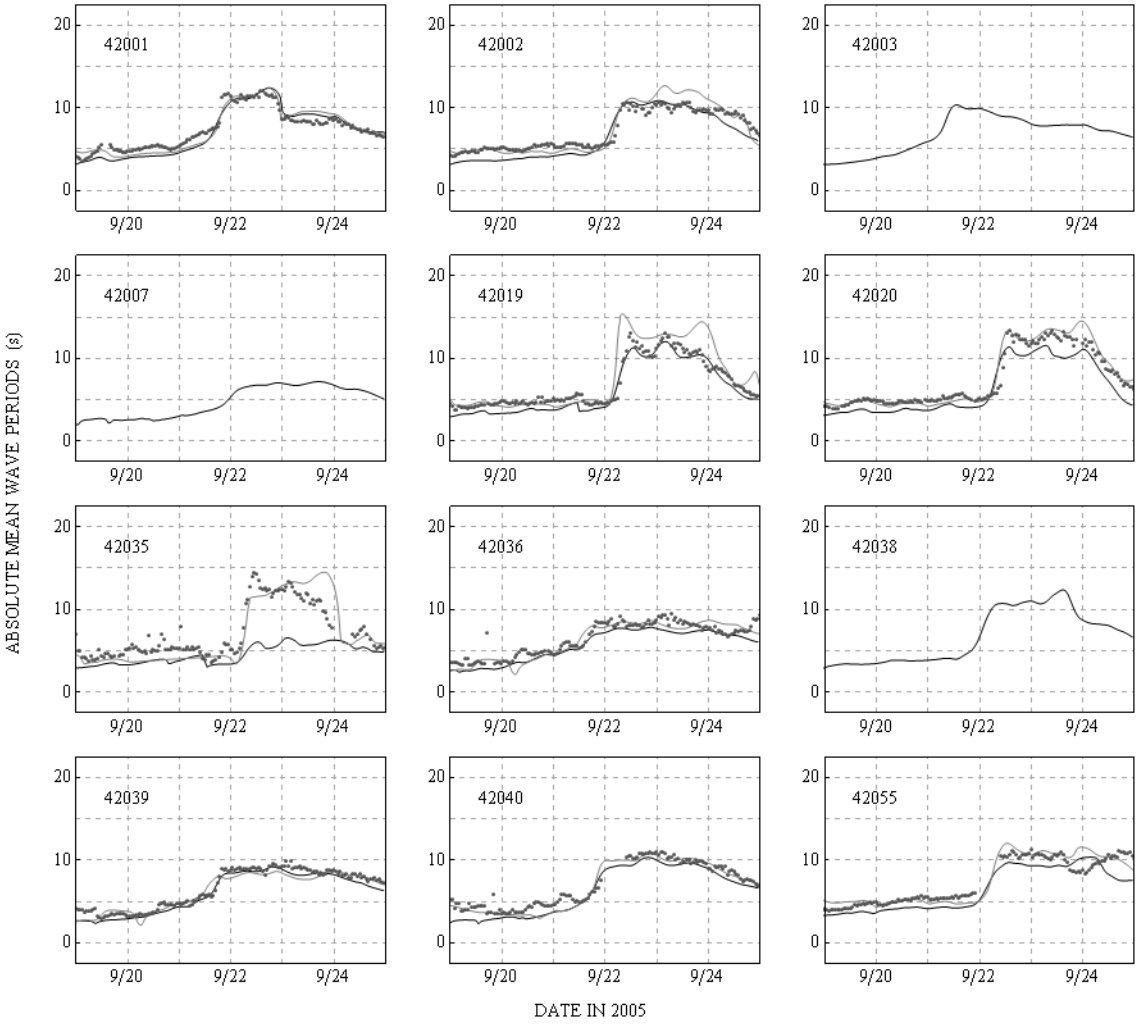

Figure 4.20. Mean wave periods (s) during Hurricane Rita at 12 NDBC buoys. The measured data is shown with black dots, the modeled SWAN results are shown with black lines, and the modeled WAM results are shown with gray lines.

not as good. At buoy 42001, over which Rita passed while it was still a category-4 storm, the modeled peak height of 15 m is much larger than the measured peak height of 11 m. The mesh resolution of 12-18 km may be too large in this region. The mean directions (Figure 4.19) and mean periods (Figure 4.20) also show good agreement. At buoys to the east of the track, the waves change directions from northerly (0°) to southerly (180°) as the storm passes. This trend is reversed to the west of the track, as the waves change directions from easterly (90°) to northerly (0°). As the storm passes these buoys, the periods roughly double, from 4-6 s to about 10-12 s, and then decrease slowly as long waves continue to be generated by the storm. As shown in Table 4.3, the SWAN and WAM results are comparable, with average *SI* errors for the significant wave heights of 0.35 and 0.32, respectively. On a mesh with much coarser resolution in deep water, SWAN is similar to WAM, while offering increased resolution near the coastline and the efficiencies associated with tight coupling.

In shallow water, SWAN has been validated to the CSI measured data shown in Figure 4.21. Note the gauge at station CSI06 failed during Katrina and had not been repaired when Rita passed through the Gulf. However, modeled SWAN results match well with the measured data at CSI05. The significant wave heights reach their maximum of about 2.5 m as the storm moved toward landfall, and the mean periods jumped from about 5 s to 7-8 s. As shown in Table 4.4, the average errors produced by WAM/STWAVE are somewhat smaller than those produced by SWAN, presumably because of the better estimate of the deep water wave conditions (see above). A better representation of wave physics in the deeper Gulf in SWAN might lead to better results at these nearshore stations.

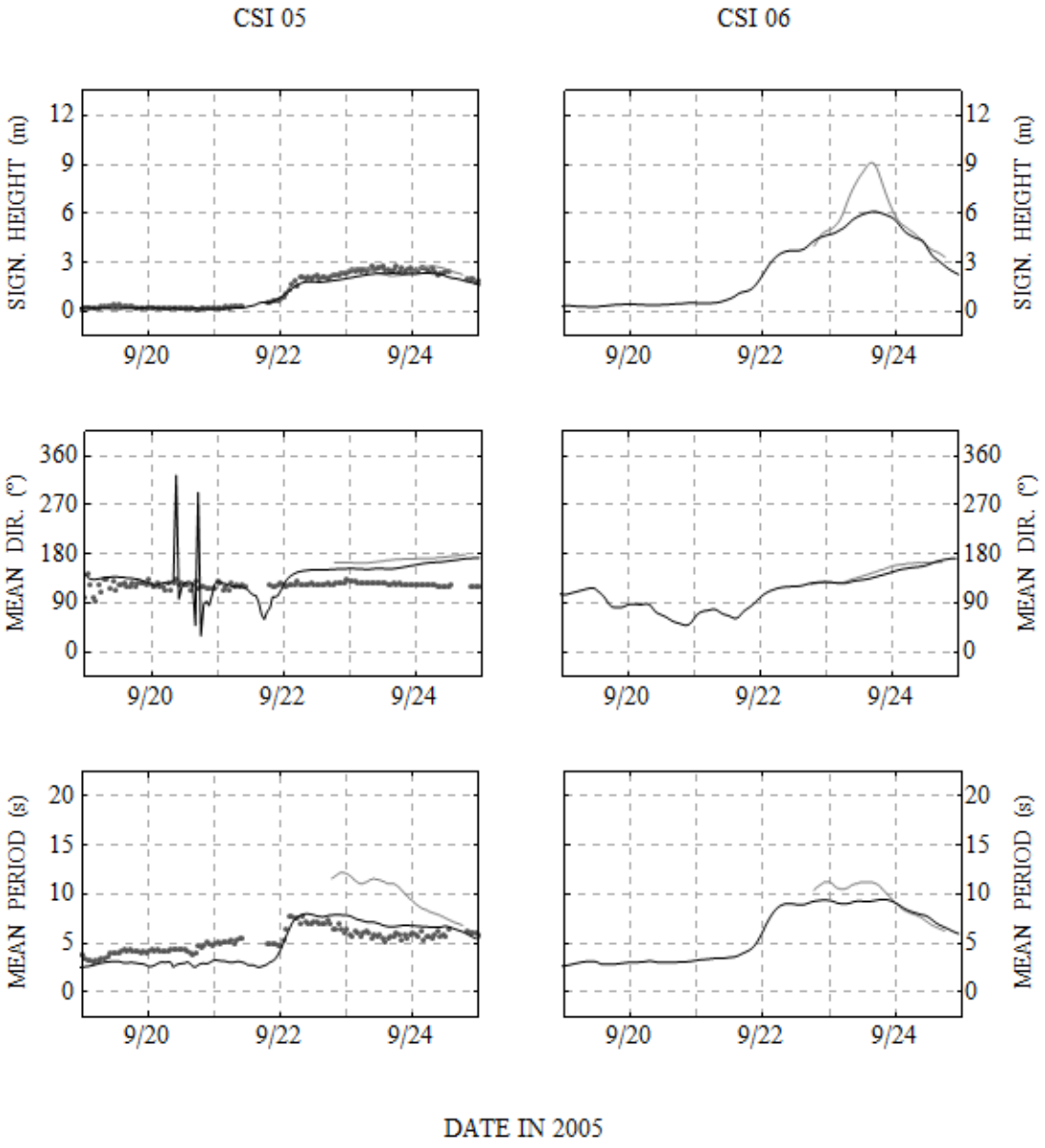

Figure 4.21. Hurricane Rita significant wave heights (m); mean wave directions (°), measured clockwise from geographic north; and mean wave periods (s) at two CSI station. The measured data is shown with black dots, the modeled SWAN results are shown with black lines, and the modeled STWAVE results are shown with gray lines. Note that station CSI 06 did not record during the storm. The CSI station data was collected by WAVCIS (`http://www.wavcis.lsu.edu`).

The ADCIRC solution has been validated to a set of 80 high-water marks collected by URS/FEMA (URS, 2006c). ADCIRC matches well the HWMs, with most points falling within an error of 0.5 m. A comparison of measured-to-modeled HWMs shows a best-fit slope of 0.94 and a correlation coefficient R^2 of 0.75. The significant differences occur near Vermilion Bay, where the modeled HWMs are much lower than those measured by URS/FEMA. This could be due to a lack of mesh resolution in this region or the viscous muddy bottom of Vermilion Bay (Stone *et al.*, 2003; Sheremet *et al.*, 2005). The removal of these points from the error statistics would increase the best-fit slope to 1.01 and the correlation coefficient R^2 to 0.85. As noted in Table 4.5, when the HWM uncertainties are disregarded, the estimated average absolute model error is 0.18-0.24 m, and the standard deviation is 0.33-0.39 m. These results are similar to the loose coupling of ADCIRC with WAM and STWAVE (Bunya *et al.*, 2010).

4.4.4 Computational Performance

SWAN+ADCIRC was benchmarked on Ranger, which is a Sun Constellation Linux Cluster at the Texas Advanced Computing Center (TACC) (`http://www.tacc.utexas.edu`). Ranger consists of 3,936 SMP compute nodes, each with four quad-core AMD Opteron processors. The nodes are connected with an InfiniBand network with a bandwidth of 1 GB s^{-1}. The overall system has 62,976 cores, 123 TB of memory and a theoretical peak performance of 579 TFLOPS.

The Katrina simulation described above was run with the coupled model and again with its individual components in order to discern coupling effects on simulation times. When ADCIRC was run individually, it did not receive radiation stress gradients from any source. When SWAN was run individually, it read the

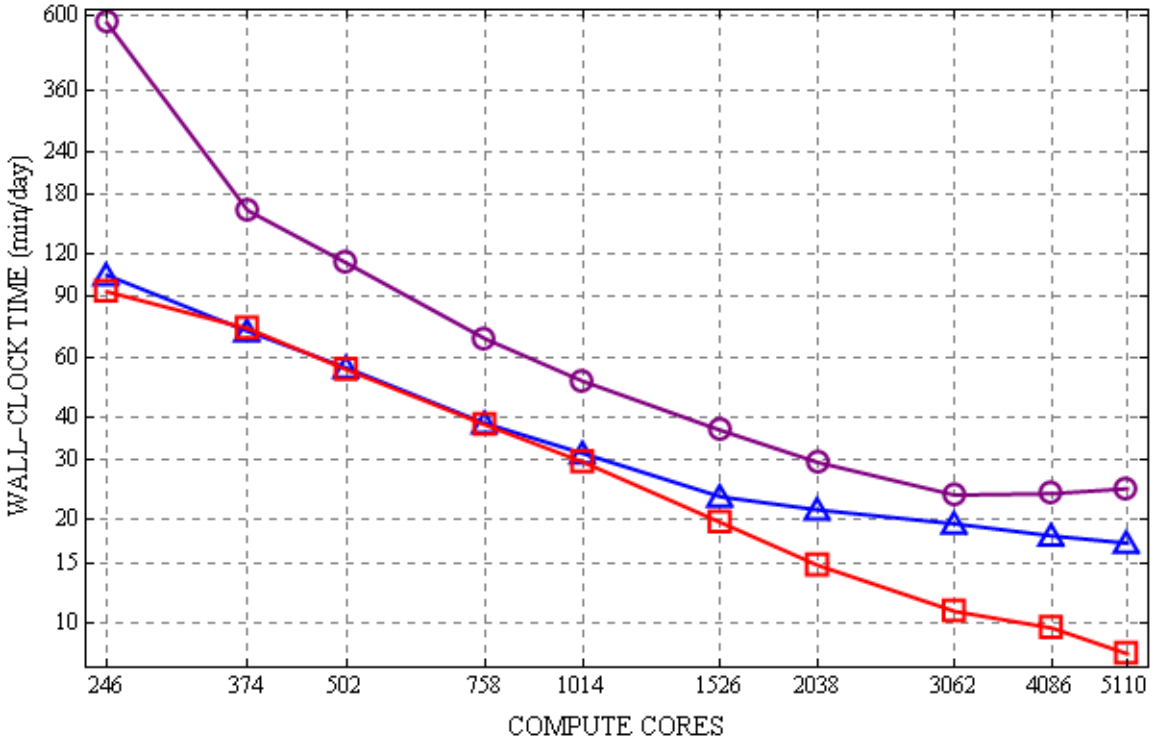

Figure 4.22. Timing results for SWAN+ADCIRC and its components on the TACC Ranger machine. The times shown are wall-clock minutes per day of Katrina simulation on the SL15 mesh. SWAN results are shown in red, ADCIRC results are shown in blue, and SWAN+ADCIRC results are shown in purple.

wind speeds from external files, but it did not receive water levels or currents from any source. The models were run on 256 to 5,120 cores, of which ten cores were always dedicated for file output by ADCIRC. Wall- clock times were reported by the Sun Grid Engine batch system.

As shown in Figure 4.22, the individual SWAN and ADCIRC models both scale linearly through about 1,000-1,500 cores, but they diverge at higher numbers of computational cores. ADCIRC's timing results level off, because the global communication associated with its implicit, conjugate-gradient solver begins to

dominate the simulation time. The highly localized solution procedure in SWAN allows it to scale linearly through 5,000 cores, enabling performance of less than 10 min per day of Katrina simulation.

In the SWAN+ADCIRC timing results, note the sharp increase in performance between 246 and 374 computational cores, which suggests the coupled model requires less than about 8,000 mesh vertices per core to maintain memory in cache. Also note the coupled model shows linear scaling to about 3,000 computational cores, but then it levels off. At this point, the communication overhead from ADCIRC slows down the coupled model. However, the performance in this range is about 24 min per day of Katrina simulation, which is sufficient for forecasts of large storms.

With the exception of the run on 246 cores, when the combined problem size was too large to maintain in cache, the SWAN+ADCIRC timing results are never larger than the combination of the timing results from each component. The tight coupling adds no overhead to the simulation, and it even increases the efficiency at large numbers of cores. For example, at 3062 cores, the SWAN+ADCIRC timing of 24 min per day is less than the combined total of 20 min per day for ADCIRC and 11 min per day for SWAN. This efficiency is created by the sharing of tasks, such as the reading and interpolation of the wind input files. In addition, the computational load per file output interval is increased in the coupled model, so the dedicated file output cores have more time to complete their tasks while the computational cores are working. Thus, at large numbers of cores, it is faster to run the coupled model than its components individually.

4.5 Conclusions

The recent introduction of the unstructured-mesh SWAN allows for wave simulation on the same unstructured meshes used by ADCIRC, which utilizes basin-to-floodplain scale domains and increases locally the resolution in regions with large spatial gradients. This work implemented the tight coupling of SWAN+ADCIRC, so that these models run as an integrated system on the same mesh, and vertex-based solutions and forcing information are passed through local cache.

SWAN+ADCIRC simulates hurricane storm surge with high levels of accuracy. Hindcasts of Katrina and Rita show the models generate waves in deep water; dissipate waves due to changes in wave-wave interactions, bathymetry and bottom friction in southern Louisiana; apply the radiation stress gradients to create set-up and wave-driven currents in the circulation model; and then return those water levels and currents to the wave model. SWAN compares well to measured wave parameters at 12 NDBC buoys in the Gulf, even though the mesh resolution is 12-18 km in those areas. Major differences were at buoys located west of the hurricane track, where SWAN+ADCIRC tends to over-predict the significant wave heights. This over-prediction may be due to missing physics (such as the warm-core eddy) or poor numerics (such as the coarseness of the mesh). In the nearshore, validation of SWAN to measured data at two CSI stations showed that SWAN matches well the wave behavior on the continental shelf. The ADCIRC modeled water levels compare well with measured HWMs. Comparisons to WAM and STWAVE showed that the errors in the SWAN results are slightly larger than in the WAM/STWAVE results, which may be due to a larger mesh size for SWAN in deep water. SWAN's physics can be optimized for deep water, and it is well-positioned to increase its localized resolution to improve accuracy in the future.

SWAN+ADCIRC is also highly efficient. It eliminates the need for interpolation between models with heterogeneous meshes, interpolation at the boundaries of nested meshes, and the consideration of overlapping or inconsistent solutions. It shows linear scaling to about 2,000 cores and wall-clock times of 24 min per day of Katrina simulation on a mesh with 2.4 million vertices. The coupled model maintains linear scaling to larger numbers of computational cores when applied to meshes with larger numbers of vertices. It does not add overhead due to interpolation, global communication or the mechanics of managing the coupling. Instead, SWAN+ADCIRC shares the work among model components in a way that can speed up the combined run time. The result is a coupled model that is well-positioned for applications in high-performance computing environments.

Future work will improve the efficiency and accuracy of the coupled model. The new generation of computational meshes in southern Louisiana and Texas will increase resolution in the wave-generation zones in the Gulf of Mexico, the wave-breaking zones along the coastline and the barrier islands, and the channels and inlets further inland. Future generations of meshes will relax initially the resolution and then refine adaptively, by adding resolution in regions where the computed gradients are large in either model component. These meshes will represent better the wave and circulation solutions, and the highly-efficient, coupled model will allow them to be used operationally. The tight coupling of SWAN+ADCIRC enables waves, water levels and currents to interact in complex problems and in a way that is accurate and efficient.

CHAPTER 5

HURRICANE GUSTAV (2008) WAVES, STORM SURGE AND CURRENTS: HINDCAST AND SYNOPTIC ANALYSIS IN SOUTHERN LOUISIANA

5.1 Overview

This chapter employs SWAN+ADCIRC in a next-generation hindcast of Gustav. It utilizes the unstructured SL16 mesh, which contains twice the resolution of previous meshes, with mesh spacing of 4-6 km in the deeper Gulf that varies downward to 30-50 m in the fine-scale channels of southern Louisiana. It makes good use of the coupling to improve the model physics; a storm-sector-based wind drag scheme is shared between SWAN and ADCIRC, and the bottom friction in SWAN is updated to use roughness lengths derived from the Manning's n values used by ADCIRC. Furthermore, SWAN employs a larger range of discretized frequencies, to better model the short-period waves in the marshes, and a stronger set of convergence criteria, to better model the propagation of swell on the fine mesh. A careful comparison to extensive measurement data shows that SWAN+ADCIRC captures well the evolution of wave and surge from the deep water, to the continental shelf, and into the complex nearshore environment. This chapter has been submitted to *Monthly Weather Review* as Dietrich *et al.* (2010c).

Gustav made landfall in southern Louisiana, with its eye never closer than 75km to New Orleans, but its waves and storm surge threatened the city. Tropical-

storm-strength winds impacted the region east of the Mississippi River for 12-15hr, allowing for early surge propagation of 2-3.5m up the river, 3-3.5m into the city's navigation canals, and 1m against the city's northern boundary along Lake Pontchartrain. During landfall, winds shifted from easterly to southerly, resulting in late surge development and propagation of 1.5-2.25m along Grand Isle, 2m throughout Lake Pontchartrain, 2.5-3m over more than 40km of Caernarvon Marsh and against the levees at English Turn, and 1m over more than 70km of marshes on the river's west bank. The barrier islands dissipated the largest waves, and locally-generated seas existed behind these initial breaking zones. Although the levee protection system was not breached, there were reports of wave overtopping.

The hardening and innovative deployment of gages since Katrina resulted in a wealth of measured data for Gustav that describe how waves and surge are generated in deep and shallow water, propagate onto the continental shelf, and dissipate in the complex nearshore environment. Computational models, including the structured-mesh WAM and STWAVE wave models and the unstructured-mesh SWAN wave and ADCIRC circulation models, resolve the region with unprecedented levels of detail, with a mesh spacing of 100-200m in the wave-breaking zones and 20-50m in the fine-scale channels. Data-assimilated winds were applied using H*WIND and IOKA procedures. Wave and surge computations are validated at locations ranging from the Gulf into southern Louisiana, showing all four models simulate well the system's response to Gustav.

5.2 Introduction

New Orleans and its infrastructure are surrounded by extensive levees and raised features, marshes to the south and east, and barrier islands on the Louisiana-Mississippi shelf. Hurricane Katrina (2005) exposed vulnerabilities as it generated storm surge throughout the region, flooding in New Orleans due to breaches along its shipping and drainage canals, and water levels along the Mississippi coastline that were the largest measured in the United States (Ebersole *et al.*, 2007). But Katrina was considered a worst-case scenario in many ways. Katrina reached Category 5 on the Saffir-Simpson Scale in the Gulf of Mexico before weakening to Category 3 prior to its first landfall, maintained its intensity through the Breton and Chandeleur Sounds, and tracked near metropolitan New Orleans (Knabb *et al.*, 2005).

Hurricane Gustav (2008) was the first major hurricane to track through southeast Louisiana since Katrina (Figure 5.1). Gustav was much weaker than Katrina, both in the Gulf and at landfall, it tracked farther west, and its eye was never closer than 75km to New Orleans. For those reasons, its waves and surge were expected to be less threatening to the city. However, Gustav increased in size as it approached Louisiana, and its outer, tropical-storm-strength winds impacted the system for 12-15hr. Gustav generated waves that damaged infrastructure in southern Louisiana and offshore, and its surge nearly overtopped large sections of the levee/floodwall system throughout metropolitan New Orleans.

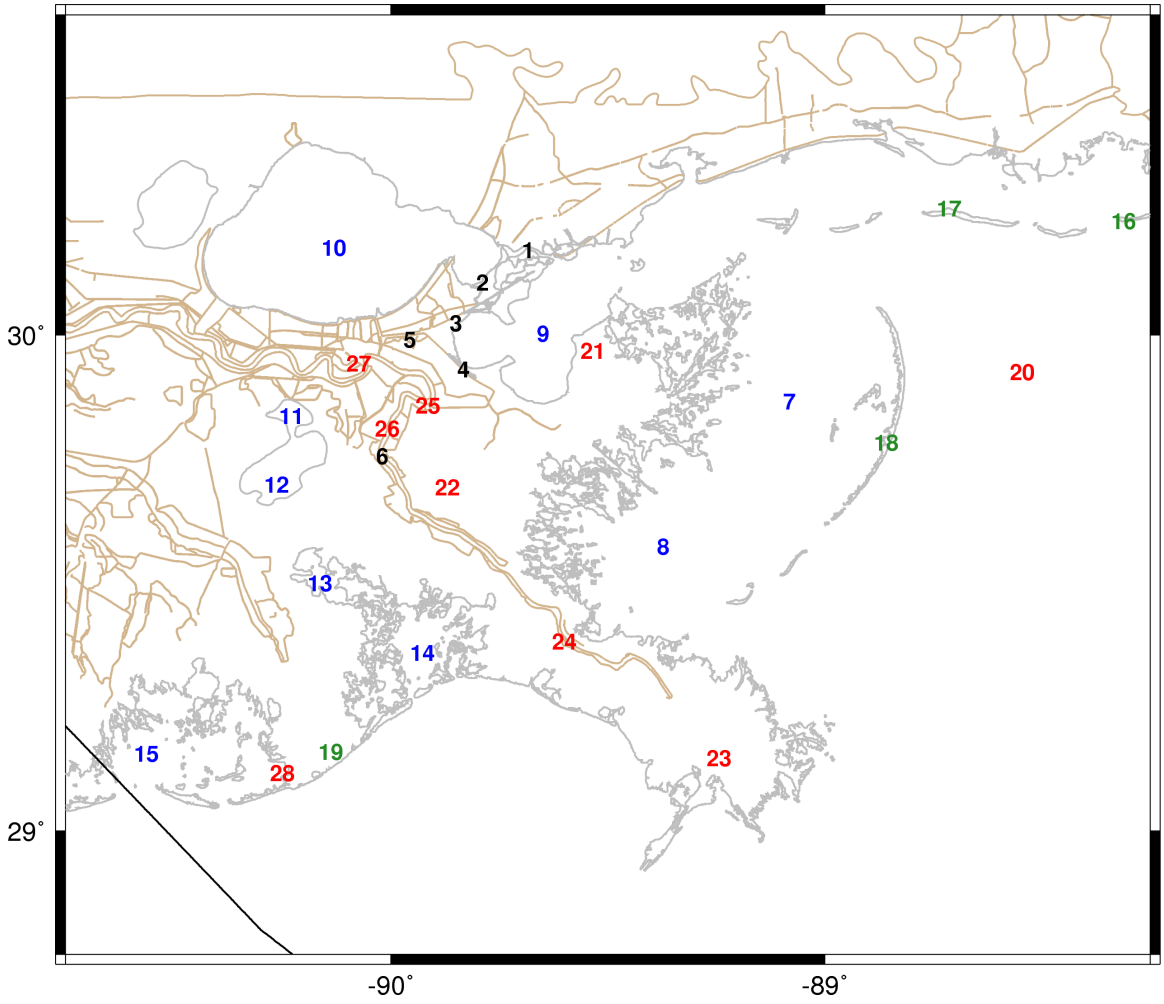

Figure 5.1. Schematic of southeastern Louisiana. Solid lines indicate Gustav's track (black), ADCIRC levee/road boundaries (brown) and the coastline (gray). Geographic locations of interest are indicated by numbers identified in Table 5.1.

TABLE 5.1

GEOGRAPHIC LOCATION BY TYPE AND NUMBER

Type	Number	Location
Rivers and channels	1	Rigolets
	2	Chef Menteur Pass
	3	Gulf Intracoastal Waterway (GIWW)
	4	Mississippi River Gulf Outlet (MRGO)
	5	Inner Harbor Navigational Canal (IHNC)
	6	Mississippi River
Bays, lakes and sounds	7	Chandeleur Sound
	8	Breton Sound
	9	Lake Borgne
	10	Lake Pontchartrain
	11	Lake Cataouatche
	12	Lake Salvador
	13	Little Lake
	14	Barataria Bay
	15	Terrebonne Bay
Islands	16	Dauphin Island
	17	Mississippi Sound Islands
	18	Chandeleur Islands
	19	Grand Isle

TABLE 5.1

Continued

Type	Number	Location
Places	20	Louisiana-Mississippi Shelf
	21	Biloxi Marsh
	22	Caernarvon Marsh
	23	Mississippi River Delta
	24	Plaquemines Parish
	25	English Turn
	26	Braithwaite
	27	New Orleans
	28	Port Fourchon

Measured data for waves and surge are more extensive and detailed than for any previous Gulf hurricane. Measured time series describe wave generation, propagation, and dissipation onto the continental shelf and into the marshes and coastal floodplains. The National Data Buoy Center (NDBC) collected measurements at its buoys throughout the Gulf, where the depths range to several kilometers and the peak wave heights reached an estimated 15-18m. On the shelf, the Coastal Studies Institute (CSI, `http://www.wavcis.lsu.edu`) collected measurements at five stations west of the Mississippi River delta, where a decrease in bathymetry and wave damping, due to cohesive sediments, limited the peak

wave heights to 3-5m. Sixteen gages deployed by Andrew Kennedy (AK) of the University of Notre Dame were located along the coastline from Calcasieu Pass to Pensacola Bay, in depths ranging from 1-20m, and they offer an unprecedented description of the nearshore wave behavior during a major hurricane (Kennedy *et al.*, 2010a). Additionally, six gages deployed by the Coastal Hydraulics Laboratory (CHL) of the US Army Corps of Engineers (USACE) show the dissipation of waves in the Terrebonne and Biloxi marshes. This level of available wave data was possible due to permanent gage hardening and the development of deployable gages since Katrina.

High-water marks (HWMs) were collected by the Federal Emergency Management Agency (FEMA), while time series of water levels were collected by AK, CHL, the USACE, the US Geological Survey (USGS), the National Oceanic and Atmospheric Administration (NOAA), and the Coastwide Reference Monitoring System (CRMS). These data show how the surge evolved throughout the storm. Surge of 2.5-3m was pushed across the shelf and against the levees of lower Plaquemines Parish, which is fronted by a relatively narrow marsh and Breton Sound. The river levees extend farther southward on the west bank, and they helped to steer this surge upriver. Surge was focused against the levees near the confluence of the Gulf Intracoastal Waterway (GIWW) and the Mississippi River Gulf Outlet (MRGO), where it flowed into the Inner Harbor Navigation Canal (IHNC) and the center of the city of New Orleans. There were reports of intermittent overtopping of the city floodwalls and levees (Figure 5.2a), although no breaches occurred. An early set-up of 1m along the southwest shore of Lake Pontchartrain became 2-2.25m after the lake filled. To the east of the river, the surge reached 2.5m against the levees near English Turn and Braithwaite (Figure 5.2b), which are fronted by

Figure 5.2. Photographs during Gustav of (a) waves overtopping the IHNC walls near the Ninth Ward, and (b) surge overtopping the earthen levee near Braithwaite (right), courtesy of Nancy Powell, USACE.

40km of Caernarvon Marsh that marginally attenuated the water levels. To the west of the river, a surge of 2-2.5m developed near Port Fourchon and Grand Isle as the storm was making landfall. When the winds shifted, surge was pushed into Terrebonne and Barataria Bays, northward through the interconnected marshes and waterways, and reached 1m near the west bank of New Orleans, but not until 12-36hr after landfall. Thus, despite making landfall more than 75km from New Orleans, Gustav created significant surge on all sides of the city.

Due to the complexities of southern Louisiana and its response to hurricane forcing, computational models have been developed that utilize unstructured meshes to resolve at basin, shelf, floodplain and channel scales (Westerink *et al.*, 2008). These meshes incorporate the frictional dissipation due to variability in land cover, local geology and bottom sediments (Sheremet and Stone, 2003). Mesh resolution

varies from kilometers in deep water to tens of meters in the small-scale channels and features inland and near the levee protection system. Surge is allowed to propagate onto the continental shelf and interact with the complex geometry nearshore. The ADvanced CIRCulation (ADCIRC) shallow-water model was validated on the unstructured SL15 mesh for Katrina and Rita (2005), and it showed high levels of model skill for tides, riverine stages, winds, waves and storm surge (Bunya *et al.*, 2010; Dietrich *et al.*, 2010). The SL15 model was used extensively for design work and analysis by the USACE, FEMA and local agencies (Ebersole *et al.*, 2007; FEMA, 2008; USACE, 2009).

The Gustav hindcast utilizes the latest SL16 mesh, which contains twice the resolution of the SL15 mesh. The Gulf is resolved with resolution of 4-6km, and the mesh size decreases accordingly on the shelf to 500-1000m. In the wave breaking zones and inland, the resolution is never greater than 200m, to improve the wave breaking and the transfer of wave radiation stress gradients to ADCIRC. In the fine-scale channels and passes, such as the Mississippi River, the MRGO, and the Rigolets and Chef Menteur passes, the resolution varies to 20-50m. Bathymetry and topography were re-applied from the latest sources, as described below.

Advancements have also been made in the coupling of wave and circulation models. ADCIRC has been coupled to two structured-mesh wave models: the deepwater WAve Model (WAM) on a basin scale, and the nearshore STeady-state WAVE (STWAVE) model on regional scales (Komen *et al.*, 1994; Smith, 2000; Smith *et al.*, 2001; Gnther, 2005; Bunya *et al.*, 2010; Dietrich *et al.*, 2010a). The spectral wave energy from WAM was interpolated and used as boundary conditions for five nearshore STWAVE meshes, four of which allowed waves to propagate only in the half plane directed onshore. Now STWAVE has been applied with full-plane

propagation in all nearshore meshes. Alternatively, ADCIRC has been coupled with the unstructured-mesh version of the Simulating WAves Nearshore (SWAN) model (Zijlema, 2010; Dietrich *et al.*, 2010b). SWAN+ADCIRC employs the same unstructured mesh on the same computational cores, passing information between models through local cache, and thus it can simulate the propagation of waves from deep water to the nearshore with accuracy and efficiency (SiadatMousavi *et al.*, 2009).

These new models are well-positioned to simulate hurricanes in southern Louisiana, and Gustav is an appropriate validation test because of its size and track, the quality of data-assimilated wind fields available to force models, and the wealth of measured waves and water levels. In the sections that follow, we describe the models and characterize the system, discuss how the storm evolved and impacted the region at landfall, and validate the hindcast using the measured time series of waves and water levels.

5.3 SL16 Model Development

5.3.1 Hurricane Wind Field

Hurricane wind fields for Gustav were developed using NOAA's Hurricane Research Division Wind Analysis System (H*Wind) to assimilate winds in the core from extensive aircraft, buoy, space-based remote sensing, wind-tower and other measurement data (Powell, 1996; 1998; 2010). H*Wind analyses of Gustav benefited from the deployment of Stepped-Frequency Microwave Radiometers aboard the Air Force Hurricane Hunter Aircraft (Uhlhorn *et al.*, 2007), increasing the availability of high radial resolution surface winds since the Katrina wind field post-analysis (Ebersole *et al.*, 2007). Additional improvements to the H*Wind

analysis included the use of improved terrain conversions (Vickery *et al.*, 2009) and high-resolution tower data from Texas Tech University and the Florida Coastal Monitoring Program. H*Wind analyses cover an 8 latitude-longitude domain on a 3hr frequency for Gustavs entire Gulf track. To provide forcing to our circulation and wave models, the H*Wind fields are blended with larger scale winds using the Interactive Objective Kinematic Analysis (IOKA) system (Cox *et al.*, 1995; Cardone *et al.*, 2007). The resulting wind fields apply to the reference condition of 10m height, peak 30min "sustained" wind speed and marine exposure. Wind fields were interpolated to 15min intervals, starting at 0000 UTC 26 August 2008 (approximately 6.5 days before landfall) and ending at 0000 UTC 04 September 2008 (approximately 2.5 days after landfall). The Gustav wind fields offer Gulf-wide resolution on a 0.05° mesh, with increased resolution of 0.015° on a smaller mesh near landfall.

These resulting wind fields and Holland (1980) model-generated pressure fields are read and interpolated by ADCIRC onto its unstructured mesh and then passed to the wave models. ADCIRC applies a factor of 1.09 to convert from 30min-averaged to 10min-averaged wind speeds, and directional wind reduction factors are applied (Bunya *et al.*, 2010). In addition, ADCIRC applies a wind drag coefficient based on recent analyses of the azimuthal dependence of the drag coefficient determined from mean GPS sonde wind speed profiles (Powell *et al.*, 2003; 2006). Data were inconclusive to determine whether an azimuthal drag dependence exists near coastal areas. However, for the results based primarily on open-ocean, deepwater wind profiles, the drag coefficient increases in sectors where the winds are blowing across or counter in direction to the waves. ADCIRC detects the location and direction of the eye, and then the sector-based wind drag coefficients

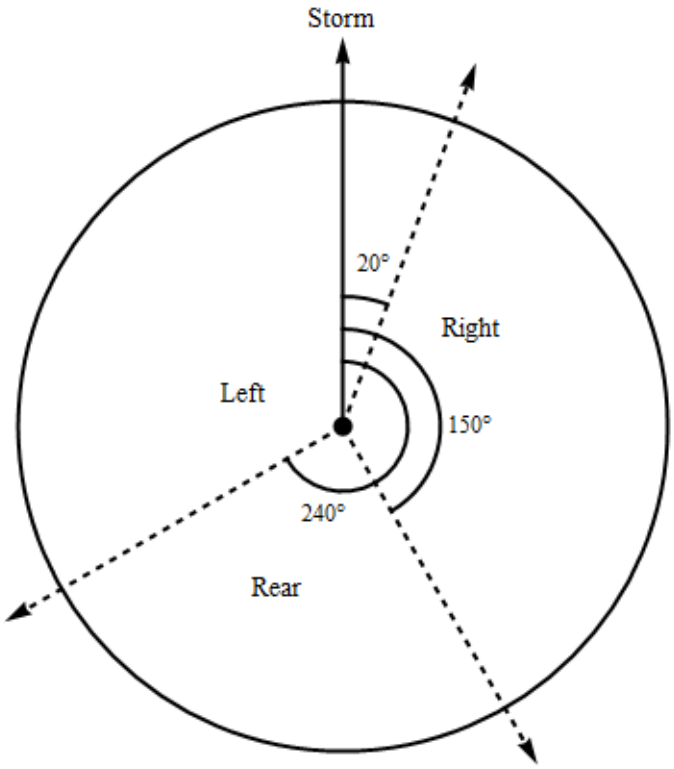

Figure 5.3. Extents of sectors in relation to direction of storm movement, from Powell (2006).

are applied as shown in Figures 5.3 - 5.4. These wind drag coefficients are shared with SWAN.

WAM utilizes an atmospheric input source term based on Janssen (1991) that includes the net impact surface roughness resulting from a growing wave field, with an upper limit where the dependency of frictional velocity becomes linear with the equivalent neutral stable marine exposure wind field at 10m. STWAVE applies a drag coefficient consistent with Cardone (1969).

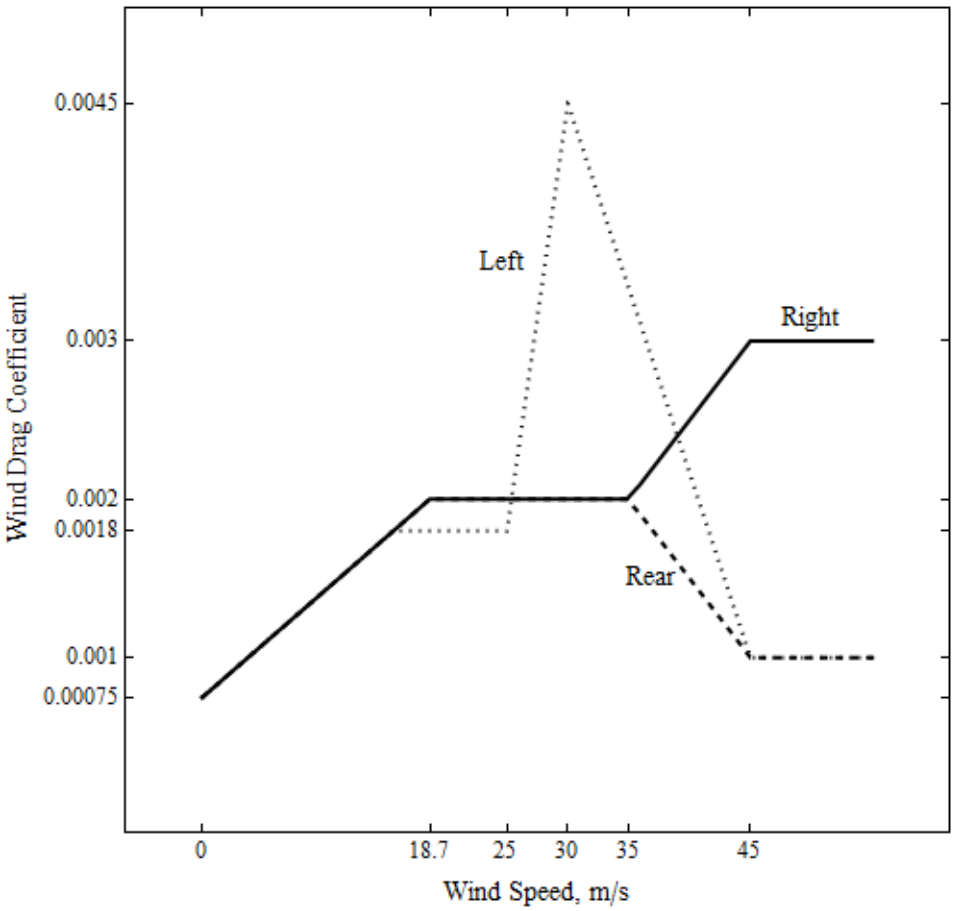

Figure 5.4. Wind drag coefficient variability by storm sector, from Powell (2006).

5.3.2 Wave and Surge Models

The coupling of ADCIRC and STWAVE is performed through external files. WAM is run first, on a Gulf-wide mesh with fixed 0.05° resolution, to generate boundary conditions at the nearshore, structured STWAVE meshes (Komen *et al.*, 1994; Smith, 2000; Smith *et al.*, 2001; Günther, 2005; Smith, 2007). WAM is a third-generation, discrete spectral wave model solving the action balance equation (including refraction and shoaling) and accounting for arbitrary water depth in

source/sink term specification to compute the generation and dissipation of wave action. It uses 28 frequency bins that increase in bandwidth logarithmically, and 24 directional bins of constant width 15°. ADCIRC is then run, and its wind fields and water levels are output to use as forcing for a set of STWAVE simulations on two nearshore meshes with 200m resolution. STWAVE solves the action balance equation along piecewise, backward-traced wave rays. STWAVE utilizes 45 frequency bins, on the range 0.0314-2.08Hz and increasing in bandwidth logarithmically ($\Delta\sigma/\sigma \approx 0.1$), and 72 directional bins of constant width 5°. This coupling provides good matches for nearshore waves and storm surge, and a reasonable wave set-up (Bunya *et al.*, 2010; Dietrich *et al.*, 2010a).

In the coupling of SWAN+ADCIRC, the unstructured-mesh version of SWAN is applied so that both models run on the same mesh, thus eliminating the need for interpolation between models (Dietrich *et al.*, 2010b; Zijlema, 2010). Water levels and currents are computed by ADCIRC and passed at each SWAN time step. SWAN solves the action balance equation for the wave action (Booij *et al.*, 1999; Ris *et al.*, 1999). The SWAN time step and coupling interval are 600s (Dietrich *et al.*, 2010b). The wave directions are discretized into 36 directional bins of constant width 10°, and the frequencies are discretized over 40 bins on a logarithmic scale, over the range 0.031-1.42Hz. The hindcast uses the wind input formulation based on Snyder *et al.* (1981), the modified whitecapping expression of Rogers *et al.* (2003), and quadruplet nonlinear interactions via the Discrete Interaction Approximation (Hasselmann *et al.*, 1985). For the shallow-water source terms, depth-induced breaking is computed with a spectral version of the model due to Battjes and Janssen (1978) with the breaking index $\gamma = 0.73$; bottom friction is described below. Wave refraction is enabled in regions where the resolution of

the bathymetry is sufficient to prevent spurious wave refraction over one spatial element, specifically in the northern Gulf.

ADCIRC solves the 2D and 3D shallow-water equations for water levels ζ and the vertically-integrated momentum equations for currents U and V (Kolar *et al.*, 1994; Luettich and Westerink, 2004; Dawson *et al.*, 2006; Westerink *et al.*, 2008). The depth-averaged 2D equations are employed herein because there is significant, wave-induced vertical mixing on the continental shelf. The unstructured mesh allows for resolution to increase as waves and surge propagate from the deeper Gulf to the continental shelf and into the inlets and floodplains of coastal regions. ADCIRC uses a 1s time step in the present hindcasts.

5.3.3 SL16 Unstructured Mesh

This study employs the high-resolution SL16 mesh, which has 5,036,960 vertices and 9,949,317 triangular elements. As shown in Figures 5.5 - 5.7, the mesh provides coverage of southern Louisiana, Mississippi and Alabama, and it extends outward through the Gulf of Mexico and the Caribbean Sea to the western North Atlantic Ocean. This wide coverage allows tides to be specified at a boundary outside the resonant basin of the Gulf, and storms to be started inside the domain but far from the area of interest. As highlighted in Figure 5.8, the mesh resolution varies from 15-20km in the Atlantic Ocean, to 4-6km in the Gulf, to 100-200m in the wave-breaking zones and marshes of southern Louisiana, to 20-50m in fine-scale channels.

Bathymetry in the Gulf was specified using the 1 arc-minute global relief model ETOPO1 in deep water (Amante and Eakins, 2009) and Coastal Relief DEMs nearshore (NOAA, 2008). Bathymetry in nearshore water bodies and channels,

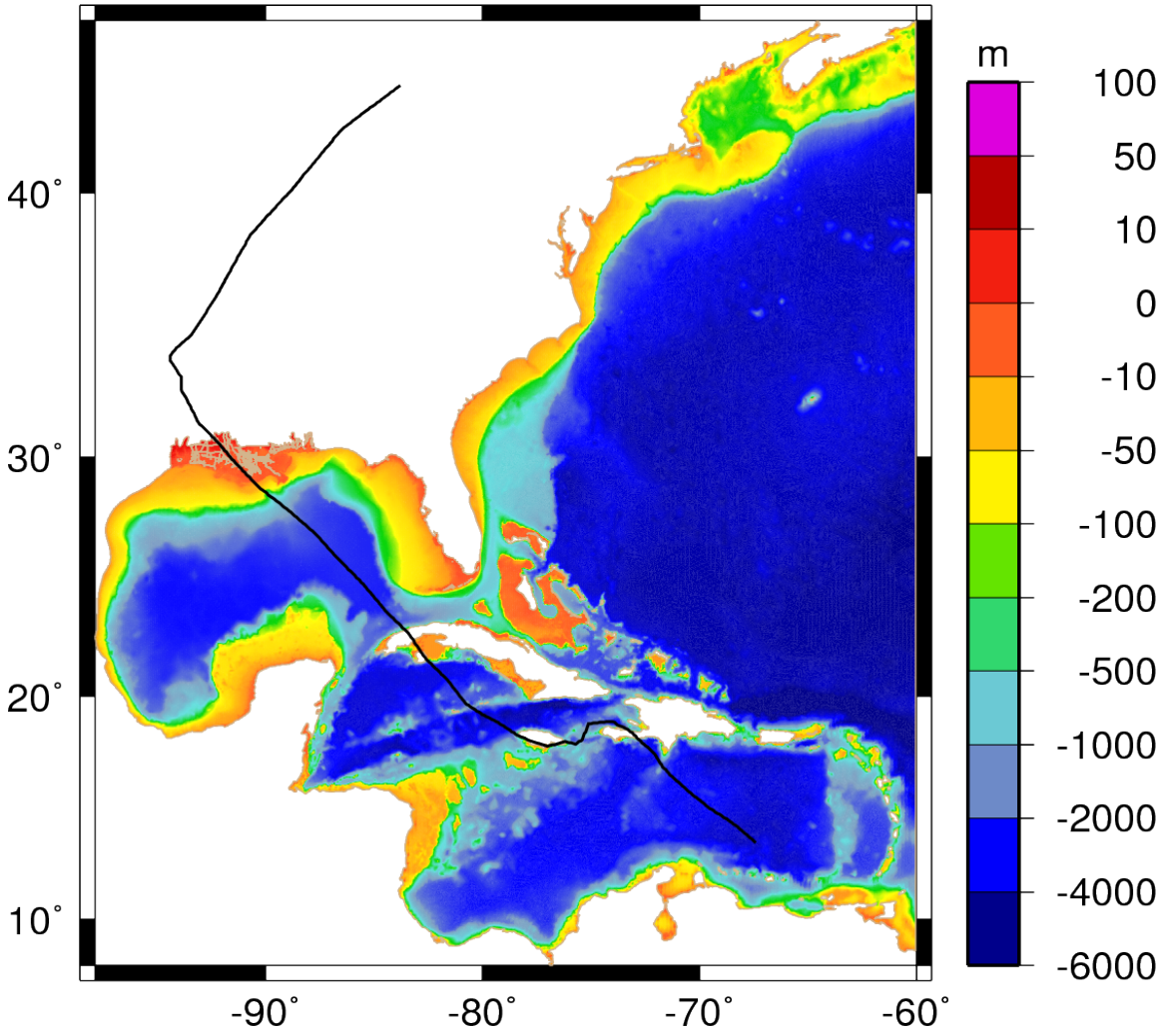

Figure 5.5. Bathymetry/topography (m) of the SL16 mesh. Gustav's track is shown with a solid black line.

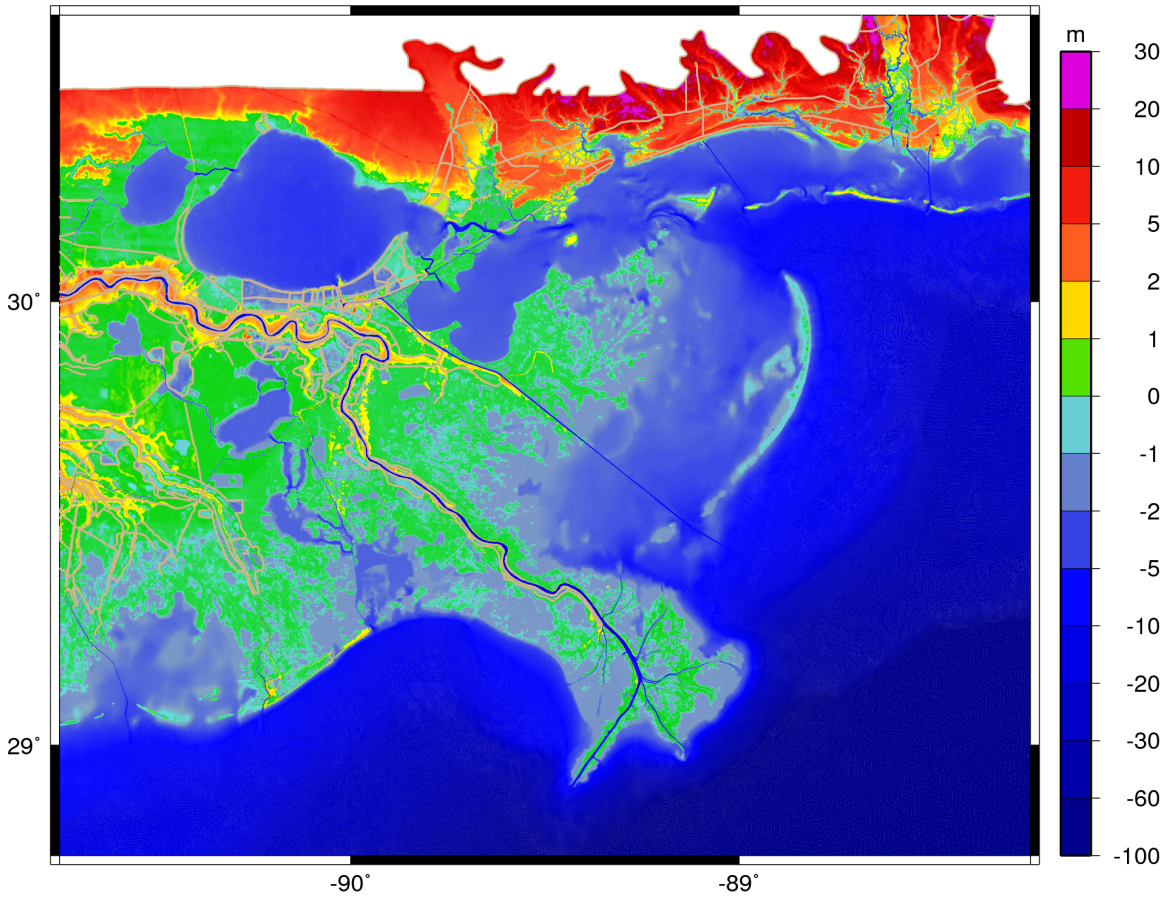

Figure 5.6. Bathymetry/topography (m) of the SL16 mesh in southeastern Louisiana.

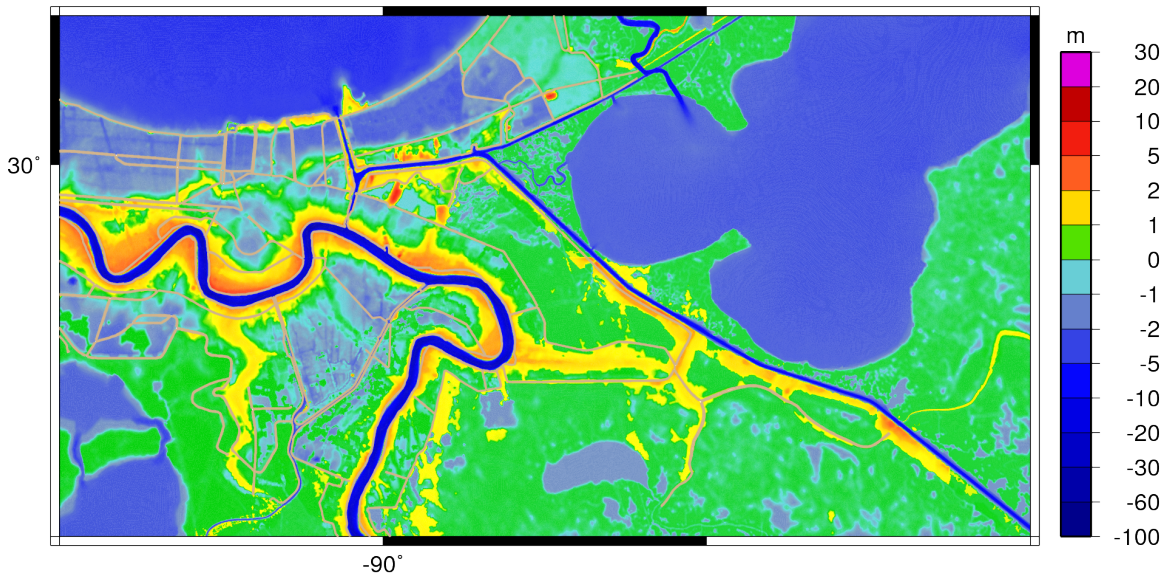

Figure 5.7. Bathymetry/topography (m) of the SL16 mesh near New Orleans.

such as the Mississippi River, Lakes Borgne and Pontchartrain, and the Rigolets and Chef Menteur passes, was applied from recent surveys by the USACE and NOAA. Topography in the marshes was specified based on the land cover databases described below, while topography farther inland was specified using LiDAR (`http://atlas.lsu.edu/lidar/`). These bathymetric/topographic data were applied via mesh-scale averaging to avoid irregularities or discontinuities in the SL16 mesh. Levee and road systems that are barriers to flood propagation are included, with geographical placement based on USACE surveys and heights from USACE or LiDAR; these levees are handled as lines of vertices or sub-mesh-scale weirs (Westerink *et al.*, 2008). Levee and road heights were established to reflect pre-Gustav conditions.

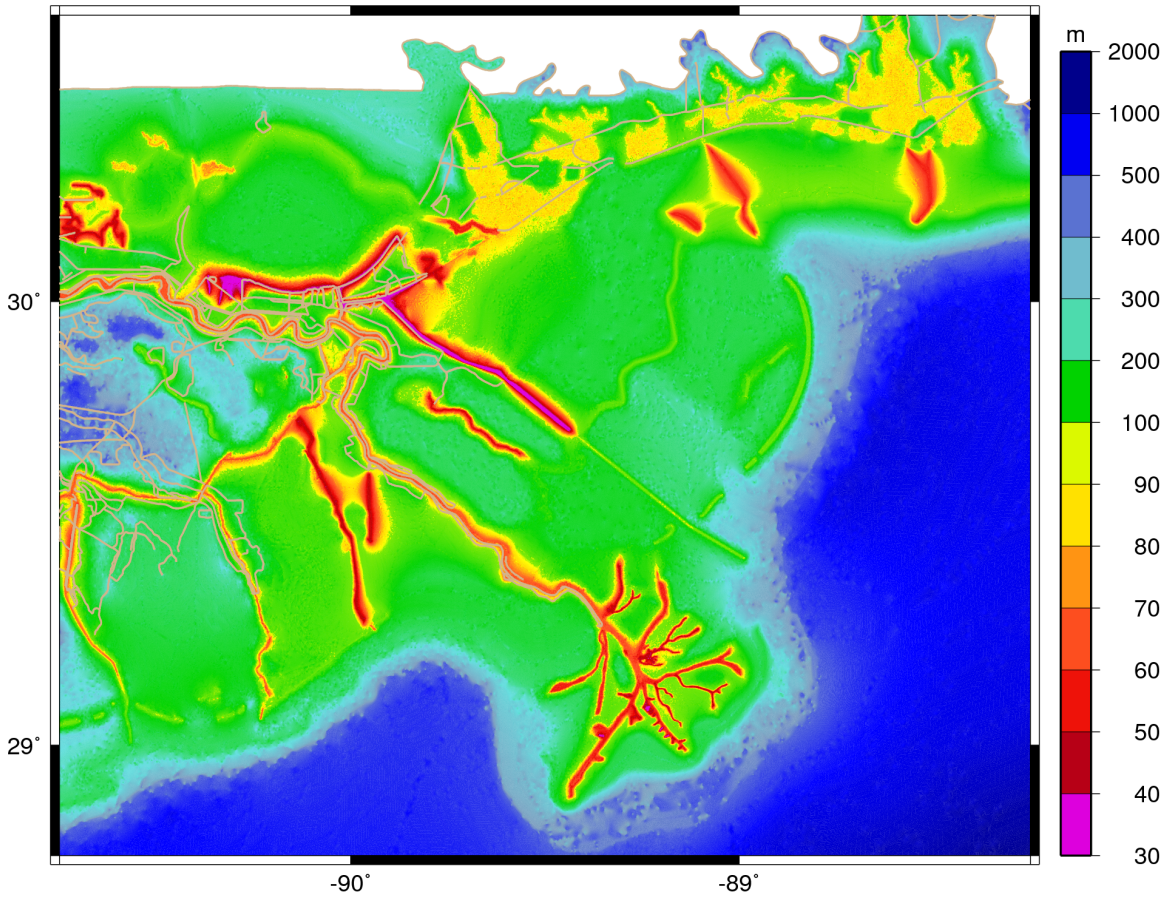

Figure 5.8. Mesh resolution (m) of the SL16 mesh in southeastern Louisiana.

5.3.4 Adjustments for Steric Expansion and Vertical Datum

Water levels are increased at the beginning of the ADCIRC simulation to account for the vertical datum and the intra-annual mean sea surface variability of the Gulf of Mexico. The computed water levels in ADCIRC are relative to local mean sea level, and they are adjusted to the North American Vertical Datum of 1988 updated to the 2004.65 epoch, NAVD88 (2004.65), by adding 0.134m (Bunya *et al.*, 2010). A further adjustment is required because of the intra-annual fluctuation in sea level due to the thermal expansion of the Gulf and other processes. Long-term NOAA stations at Dauphin Island, MS, and Grand Isle and Eugene Island, LA, indicate a steric increase of 0.086m in the averaged water levels in early September (`http://tidesandcurrents.noaa.gov/sltrends/sltrends.html`). Thus the combined increase in water levels for Gustav is 0.134m + 0.086m = 0.22m.

5.3.5 Integrally-Coupled Bottom Friction

Hydraulic friction is computed in ADCIRC using a Manning's n formulation (Figure 5.9), with spatially-variable values that are applied based on land-cover databases (Bunya *et al.*, 2010), specifically LA-GAP (`http://atlas.lsu.edu/rasterdown.htm`), MS-GAP (`http://www.basic.ncsu.edu/segap/index.html`) and C-CAP (`http://www.csc.noaa.gov/digitalcoast/data/ccapregional/`). These values are summarized in Tables 5.2 - 5.4. On the continental shelf in the Gulf of Mexico, the values have been set to $n = 0.022$ for sand/gravel bottoms, and $n = 0.012$ for muddy bottoms, such as the LA-MS continental shelf (Buczkowski *et al.*, 2006). These values also enable the currents and geostrophic set-up associated with the forerunner surge in Hurricane Ike (Kennedy *et al.*, 2010b).

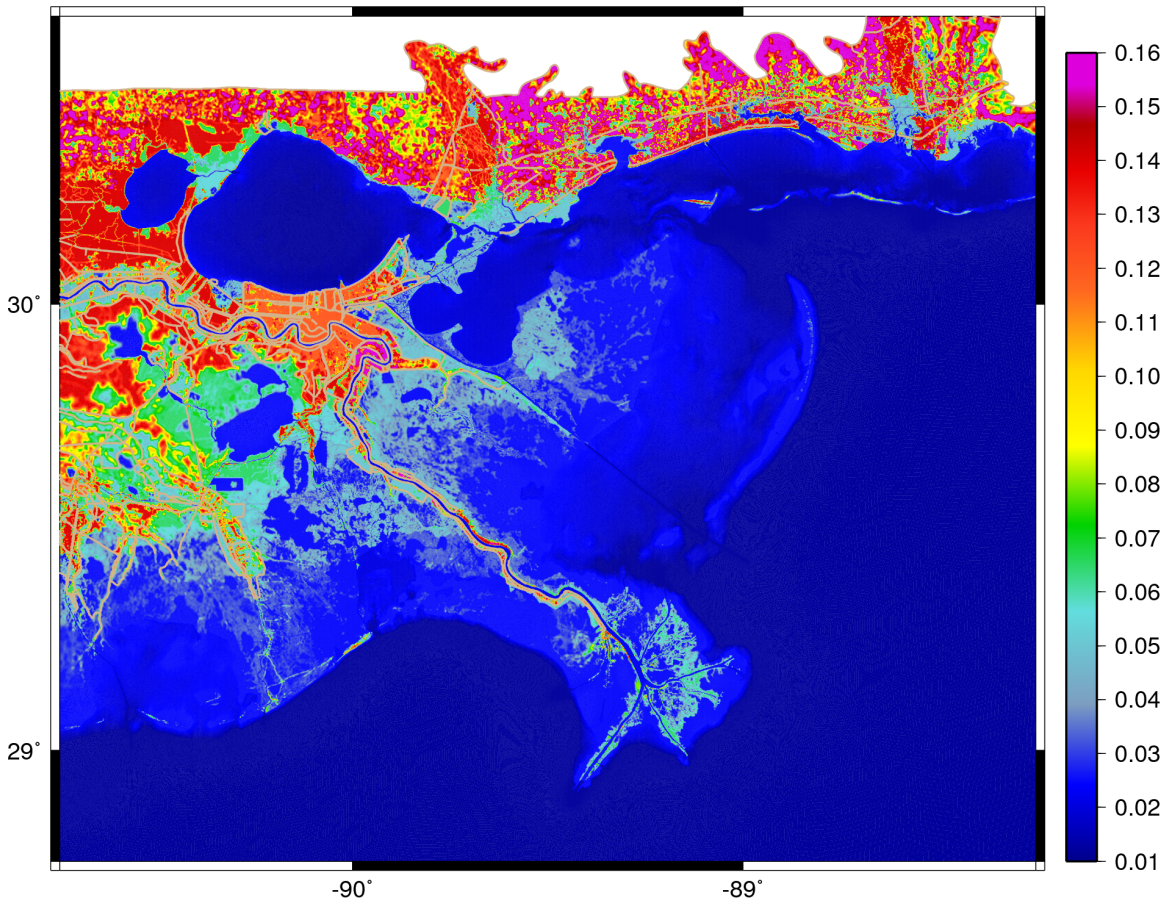

Figure 5.9. Manning's n values for the SL16 mesh in southeastern Louisiana.

TABLE 5.2

MANNING's n VALUES FOR LA-GAP CLASSIFICATION

LA-GAP Class	Description	Manning's n
1	Fresh marsh	0.065
2	Intermediate marsh	0.055
3	Brackish marsh	0.050
4	Saline marsh	0.035
5	Wetland forest deciduous	0.140
6	Wetland forest evergreen	0.160
7	Wetland forest mixed	0.150
8	Upland forest deciduous	0.160
9	Upland forest evergreen	0.180
10	Upland forest mixed	0.170
11	Dense pine thicket	0.180
12	Wetland scrub/shrub deciduous	0.065
13	Wetland scrub/shrub evergreen	0.080
14	Wetland scrub/shrub mixed	0.070
15	Upland scrub/shrub deciduous	0.075
16	Upland scrub/shrub evergreen	0.090
17	Upland scrub/shrub mixed	0.080
18	Agriculture/crops/grass	0.050
19	Vegetated urban	0.120
20	Non-vegetated urban	0.120

TABLE 5.2

Continued

LA-GAP Class	Description	Manning's n
21	Wetland barren	0.030
22	Upland barren	0.035
23	Water	0.025

TABLE 5.3

MANNING's n VALUES FOR MS-GAP CLASSIFICATION

MS-GAP Class	Description	Manning's n
1	Agriculture	0.050
2	Fresh water	0.025
3	Aquaculture	0.045
4	Estuarine water	0.025
6	Farmed wetlands	0.035
7	Estuarine emergent	0.050
8	Estuarine woody	0.140
9	Palustrine emergent	0.060
10	Bottomland hardwood	0.140
11	Riverine swamp	0.140

TABLE 5.3

Continued

MS-GAP Class	Description	Manning's n
12	Pine savannah	0.090
13	Fresh water shrub/scrub	0.075
14	Palustrine non-vegetated	0.035
15	Transportation	0.032
16	High density urban	0.150
24	Urban fresh water	0.025
25	Wet soil/water/shadow	0.040
26	Urban pine	0.180
27	Urban hardwood	0.160
28	Urban low herbaceous	0.070
29	Urban grassy/pasture	0.055
30	Bare urban I	0.120
31	Bare urban II	0.120
32	Clear cuts	0.036
50	Low density pine	0.160
51	Medium density pine	0.180
52	High density pine	0.200
53	Medium density hardwood	0.170
54	High density hardwood	0.170
55	Mixed forest	0.160

TABLE 5.3

Continued

MS-GAP Class	Description	Manning's n
56	Recent harvest	0.045
57	Cypress/tupelo	0.180
60	Agriculture	0.050
61	Grassy/pasture/range	0.050
62	Low herbaceous vegetation	0.050
63	Evergreen shrub	0.080
71	Wetland	0.050
80	Bare	0.035
81	Sand bar/beach	0.030

TABLE 5.4

MANNING's n VALUES FOR C-CAP CLASSIFICATION

C-CAP Class	Description	Manning's n
2	High intensity developed	0.120
3	Medium intensity developed	0.120
4	Low intensity developed	0.120
5	Developed open space	0.035

TABLE 5.4

Continued

C-CAP Class	Description	Manning's n
6	Cultivated land	0.100
7	Pasture/hay	0.050
8	Grassland	0.035
9	Deciduous forest	0.160
10	Evergreen forest	0.180
11	Mixed forest	0.170
12	Scrub/shrub	0.080
13	Palustrine forested wetland	0.150
14	Palustrine scrub/shrub wetland	0.075
15	Palustrine emergent wetland	0.060
16	Estuarine forested wetland	0.150
17	Estuarine scrub/shrub wetland	0.070
18	Estuarine emergent wetland	0.050
19	Unconsolidated shore	0.030
20	Bare land	0.030
21	Open water	0.025
22	Palustrine aquatic bed	0.035
23	Estuarine aquatic bed	0.030

STWAVE applies bottom friction based on the same Manning's n values used by ADCIRC (Smith, 2007), but with a minimum of $n \geq 0.03$. In addition, the integrated coupling of SWAN+ADCIRC allows for friction to be adjusted during the simulation, based on the computed solution of the model components. This hindcast utilizes the formulation of Madsen *et al.* (1988), who employ a roughness length z_0, which is expressed in terms of the water depth H and the Manning's n:

$$z_0 = H \exp\left[-\left(1 + \frac{\kappa H^{1/6}}{n\sqrt{g}}\right)\right], \tag{5.1}$$

where $\kappa = 0.4$ is the von Karman constant, and g is the gravitational acceleration (Bretschneider *et al.*, 1986). New roughness lengths are computed at each SWAN time step, based on the computed ADCIRC water depth and Manning's n value at each mesh vertex. The Manning's n values are raised to $n \geq 0.03$ to prevent the use of unrealistically small roughness lengths in SWAN; the values remain unchanged for ADCIRC.

5.3.6 Riverine Inflows

River inflows are specified for the Mississippi and Atchafalaya Rivers at Baton Rouge and Simmesport, LA, respectively, using a wave radiation boundary condition (Bunya *et al.*, 2010). A steady flow boundary condition is applied during a 0.5 day hyperbolic ramp, and then the river is allowed to reach equilibrium over the next 3.5 days. After four days of simulation, the boundary condition is switched to a wave radiation condition, and tide, wind, pressure and wind wave forcings are applied. River flow rates were determined from the New Orleans District of the US Army Corps of Engineers (`http://www.mvn.usace.army.mil`), and were applied as 8,920 $\mathrm{m^3\ s^{-1}}$ and 3,823 $\mathrm{m^3\ s^{-1}}$ for the respective rivers.

5.4 Measured Time Series and High-Water Marks

Gustav is characterized by measurement data that describe how the storm evolved as it traversed the Gulf and made landfall in southeast Louisiana. More permanent gages survived Gustav than Katrina, partly due to efforts to harden the gages and increase their reliability. Additional gages were deployed before landfall, in regions such as the marshes and nearshore that have been under-represented. These data offer valuable descriptions of the hurricane behavior in those regions, and they are excellent validation tests for WAM, STWAVE, SWAN and ADCIRC.

5.4.1 NDBC Waves

The NDBC operates discus buoys throughout the Gulf; they have diameters that range from 3m nearshore to 10-12m in the deeper Gulf. They measure heave acceleration or vertical displacement, which are processed both on the buoy and then onshore to derive spectral wave energies, which are integrated to derive wave properties such as significant height, peak and mean period, and mean direction (`http://www.ndbc.noaa.gov/`). These measured wave properties are compared to modeled results from WAM, STWAVE and SWAN at 12 NDBC buoys within the Gulf.

5.4.2 CSI Waves and Water Levels

The CSI at Louisiana State University operates stations along the continental shelf offshore of Louisiana. Each station utilizes a digiquartz pressure transducer and a March-McBirney current meter at depths of 1-2m below mean sea level, and these measurements are processed to derive water depths and directional wave spectra (WAVCIS, `http://www.wavcis.lsu.edu/`). The measured signifi-

cant wave heights, peak periods and water levels are compared to modeled results from STWAVE, SWAN and ADCIRC at five stations located along the south-central Louisiana coast between the Vermilion and Barataria Bays. The water depths are converted to water levels by subtracting the mean depth at each station and accounting for the steric expansion and datum adjustment to NAVD88 (2004.65).

5.4.3 AK Waves and Water Levels

The AK gages measured waves and water levels using bottom-mounted pressure sensors recording continuously at 1Hz (Kennedy *et al.*, 2010a). These gages were deployed over two days pre-landfall using helicopters, and were retrieved using boats and divers post-storm. Measured absolute pressures were converted to water depths using records of atmospheric pressure. Surge elevations were then computed as the low-pass filtered water levels, while significant wave heights were computed using standard spectral methods, corrected using computed depth-averaged currents. The measured significant wave heights, peak periods, and water levels are compared to modeled results from STWAVE, SWAN and ADCIRC at 16 gages located along the coastline from Calcasieu Pass in the west to Pensacola Bay in the east.

5.4.4 CHL Waves and Water Levels

CHL deployed three bottom-mounted pressure gauges in Biloxi Marsh and three in Terrebonne Marsh in depths of 0.5-1.2m. The gages were YSI 600XLM pressure gages, and they were sampled hourly at 2Hz. Analysis of the inner marsh gages resulted in peak periods around 2s (0.5Hz) at the peak of the storm, which

was near the high-frequency cut-off for the spectral analysis. This can result from amplification of noise and either over- or under-estimate wave height and under-estimate of wave period.

5.4.5 NOAA Water Levels

NOAA operates tide measurement stations along the coastline of the United States (`http://www.tidesandcurrents.noaa.gov/`). The measured water levels are compared to modeled results from ADCIRC at 12 selected stations along the coastline from the Florida Keys to Vermilion Bay. At those NOAA stations in southern Louisiana where the water levels were not available relative to NAVD88 (2004.65), the data is relative to MLLW, but the difference is on the order of cm.

5.4.6 USACE Water Levels

The USACE operates pressure gages throughout southern Louisiana, and a total of 45 gages produced time series of water levels during part or all of Gustav. These data were obtained from the New Orleans District (USACE-MVN), and these water levels are relative to NAVD88 (2004.65). The measured water levels are compared to modeled results from ADCIRC at 18 selected stations in southeast Louisiana. These stations were selected because of the completeness of their record, the importance of their location, and/or their contribution to the description of the storm surge during Gustav.

5.4.7 USGS Water Levels

The USGS operates pressure gages throughout southern Louisiana, and a total of 44 gages produced time series of water levels during Gustav (Walters, 2009).

Most of the gages provide water levels relative to NAVD88 (2004.65), but a few gages near the Terrebonne and Barataria Bays were reported relative to NGVD29. The measured water levels are compared to modeled results from ADCIRC at nine selected stations in southeast Louisiana. In addition, the USGS deployed 42 pressure gages during Gustav that also produced time series of water levels during all or part of Gustav (Walters, 2009). These measured water levels are all relative to NAVD88 (2004.65), and they are compared to modeled results from ADCIRC at six selected gages near New Orleans. These subsets of permanent stations and deployable gages were selected because of the completeness of their record, the importance of their location, and/or their contribution to the description of the storm surge during Gustav.

5.4.8 CRMS High-Water Marks

The Coastwide Reference Monitoring System (CRMS, `http://www.lacoast.gov/crms2/home.aspx`) is a joint effort by federal and Louisiana state agencies to collect data about water quality. The gages provide water levels relative to NAVD88 (2004.65). The data set was trimmed to 238 gages by removing gages whose records were incomplete or otherwise were limited near the peak of the storm, and also the gages with obvious datum inconsistencies. The peak hydrograph values at the 238 gages are compared to modeled results from ADCIRC.

5.4.9 FEMA High-Water Marks

Finally, FEMA measured HWMs relative to NAVD88 (2004.65) throughout southern Louisiana. These HWMs were collected in mid-November 2008, more than two months after Gustav made landfall, and thus they contain contributions

from Hurricane Ike as well. The measured HWMs are compared to the modeled results from ADCIRC at 82 selected locations in southeast Louisiana. These marks were selected because they are still-water measurements without the effects of wave action or run-up, and their quality was listed as excellent. In addition, they are located east of Gustav's track and judged to not contain contributions from Ike, by comparing to hydrographs from the sources listed above.

5.5 Synoptic History and Validation of Gustav

The following sections describe the evolution of Gustav's winds (Figure 5.10), waves (Figures 5.11 - 5.12), and circulation (Figures 5.13 - 5.14) in southeast Louisiana. Although station time series of wave parameters are shown from WAM, STWAVE and SWAN, the water levels shown are produced via the coupling of SWAN+ADCIRC. Geographical locations referenced in the text are summarized in Table 5.1 and shown in Figure 5.1.

5.5.1 Evolution of Winds

Gustav tracked through the Caribbean Sea (Figure 5.5) and strengthened to a Category 4 storm on the Saffir-Simpson scale, with maximum 10min-averaged wind speeds of 70 m s^{-1} (Beven and Kimberlain, 2009). After passing over western Cuba and into the Gulf, Gustav weakened to Category 3 and maintained this intensity until dropping to Category 2 approximately 10hr before landfall, and then continued to weaken as it progressed northwestward to Category 1 at landfall in Terrebone Bay in southern Louisiana. This behavior is in contrast to Katrina and Rita, which reached their peak intensities in the Gulf.

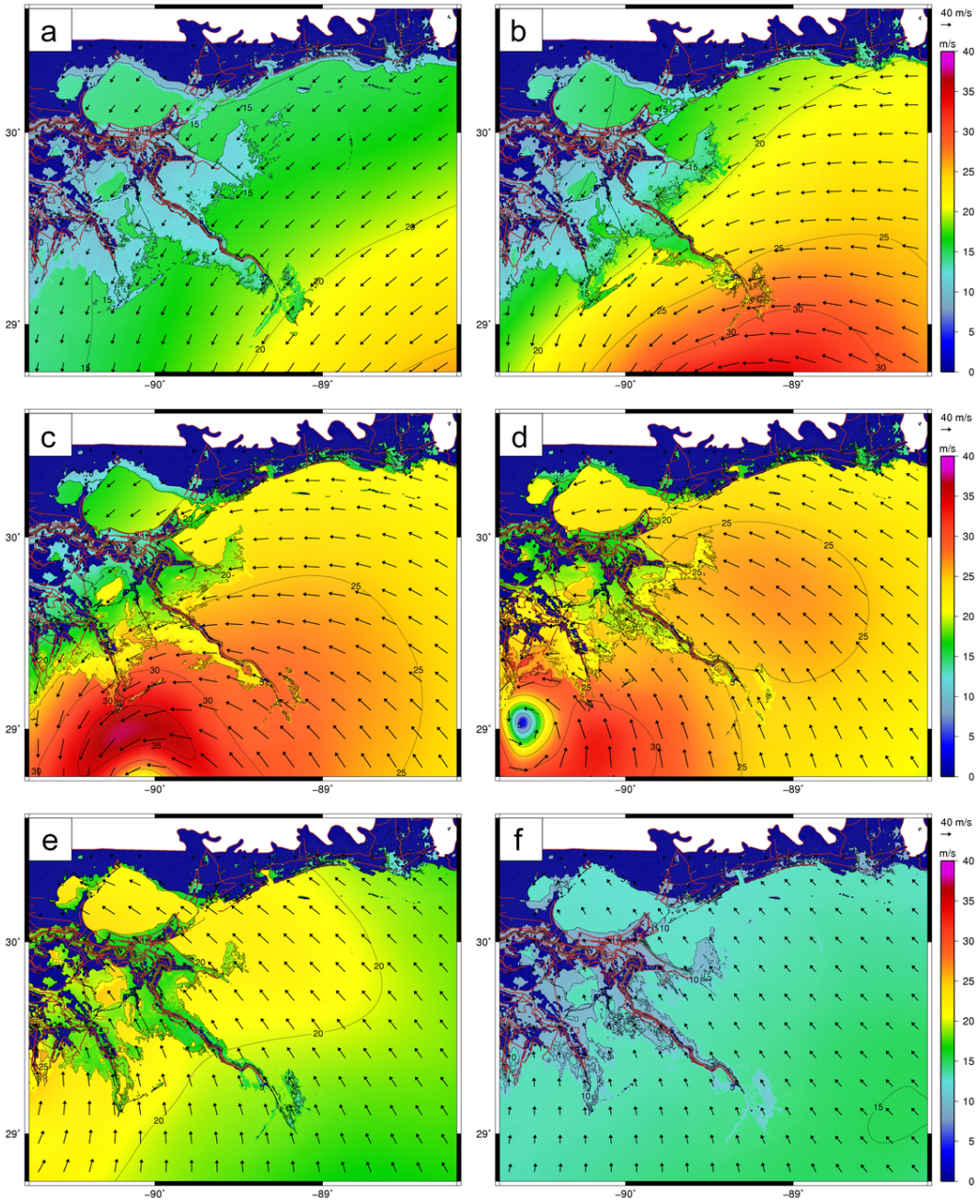

Figure 5.10. Wind speeds (m s^{-1}) in southern Louisiana during Hurricane Gustav. The panels correspond to the following times: (a) 0200 UTC 01 September 2008, (b) 0800 UTC 01 September 2008, (c) 1100 UTC 01 September 2008, (d) 1400 UTC 01 September 2008, (e) 1700 UTC 01 September 2008, (f) 0200 UTC 02 September 2008.

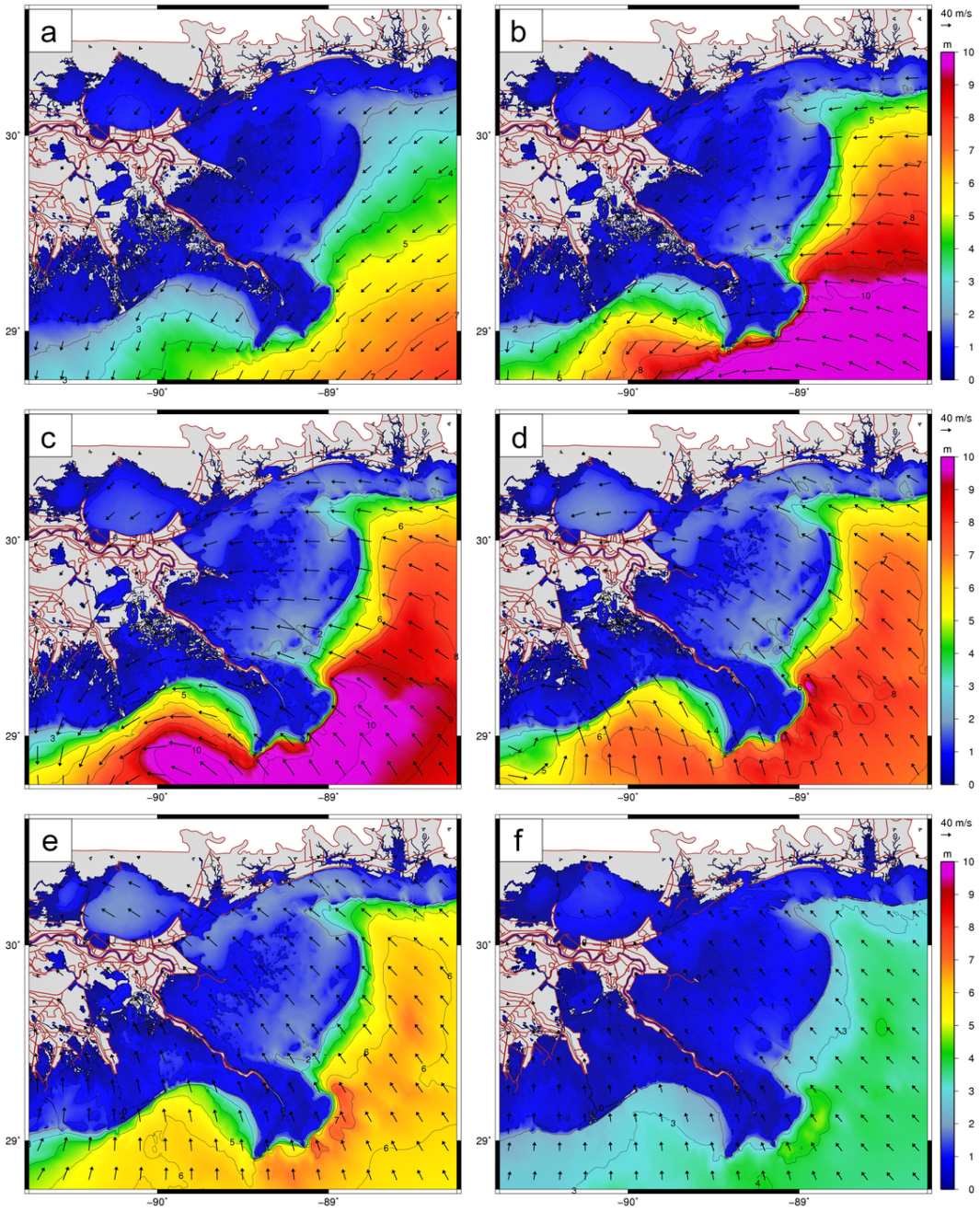

Figure 5.11. Contours of SWAN significant wave heights (m) and vectors of wind speeds (m s^{-1}) in southern Louisiana during Hurricane Gustav. The panels correspond to the following times: (a) 0200 UTC 01 September 2008, (b) 0800 UTC 01 September 2008, (c) 1100 UTC 01 September 2008, (d) 1400 UTC 01 September 2008, (e) 1700 UTC 01 September 2008, (f) 0200 UTC 02 September 2008.

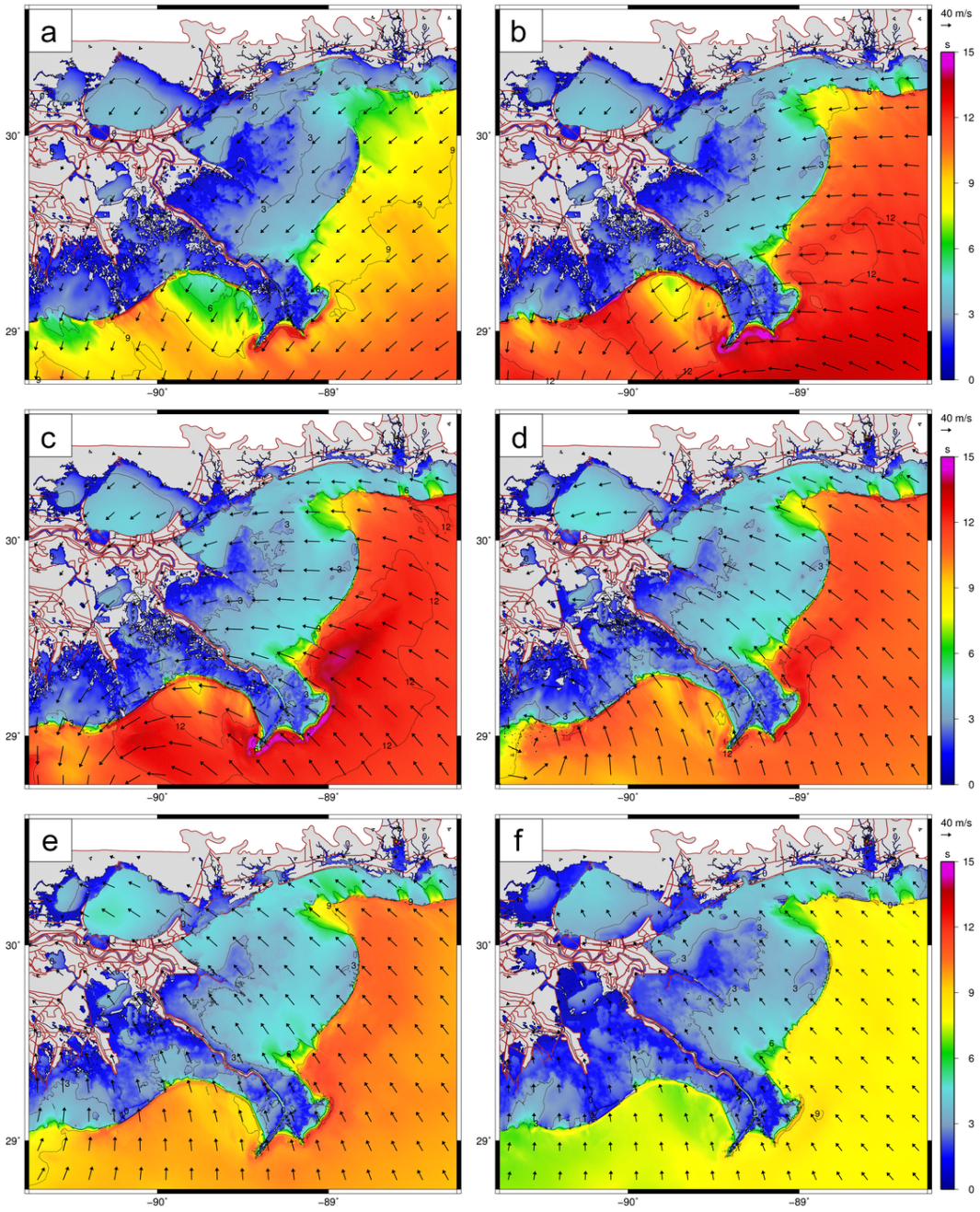

Figure 5.12. Contours of SWAN mean wave periods (s) and vectors of wind speeds (m s^{-1}) in southern Louisiana during Hurricane Gustav. The panels correspond to the following times: (a) 0200 UTC 01 September 2008, (b) 0800 UTC 01 September 2008, (c) 1100 UTC 01 September 2008, (d) 1400 UTC 01 September 2008, (e) 1700 UTC 01 September 2008, (f) 0200 UTC 02 September 2008.

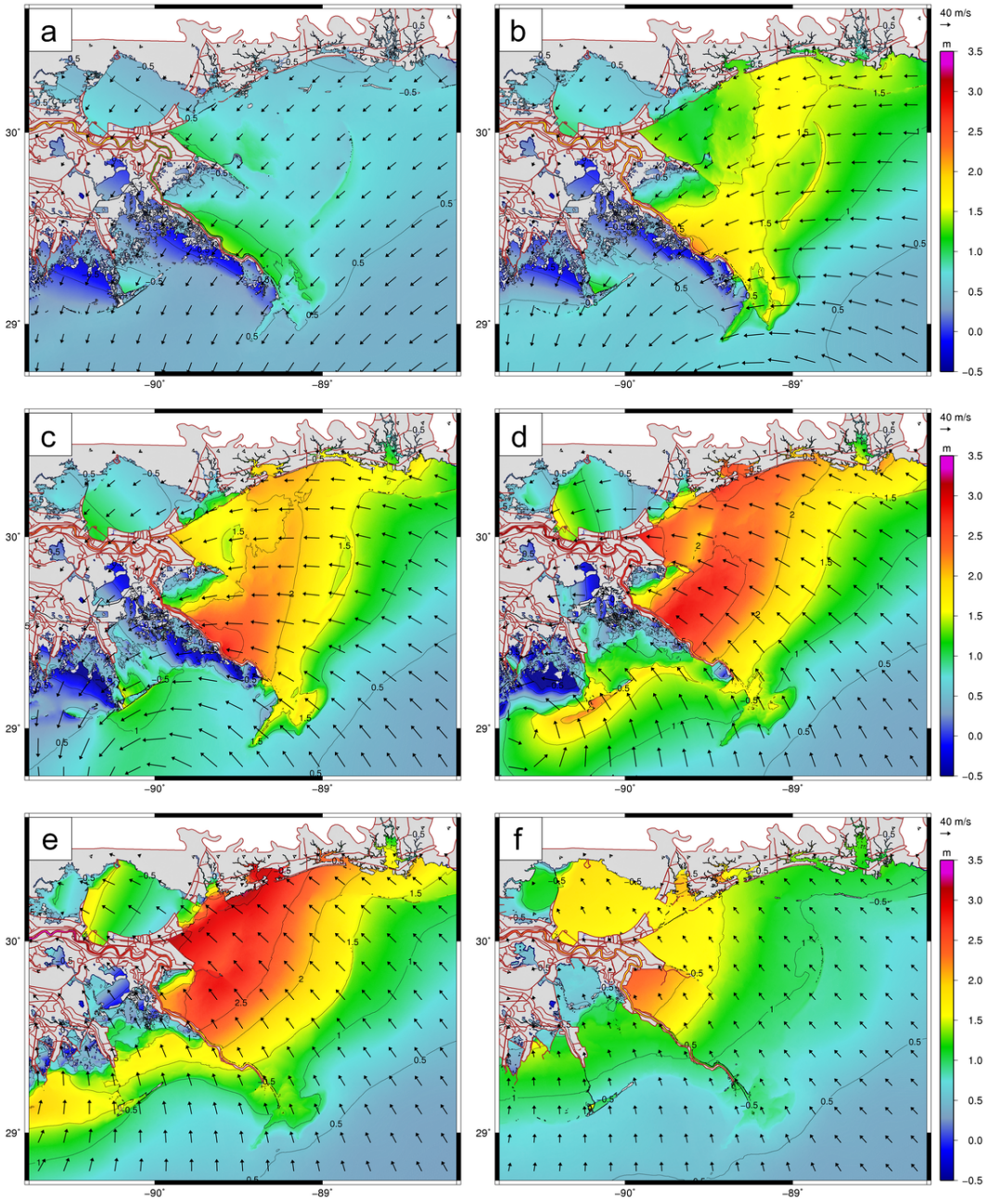

Figure 5.13. Contours of ADCIRC water levels (m) and vectors of wind speeds (m s^{-1}) in southern Louisiana during Hurricane Gustav. The panels correspond to the following times: (a) 0200 UTC 01 September 2008, (b) 0800 UTC 01 September 2008, (c) 1100 UTC 01 September 2008, (d) 1400 UTC 01 September 2008, (e) 1700 UTC 01 September 2008, (f) 0200 UTC 02 September 2008.

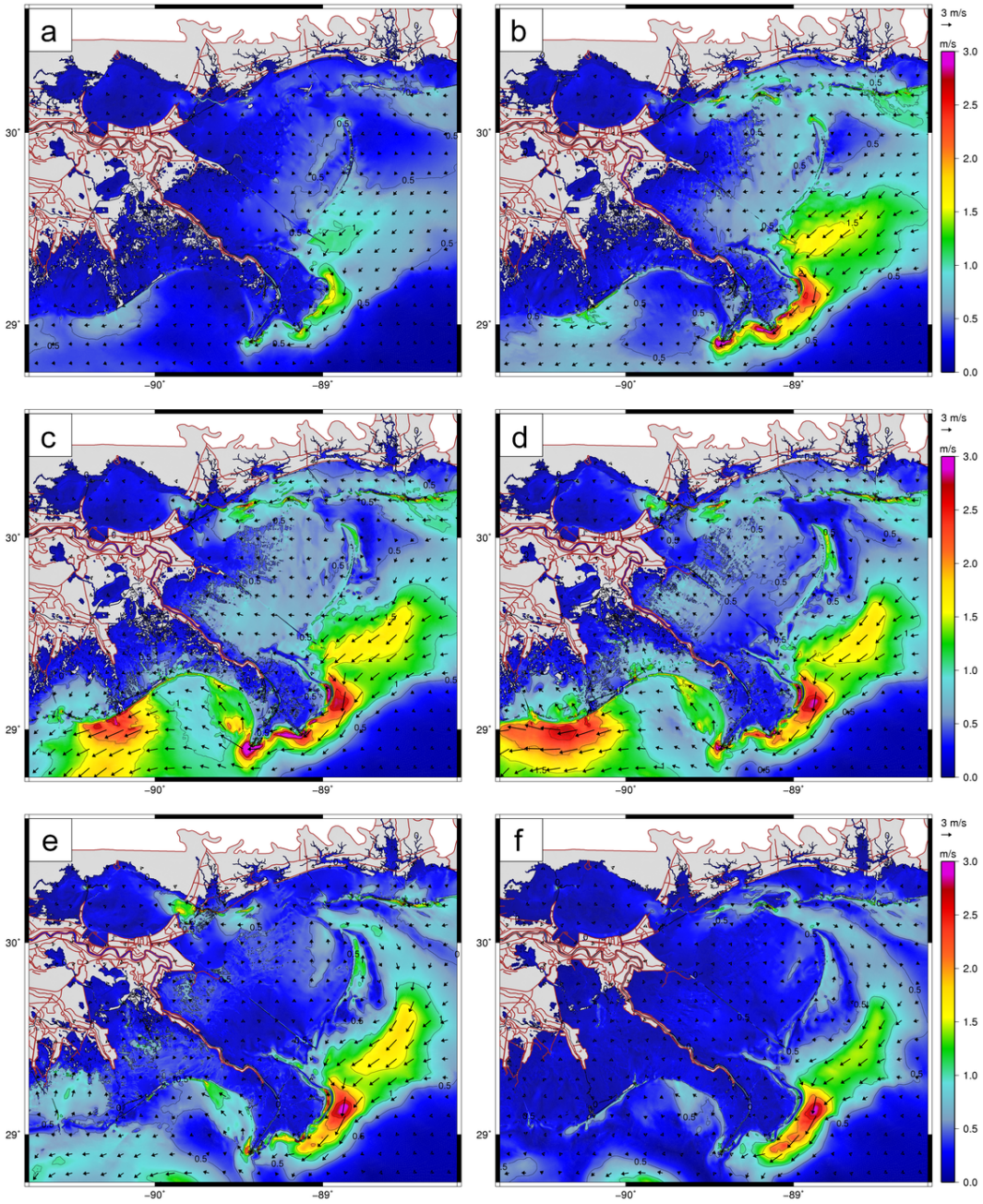

Figure 5.14. Contours and vectors of ADCIRC currents (m s^{-1}) in southern Louisiana during Hurricane Gustav. The panels correspond to the following times: (a) 0200 UTC 01 September 2008, (b) 0800 UTC 01 September 2008, (c) 1100 UTC 01 September 2008, (d) 1400 UTC 01 September 2008, (e) 1700 UTC 01 September 2008, (f) 0200 UTC 02 September 2008.

However, Gustav's outer extent of tropical-storm-strength winds was large enough to produce integrated kinetic energy values over 40 TJ, rating Gustav as a Category 3 on the Surge Destructive Potential Scale at landfall (Powell and Reinhold, 2007). Tropical-storm-strength winds reached the bird's foot of the Mississippi River delta approximately 12hr before landfall (Figure 5.10a) and enveloped large portions of southern Louisiana and the LA-MS continental shelf by 6hr before landfall (Figure 5.10b). Predominantly easterly coastal winds were relatively constant strength for 12-15hr as the storm moved through the region. On the shallow shelf, winds created local waves and surge, which were then pushed across the sounds and against the levee protection system. These winds also pushed surge into Lake Pontchartrain.

As Gustav neared landfall, its strongest winds were 30-35 m s^{-1}, and they were limited to the narrow shelf to the southwest of the Mississippi River (Figure 5.10c-d). Barataria and Terrebonne Bays experienced the worst of the hurricane winds as it made landfall. However, by this late stage, the winds shifted quickly to onshore, and then continued onshore for several hours after landfall (Figure 5.10e), aligning with the lake/marsh system connecting northward from Barataria Bay to the west bank of New Orleans.

Winds continued northwestward for more than 12hr after landfall (Figure 5.10f). Although decreased in strength, the direction caused the winds to slow the recession of surge back into the deeper Gulf. The wind held the surge in Lake Pontchartrain, and it assisted the surge propagation over the Caernarvon Marsh to the east of the river and over the marshes to the south and west of New Orleans.

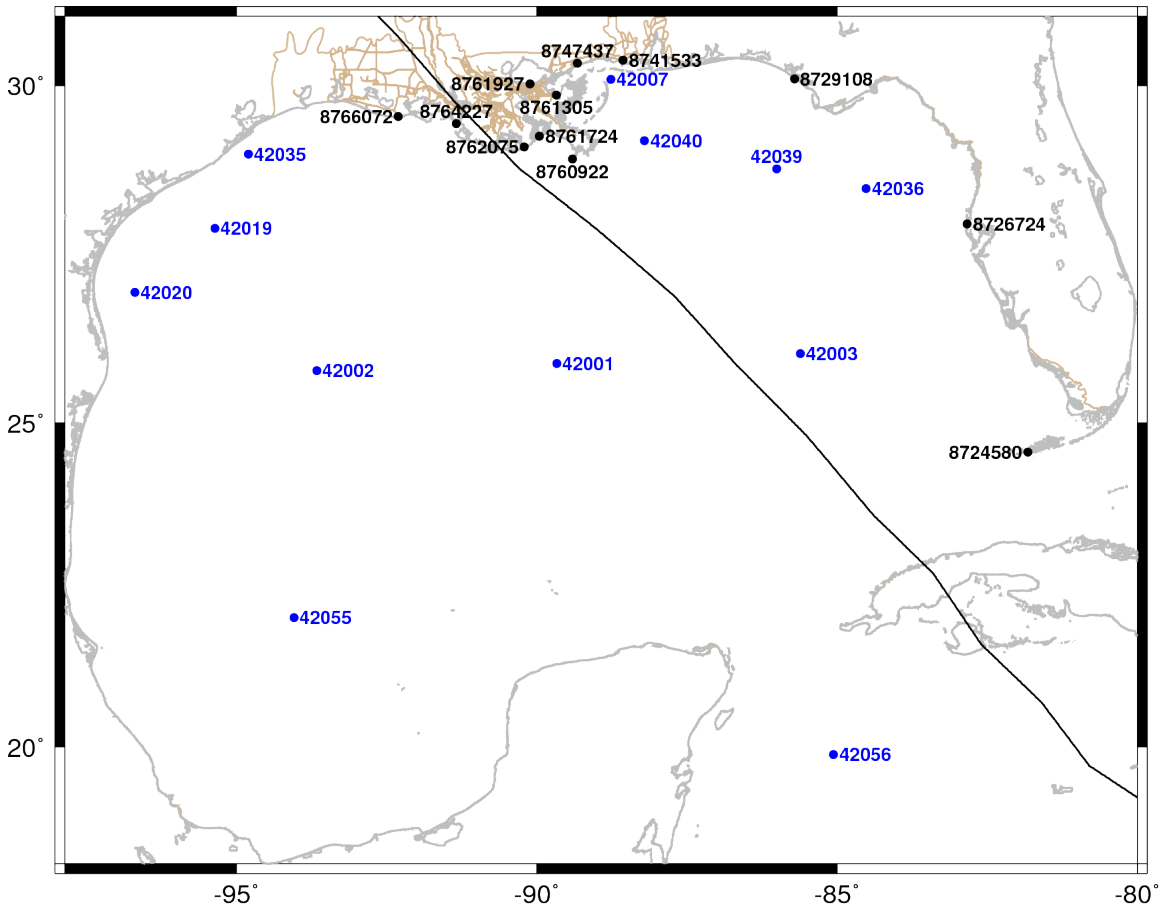

Figure 5.15. Locations of selected NDBC buoys (blue points) and NOAA stations (black points) in the Gulf of Mexico. The Gustav track is shown in black, the coastline and water bodies are shown in gray, and the boundaries of the SL16 mesh are shown in brown.

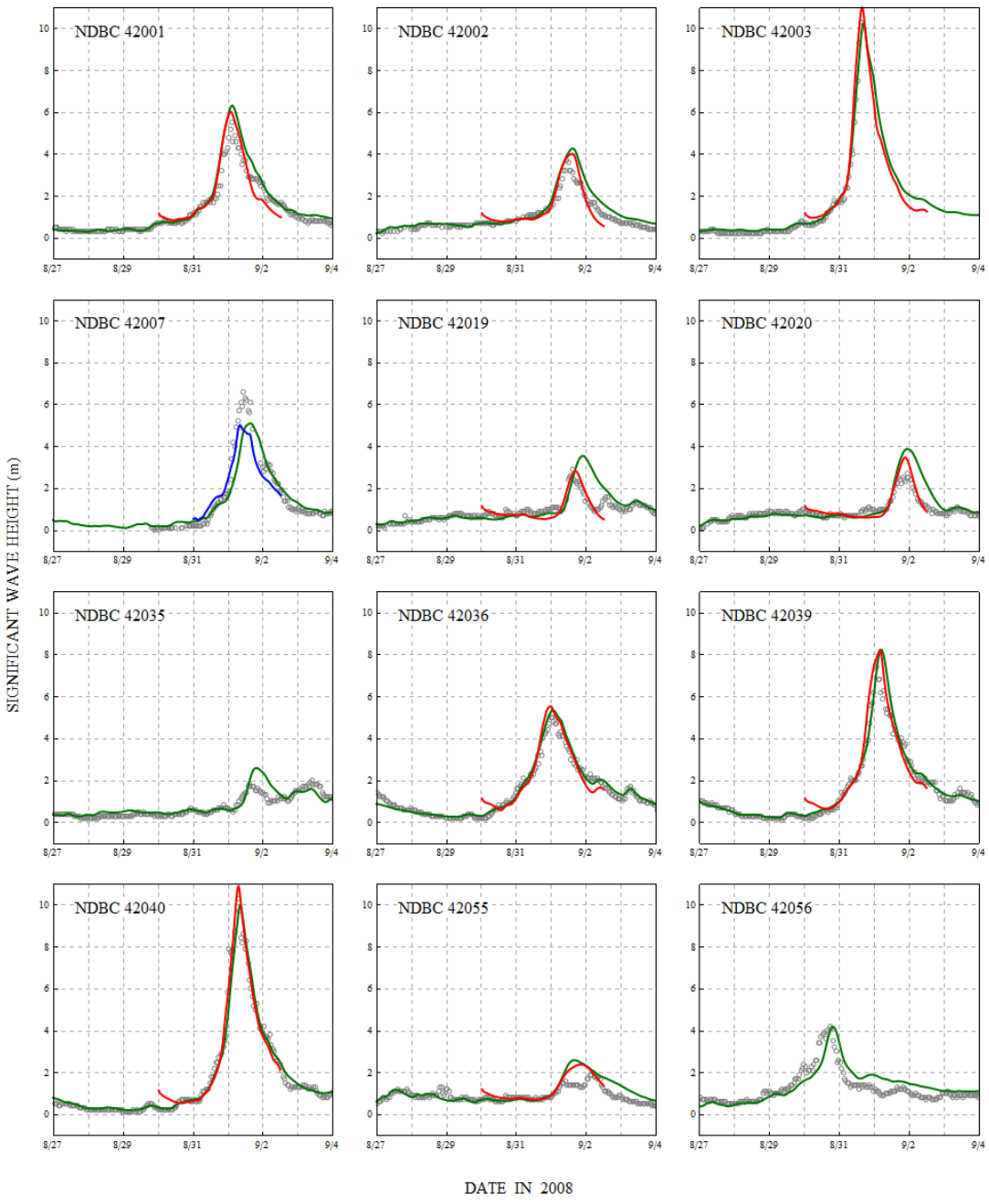

Figure 5.16. Time series of significant wave heights (m) at the 12 NDBC buoys shown in Figure 5.15. Measured NDBC values are shown with gray circles, while modeled results from SWAN (green), WAM (red) and STWAVE (blue) are shown with solid lines. Buoy 42003 stopped recording as the storm passed.

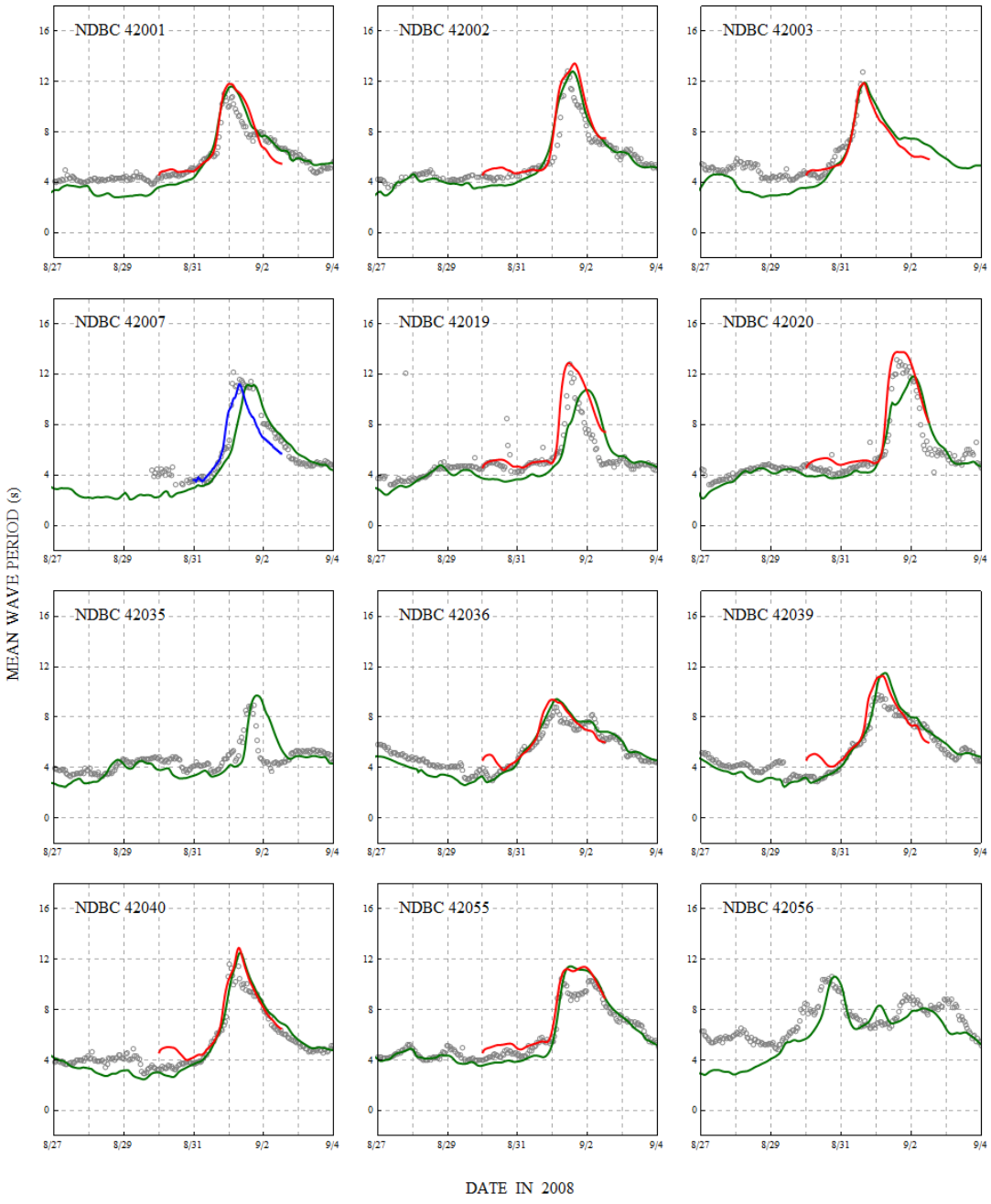

Figure 5.17. Time series of mean periods (s) at the 12 NDBC buoys shown in Figure 5.15. Measured NDBC values are shown with gray circles, while modeled results from SWAN (green), WAM (red) and STWAVE (blue) are shown with solid lines. Buoy 42003 stopped recording as the storm passed.

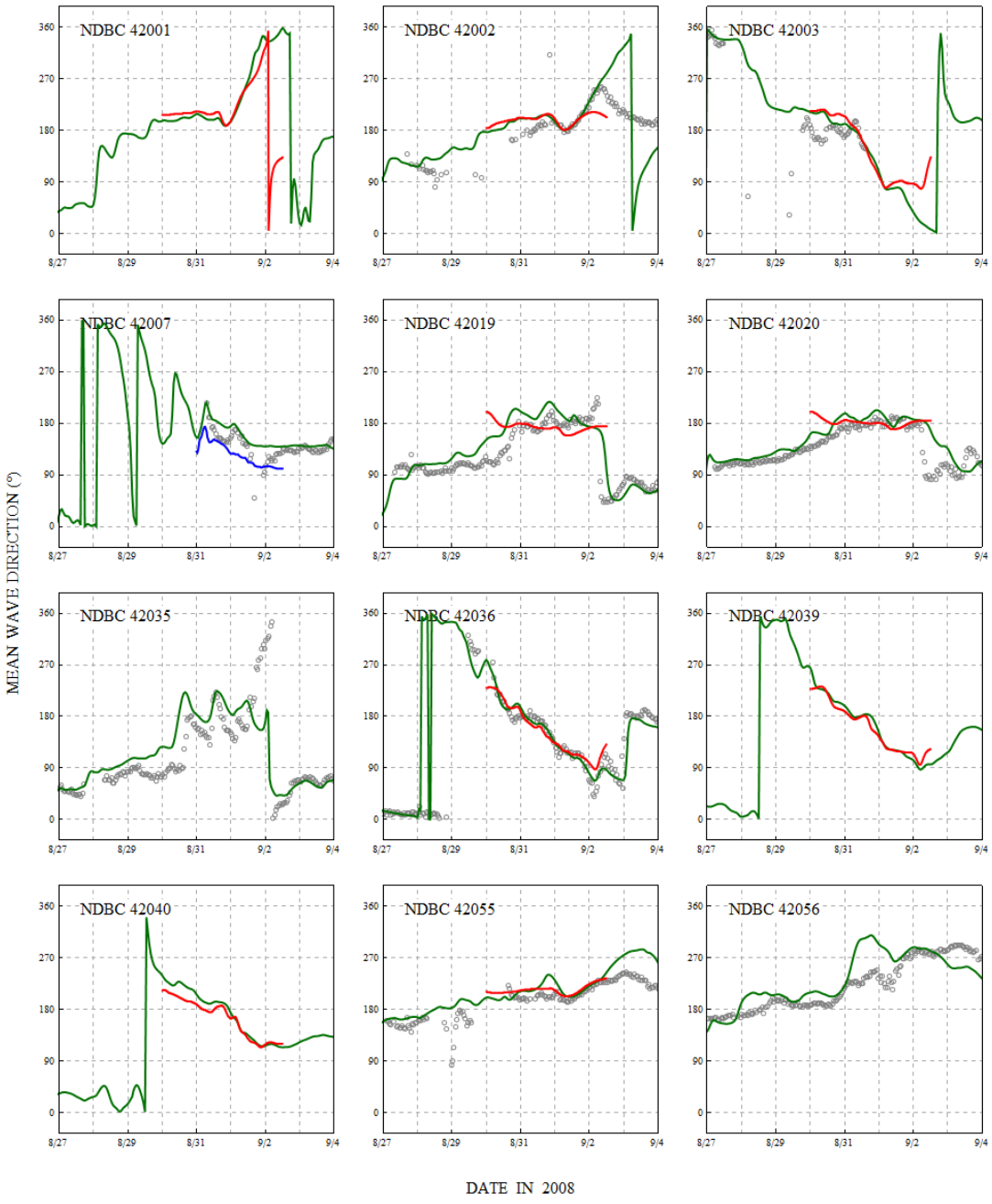

Figure 5.18. Time series of mean directions (°) at the 12 NDBC buoys shown in Figure 5.15. Measured NDBC values are shown with gray circles, while modeled results from SWAN (green), WAM (red) and STWAVE (blue) are shown with solid lines. Buoy 42003 stopped recording as the storm passed.

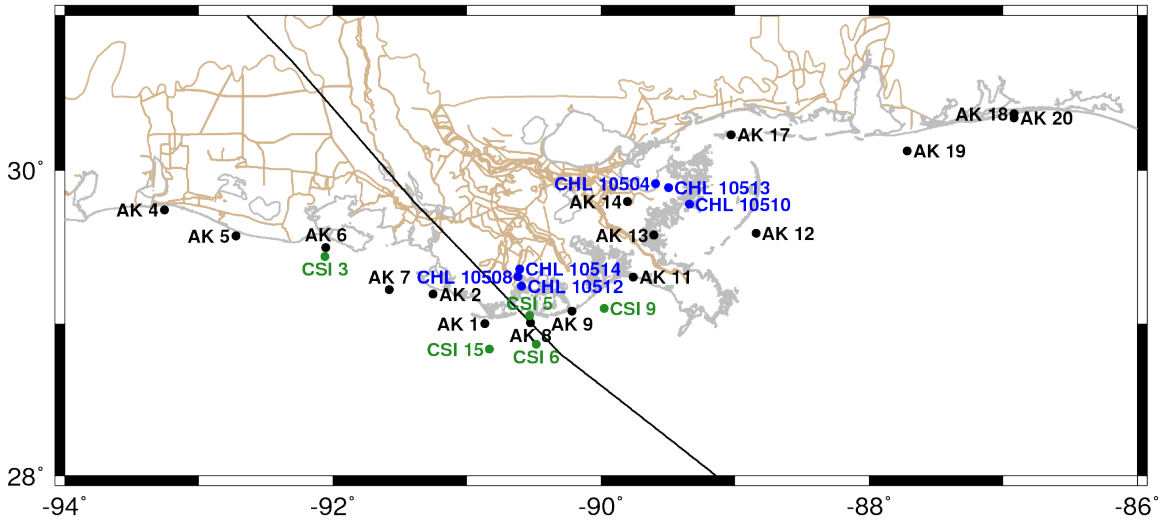

Figure 5.19. Locations of the nearshore AK gages (black points), CHL gages (blue points) and CSI stations (green points) in the northern Gulf of Mexico. The Gustav track is shown in black, the coastline and water bodies are shown in gray, and the boundaries of the SL16 mesh are shown in brown.

5.5.2 Evolution of Waves

Gustav generated waves with significant heights of 12-15m in deep water in the northeast quadrant of the storm, where the winds were strongest. These waves propagated as swell in all directions, but were largest to the east of the track. NDBC buoys 42036, 42039 and 42040 are located in the northeastern Gulf between Tampa Bay and the Mississippi River delta (Figure 5.15), and their measured significant heights increased at the peak of the storm. At buoy 42040, the largest significant wave heights exceeded 10m (Figure 5.16). To the west of the track, wave heights decreased with distance from the track, with peak waves of 6m at NDBC buoy 42001 decreasing to 3m at buoys 42019 and 42020 nearer to Texas (SiadatMousavi *et al.*, 2009). The mean wave periods also increased as the swell propagated outward from its generation near the eye (Figure 5.17), and the

mean wave directions changed dramatically after the storm moved past the buoys (Figure 5.18). In all of these validation plots, note the good agreement between the measured data and the computed results of WAM and SWAN.

The waves also propagated northward, where they moved onto the LA-MS continental shelf and dissipated due to changes in bathymetry and bottom friction. The largest and longest waves reached the Mississippi River delta 3-6hr before landfall (Figure 5.11b-c and Figure 5.12b-c). These waves had significant heights of 10-12m and mean periods of 12-15s, and they dissipated quickly due to the steep, narrow shelf near the delta. As the storm approached landfall, its local hurricane-strength winds created large waves offshore of the Barataria and Terrebonne Bays (Figure 5.11c-d and Figure 5.12c-d). At CSI stations 6, 9 and 15 located in 18-20m of water depth (Figure 5.19), the measured significant heights at the peak of the storm were 7m (Figure 5.20), and the peak periods were 12-15s (Figure 5.21). The waves began to dissipate due to depth-limited breaking before reaching these stations and gages closer to shore. At CSI station 5 and at the AK gages 1, 8 and 9 located outside of Terrebonne Bay in 7-10m of water depth, the peak wave heights decreased to 3-5m. At AK gage 11 farther east near Barataria Bay and in 3.5m of water depth, the peak significant heights were 1-2m, and the peak periods were 16s. Dissipation of the swell and local wind-sea waves is captured by the measured time series and matched well by STWAVE and SWAN.

To the east of the Mississippi River, tropical-storm-strength winds pushed waves onto the LA-MS continental shelf (Figure 5.11c-d and Figure 5.12c-d). At NDBC buoy 42007 and AK gage 12 located outside the Chandeleur Islands, peak waves were 6m, and they decreased farther east near Mobile and Pensacola Bays to 4m at AK gages 18, 19 and 20 (Figure 5.19 - 5.20). Wave heights decreased

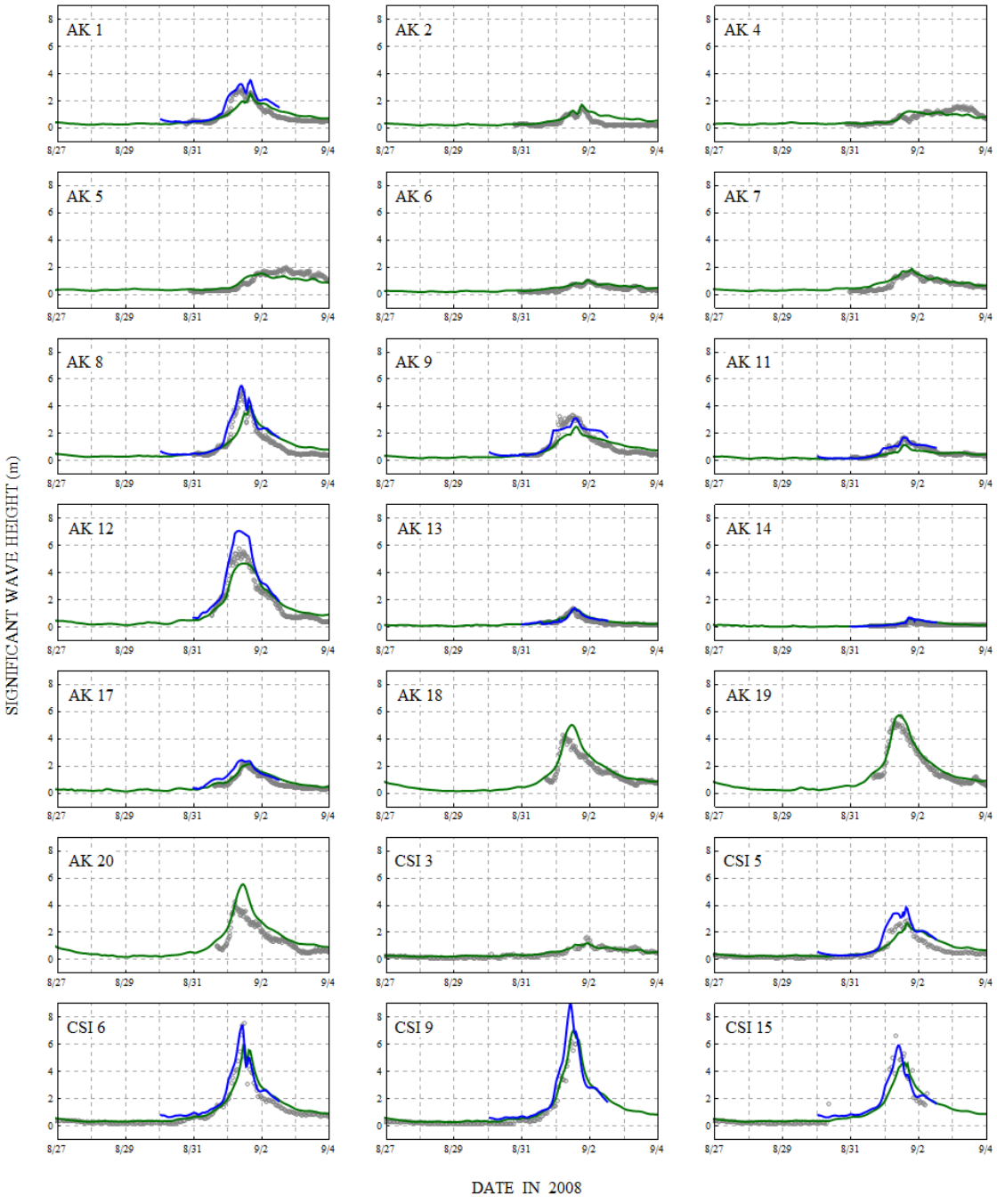

Figure 5.20. Time series of significant wave heights (m) at the 16 AK gages and five CSI gages shown in Figure 5.19. Measured values are shown with gray circles, modeled results from SWAN (green) and STWAVE (blue) are shown with solid lines.

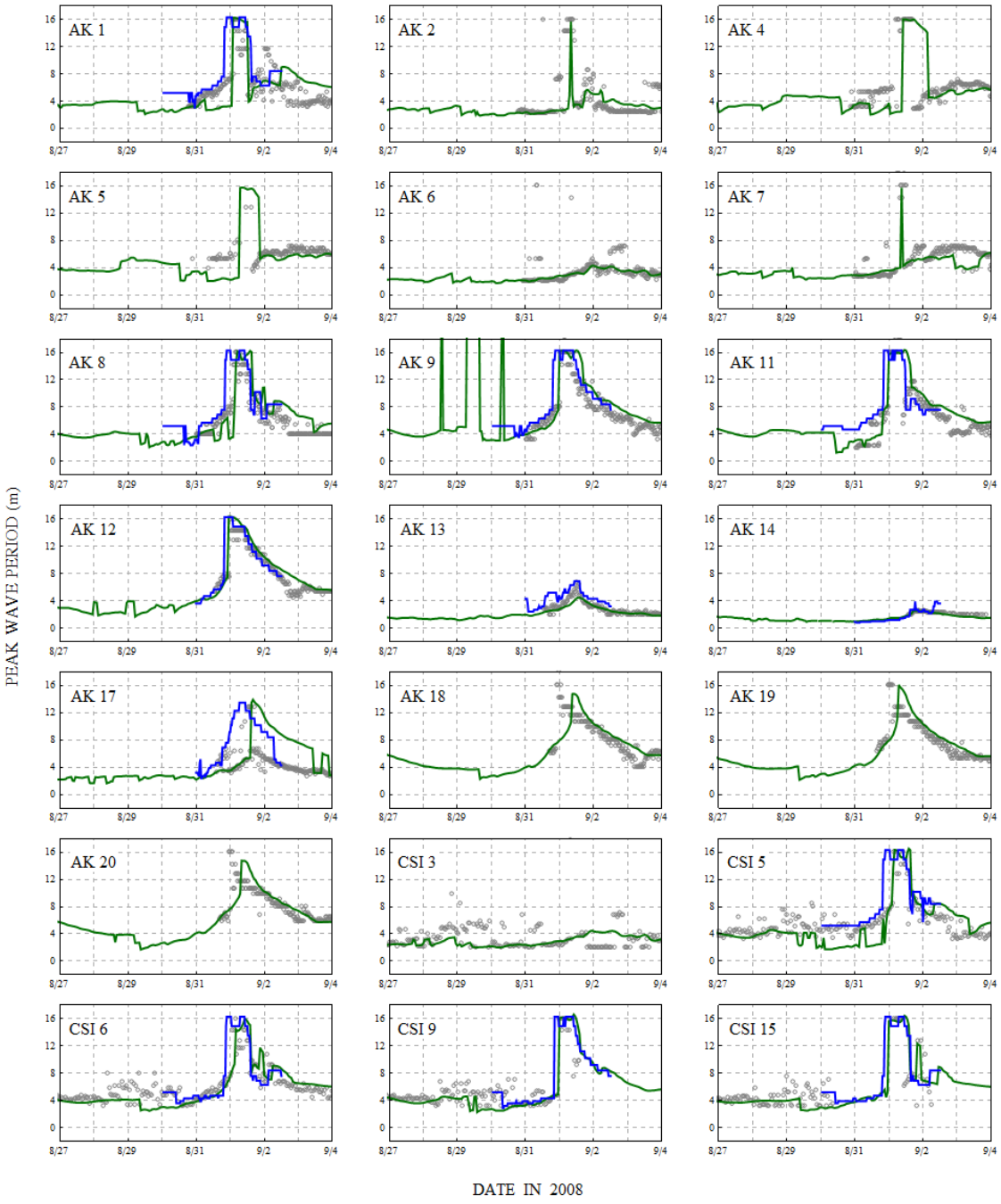

Figure 5.21. Time series of peak wave periods (s) at the 16 AK gages and five CSI gages shown in Figure 5.19. Measured values are shown with gray circles, modeled results from SWAN (green) and STWAVE (blue) are shown with solid lines.

behind the barrier islands, such as at AK gage 17, which is located in 4.5m of water depth and had a peak wave height of 2m.

Behind the barrier islands, which attenuated the larger waves propagating onshore from deep water, predominantly local waves were generated within the sounds and marshes. They generally had mean periods less than 3s (Figure 5.12), and their significant heights were 2m in the sounds and lakes and 1m or less in the wetlands (Figure 5.11). Near landfall, CHL gages 10512, 10508 and 10514 measured local wave generation and dissipation within the marshes north of Terrebonne Bay; note the decrease in the wave heights from 0.8m to 0.5m at the northernmost gages. To the east of the river, the AK gages 13 and 14 measured 0.5-1m waves over the Caernarvon Marsh (Figure 5.20), while the CHL gages 10510, 10513 and 10504 measured 0.5-1m waves over the Biloxi Marsh (Figure 5.22). The peak periods were also small in the marshes, ranging from 2-4s at landfall, although the uncertainty in the measurements was very high (Figure 5.23). These measurements are excellent validation tests for STWAVE and SWAN, because they are located in regions with rapidly-changing bathymetry and bottom friction. Both models perform well, with good matches to the measured data.

5.5.3 Evolution of Storm Surge

As Gustav moved through the Gulf, its easterly and southeasterly winds blew with tropical-storm strength for 12-15hr over the LA-MS shelf. These winds also stretched to the Florida shelf, creating a surge of 0.5-1m at NOAA stations 8726724 and 8729108 (Figure 5.15 and 5.24).

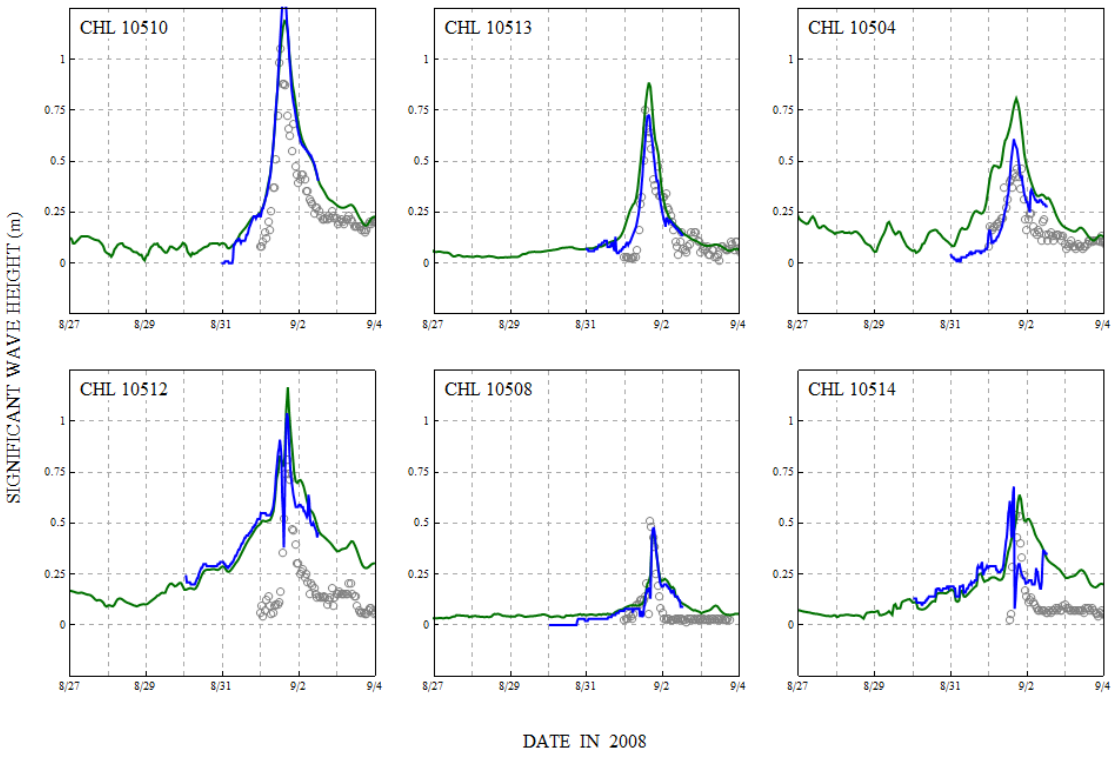

Figure 5.22. Time series of significant wave heights (m) at the six CHL gages shown in Figure 5.19. Measured values are shown with gray circles, modeled results from SWAN (green) and STWAVE (blue) are shown with solid lines.

During this early part of the storm, the levees of lower Plaquemines Parish experienced more than 2m of surge (Figure 5.13b-c). Northeasterly winds pushed water across Breton Sound and against the river levees, which are relatively unprotected by marshes in their southernmost reach. AK gage 13 and CHL gage 10510 are located in the wetlands near the edge of Breton Sound (Figure 5.19), and they measured peak surge of 3-3.25m (Figure 5.25 - 5.26). The levee on the west bank in lower Plaquemines Parish extends farther south, and thus surge can enter the Mississippi River from the east and then propagate up the deep and

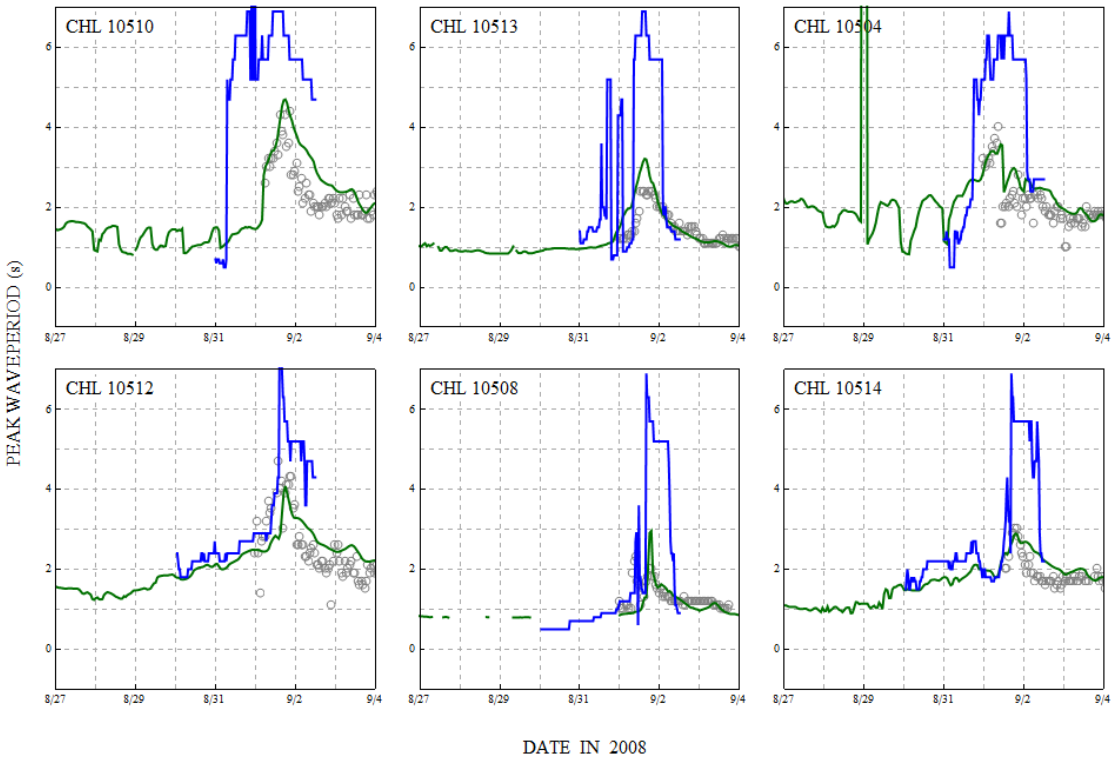

Figure 5.23. Time series of peak wave periods (s) at the six CHL gages shown in Figure 5.19. Measured values are shown with gray circles, modeled results from SWAN (green) and STWAVE (blue) are shown with solid lines.

efficient river, as shown in the gages of the USACE (Figure 5.27). At gages south of the levees and near the delta, such as USACE gages 1545 and 1516, the surge was relatively small, with peaks of 1.5-2m (Figure 5.28). However, the surge was larger at the gages upriver. At USACE gages 1380 and 1300 in New Orleans, the peak surge was 2.5m above the pre-storm levels and 3m relative to NAVD88 (2004.65). At USACE 1220 near Donaldsonville, the surge attenuated to 2m above the pre-storm levels. The Mississippi River had a flow rate of 8,920 $m^3\ s^{-1}$ during Gustav, and thus this surge did not overtop the levees along the river. However,

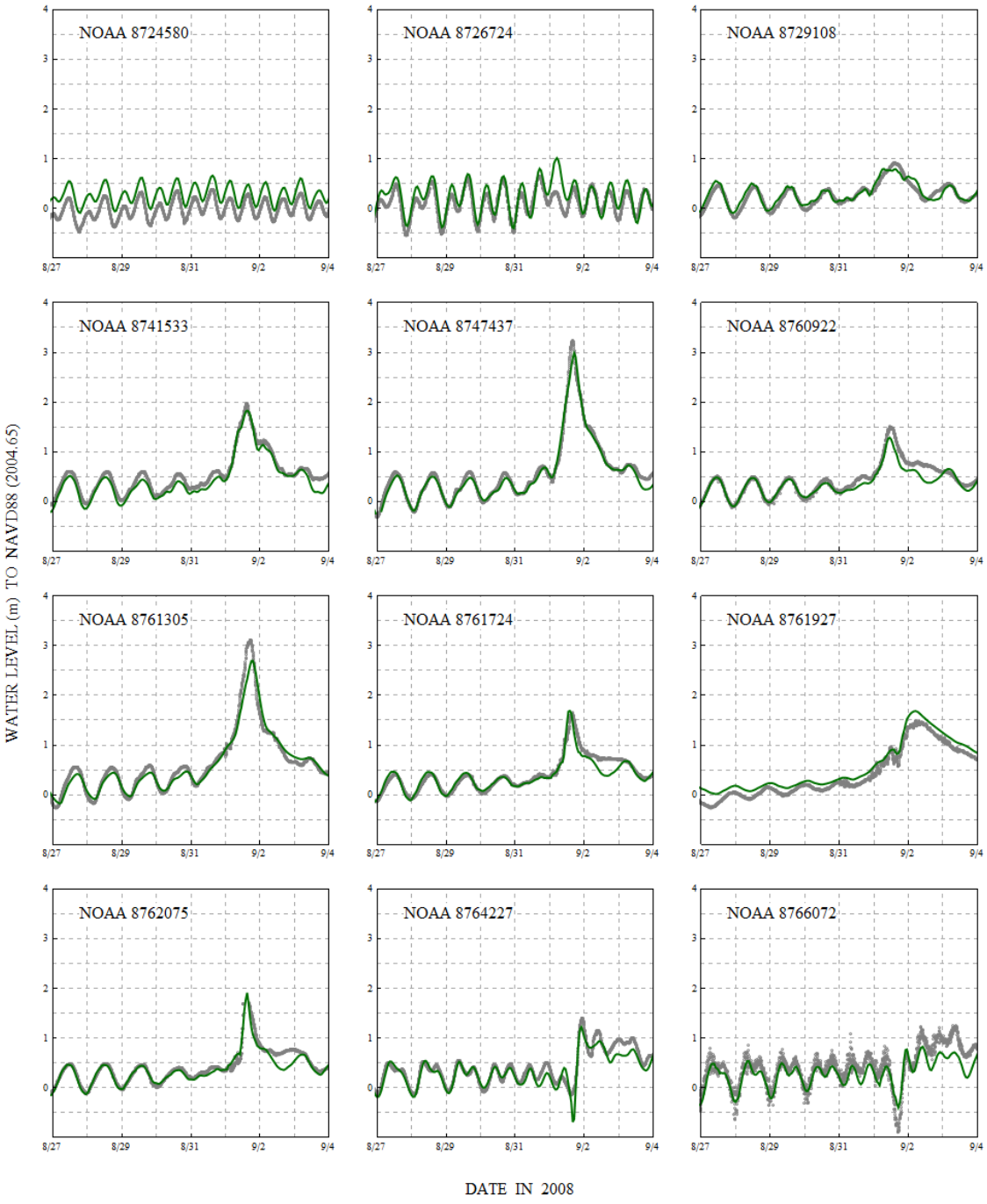

Figure 5.24. Time series of water levels (m) at the 12 selected NOAA stations shown in Figure 5.15. Measured NOAA values are shown with gray circles, and modeled ADCIRC results are shown with a green line.

surge would propagate similarly at higher flow rates with correspondingly higher pre-storm river stages, which are possible during hurricane season.

New Orleans was also threatened by surge in the channels near the city. Water in Mississippi Sound and Lake Borgne was pushed by northeasterly winds into the wetlands and the confluence of the MRGO and GIWW, and eventually into the IHNC. Water levels were 2.5-3m in Lake Borgne and higher in the canals (Figure 5.13c-d). This relatively fast process corresponded to water being blown efficiently through Lake Borgne and to the timing of the peak winds as Gustav made landfall. At NOAA 8761305 (Figure 5.24), USACE 76010 (Figure 5.28), and the deployable USGS STB-04 (Figure 5.30), which are located along the MRGO and the south shore of Lake Borgne, note the sharp peak of 3.25m in the water levels at 1400 UTC 01 September 2008. This surge was focused by the confluence and reached higher levels of 3.5-3.75m within the IHNC. This trend is shown at gages located at the entrance to the IHNC (deployable USGS ORL-13) and within the southern reach of the IHNC (USACE 76160 and deployable USGS ORL-13). The peaks are narrow in these hydrographs, indicating that the surge enters and recedes quickly in the canal-lake-sound system. This 3.5-3.75m of surge in the IHNC was a serious threat to New Orleans. The levees were not breached, however, water levels were within 0.5m of the tops of the levees, and some wave overtopping was reported.

Figure 5.13b-f shows the Biloxi and Caernarvon marshes tend to slow the time of arrival of the surge but do not significantly attenuate the peaks due to the sustained northeasterly-to-southeasterly winds. The CHL gages 10510, 10513 and 10504 show the limited dissipation of the surge as it moved over the friction-dominated Biloxi marsh. Note the decrease of 0.25m in the peak surge at these

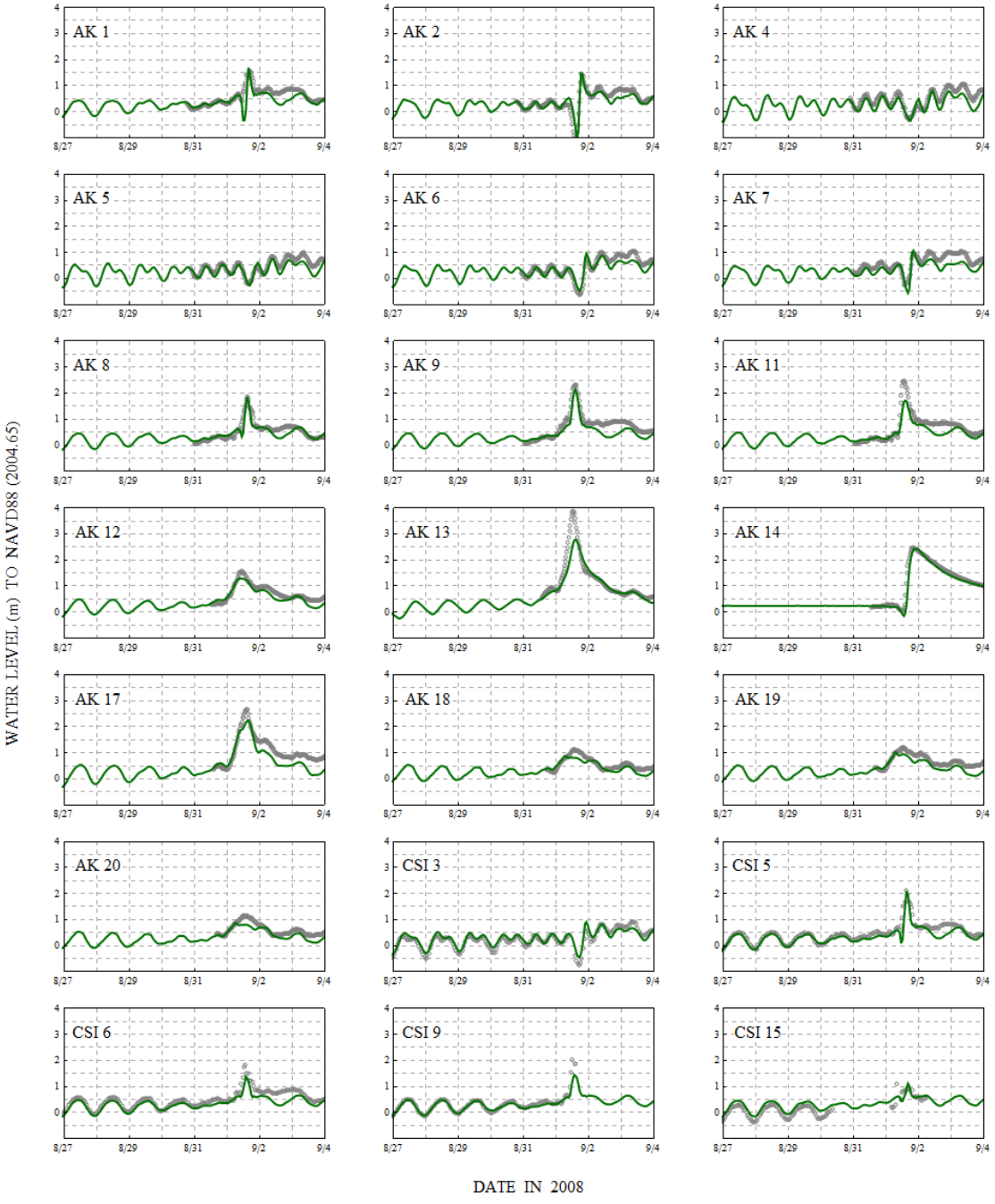

Figure 5.25. Time series of water levels (m) at the 16 AK gages and five CSI gages shown in Figure 5.19. Measured values are shown with gray circles, and modeled ADCIRC results are shown with a green line.

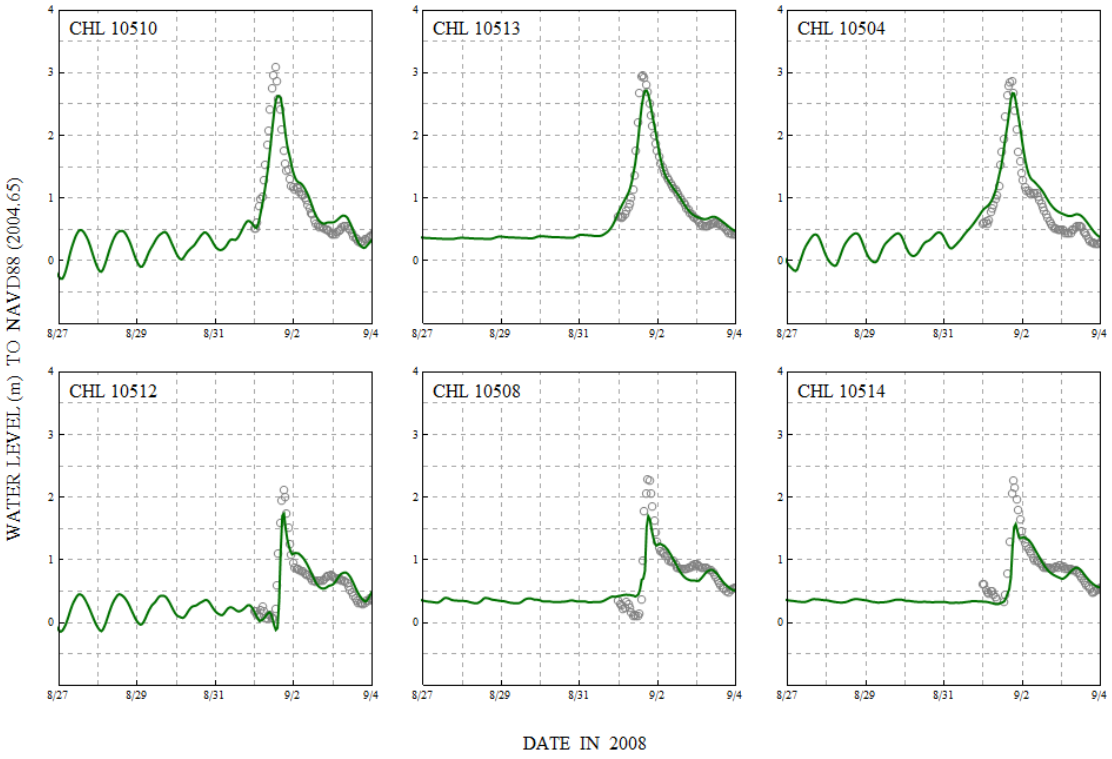

Figure 5.26. Time series of water levels (m) at the six CHL gages shown in Figure 5.19. Measured values are shown with gray circles, and modeled ADCIRC results are shown with a green line.

gages from east to west (Figure 5.26). The Caernarvon marsh also caused limited dissipation of the peak surge. At AK gage 13 located at the edge of the marsh, the peak surge is 3.35m, whereas the surge is 2.25m at AK gage 14 in Lake Lery (Figure 5.25). Farther north against the levees, the permanent USGS gage 295124089542100 also shows a peak of 2.25m. This surge existed against the levees of lower Plaquemines Parish, prior to being pushed northward over the marsh by the shifting winds. The marshes are believed to attenuate surge by as much as 1m per 14.5km (USACE, 1963; Resio and Westerink, 2008). However, after the winds shifted, the surge pushed effectively over the marshes; note the

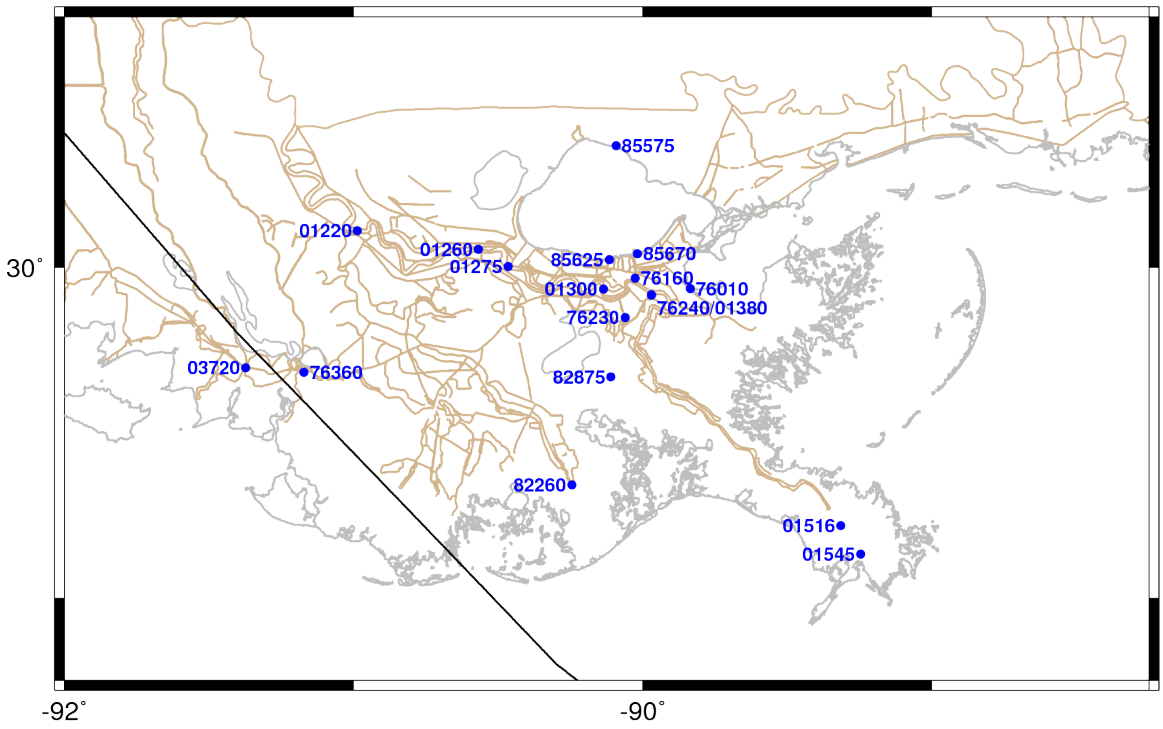

Figure 5.27. Locations of the 18 selected USACE stations (blue points) in southeastern Louisiana. The Gustav track is shown in black, the coastline and water bodies are shown in gray, and the boundaries of the SL16 mesh are shown in brown.

lack of attenuation in the Caernarvon marsh 9-12hr after landfall (Figure 5.13f). Similar to other hurricanes that have impacted the region, when Gustav's winds aligned northwestward for an extended period over the marshes, surge was pushed effectively against the levees of Plaquemines Parish and English Turn.

From the north, New Orleans experienced surge along the levees at the south shore of Lake Pontchartrain. Before landfall, northeasterly winds pushed surge within the lake; note the northeast-to-southwest gradient in the lake in Figure 5.13b-c. However, as the storm made landfall and the winds shifted, surge was pushed around the barrier islands, through Lake Borgne and the passes, and into

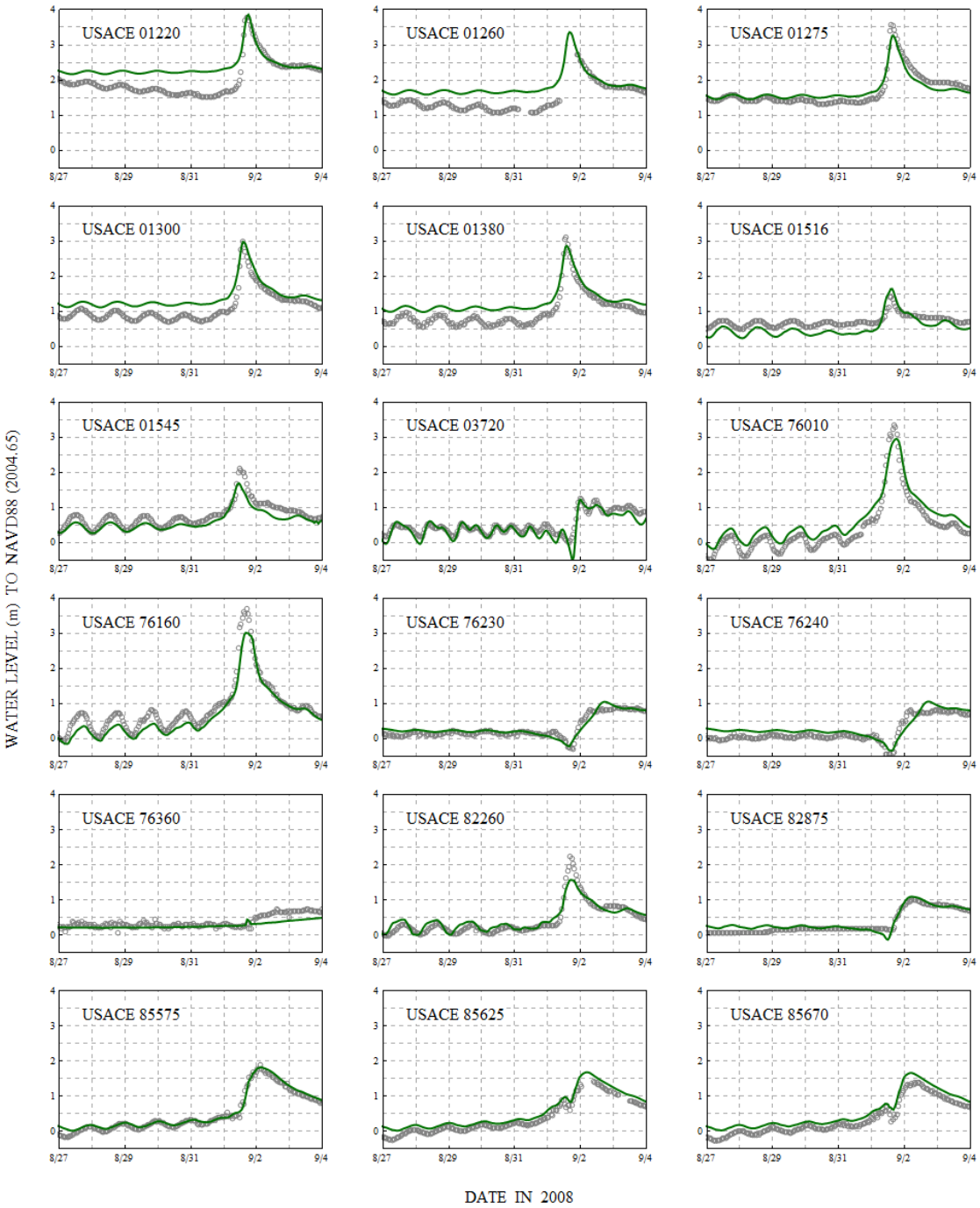

Figure 5.28. Time series of water levels (m) at the 18 selected USACE stations shown in Figure 5.27. Measured USACE values are shown with gray circles, while modeled ADCIRC results are shown with a green line.

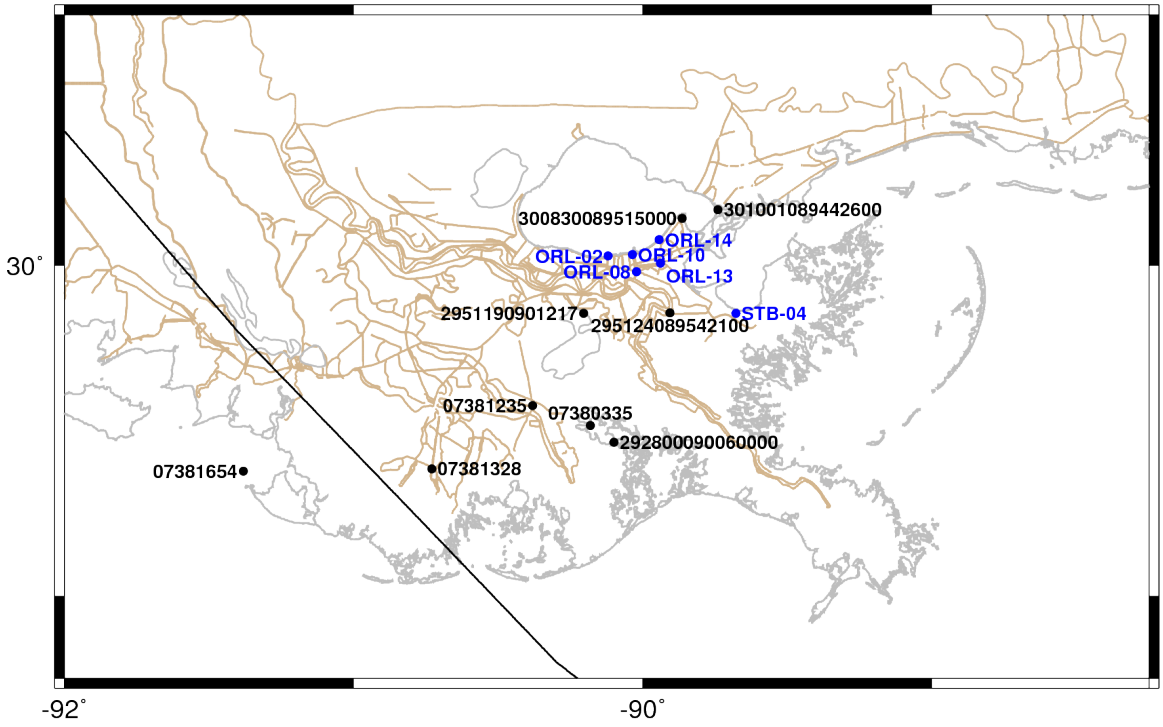

Figure 5.29. Locations of the selected nine permanent USGS stations (black points) and six deployable USGS gages (blue points) in southeastern Louisiana. The Gustav track is shown in black, the coastline and water bodies are shown in gray, and the boundaries of the SL16 mesh are shown in brown.

Lake Pontchartrain. Note the surges of 2.25m at AK gage 17 (Figure 5.25) and 3.25m at the NOAA station 8747437 (Figure 5.24) located near the entrance to Lake Borgne. This flow into the lake was caused by the southeasterly winds and by a strong gradient between the lakes (Figure 5.13e). This exchange is shown at the permanent USGS gages 301001089442600 and 30830089515000 in eastern Lake Pontchartrain (Figure 5.29); the lake fills over the second half of 01 September 2008 and then drains gradually over 02-03 September 2008 (Figure 5.30). As measured at NOAA station 8761927 (Figure 5.24), the USACE gages 85575, 85625 and 85670 (Figures 5.27 - 5.28), and the deployable USGS gages ORL-02, ORL-10

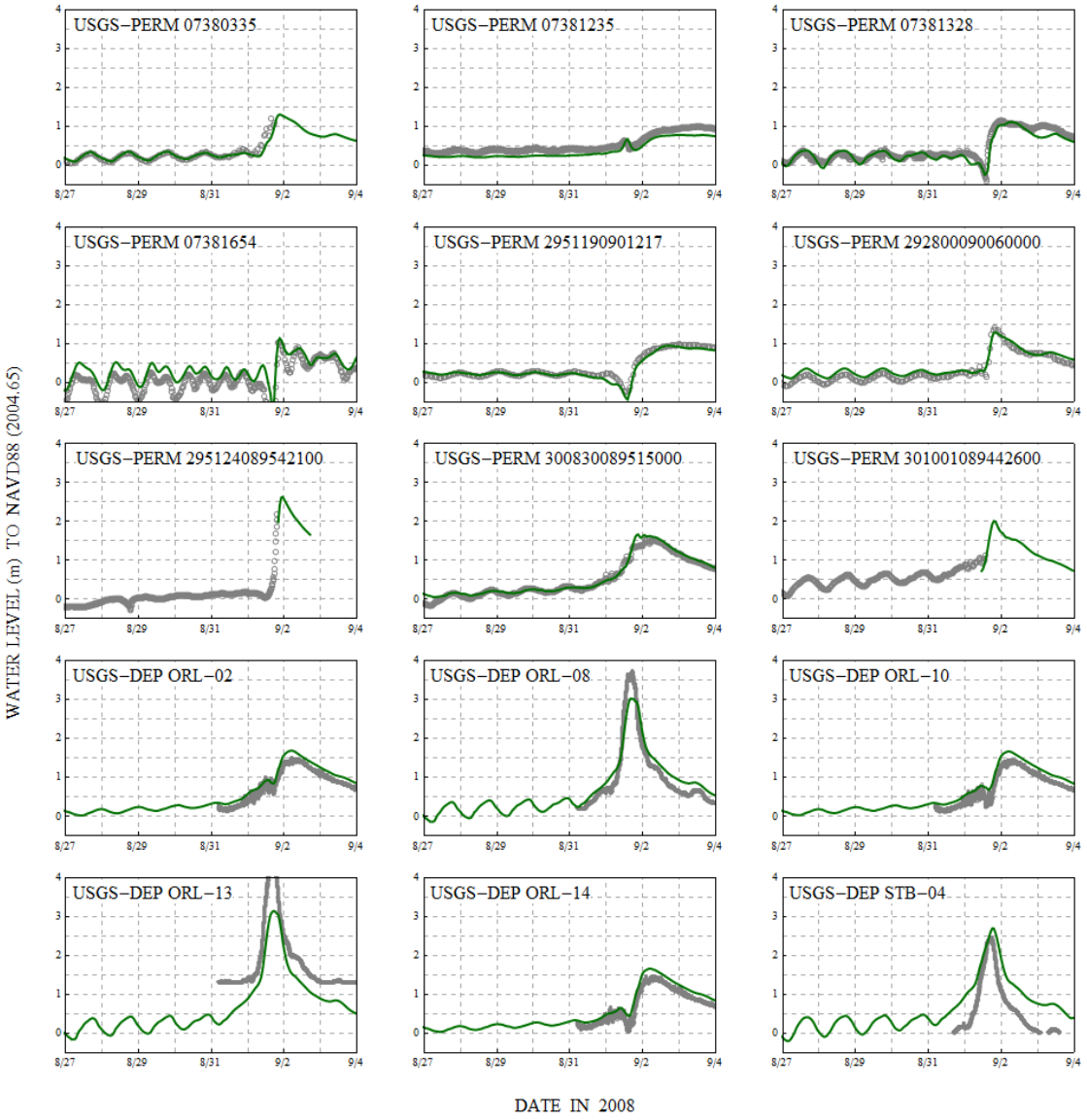

Figure 5.30. Time series of water levels (m) at the selected nine permanent USGS stations and six deployable USGS gages shown in Figure 5.29. Measured USGS values are shown with gray circles, and modeled ADCIRC results are shown with a green line.

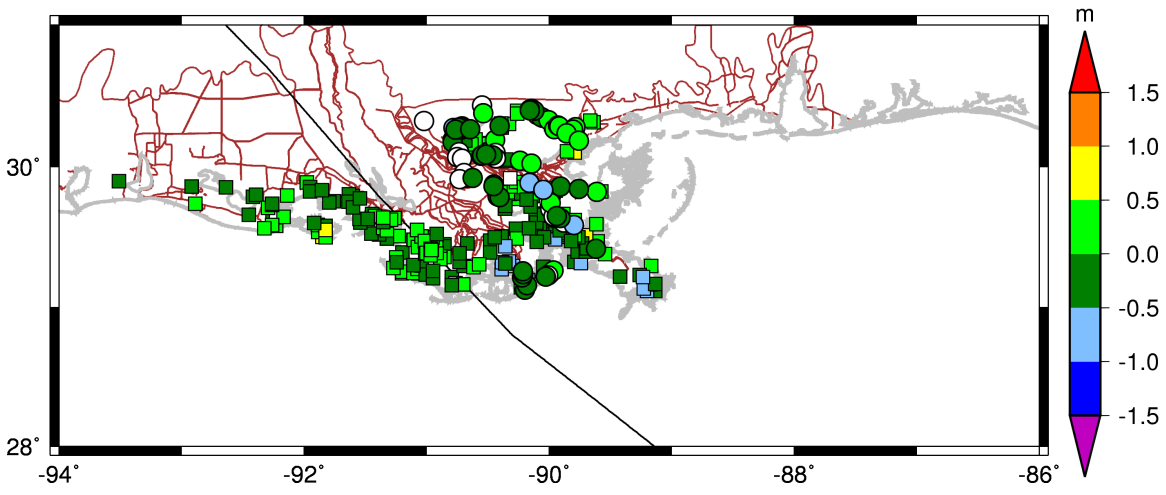

Figure 5.31. Locations of the 82 URS/FEMA HWMs (circles) and 238 CRMS hydrographs (squares) in southeastern Louisiana. The points are color-coded to show the errors between measured and modeled peak water levels; green points indicate matches within 0.5m. White points indicate locations that were never wetted by ADCIRC.

and ORL-14 (Figure 5.30), the maximum surge levels in the lake were 1.5-2m, but they occurred 9-12hr after landfall, when the lake had come to an equilibrium with Lake Borgne (Figure 5.13f). This behavior is matched well by ADCIRC at all gages.

Finally, on the west bank of the river, the surge was smaller, but it propagated far inland and approached the west bank of New Orleans. As Gustav made landfall, its winds shifted northward over Barataria Bay, creating surge of 1.5-2.25m along Grand Isle and adjacent barrier islands (Figure 5.13d). As measured at NOAA stations 8761724 and 8762075 and AK gage 11, the coastal surge built and receded quickly. However, much of the surge pushed inland because the winds continued to blow northward for more than 12hr after landfall. Surge propagated into the marsh/lake system through Little Lake, Lake Salvador and

Lake Cataouatche, located south of New Orleans. As the surge moved northward, it became less peaked in the hydrographs. At the permanent USGS gages 292800090060000 and 07380335 located in Little Lake, the peak surge is 1.5m and occurs 6-8hr after landfall (Figure 5.30). Farther north, at the USACE gages 82875, 76230 and 76240 and USGS permanent gage 2951190901217 located near Lake Salvador, the peak surge is 1m and persists for 12-36hr after landfall (Figure 5.28). Farther west, at the CHL gages 10512, 10508 and 10514 located in the marsh north of Terrebonne Bay, the inland push and slow recession is also evident in the days following landfall (Figure 5.26).

Overall, ADCIRC correlates well to water levels throughout the region, including at most of the 72 hydrographs herein. This behavior is confirmed by the comparison in Figure 5.31 to measured HWMs from CRMS and FEMA. The modeled peak water levels are within 0.5m at 269 of the 291 (92 percent) measured peaks that were wetted by ADCIRC. In a scatter plot of measured-to-modeled peaks, the CRMS data have a best-fit slope of 0.94 and an R^2 of 0.71, while the FEMA data have a best-fit slope of 0.92 and an R^2 of 0.82. When the two data sets are combined, the best-fit line has a slope of 0.93 and R^2 of 0.75, as shown in Figure 5.32. Some portion of these differences can be attributed to measurement error; when it is removed (Table 5.5), the average absolute ADCIRC errors are 0.13-0.19m, and the standard deviations are 0.21-0.23m.

This good correlation can be attributed to the quality of both ADCIRC and the SL16 mesh, but it is also a result of the wave-induced set-up (Figure 5.33). STWAVE focuses its wave dissipation, and thus the peaks in its set-up are larger at the Chandeleur Islands and the Mississippi River delta. SWAN spreads its dissipation over a larger area. Behind the breaking zones, however, the wave-

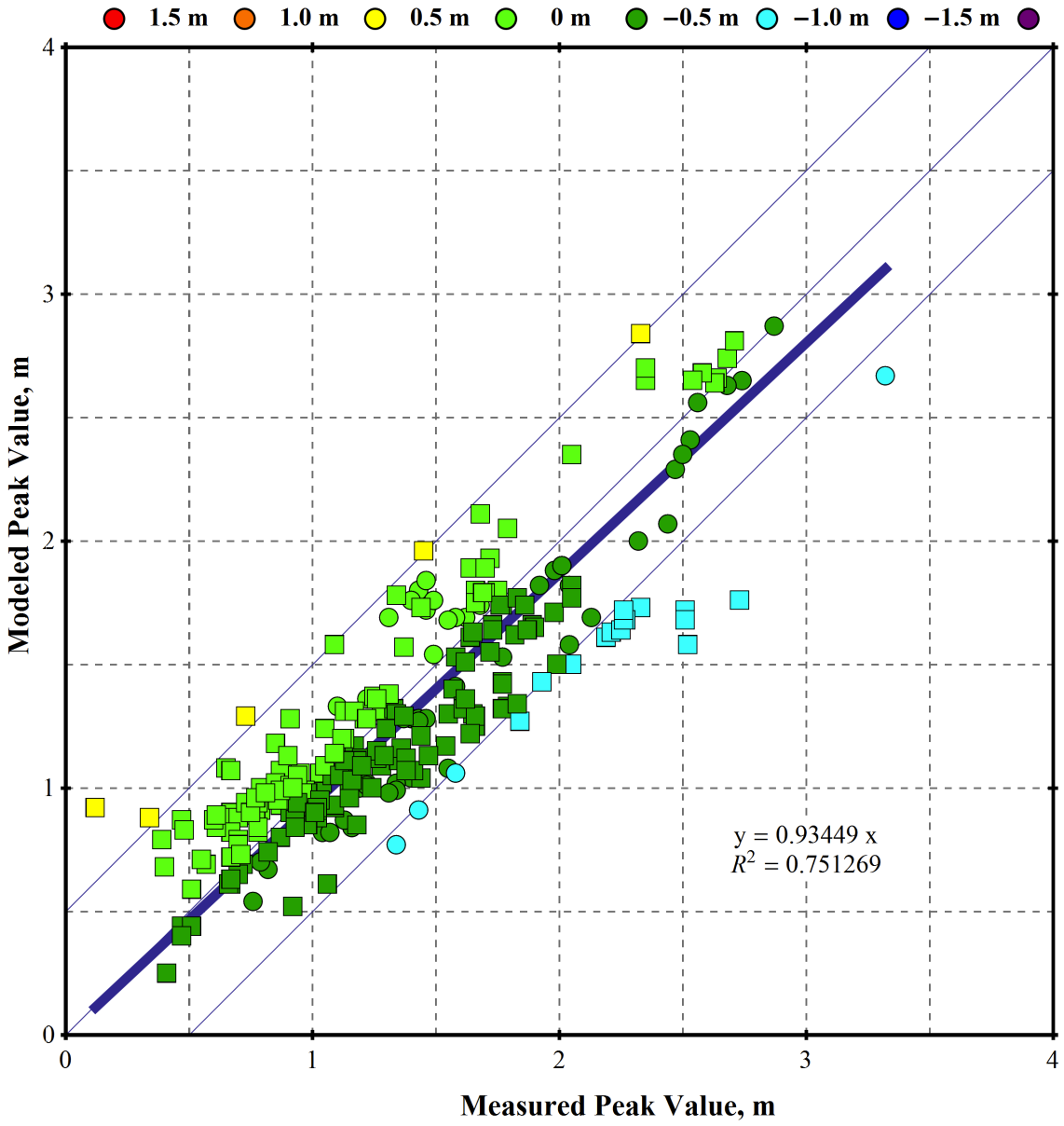

Figure 5.32. Scatterplot of FEMA HWMs (circles) and peak CRMS hydrograph water levels (squares) for Gustav. Green points indicate a match within 0.5m. Red, orange, yellow and light green circles indicate overprediction by the model; green, blue, dark blue and purple circles indicate underpredictions. The slope of the best-fit line through all points is 0.93 and the R^2 value is 0.75.

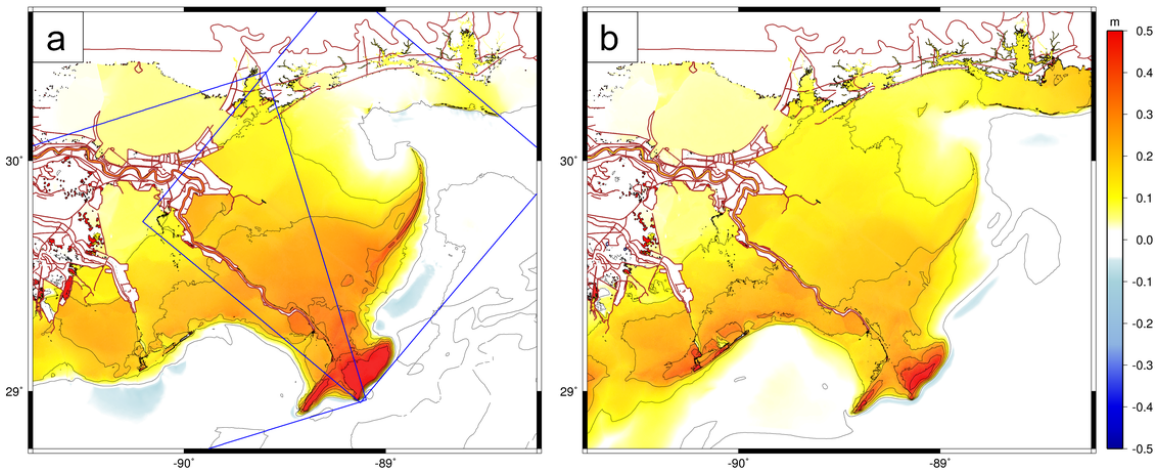

Figure 5.33. Maximum wave-induced set-up produced by coupling ADCIRC to (a) STWAVE and (b) SWAN. The extents of the two structured STWAVE domains are shown in blue lines.

induced set-up from both models accounts for 0.1-0.2m throughout much of the region, and 0.5m in regions near the wave dissipation zones. These contributions are significant when compared to the overall peak water levels, which were 2-3m in the marshes and lakes behind the barrier islands.

TABLE 5.5

SUMMARY OF DIFFERENCE / ERROR STATISTICS

Dataset	ADCIRC to measured HWMs		Measured HWMs		Estimated ADCIRC Errors	
	Avg abs diff (m)	Std dev (m)	Avg abs diff (m)	Std dev (m)	Avg abs diff (m)	Std dev (m)
URS/FEMA	0.23	0.24	0.04	0.08	0.19	0.23
CRMS	0.19	0.24	0.05	0.11	0.13	0.21

5.6 Conclusions

Gustav made landfall as a Category 1 storm in the sparsely-populated region near Terrebonne Bay in southern Louisiana. Its strongest winds were concentrated west of the Mississippi River, and its largest waves dissipated along the delta and continental shelf break. However, because of its large size, the hurricane blew strong winds over the LA-MS shelf, pushing surge through the Mississippi Sound and Lake Borgne, over the marshes and against the levee protection system near New Orleans. The largest water levels were observed in the channels near the city, and levees were threatened with overtopping and breaching. New Orleans was protected by its levees, the marshes to the south and east, the relative weakness of the storm, and the distance from landfall. Nevertheless, Gustav created significant surge on all sides of the city.

As Gustav moved in deep water, it created large waves that radiated outward and impacted most of the Gulf. NDBC buoys measured waves with significant heights of 8-10m, and the timing and magnitudes of these waves are matched well by WAM and SWAN. The waves had significant heights of 15m nearer to the storm's track, but they were smaller to the west of the storm, along the Texas shelf. In shallow water, the nearshore instruments of CSI platforms and AK buoys measured the waves as they were dissipated on the continental shelf. The largest waves were dissipated by the barrier islands, and only local waves were generated and dissipated in the marshes, as shown by the gages of AK and CHL. STWAVE and SWAN correlate well with measured data at almost all of the buoy, station and gage locations.

The storm surge is also described by a wealth of measured data, and ADCIRC correlates well with its water levels. The storm's large size caused its tropical-

storm-strength winds to impact the region for 12-15hr before and during landfall, and these winds pushed surge across the LA-MS shelf and against the levees of lower Plaquemines Parish. Surge of 2-2.75m above the pre-storm levels was pushed up the Mississippi River, and surge of 3-3.5m was pushed into the IHNC. The peak surge occurred east of the river, in regions where the maximum winds did not reach, because the storm was large enough in size to blow medium-strength winds over the shelf for an extended length of time. The increased resolution of the SL16 mesh allows ADCIRC to model well the surge in these fine-scale channels.

In Lake Pontchartrain, water levels increased to 1.5-2m as surge was pushed through the Rigolets and Chef Menteur passes. To the southwest, the Caernarvon and Biloxi marshes are widely believed to attenuate storm surge by as much as 3m, but the surge from the levees along lower Plaquemines Parish was pushed northward effectively over the marshes and against the levees near Braithwaite and English Turn. The marshes offered little protection as the water levels were within 0.5m of the tops of the levees. Finally, the interconnected marshes south and west of New Orleans allowed storm surge to propagate from the landfall location and threaten the city many hours after the storm passed. Surge of 0.75-1m was observed on the west bank even 12-36hr after landfall.

These results emphasize the ease with which surge can develop in southern Louisiana. The channels that connect the region to deep water also work in the reverse direction, and surge can propagate quickly through the Mississippi Sound and Lake Borgne, the Rigolets and Chef Menteur passes into Lake Pontchartrain, into the IHNC near downtown, and up the Mississippi River itself. The marshes to the south and east offer protection from rapid development of surge, but they can be inundated completely by surge that is driven by constant winds for six or more

hours during a storm. The large size and sustained easterly and southeasterly winds of Gustav, combined with the unique geometry of southern Louisiana, were effective drivers of waves and surge throughout the region. It is only through the use of high-resolution meshes and advanced coupling of waves and circulation that Gustav can be validated with a high degree of skill against the measured data.

CHAPTER 6

PERFORMANCE OF THE UNSTRUCTURED-MESH, SWAN + ADCIRC MODEL IN COMPUTING HURRICANE WAVES AND SURGE

6.1 Overview

Coupling wave and circulation models is vital in order to define shelf, nearshore and inland hydrodynamics during a hurricane. The nearshore domain size, level of required mesh resolution, and physics make these complex computations very cycle-intensive. Nonetheless, fast wall-clock times are important, especially when forecasting an incoming hurricane.

In this chapter, we examine the performance of the unstructured-mesh, SWAN+ ADCIRC wave and circulation model applied to the new high-resolution, 5M-vertex, finite-element SL16 mesh of the Gulf of Mexico and Louisiana. This multi-process, multi-scale modeling system has been integrated by utilizing inter-model communication that is intra-core. This modeling system is validated through hindcasts of Hurricanes Katrina and Rita (2005), Gustav and Ike (2008) and comprehensive comparisons to wave and water level measurements throughout the region. The performance is tested on a variety of platforms, via the examination of output file requirements and management, and the establishment of wall-clock times and scalability using up to 9,216 cores. This chapter will be submitted to the *Journal of Scientific Computing* as Dietrich *et al.* (2010d).

6.2 Introduction

Several recent hurricanes have damaged critical infrastructure in New Orleans and southern Louisiana. In 2005, Katrina caused devastating flooding within the city itself and created storm surge along the Mississippi-Alabama coastline that was the largest ever measured in the continental United States (Ebersole *et al.*, 2007), while Rita made landfall in southwestern Louisiana and flooded large portions of the marshes and bayous in the region (Bunya *et al.*, 2010; Dietrich *et al.*, 2010a). In 2008, Gustav made landfall in southeastern Louisiana and threatened New Orleans with wave overtopping of its levee protection system (Dietrich *et al.*, 2010c), while Ike made landfall in Galveston but created currents and extensive flooding along the coastlines of all of Louisiana and eastern Texas (Kennedy *et al.*, 2010b).

These hurricanes created complex environments of waves, currents and storm surge throughout the region. In the deep water of the Gulf of Mexico, large, long waves were developed that propagated as swell in all directions. These waves have been measured at buoys to have peak periods up to 25s and significant heights up to 17.5m, but their significant heights are probably 20-25m closer to the hurricane track. In regions where the continental shelf is narrow, such as at the bird's foot of the Mississippi River, these large waves approach closely to the shoreline before breaking due to rapid changes in bathymetry. Behind the breaking zones and inside the marshes and bayous of southern Louisiana, the wave environment is completely different, with wind-sea waves generated locally but limited by depth and bottom friction to periods of 0.5-4s and significant heights of 1-2m.

The storm surge also varies widely from its generation on the continental shelf to its interaction with the nearshore estuaries, floodplains and channels. Currents

of 2 m s^{-1} or greater can exist on the shelf, around the delta and the barrier islands, and within the natural and man-made passes and channels that connect New Orleans to the Gulf. Water levels reached 4-5m along the coastline of southwest Louisiana during Rita, 3-4m along the Mississippi River levees during several storms, and up to 10m along the Mississippi-Alabama coastline during Katrina.

Waves and storm surge interact strongly, despite being separated in frequency space. Short waves, such as wind-sea waves and swell, have periods ranging from 0.5-25s, whereas longer waves, such as storm surge and tides, can have periods ranging from minutes to months. However, short waves are impacted by circulation; currents can shift wave energy due to the Doppler effect, and water levels affect dissipation due to depth-limited breaking. And the transformation of short waves exerts radiation stress gradients, which drive currents and surge. Water levels can be increased by as much as 35 percent due to local wave-driven set-up (Resio and Westerink, 2008; Dietrich *et al.*, 2010a).

Hurricanes also act over a wide range of spatial scales. Waves and storm surge are generated in the deep waters of the Gulf of Mexico, propagate and then transform on the continental shelf and in the complex nearshore environment due to rapid changes in bathymetry and bottom friction. Wave dissipation can be spread over large, smoothly-varying shelfs, or it can be focused near the barrier islands or other breaking zones. Storm surge is pushed over the sounds and marshes and then interacts with the levees and channels in the region. In hurricane modeling applications, these spatial scales necessitate the use of unstructured meshes, so that resolution can be varied from kilometers in the deeper Gulf, to hundreds of meters on the continental shelf and behind the breaking zones, to tens of meters near the small-scale features.

Wave and circulation models have been developed to apply unstructured meshes during hurricane simulations. The unstructured-mesh version of the Simulating WAves Nearshore (SWAN) model employs an analog of the Gauss-Seidel sweeping method used by the structured-mesh version, in order to propagate efficiently the wave energy (Zijlema, 2010). SWAN incorporates the source/sink terms for nearshore wave physics, such as the triad nonlinear interactions, bottom friction and depth-limited breaking, but it also contains the deep-water physics of quadruplet nonlinear interactions and whitecapping. The ADvanced CIRCulation (ADCIRC) model for tidal-, wind- and density-driven circulation employs a Continuous-Galerkin solution of the Generalized Wave Continuity Equation (GWCE), and the two-dimensional version employs the depth-integrated momentum equations on an unstructured, finite-element mesh. ADCIRC has been validated for several hurricanes in southern Louisiana (Westerink *et al.*, 2008; Bunya *et al.*, 2010; Dietrich *et al.*, 2010a), and it has been used extensively by the US Army Corps of Engineers (USACE), the Federal Emergency Management Agency (FEMA) and local agencies to design levee and flood mitigation systems, and to evaluate hurricane flooding risk.

SWAN and ADCIRC have been integrated and coupled closely so that they run on the same global unstructured mesh (Dietrich *et al.*, 2010b). The resulting SWAN+ADCIRC model employs an identical, unstructured sub-mesh on each computational core, so that information can be passed between these two models without interpolation. Inter-model communication is performed intra-core, via local cache, and thus is highly efficient. In addition, both models make use of the same parallel infrastructure and pass information at boundaries between the local sub-meshes, so that the intra-model communication is inter-core. Thus the sharing

of the same unstructured mesh allows the coupled model to be both accurate (by increasing mesh resolution in regions with large spatial gradients) and efficient (by eliminating the need for costly interpolation and extensive global communication as information is passed between models). SWAN+ADCIRC is well-positioned to simulate waves and surge from their generation in deep and shallow water to their dissipation nearshore.

Hurricane forecasting applications demand both accuracy and efficiency. Model results must be reliable for a wide range of storm characteristics, and thus a high-resolution mesh should be employed to resolve the complex geometry throughout the region. But model results must also be timely, often on the order of 1hr, so that they can be useful to emergency management officials to aid with decision-making. In this work, we validate the accuracy and efficiency of SWAN+ADCIRC on the SL16 unstructured mesh, which employs 5M vertices and 10M finite elements to provide a high-resolution description of southern Louisiana. The model is validated against measured waves and storm surge during the four recent hurricanes to impact the region, namely Katrina and Rita (2005), and Gustav and Ike (2008). Validation results show SWAN+ADCIRC simulates accurately the evolution of waves and surge in this region.

Benchmarking results show SWAN+ADCIRC is efficient to thousands of computational cores. As meshes continue to grow in size and complexity, it is imperative that models make good use of the expanding computational resources. The coupling paradigm employed by SWAN+ADCIRC does not interfere with the already-excellent scalability of the component models, and the coupled model also manages well its file output through the use of dedicated writer cores. The SWAN+ADCIRC model maintains its scalability to 7,168 computational cores,

demonstrating that it can simulate accurately and efficiently the hurricane waves and surge.

6.3 Computational Models

6.3.1 SWAN

Individual waves exist on length and time scales that are too small to be resolved when computational models are applied to large domains. Thus, instead of resolving the phases of the waves and their associated processes, SWAN represents the wave field as an energy spectrum (Booij *et al.*, 1999). The wave action density $N(\vec{x}, t, \sigma, \theta)$ is allowed to evolve in time (t), geographic space ($\vec{x}$) and spectral space (with relative frequencies σ and directions θ), as governed by the action balance equation:

$$\frac{\partial N}{\partial t} + \nabla_{\vec{x}} \cdot [(\vec{c}_g + \vec{\overline{U}})N] + \frac{\partial}{\partial \theta} c_\theta N + \frac{\partial}{\partial \sigma} c_\sigma N = \frac{S_{tot}}{\sigma}, \tag{6.1}$$

where $\vec{c}_g$ is the group velocity, $\vec{\overline{U}}$ is the ambient current, and c_θ and c_σ are the propagation velocities in the θ- and σ-spaces. The source terms S_{tot} represent wave growth by wind; action lost due to whitecapping, surf breaking and bottom friction; and action exchanged between spectral components due to nonlinear effects in deep and shallow water.

The structured-mesh version of SWAN employs a Gauss-Seidel sweeping algorithm to propagate the wave action density in geographic space, and an analog of that algorithm was used recently to extend SWAN to run on unstructured meshes (Zijlema, 2010). The mesh vertices are ordered so that SWAN can sweep through them in alternating directions and update the action density from neighboring

vertices. A schematic representation of SWAN's solution algorithm is shown in Figure 6.1. In a parallel computing environment, after the action density has been updated at all vertices within a computational sub-mesh, it is updated at the shared boundaries between neighboring sub-meshes. This method does not require the global communication associated with the solution of matrix systems, and thus it is highly scalable. The local communication occurs at the end of each iteration, and SWAN will iterate until the action density has converged on its time step. In the present hindcasts, SWAN iterates until 95 percent of the vertices in the global domain have converged, to a maximum of 20 iterations.

6.3.2 ADCIRC

ADCIRC solves forms of the shallow-water equations (SWE) for water levels ζ and the vertically-integrated momentum equations for currents $\overline{\overrightarrow{U}}$ (Kolar *et al.*, 1994; Luettich and Westerink, 2004; Dawson *et al.*, 2006; Westerink *et al.*, 2008). The model applies the continuous-Galerkin finite-element method to discretize and solve the SWE on unstructured meshes, and thus it allows localized refinement in regions where the solution gradients are largest.

ADCIRC computes water levels via the solution of the Generalized Wave Continuity Equaton (GWCE), which is a combined and differentiated form of the continuity and momentum equations. The GWCE can be solved implicitly or explicitly, as represented schematically in Figures 6.2 - 6.3. The implicit solution requires the assembly of a matrix system and the application of the Jacobi Conjugate Gradient (JCG) method, which iterates to convergence. The explicit solution utilizes a lumped diagonal in the mass matrix to solve directly; it is faster per time step than the implicit solution, but it may require a smaller time

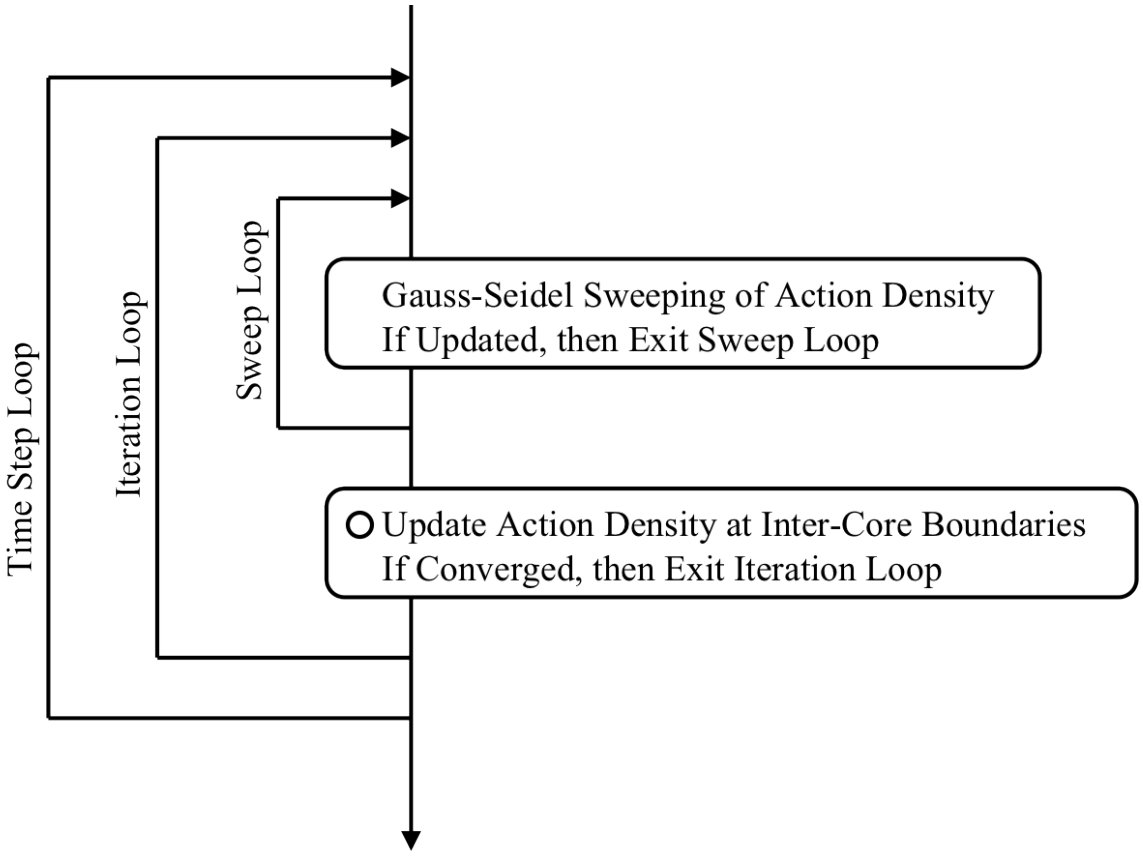

Figure 6.1. Schematic of SWAN's solution algorithm. Local communication to neighboring computational cores is marked with a circle.

step. After the new water levels are computed, wetting and drying is allowed, and then the vertically-integrated momentum equations are solved explicitly for the currents.

In a parallel computing environment, ADCIRC's solution algorithm can require local and global communication between computational cores. Several quantities, including the water levels and currents, must be updated along the overlapping boundaries of neighboring sub-meshes, but this communication is local and highly scalable. However, the implicit solution of the GWCE requires costly global communication to take the dot product of the diagonal vector for scaling of the GWCE matrix system, to take the dot product of the residual vector after each JCG iteration, and to determine if wetting and drying has occurred within the global domain. These instances of global communication utilize the *MPI_ALLREDUCE* command to collect information and broadcast it to all of the computational cores, and thus they hinder the scalability of ADCIRC. As the number of cores increases, this global communication becomes more costly (Tanaka *et al.*, 2010). The explicit solution of the GWCE does not require any global communication, and thus it is highly scalable.

6.3.3 Model Coupling

SWAN and ADCIRC are coupled so that they run on the same computational core and on the same unstructured sub-mesh (Dietrich *et al.*, 2010b). ADCIRC passes wind speeds, water levels and currents through local cache to SWAN, which utilizes those quantities to force its computations. At the end of each of its time steps, SWAN computes the wave radiation stresses and their gradients, and then it passes those gradients as forcing to ADCIRC as forcing.

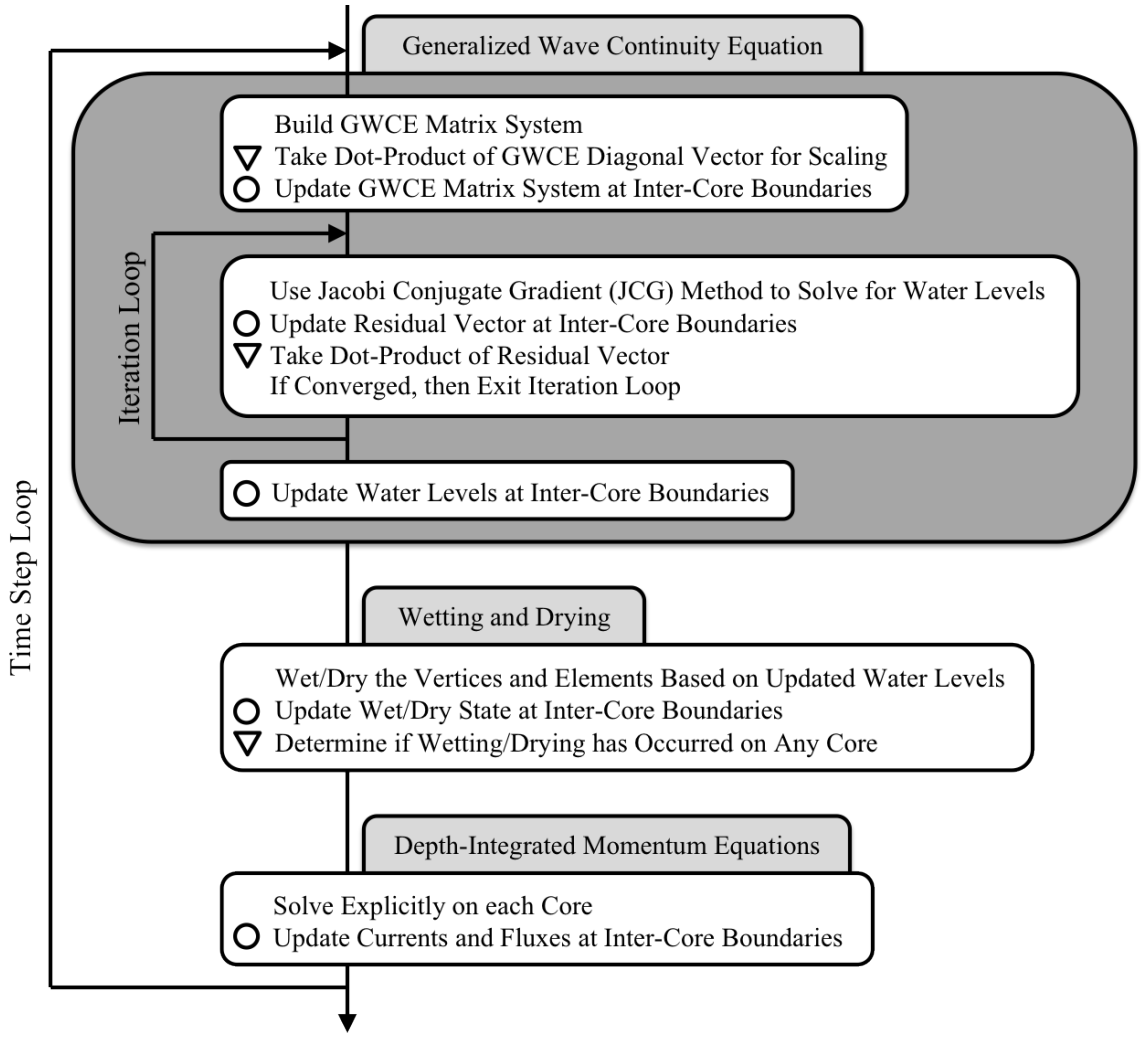

Figure 6.2. Schematic of ADCIRC's algorithm with implicit solution of the GWCE. Local communication to neighboring computational cores is marked with circles, while global communication over all computational cores is marked with triangles.

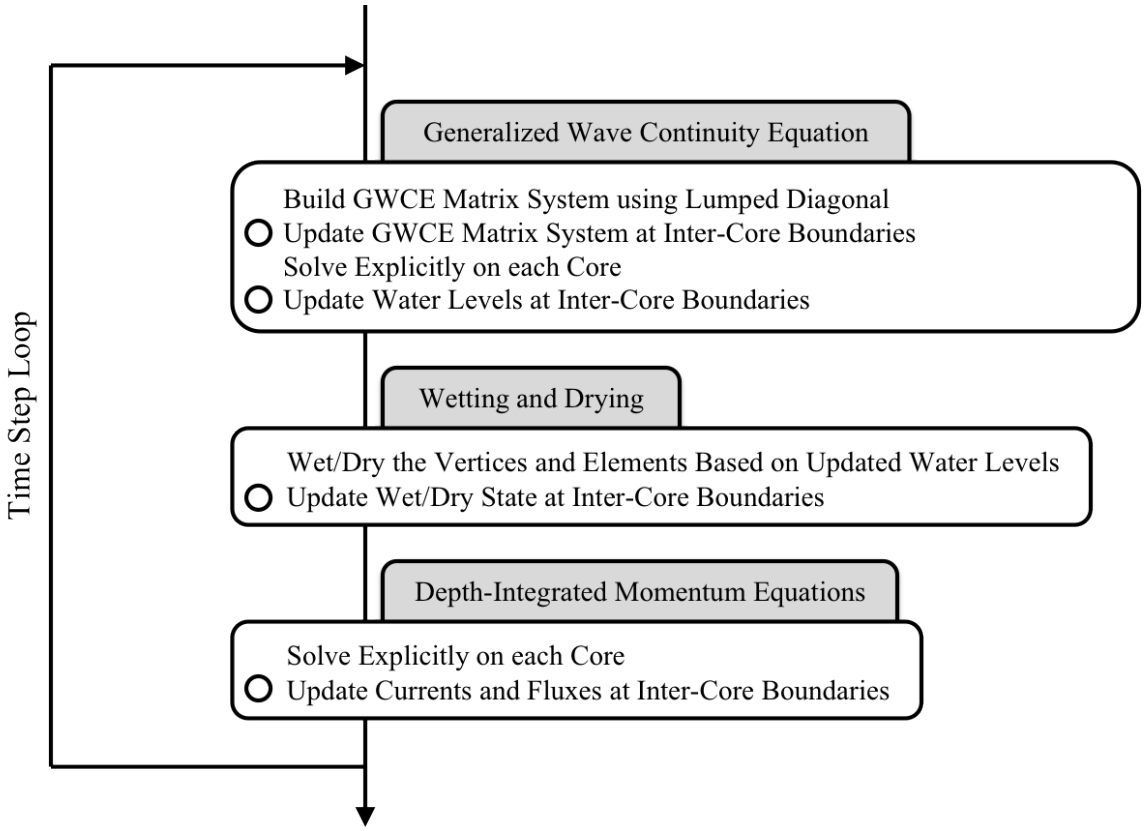

Figure 6.3. Schematic of ADCIRC's algorithm with explicit solution of the GWCE. Local communication to neighboring computational cores is marked with circles.

ADCIRC is Courant-limited algorithmically and also limited by the speed associated with its wetting front (because only one layer of triangular elements is activated at the wetting front during a time step), so its time step must be relatively small. However, SWAN is unconditionally stable, and thus its time step can be relatively large. The coupling interval is taken to be the same as the SWAN time step. For example, the present hindcasts utilize a coupling interval and SWAN time step of 600s, and the ADCIRC time step is 1s. The models alternate in real time, so that the computational core is always running either SWAN or ADCIRC.

ADCIRC runs first on the coupling interval, and it uses the SWAN radiation stress gradients from the previous interval to extrapolate forward its wave forcing in time. After its time steps on the coupling interval, ADCIRC passes information to SWAN. Then SWAN is run on the same interval, using the average of the ADCIRC water levels and currents from the interval to force its computations. After its time step, SWAN computes the radiation stress gradients and passes them to ADCIRC, which then begins the process anew on the next interval.

This coupling paradigm maximizes efficiency in a parallel computing environment. Figure 6.4 shows a schematic of the communication between models and cores. SWAN and ADCIRC utilize the same local sub-mesh, and thus there is a one-to-one correspondence between the geographic locations of the mesh vertices. No interpolation is required; water levels, currents, wind speeds and radiation stress gradients can be passed directly through local cache. Inter-model communication is intra-core, and thus unaffected by the parallel computing environment. Intra-model communication is handled as described above, with SWAN utilizing only local, neighbor-to-neighbor communication along sub-mesh boundaries, and

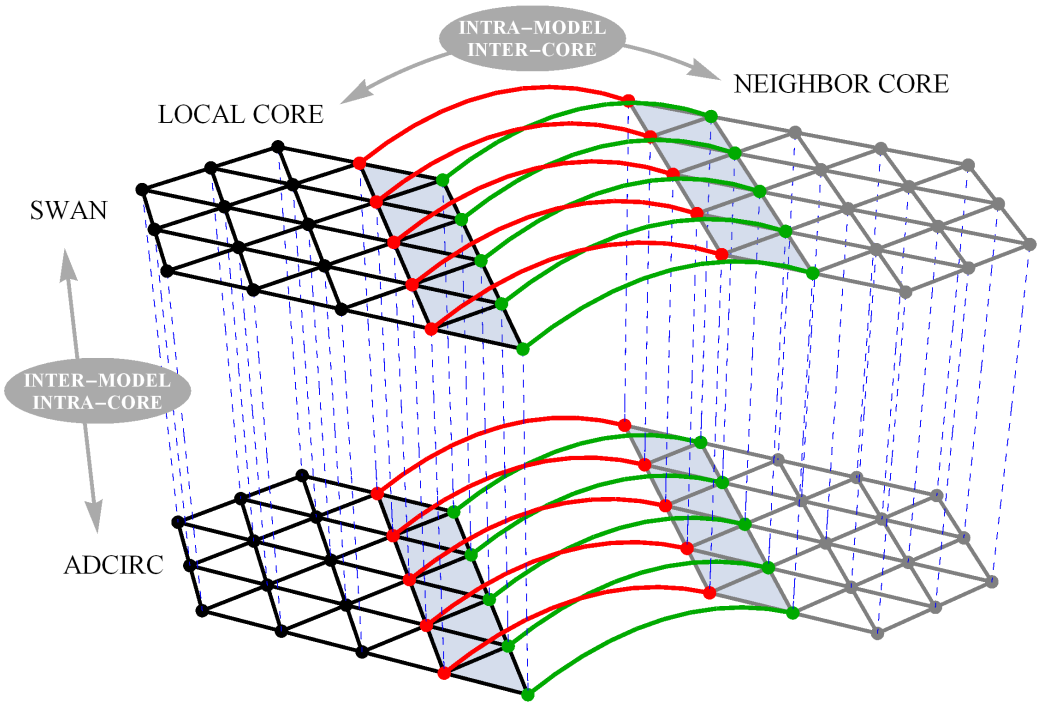

Figure 6.4. Schematic of parallel communication between models and cores (Dietrich *et al.*, 2010b). Dashed lines indicate communication for all vertices within a sub-mesh, and are inter-model and intra-core. Solid lines indicate communication for the edge-layer-based vertices between sub-meshes, and are intra-model and inter-core.

with ADCIRC utilizing both local and global communication. It should be noted that this coupling paradigm avoids the costs associated with the interpolation of forcing information between heterogeneous meshes; in that case, the inter-model communication would be inter-core and increasingly expensive.

6.3.4 File Output

The coupled SWAN+ADCIRC model utilizes ADCIRC's ability to dedicate cores for file output (Tanaka *et al.*, 2010). Most of the cores run SWAN+ADCIRC,

using the coupling paradigm described above, but a small subset of cores is set aside for writing the large, global output files to disk. When the computational cores are ready to write a time snap of computed solutions, they send these data to a single writer core, which collects the data into large, global arrays. Then each array is written to the appropriate output file. The computational cores can proceed with the next stage of their calculations, while the writer cores write independently. When the computational cores are ready to write the next time snap, the writer cores have finished their work and are ready to receive the next set of global arrays.

This output method is most efficient when there is at least one dedicated writer core for each global output file. For example, the present hindcasts require SWAN+ADCIRC to generate 10 global output files containing: water levels, currents, wind pressures, wind speeds, radiation stress gradients, significant wave heights, mean wave directions, two types of mean wave periods, and peak wave periods. Thus, when file output is enabled in the timing results that follow, SWAN+ADCIRC utilizes at least 10 dedicated writer cores. On large numbers of cores, it is also important to employ a sequential approach to the writer cores, because the computational cores may produce the data for the next time snap before the writer cores finish writing the data from the previous time snap. The sequential approach expands the number of writer cores, so that at least one set of 10 writer cores is available to receive data (Tanaka *et al.*, 2010).

6.4 Unstructured Mesh

Unstructured meshes allow for resolution to be increased in regions where gradients are large, such as in regions with rapid changes in bathymetry/topography,

variability in bottom roughness or some other parameter, wave dissipation over short distances, or the build-up of surge against a raised feature. Resolution is varied from kilometers in the deep ocean, to hundreds of meters on the continental shelf, to tens of meters in the marshes, floodplains and channels onshore. The SL16 mesh provides this variability in resolution, as shown in Figures 6.5 - 6.7. The mesh extends outward to the Atlantic Ocean, so that storms can be started inside the computational domain. The mesh sizes are 4-6km in the Gulf of Mexico, to capture the generation and propagation of hurricane waves in SWAN. On the continental shelf and in the wave breaking zones, the resolution varies down to 200m, to capture the wave dissipation in SWAN and the accurate transfer of wave radiation stress gradients to ADCIRC. The mesh sizes are no larger than 200m in the marshes and floodplains of southern Louisiana, and they vary down to 30-50m in the fine-scale channels, such as the distributaries of the Mississippi River delta. The SL16 mesh contains 5,036,960 vertices and 9,949,317 triangular elements.

Figures 6.5 - 6.6 show the SL16 mesh bathymetry and topography, which were applied as described in Dietrich *et al.* (2010c). Hydraulic friction is computed in ADCIRC using a Manning's n formulation, and SWAN converts the same Manning's n values to roughness lengths that vary in space and time, for use in a friction formulation from Madsen *et al.* (1988). The details of this bottom friction formulation are also in Dietrich *et al.* (2010c).

6.5 Validation

SWAN+ADCIRC was validated on the SL16 mesh for the four recent historical storms: Katrina and Rita (2005), and Gustav and Ike (2008). As shown in

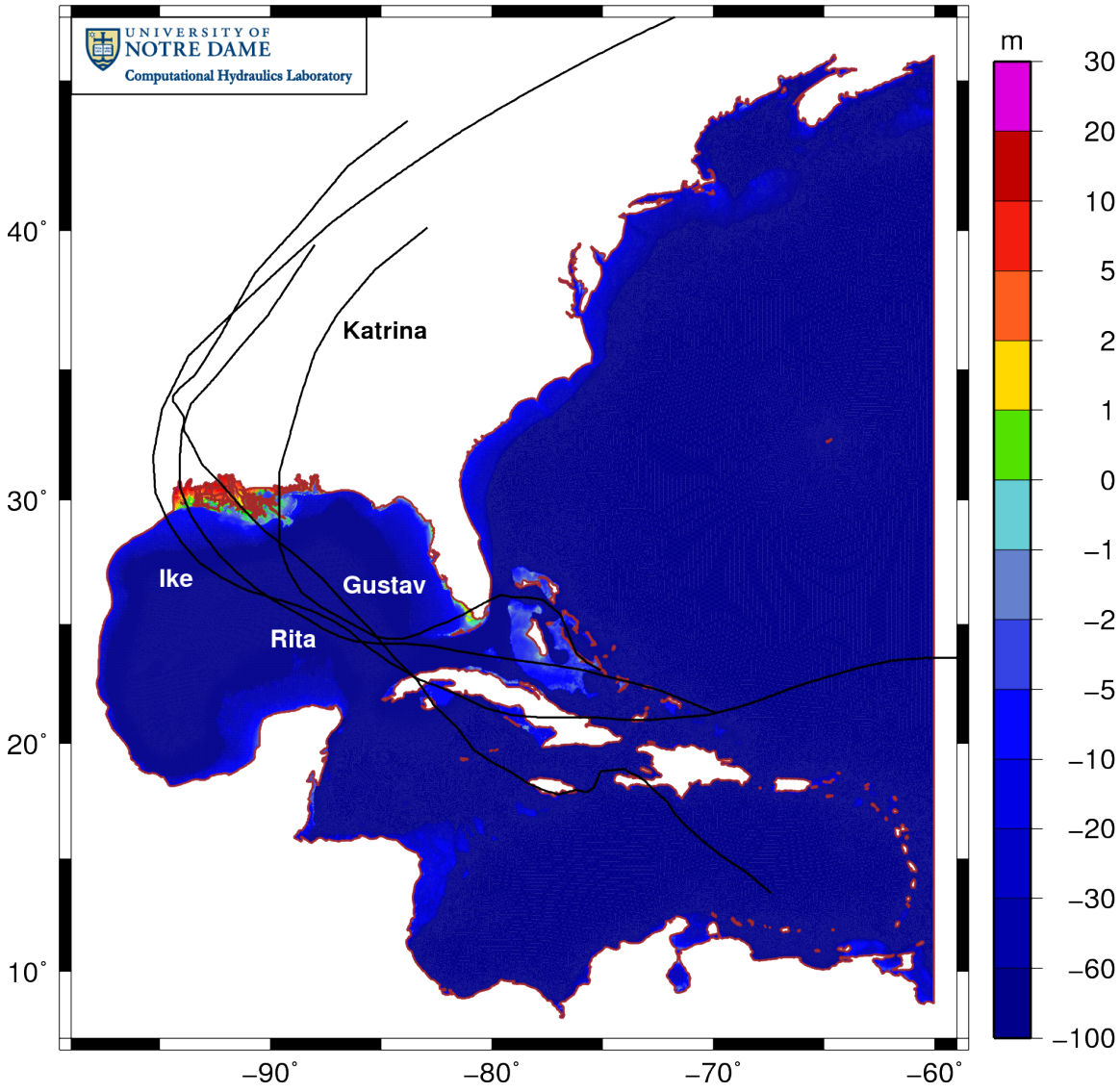

Figure 6.5. Bathymetry/topography (m) of the SL16 mesh. The tracks of the four historical storms are shown.

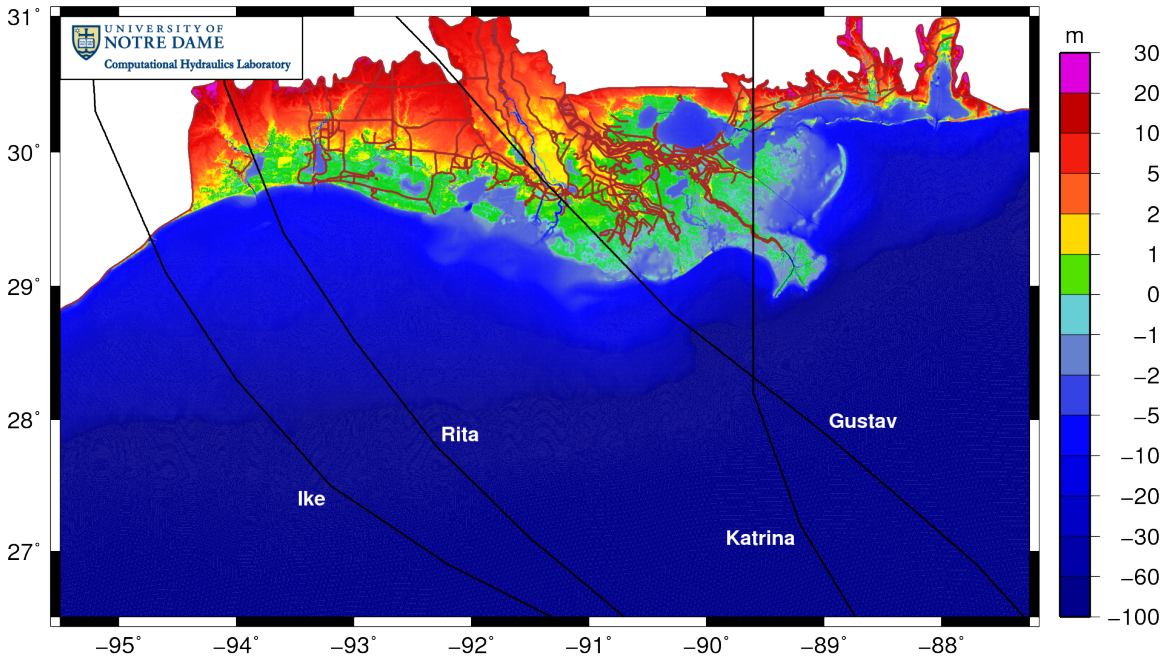

Figure 6.6. Bathymetry/topography (m) of the SL16 mesh in the northern Gulf of Mexico. The tracks of the four historical storms are shown.

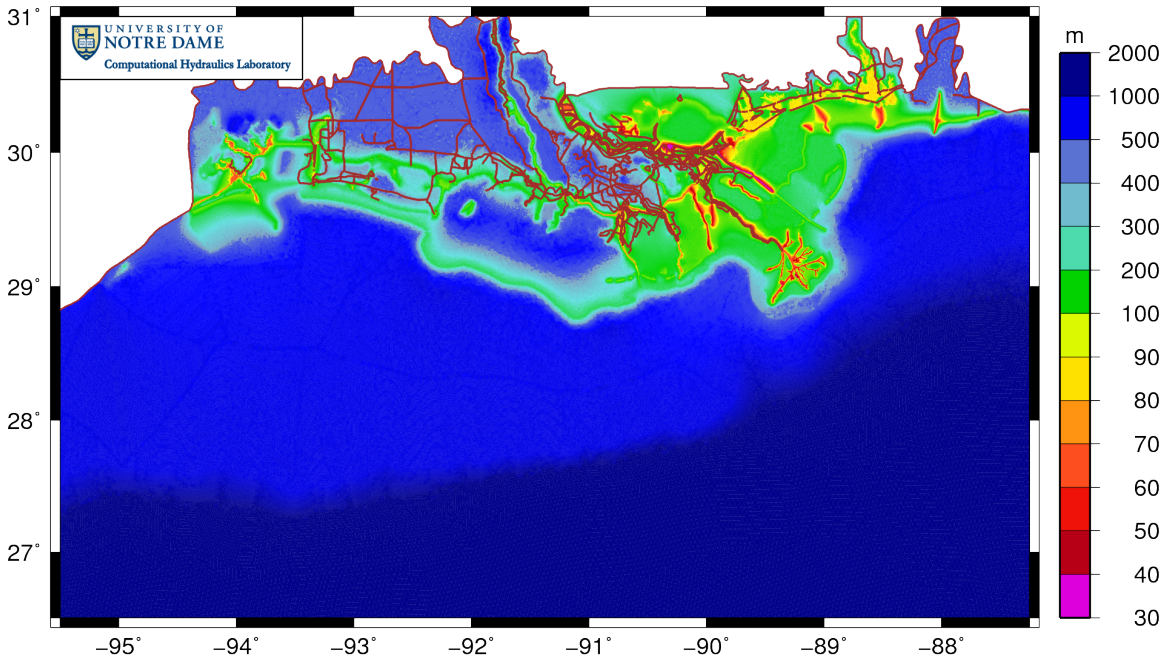

Figure 6.7. Mesh resolution (m) of the SL16 mesh in the northern Gulf of Mexico.

Figures 6.5 - 6.6, the tracks of these storms provide good coverage of southern Louisiana, with Katrina and Gustav impacting the Mississippi River and New Orleans in the southeast, and Rita and Ike impacting the low-lying marshes and bayous throughout southern Louisiana. In addition, the measurement data associated with these storms is extensive and a good test of the models' skill at simulating waves and surge.

Wind fields for the four storms were data-assimilated by using NOAA's Hurricane Research Division Wind Analysis (H*Wind) system (Powell, 1996; 1998; 2010), and then blended with larger scale winds using the Interactive Objective Kinematic Analysis (IOKA) system (Cox *et al.*, 1995; Cardone *et al.*, 2007). ADCIRC interpolates these wind fields to its unstructured mesh, and then shares the wind speeds with SWAN. Both models apply a wind drag coefficient that depends on storm sector (Powell *et al.*, 2003; 2006; Dietrich *et al.*, 2010c).

In the present hindcasts, the SWAN time step (and thus the coupling interval) is taken to be 600s. SWAN utilizes 36 directional bins of constant width 10°, and 40 frequency bins that increase logarithmically over the range 0.031-1.42Hz. Wind input is based on the formulation from Snyder *et al.* (1981), whitecapping is applied via the modified expression of Rogers *et al.* (2003), and nonlinear interactions are allowed for the quadruplets by using the Discrete Interaction Approximation of Hasselmann *et al.* (1985). In shallow water, bottom friction is parameterized as described above, while depth-induced breaking is computed with a spectral version of the model due to Battjes and Janssen (1978) with the breaking index $\gamma = 0.73$. Wave refraction is enabled only in the northern Gulf.

ADCIRC utilizes an implicit solution of the GWCE, with a time step of 1s. Its water levels are adjusted for the regional difference between LMSL and NAVD88

(2004.65) and the seasonal fluctuation in sea level in the Gulf of Mexico. Bottom friction is parameterized using a Manning's n formulation, as described above. The Mississippi and Atchafalaya Rivers are forced with flow rates that are representative of the conditions during the storms. In addition, seven tidal constituents are forced on the open boundary in the Atlantic Ocean. The rivers and tides are allowed to ramp to a dynamic equilibrium for 18 days prior to the start of the wind and wave forcing.

Because of the large amount of measured data, the validation results will be presented as summary statistics that describe generally the model's performance.

6.5.1 Katrina (2005)

Katrina devastated large portions of southern Louisiana, Mississippi and Alabama during the 2005 hurricane season (Bunya *et al.*, 2010; Dietrich *et al.*, 2010a). It strengthened to a Category 5 storm while in the Gulf, and it generated large waves with measured significant heights of 17m offshore of the Mississippi River delta (Figure 6.8a). Its easterly winds pushed storm surge across the Louisiana-Mississippi continental shelf and against the protruding delta, where it collected against the levees of the Mississippi River. The storm made landfall in Plaquemines Parish and tracked northward, over the levees and sounds to the east of New Orleans, and its eye passed within 50km of the city itself. As the storm moved through the system, it pushed northward the surge that had collected against the river levees; this surge moved over the marshes and built along the coastlines of Mississippi and Alabama (Figure 6.8b). The recorded peak surge of 8.8m is the largest ever measured in the United States (Ebersole et al., 2007). Table 6.1 summarizes the available measured data for Katrina. For waves, the

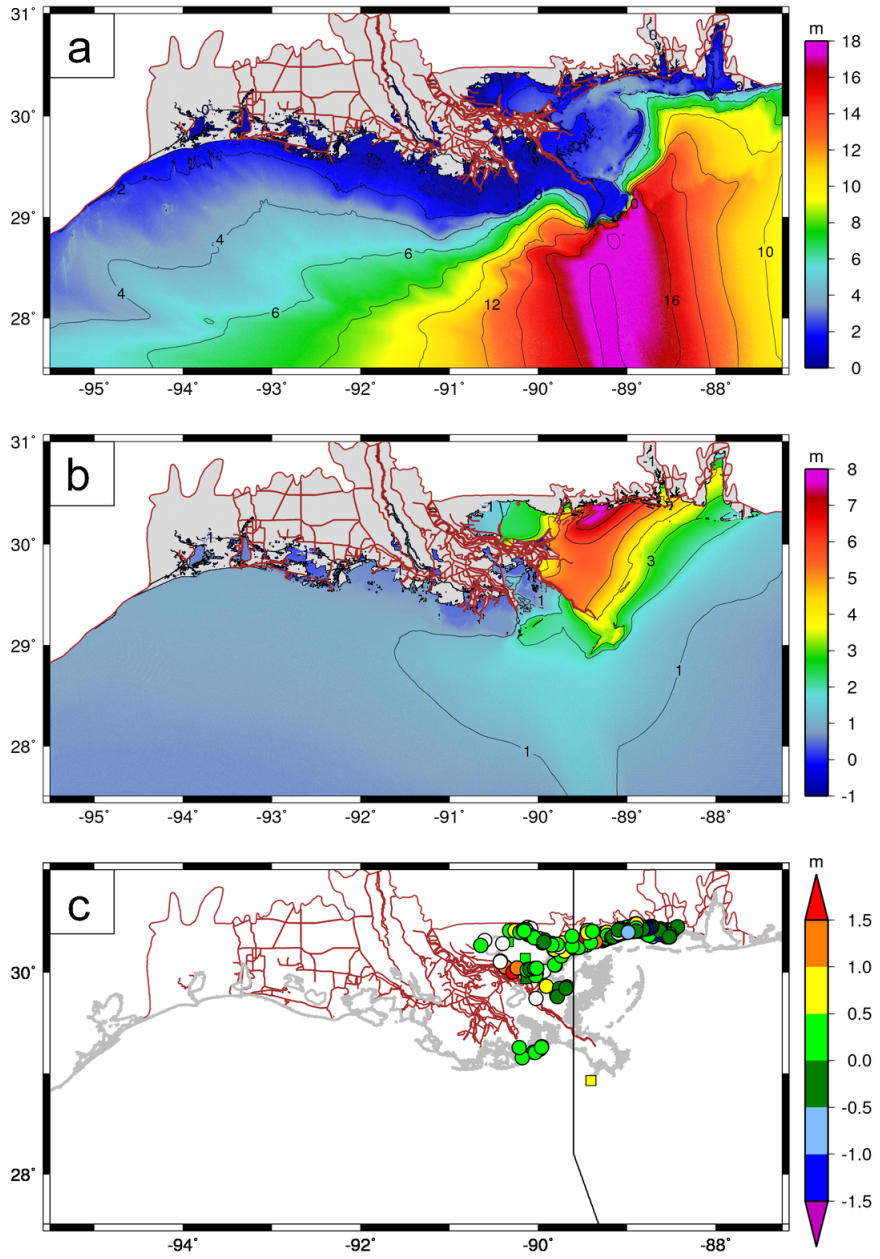

Figure 6.8. Contour plots of maximum (a) wave heights (m) and (b) water levels relative NAVD88 (2004.65) during Katrina in southern Louisiana. Panel (c) indicates locations of the URS/FEMA HWMs (circles) and hydrographs (squares) for Katrina in southern Louisiana. The points are color-coded to show the errors between measured and modeled peak water levels; green points indicate matches within 0.5m. White points indicate locations that were never wetted by ADCIRC.

NDBC and CSI measured time series of wave parameters at buoys in the deeper Gulf and stations in the nearshore. And for water levels, the USGS and NOAA measured time series at a total of nine stations in southeastern Louisiana, while the URS/FEMA and USACE collected a total of 399 HWMs after the storm. These locations are shown spatially in Figure 6.8c and are color-coded based on the error between the measured and modeled peak water levels; note the computed SWAN+ADCIRC water levels are within 0.5m at 305 of the 367 (83 percent) locations that were wetted during the simulation. A scatter plot of measured-to-modeled peak water levels (Figure 6.9) indicates that SWAN+ADCIRC matches well the peak surge, as the best-fit slope is 0.999 and the R^2 value is 0.935.

To quantify the models' skill at capturing all aspects of the measured time series, the Scatter Index (SI) is used as:

$$SI = \frac{\sqrt{\frac{1}{N}\sum_{i=1}^{N}(E_i - \bar{E})^2}}{\frac{1}{N}\sum_{i=1}^{N} O_i}, \tag{6.2}$$

where N is the number of observations, $E_i = S_i - Oi$ is the error between the measured (S_i) and modeled (O_i) values, and $\bar{E}$ is the mean error. Thus the SI is the ratio of the standard deviation of the measured-to-modeled errors to the mean measured value. Table 6.2 summarizes the mean SI for water levels, significant wave heights, and peak and mean periods for the four historical storms. Note that this analysis is performed over 3-5 days near the landfall of each storm, and it excludes comparisons at locations where the measurements stopped during the peak of the storm, where there was an obvious datum error, or where SWAN+ADCIRC never wetted due to a lack of sub-mesh-scale features. The SI for Katrina are good, with a value of 0.173 for the water levels and values in the range of 0.150-0.243 for the wave parameters.

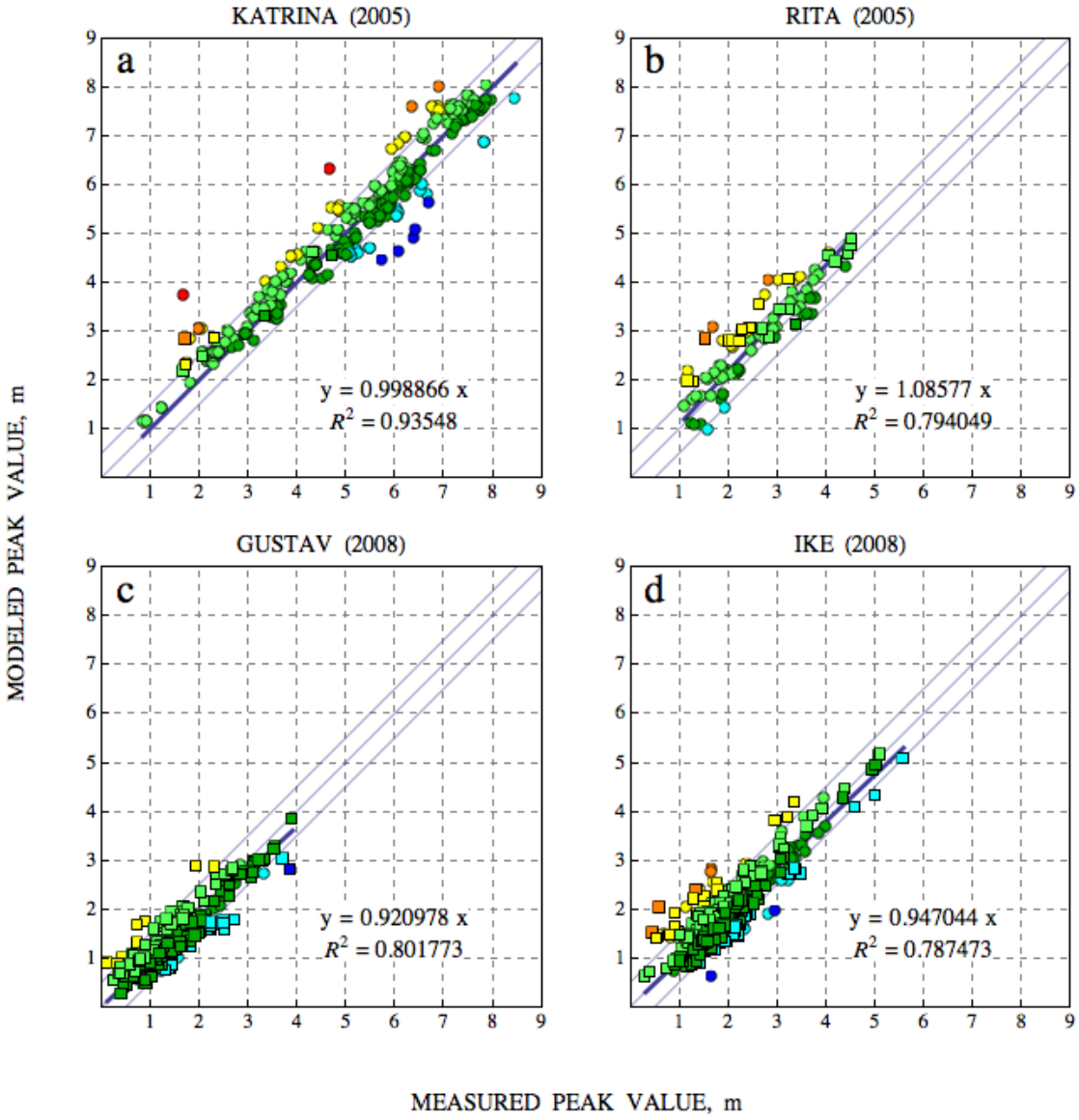

Figure 6.9. Scatter plot of USACE and URS/FEMA HWMs (circles) and peak hydrograph water levels (squares) for: (a) Katrina, (b) Rita, (c) Gustav and (d) Ike. Green points indicate a match within 0.5m. Red, orange, yellow and light green circles indicate overprediction by the model; green, blue, dark blue and purple circles indicate underprediction.

TABLE 6.1

SUMMARY OF AVAILABLE MEASUREMENT DATA

Type	Source	Katrina	Rita	Gustav	Ike	Reference
Waves	NDBC	14	11	12	12	http://www.ndbc.noaa.gov
	CSI	3	2	5	5	http://www.wavcis.lsu.edu
	AK			16		Kennedy *et al.*, 2010a
	USACE-CHL			6	4	Dietrich *et al.*, 2010c
Water levels	CSI			5	5	http://www.wavcis.lsu.edu
	AK			16		Kennedy *et al.*, 2010a
	NOAA	3		26	26	http://www.tidesandcurrents.noaa.gov
	USACE-CHL			6	4	Dietrich *et al.*, 2010c
	USACE			54	54	USACE New Orleans District
	USGS (Deployable)		23	61	16	McGee *et al.*, 2006; Walters, 2009
	USGS (Permanent)	6		48	48	Walters, 2009
	CRMS			243	256	http://www.lacoast.gov
High-water marks	URS/FEMA	193	84	82	181	URS, 2006a; URS, 2006b; FEMA, 2009
	USACE	206				Ebersole *et al.*, 2007

TABLE 6.2

SUMMARY OF ERROR STATISTICS

Storm	Water Levels			Significant Wave Heights	Peak Periods	Mean Periods
	Best-Fit Slope	Best-Fit R^2	Mean *SI*	Mean *SI*	Mean *SI*	Mean *SI*
Katrina	0.999	0.935	0.173	0.243	0.227	0.150
Rita	1.086	0.794	0.292	0.229	0.181	0.120
Gustav	0.921	0.802	0.345	0.398	0.545	0.223
Ike	0.947	0.787	0.204	0.309	0.579	0.173

6.5.2 Rita (2005)

Rita was a strong Category 5 storm, and it generated large waves as it moved across the Gulf. It was a threat to impact Galveston and Houston, but it turned northward and made landfall near the border between Texas and Louisiana. As it moved onto the continental shelf near southwestern Louisiana, it created storm surge along the coastline that peaked at 4.7m (Bunya *et al.*, 2010; Dietrich *et al.*, 2010a). As the storm made landfall, the winds shifted to blow northward, pushing the surge over the low-lying marshes and bayou in the southwestern part of the state (Figure 6.10). Rita is a good validation test because it allows for an examination of the model's skill in representing the friction-dominated flooding and recession processes.

The NDBC collected deep-water wave measurements at 11 buoys in the Gulf, and the CSI collected nearshore wave measurements at two stations on the continental shelf. The USGS deployed 23 gages to record water levels in southwestern Louisiana as Rita made landfall, and the URS/FEMA collected 84 HWMs after the storm. These data are summarized in Table 6.1. The USGS hydrographs are of particular interest because they include the slow recession of surge from the marshes back into the Gulf (Bunya *et al.*, 2010; Dietrich *et al.*, 2010a).

The locations of the USGS gages and URS/FEMA HWMs are shown in Figure 6.10c. The match is generally good, although SWAN+ADCIRC tends to overpredict at some locations west of Vermilion Bay, near Calcasieu Lake, and near Sabine Pass. This trend is confirmed in the scatter plot of measured-to-modeled peak water levels (Figure 6.9), as 73 of the 99 (73 percent) of the locations show a match within 0.5m, and the slope of the best-fit line is 1.086 and the R^2 value is 0.794. The scatter indices, *SI*, for the ADCIRC water levels and SWAN wave

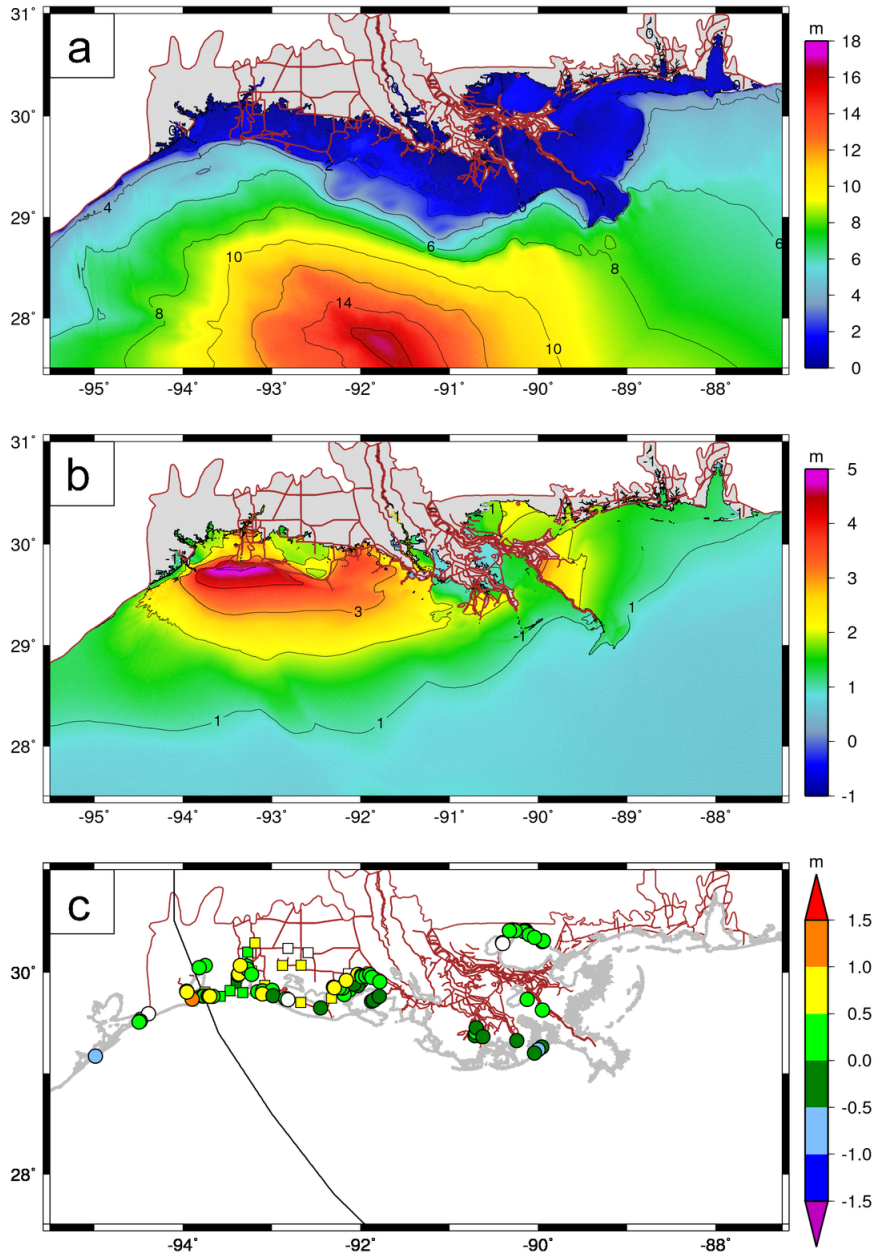

Figure 6.10. Contour plots of maximum (a) wave heights (m) and (b) water levels relative NAVD88 (2004.65) during Rita in southern Louisiana. Panel (c) indicates locations of the URS/FEMA HWMs (circles) and hydrographs (squares) for Katrina in southern Louisiana. The points are color-coded to show the errors between measured and modeled peak water levels; green points indicate matches within 0.5m. White points indicate locations that were never wetted by ADCIRC.

parameters are shown in Table 6.2. Note the excellent agreement between the computed SWAN wave parameters and the measured results, indicating that SWAN simulates well the deep-water wave behavior in the Gulf.

6.5.3 Gustav (2008)

Gustav reached Category 4 strength on the Saffir-Simpson scale while in the Caribbean Sea, but it weakened as it crossed western Cuba. It tracked northwestward across the Gulf, peaking at Category 3 strength before making landfall near Grand Isle as a strong Category 1 storm. It generated large waves in the Gulf that propagated northward before breaking near the Mississippi River delta and the barrier islands offshore of Louisiana and Mississippi (Figure 6.11a). Its eye never came closer than 75km to New Orleans, but it created significant surge on all sides of the city. Surge was pushed into Lake Pontchartrain to the north, up the Mississippi River and into the canals that run into the heart of the city, and over the marshes to the south and east (Figure 6.11b). The levee protection system was not breached, but there were reports of wave overtopping (Dietrich *et al.*, 2010c).

The storms of 2008 are described by a relatively large amount of measured data. Advancements in gage hardening and innovative deployment techniques resulted in expanded measurements of waves in deep water and nearshore, and water levels throughout the marshes of southern Louisiana. These data are summarized in Table 6.1 and describe how Gustav's waves and surge impacted the region; a detailed description of the storm's evolution is given in Dietrich *et al.* (2010c). The nearshore wave measurements from Kennedy *et al.* (2010a) and the USACE-CHL are particularly interesting because they represent some of the first measurements

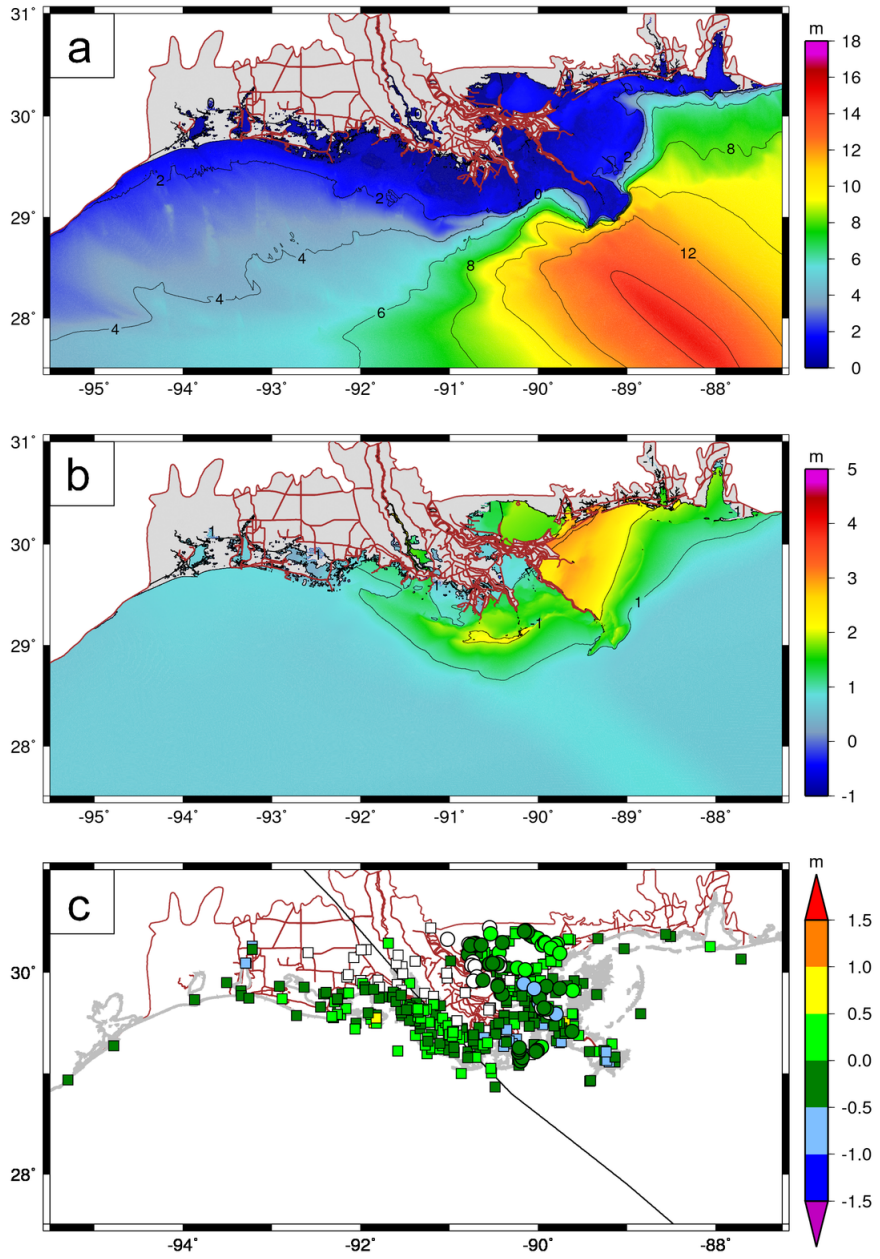

Figure 6.11. Contour plots of maximum (a) wave heights (m) and (b) water levels relative NAVD88 (2004.65) during Gustav in southern Louisiana. Panel (c) indicates locations of the URS/FEMA HWMs (circles) and hydrographs (squares) for Katrina in southern Louisiana. The points are color-coded to show the errors between measured and modeled peak water levels; green points indicate matches within 0.5m. White points indicate locations that were never wetted by ADCIRC.

taken along the coastline and inside the marshes during a hurricane.

The SWAN+ADCIRC hindcast of Gustav on the SL16 mesh provides a good match to the measured data. The locations of the HWMs and hydrographs are shown in Figure 6.11c; note that SWAN+ADCIRC matches within 0.5m of the peak water level at most locations. A scatter plot of measured-to-modeled peak water levels (Figure 6.9) has a best-fit slope of 0.921 and an R^2 value of 0.802. Furthermore, the *SI* in Table 6.2 indicate good matches between the measured waves and surge and the computed SWAN+ADCIRC results. The mean *SI* are larger for Gustav than for the previous storms, especially for the significant wave heights and peak wave periods, but these larger values reflect the variability in the measured data in the nearshore environment. For example, the measured significant wave heights and peak wave periods show extreme variability at the USACE-CHL gages located inside the Biloxi and Terrebonne marshes. If we disregard those gages, then the mean *SI* for the significant wave heights improve to 0.376, and the mean *SI* for the peak wave periods improve to 0.410. The Kennedy and USACE-CHL gages did not measure the mean wave periods, and the mean *SI* for that parameter is a relatively small 0.223.

6.5.4 Ike (2008)

Although Ike tracked farther west than the other three hurricanes and made landfall in Galveston, outside the coverage of the SL16 mesh, it impacted all of southern Louisiana. It created a forerunner surge that traveled down the Louisiana-Texas shelf about 12-24hr before landfall (Kennedy *et al.*, 2010b), and its waves and storm surge inundated large sections of the marshes and bayou of southwest Louisiana (Figure 6.12). The storm was large enough that its outer

winds also pushed waves and surge to the east, on the Louisiana-Mississippi shelf and against the levee protection system near New Orleans.

There is a wealth of measured data to describe Ike's impact on southern Louisiana, as summarized in Table 6.1. As with the other storms, we note that data was excluded from the analysis at locations where the measurements stopped during the peak of the storm, where there was an obvious datum error, or where SWAN+ADCIRC never wetted due to a lack of sub-mesh-scale features. The stations are shown spatially in Figure 6.12c; note that the overall agreement is good, with many green points indicating errors within 0.5m. The notable exception is at the locations in the Atchafalaya River basin, which has significantly less resolution relative to other regions of the mesh, as shown in Figure 6.7. The fine-scaled channels and distributaries are not resolved, and thus the surge is not modeled as having propagated to these locations. In regions where the resolution is sufficient, however the match is quite good.

Table 6.2 contains a summary of the error statistics for Ike, including the best-fit slope of 0.947 and R^2 value of 0.787 from the scatter plot in Figure 6.9. The mean SI values are also good, except for the wave parameters when the marsh gages of USACE-CHL are included in the analysis. For example, the relatively large SI of 0.579 for the peak wave periods decreases to 0.234 when the four USACE-CHL gages are excluded from the analysis. The data from those gages, although invaluable for their description of the wave behavior in the Terrebonne and Biloxi marshes, contain more measurement uncertainty than the data from the offshore gages, stations and buoys.

When combined with the summary error statistics from the previous three storms, these results indicate that SL16 provides a faithful representation of south-

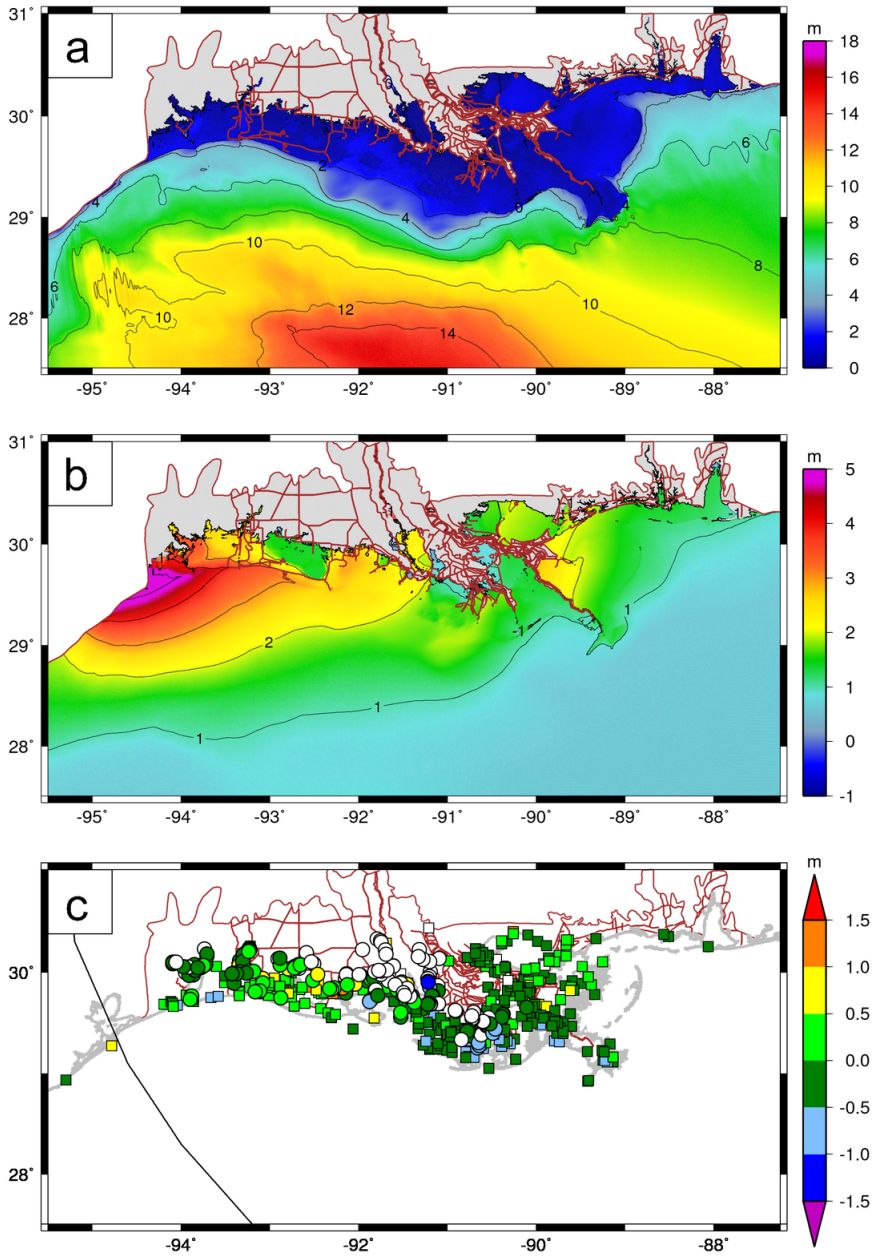

Figure 6.12. Contour plots of maximum (a) wave heights (m) and (b) water levels relative NAVD88 (2004.65) during Ike in southern Louisiana. Panel (c) indicates locations of the URS/FEMA HWMs (circles) and hydrographs (squares) for Katrina in southern Louisiana. The points are color-coded to show the errors between measured and modeled peak water levels; green points indicate matches within 0.5m. White points indicate locations that were never wetted by ADCIRC.

ern Louisiana and its response to hurricane waves and storm surge. These four recent hurricanes impacted different parts of the region and in different ways. Katrina and Gustav pushed waves and surge onto the relatively narrow Louisiana-Mississippi shelf and threatened New Orleans, while Rita and Ike made landfall farther west and flooded large portions of the marshes and bayou of southwest Louisiana. SWAN+ADCIRC and the SL16 mesh simulate well these different responses.

6.6 Performance

6.6.1 Ranger and Kraken

Ranger is a Sun Constellation Linux cluster located at the Texas Advanced Computing Center (TACC, `http://www.tacc.utexas.edu`) at the University of Texas in Austin. It contains 3,936 SMP compute nodes, each of which has four quad-core AMD Opteron processors, and thus the system has a total of 62,976 computational cores. Each node contains 32 GB of memory that is shared among the cores, and the overall system has 123 TB of memory and a theoretical peak performance of 579 TFLOPS. The specifications of the nodes are shown in Table 6.3.

Kraken is a Cray XT5 cluster located at the National Institute for Computational Sciences (NICS, `http://www.nics.tennessee.edu`). It contains 8,256 compute nodes, each of which has two six-core AMD Opteron processors, and thus the system has a total of 99,072 compute cores. Each node contains 16 GB of memory that is shared among the cores, and the overall system has 129 TB of memory and a theoretical peak performance of 1030 TFLOPS. The specifications of the nodes are shown in Table 6.3.

TABLE 6.3

SPECIFICATIONS OF COMPUTE NODES

	TACC Ranger	NICS Kraken
Node	Sun Blade x6420	Cray XT5
CPU	4 Quad-core AMD Opteron 8356	2 Six-core AMD Opteron 8435
Core	AMD Opteron 8356	AMD Opteron 8435
Frequency	2.3 GHz	2.6 GHz
Architecture	AMD K10 (Barcelona)	AMD K10 (Istanbul)
L1-Cache	64 + 64 KB per core	64 + 64 KB per core
L2-Cache	512 KB per core	512 KB per core
L3-Cache	2048 KB on die shared	6144 KB on die shared

6.6.2 Timing Studies

SWAN+ADCIRC and its individual model components were run on both Ranger and Kraken to produce timing statistics. For these simulations, the wind field for Katrina was used as forcing for both models. Both SWAN and ADCIRC were hot-started at 2005/08/28/0000Z and then run for two days until 2005/08/30/0000Z, thus capturing the peak of the storm as it was making landfall in southeast Louisiana. SWAN+ADCIRC employed the full coupling, with ADCIRC passing winds, water levels, currents and roughness lengths to SWAN, and SWAN passing wave radiation stress gradients to ADCIRC. When ADCIRC was run individually, it did not receive wave forcing from any source. When SWAN was run individually, it read and interpolated the wind field to its unstructured

sub-meshes, but it did not receive water levels, currents or roughness lengths from any source. File output was disabled in both models.

Figure 6.13 shows timing results using the implicit and explicit solutions of the GWCE in ADCIRC, for both Ranger and Kraken. We note several aspects of the behavior of the coupled model and its components.

First, SWAN and the explicit version of ADCIRC scale linearly through 7,168 compute cores. A comparison of the maximum water levels between implicit and explicit solutions in ADCIRC showed only minor differences in regions near wetting and drying, and thus the explicit version of ADCIRC was deemed acceptable on the SL16 mesh with a time step of 1s. Because of this, the explicit version of ADCIRC is much faster than the implicit version; for example, on 1,014 cores, it requires only 35 min/day of Katrina simulation, compared to 76 min/day for the implicit version. When SWAN is coupled to the explicit version, the resulting model also scales linearly, achieving minima of 28 and 32 min/day of Katrina simulation on Ranger and Kraken, respectively. As expected, the implicit version of ADCIRC scales linearly as well, but only through about 3,072 cores. Its required global communication causes its scaling to tail off at higher numbers of compute cores. This deterioration also affects the coupled model, which loses its linear scaling when it is decomposed on numbers of cores larger than 3,072.

Second, the individual compute cores are faster on Kraken than Ranger, but its interconnect is slower. The faster speed is evident in the timing curves; for example, on 1,024 cores and using the implicit solution of the GWCE (Figure 6.13a-b), the simulation requires 222 min/day on Ranger, but only 170 min/day on Kraken. However, at high numbers of cores, the network on Kraken deteriorates the models' performance, especially that of the implicit version of ADCIRC. The scaling

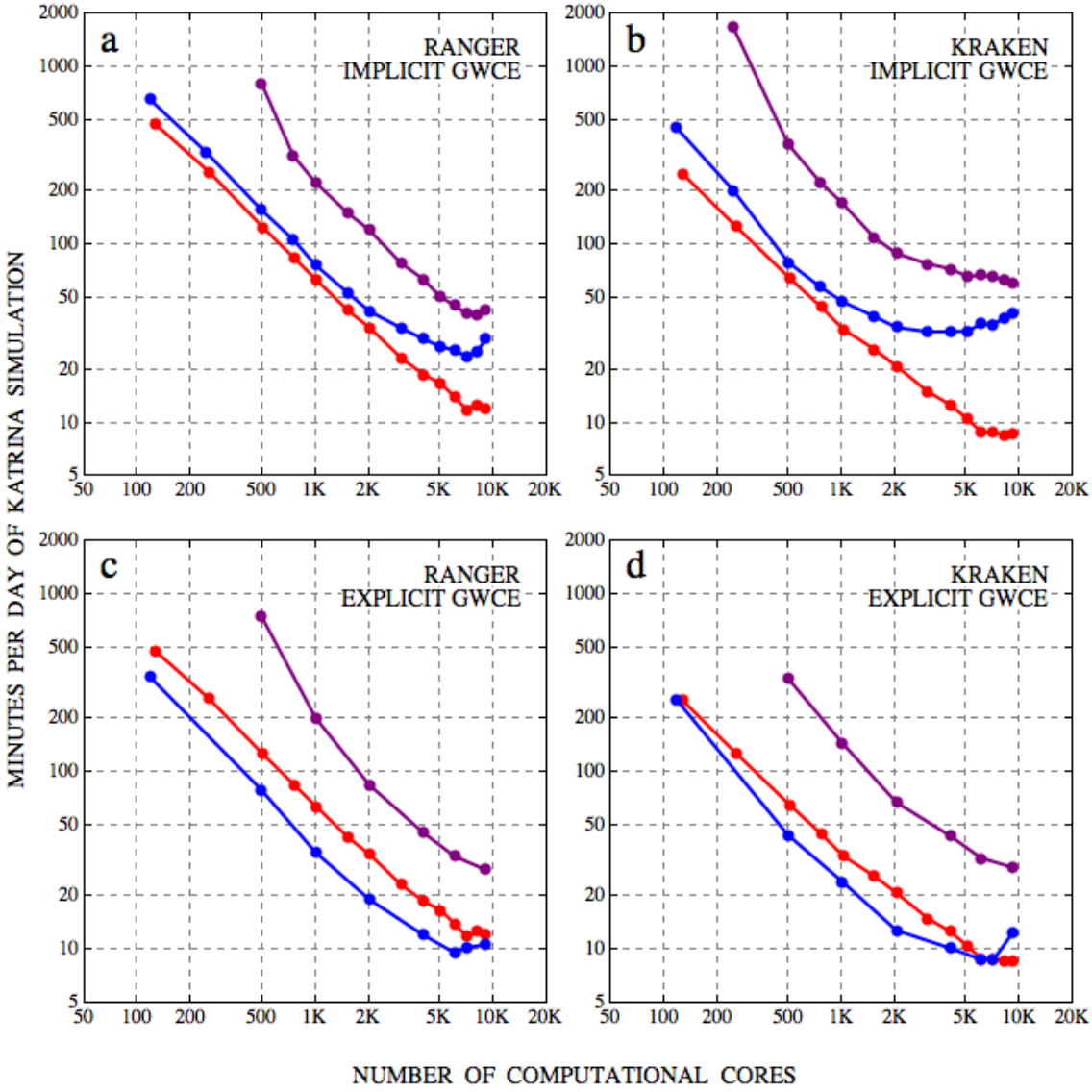

Figure 6.13. Benchmarking results for SWAN (red), ADCIRC (blue) and SWAN+ADCIRC (purple). The left column shows results on TACC Ranger, while the right column shows results on NICS Kraken. The top row shows ADCIRC results using an implicit solution of the GWCE, while the bottom row shows ADCIRC results using an explicit solution of the GWCE.

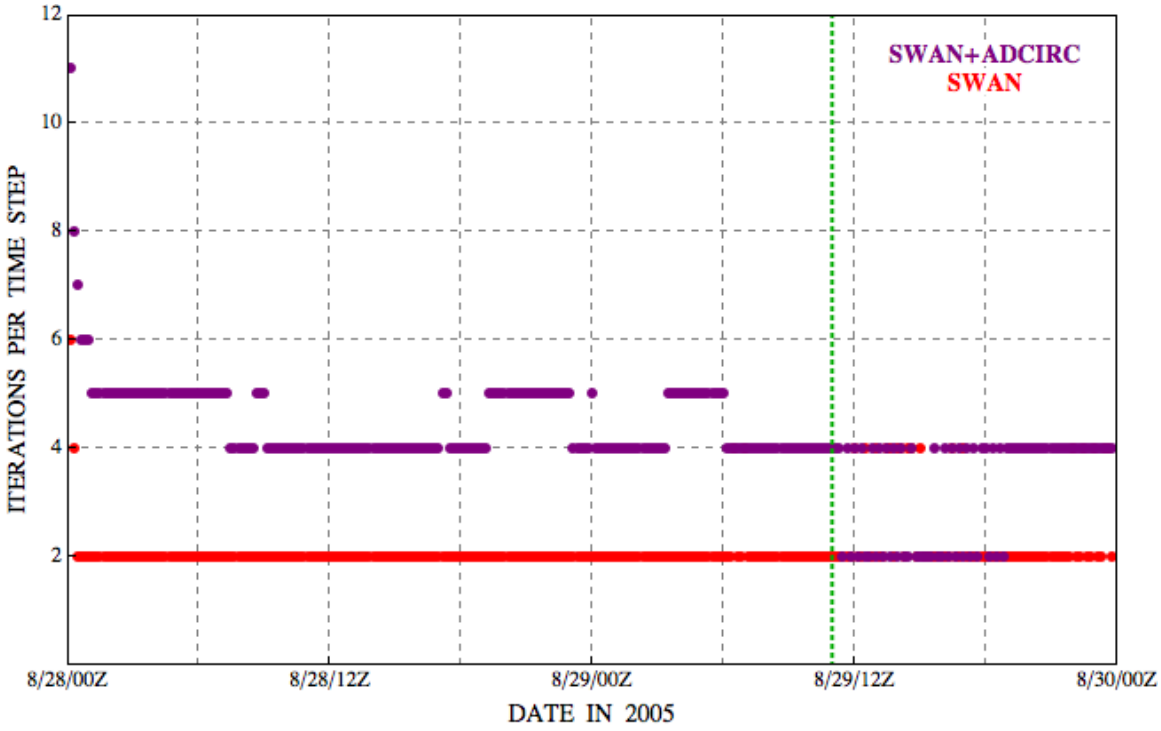

Figure 6.14. Iterations per time step for SWAN when it is run individually (red dots) and as part of the coupled model (purple dots), for the two-day Katrina timing simulation on 1,024 cores. The vertical, dotted green line indicates the initial landfall of Katrina along the lower Mississippi River.

tails off quickly, starting at about 3,072 cores, and prevents the implicit ADCIRC timings from reaching any lower than 32 min/day of Katrina simulation. This behavior deteriorates the performance of the implicit SWAN+ADCIRC, which also does not scale as well on Kraken.

Third, the timings for the coupled model are greater than the combined total of the timings of its individual components. For example, on 1,024 cores on Ranger and using the implicit solution of the GWCE (Figure 6.13a), the SWAN+ADCIRC timing of 222 min/day of Katrina simulation is about 60 percent larger than the

combined total of 63 min/day for the stand-alone SWAN and 76 min/day for the stand-alone ADCIRC. This behavior is caused by the SWAN convergence requirements. When SWAN is run by itself, its only forcing is the wind input, and it requires only two iterations per time step. However, when SWAN is run as part of the coupled model, it receives winds, water levels, currents and roughness lengths from ADCIRC, and thus its solution is more complex. More iterations per time step are required, as shown in Figure 6.14. The convergence requirements remain the same, but the coupled SWAN must iterate more to achieve them, and thus it becomes more expensive computationally. The mechanics of the SWAN+ADCIRC coupling do not add any overhead to the simulation, but the coupled physics do require additional work from the individual model components.

Fourth, at small numbers of cores, the timings increase significantly for the coupled model. For 512 cores on Ranger and 256 cores on Kraken, the problem size becomes too large to maintain within local cache, and thus the coupled model must access data from memory. This timing increase corresponds to about 10,000 mesh vertices per core on Ranger, and 20,000 mesh vertices per core on Kraken. However, as noted in Table 6.3, Ranger shares 2MB of L3 cache on each of its quad-core processors, while Kraken shares 6MB of L3 cache on each of its six-core processors. Thus it can be said that SWAN+ADCIRC requires less than 20,000 mesh vertices per 1MB of shared L3 cache on a per-core basis. When the global mesh is decomposed over smaller numbers of cores, the timings become much slower than expected. However, when the local problem is small enough to be contained on cache, the coupled model does scale linearly, as noted above.

Lastly, all of the models experience a hard lower limit on the timings at high numbers of cores. On Ranger, even the models that otherwise scale linearly reach a

minimum of about 10 min/day, and on Kraken, the minimum is about 8 min/day. This behavior is caused by the reading of the wind fields, which are made available to the models from a single set of files containing pressures and wind speeds. These two files must be read by all of the cores. This input method becomes increasingly expensive when large numbers of cores are accessing the same files. The models cannot continue to scale linearly because the cost of reading the wind fields begins to dominate the overall computational time.

The coupled SWAN+ADCIRC maintains the already-excellent scalability of its components, and it scales linearly to large numbers of cores, especially when ADCIRC solves explicitly the GWCE. Hurricane waves and surge can be modeled efficiently, so that results can be provided in a timely manner.

6.6.3 File Output

As noted above, the coupled model can output as many as 10 global output files containing the wind fields, water levels, currents and several wave parameters. These global files can be large; for example, a file containing water levels at all mesh vertices at 30-min intervals during the two-day Katrina timing simulation would be about 11 GB, while a similar file containing wind speeds at all mesh vertices would be about 21 GB. These file sizes would increase for longer simulations, or if data is written more frequently. This large amount of file output can slow down the computations if it is not handled properly.

The coupled SWAN+ADCIRC utilizes the stand-alone ADCIRC's capability to dedicate cores for file output (Tanaka *et al.*, 2010). Figure 6.15 shows timing results for file output during the two-day Katrina simulation at 30-min intervals. Note the increase in wall-clock timings when the files are written via standard

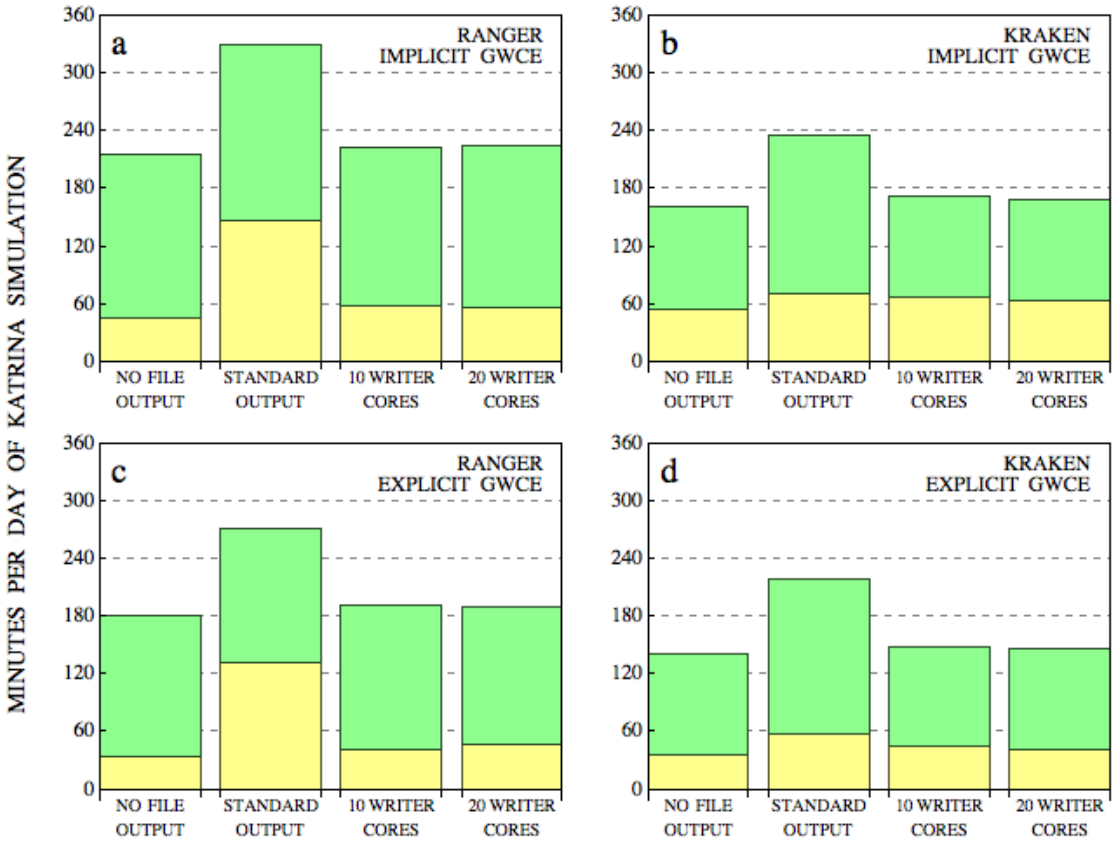

Figure 6.15. Timing results for SWAN+ADCIRC on 1,024 cores (green) and 6,144 cores (yellow). The left column shows results on TACC Ranger, while the right column shows results on NICS Kraken. The top row shows ADCIRC results using an implicit solution of the GWCE, while the bottom row shows ADCIRC results using an explicit solution of the GWCE.

output, *i.e.*, when the computational cores must also manage the writing of the global files. On Ranger with 1,024 cores, the timings increase by 53 percent when ADCIRC solves implicitly the GWCE, and 50 percent for the explicit solution of the GWCE. On Kraken, the timings increase similarly, indicating that a significant portion of the overall simulation is devoted to file output.

When the global mesh is decomposed over 1,024 cores, the results indicate that 10 writer cores are sufficient to manage the file output without slowing the simulation. Each writer core is able to write its time snap of data before the next time snap is available, and thus the compute cores do not have to wait to pass their information to the writer cores. The timings with 10 writer cores are similar to the timings without any file output, for both machines and both GWCE solution methods. Nothing is gained by employing an additional 10 writer cores (or 20 total).

When the global mesh is decomposed over 6,144 cores, the timings decrease accordingly; note the decrease of 79 percent in the wall-clock time for the case without file output in Figure 6.15c. These faster timings are more influenced by the file output, and thus a larger increase is experienced when standard output is employed. For example, when the GWCE is solved explicitly on Ranger with 6,144 cores, the increase is 294 percent. The increases are not as acute on Kraken, indicating that machine manages better its file output.

This increase is not mitigated completely when 10 cores are dedicated for file output. The use of these 10 writer cores does decrease the wall-clock timings, but not to the same level as when file output is disabled. Whereas the writer cores increase the wall-clock timings by 3-7 percent when the global mesh is decomposed over 1,024 cores, they cause an increase of 15-40 percent on 6,144 cores. In this

case, the computational cores have finished the next 30 simulation minutes before the writer cores have finished writing the last time snap of data to the output files, and thus the computational cores must wait to pass information and resume their work. When 20 writer cores are employed, the increase in the wall-clock timings is not as severe, but it does still exist.

Thus, it is important to use a sufficient number of dedicated writer cores for file output. Without them, the simulation time can be increased by 50-300 percent, depending on the domain decomposition, ADCIRC solution algorithm, and machine specifications. And, even when the writer cores are employed, it is important to employ them in a manner that does not slow down the computations. On small numbers of cores, it may be sufficient to utilize one writer core per global output file. However, on large numbers of cores, it is necessary to increase the number of writer cores by using the sequential approach, to ensure that writer cores are always available to receive information from the computational cores.

6.7 Conclusions

The recent coupling of SWAN+ADCIRC allows hurricane waves and circulation to be modeled on unstructured meshes that resolve their generation in deep water and on the continental shelf, their propagation into shallow water, and their dissipation in the complex nearshore environment. In a parallel computing environment, the component models alternate simulation on the same local submeshes. Information can be passed between models through local cache, without the necessity of interpolation, thus ensuring that inter-model communication is inter-core and highly scalable. Intra-model communication is untouched by the coupling, and the component models communicate locally and/or globally, de-

pending on their solution algorithm. The coupling paradigm adds no overhead to the computations, but it does allow waves and circulation to interact in complex problems.

This work validated the coupled model through hindcasts of four recent Gulf hurricanes on the new SL16 mesh, which offers unprecedented resolution in the Gulf of Mexico (4-6km), on the continental shelf (500-1000m), within the wave-dissipation zones (200m), and inside the fine-scale channels and features in southern Louisiana (down to 30m). These hurricanes are represented by a wealth of measurement data, for both waves and water levels, and comparisons show that SWAN+ADCIRC simulates well the evolutions of these storms. Comparisons to high-water marks and peak hydrograph values show the computed ADCIRC water levels to be a faithful match, with best-fit slopes near unity and correlation coefficients R^2 of 0.75 or larger. The scatter indices (SI) for the hydrographs were also in the range of 0.15-0.35 for the four storms, and they indicate that ADCIRC is capturing well the run-up before landfall, the peak water levels, and the recession afterward. When the measurement data with the highest scatter is removed from the analysis, the SI for significant wave heights, peak and mean wave periods are also in the range of 0.15-0.35, again indicating a faithful simulation by SWAN of the wave generation, propagation and dissipation.

SWAN+ADCIRC is also highly efficient. The coupled model was benchmarked on the high-performance computing clusters Kraken and Ranger, by applying a two-day hindcast near landfall of Katrina on the SL16 mesh. The parallel, unstructured version of SWAN scales linearly through 7,168 computational cores, when the small, local problem size is finally counter-acted by the intra-model communication along the boundaries of the sub-meshes. The scalability of ADCIRC

depends on the algorithm employed in its solution of the GWCE. The implicit solution requires global communication, and thus it scales linearly through about 3,072 cores before deteriorating. However, the explicit solution is hampered only by the costs of local communication, and thus it scales linearly through 7,168 cores.

The coupling paradigm adds no overhead to the computations, but the coupled physics do lengthen the run-times relative to those of the component models. The passing from ADCIRC of wind speeds, water levels, currents and roughness lengths requires SWAN to iterate more per time step to achieve the same level of convergence, and thus its computations are more expensive when it is coupled. However, SWAN+ADCIRC scales as well as its components, including linear scaling to 7,168 cores, on both Ranger and Kraken, when the GWCE is solved explicitly. These results indicate that the coupled model is well-positioned for hurricane forecasting applications, which require rapid dissemination of results to emergency managers. SWAN+ADCIRC simulates waves and surge in a way that is both accurate and efficient.

CHAPTER 7

EVOLUTION OF WAVE-CIRCULATION COUPLING

Waves and circulation are linked. Water levels and currents affect the propagation of waves and the location of wave-breaking zones. Wind-driven waves affect the vertical momentum mixing and bottom friction, which in turn affect the circulation. Wave transformation generates radiation stress gradients that drive set-up and currents. Water levels can be increased by 5-20 percent in regions across a broad continental shelf, and by as much as 35 percent in regions of steep slope (Funakoski *et al.*, 2008; Dietrich *et al.*, 2010a).

In the response to Katrina and Rita, ADCIRC was coupled loosely to the deepwater WAM and nearshore STWAVE spectral wave models. This coupling was beneficial; all model components were validated independently, and they were shown to provide a faithful representation of the system's response to these two storms. Waves and storm surge were allowed to develop on the continental shelf and interact with the complex nearshore environment. The resulting modeling system was used extensively for levee design and floodplain delineation.

However, the loose coupling paradigm was shown to have disadvantages. It requires intra-model interpolation at the boundaries of the nested, structured wave meshes and inter-model interpolation between the wave and circulation meshes. This interpolation creates problems with respect to both accuracy and efficiency. Overlapping nested or adjacent wave meshes often have different solutions, and

inter-mesh interpolation can smooth or enhance the integrated wave forcing. Furthermore, even if a component model is locally conservative, its interpolated solution will not necessarily be conservative. Finally, inter-model interpolation must be performed at all vertices of the meshes. This interpolation is problematic in a parallel computing environment, where the communication between sub-meshes is inter-model and semi-global. The sub-meshes must communicate on an area basis (*i.e.*, the information at all vertices on a sub-mesh must be shared). Global communication is costly and can prevent models from being scalable in high-performance computing environments.

For these reasons, the main focus of this work has been the tight coupling of SWAN and ADCIRC. These models utilize the same unstructured mesh, thus eliminating the need for interpolation. Shared information is passed directly through local cache. The resulting SWAN+ADCIRC model simulates waves and surge in a way that is both accurate and efficient. Resolution can be enhanced nearshore and relaxed in deep water, allowing the model to simulate efficiently the evolution of waves and surge. And it is scalable to thousands of computational cores, making it a suitable choice for high-performance computing applications.

A detailed hindcast of Gustav showed SWAN+ADCIRC simulates well the evolution of waves and surge from the deep water, to the continental shelf, and into the complex nearshore environment. This hindcast utilized the latest generation SL16 mesh, which contains more than 5M vertices and varies resolution down to 30-50 m in the fine-scale channels. It also made good use of the coupling, by sharing information about wind forcing and bottom friction between both models. A careful comparison to extensive measurement data showed that SWAN+ADCIRC captures well the system's response to Gustav. Waves were validated against un-

precedented measurements in the nearshore and within the marshes of southern Louisiana, and water levels were validated against gages throughout the region.

Finally, the coupled model has been validated comprehensively through hindcasts of all four recent Gulf hurricanes, which offer coverage of the entire domain of interest, and thus require a consistent, physics-based modeling approach. SWAN+ADCIRC was tested via benchmarking on the TACC Ranger and NICS Kraken machines. The coupling adds no overhead to the simulation, and the coupled model shows linear scaling through 7,168 computational cores. These results indicate that the coupled model is well-positioned for hurricane forecasting applications, which require rapid dissemination of results to emergency managers. SWAN+ADCIRC simulates waves and surge in a way that is both accurate and efficient.

REFERENCES

Amante, C., and B. W. Eakins, 2009: ETOPO1 1 Arc-Minute Global Relief Model: Procedures, Data Sources and Analysis. *NOAA Technical Memorandum NESDIS NGDC-24*, 19 pp.

Arcement, G.J., and V.R. Schneider, 1989: Guide for Selecting Manning's Roughness Coefficients for Natural Channels and Flood Plains. *U.S. Geological Survey Water-Supply Paper 2339*, U.S. Geological Survey, Denver, Colorado.

Atkinson, J.H., J.J. Westerink and J.M. Hervouet, 2004: Similarities between the wave equation and the quasi-bubble solutions to the shallow water equations. *Intl. J. Numer. Methods Fluids*, 45, 689-714.

Barnes, H.H., 1967: Roughness Characteristics of Natural Channels. *U.S. Geological Survey Water Supply Paper 1849*, U.S. Geological Survey, Washington D.C.

Battjes, J.A., 1972: Radiation stresses in short-crested waves. *Journal of Marine Research*, 30(1), 56-64.

Battjes, J.A. and J.P.F.M. Janssen, 1978: Energy loss and set-up due to breaking of random waves. *Proc. 16th Int. Conf. Coastal Engng.*, ASCE, 569-587.

Beven, J.L., and T.B. Kimberlain, 2009: Tropical Cyclone Report, Hurricane Gustav, 25 August - 4 September 2009. NOAA/National Hurricane Center, 38 pp.

Blain, C.A., J.J. Westerink and R.A. Luettich, 1994: The influence of domain size on the response characteristics of a hurricane storm surge model. *J. Geophys. Res., [Oceans]*, 99 (C9), 18467-18479.

Blain, C.A., J.J. Westerink and R.A. Luettich, 1998: Grid convergence studies for the prediction of hurricane storm surge. *Int. J. Num. Meth. Fluids*, 26, 369-401.

Booij, N., R.C. Ris and L.H. Holthuijsen, 1999: A third-generation wave model for coastal regions, Part I, Model description and validation. *J.Geoph.Research*, 104, 7649-7666.

Bretschneider, C.L., H.J. Krock, E. Nakazaki, and F.M. Casciano, 1986: Roughness of Typical Hawaiian Terrain for Tsunami Run-Up Calculations: A Users Manual. J.K.K. Look Laboratory Report, University of Hawaii, Honolulu.

Buczkowski, B.J., Reid, J.A., Jenkins, C.J., Reid, J.M., Williams, S.J., and Flocks, J.G., 2006: usSEABED: Gulf of Mexico and Caribbean (Puerto Rico and U.S. Virgin Islands) offshore surficial sediment data release. *U.S. Geological Survey Data Series 146, version 1.0*. Online at `http://pubs.usgs.gov/ds/2006/146/`.

Bunya, S., J.C. Dietrich, J.J. Westerink, B.A. Ebersole, J.M. Smith, J.H. Atkinson, R. Jensen, D.T. Resio, R.A. Luettich, C. Dawson, V.J. Cardone, A.T. Cox, M.D. Powell, H.J. Westerink, and H.J. Roberts, 2010: A High Resolution Coupled Riverine Flow, Tide, Wind, Wind Wave and Storm Surge Model for Southern Louisiana and Mississippi: Part I - Model Development and Validation. *Monthly Weather Review*, 138(2), 345-377.

Cardone, V.J., R.E. Jensen, D.T. Resio, V.R. Swail and A.T. Cox, 1996: Evaluation of Contemporary Ocean Wave Models in Rare Extreme Events: The "Halloween Storm" of October 1991 and the "Storm of the Century" of March 1993. *Journal of Atmospheric and Oceanic Technology*, 13(1), 198-230.

Cardone, V.J., A.T. Cox, and G.Z. Forristall, 2007: OTC 18652: Hindcast of Winds, Waves and Currents in Northern Gulf of Mexico in Hurricanes Katrina (2005) and Rita (2005). *2007 Offshore Technology Conference*, Houston, TX.

Cardone, V. J. and A. T. Cox, 2007: Tropical cyclone wind forcing for surge models: critical issues and sensitivities. First JCOMM International Storm Surge Symposium. Seoul, Korea. October, 2007. Submitted to *Natural Hazards*.

Chen, Q., L. Wang and R. Tawes, 2008: Hydrodynamic Response of Northeastern Gulf of Mexico to Hurricanes. *Estuaries and Coasts*, 31(6), 1098-1116.

Chow, V.T., 1959: *Open Channel Hydraulics*. McGraw-Hill Book Company, New York.

Collins, N., G. Theurich, C. DeLuca, M. Suarez, A. Trayanov and V. Balaji, 2005: Design and Implementation of Components in the Earth System Modeling Framework. *International Journal of High Performance Computing Applications*.

Cox, A.T., J.A. Greenwood, V.J. Cardone, and V.R. Swail, 1995: An interactive objective kinematic analysis system. *Fourth International Workshop on Wave Hindcasting and Forecasting*, Banff, Alberta, Canada, Atmospheric Environment Service, 109-118.

Dawson, C., J.J. Westerink, J.C. Feyen and D. Pothina, 2006: Continuous, Discontinuous and Coupled Discontinuous-Continuous Galerkin Finite Element Methods for the Shallow Water Equations. *Int. J. for Num. Meth. Fluids*, 52, 63-88.

Dietrich, J.C., S. Bunya, J.J. Westerink, B.A. Ebersole, J.M. Smith, J.H. Atkinson, R. Jensen, D.T. Resio, R.A. Luettich, C. Dawson, V.J. Cardone, A.T. Cox, M.D. Powell, H.J. Westerink, and H.J. Roberts, 2010a: A High Resolution Coupled Riverine Flow, Tide, Wind, Wind Wave and Storm Surge Model for Southern Louisiana and Mississippi: Part II - Synoptic Description and Analyses of Hurricanes Katrina and Rita. *Monthly Weather Review*, 138, 378-404.

Dietrich, J.C., M. Zijlema, J.J. Westerink, L.H. Holthuijsen, C.N. Dawson, R.A. Luettich, R. Jensen, J.M. Smith, G.S. Stelling, and G.W. Stone, 2010b: Modeling Hurricane Waves and Storm Surge using Integrally-Coupled, Scalable Computations. *Coastal Engineering*, in press, DOI: 10.1016/j.coastaleng.2010.08.001.

Dietrich, J.C., J.J. Westerink, A.B. Kennedy, J.M. Smith, R. Jensen, M. Zijlema, L.H. Holthuijsen, C.N. Dawson, R.A. Luettich, M.D. Powell, V.J. Cardone, A.T. Cox, G.W. Stone, H. Pourtaheri, M.E. Hope, S. Tanaka, L. Westerink, H. Westerink, and Z. Cobell, 2010c: Hurricane Gustav (2008) Waves, Storm Surge and Currents: Hindcast and Synoptic Analysis in Southern Louisiana. *Monthly Weather Review*, in review.

Dietrich, J.C., S. Tanaka, J.J. Westerink, C.N. Dawson, R.A. Luettich Jr., M. Zijlema, L.H. Holthuijsen, J.M. Smith, L.G. Westerink, and H.J., Westerink, 2010d: Performance of the Unstructured-Mesh, SWAN+ADCIRC Model in Computing Hurricane Waves and Surge. *Journal of Scientific Computing*, in preparation.

Ebersole, B.A., J.J. Westerink, D.T. Resio, and R.G. Dean, 2007: Performance Evaluation of the New Orleans and Southeast Louisiana Hurricane Protection System, Volume IV - The Storm. *Final Report of the Interagency Performance Evaluation Task Force*, U.S. Army Corps of Engineers, Washington, D.C., 26 March.

Eldeberky, Y., 1996: Nonlinear transformation of wave spectra in the nearshore zone. *Ph.D. thesis*, Delft University of Technology, Delft, The Netherlands.

Federal Emergency Management Agency, 2005: HAZUS: Hazard loss estimation methodology. http://www.fema.gov/hazus/hzindex.shtm.

Federal Emergency Management Agency, 2009: Flood Insurance Study: Southeastern Parishes, Louisiana, Intermediate Submission 2: Offshore Water Levels and Waves, US Army Corps of Engineers, New Orleans District.

Funakoshi, Y., S.C. Hagen and P. Bacopoulos, 2008: Coupling of Hydrodynamic and Wave Models: Case Study for Hurricane Floyd (1999) Hindcast. *ASCE J. Waterway, Port, Coastal, and Ocean Engineering*, 134(6) 321-335.

Garratt, J.R., 1977: Review of drag coefficients over oceans and continents. *Monthly Weather Review*, 105, 915-929.

General Bathymetric Chart of the Oceans, *British Oceanographic Data Centre Centenary Edition-2003*, http://www.bodc.ac.uk.

Garster, J.K., B. Bergen, and D. Zilkoski, 2007: Performance Evaluation of the New Orleans and Southeast Louisiana Hurricane Protection System, Volume II - Geodetic Vertical and Water Level Datums. *Final Report of the Interagency Performance Evaluation Task Force*, U.S. Army Corps of Engineers, Washington, D.C., 26 March.

Gregersen, J.B., P.J.A. Gijsbers, S.J.P. Westen and M. Blind, 2005: OpenMI: The Essential Concepts and their Implications for Legacy Software. *Advances in Geosciences*, 4, 37-44.

Gorman, R.M. and C.G. Neilson, 1999: Modelling shallow water wave generation and transformation in an intertidal estuary. *Coastal Engineering*, 36, 197-217.

Günther, H., 2005: *WAM Cycle 4.5 Version 2.0*, Institute for Coastal Research, GKSS Research Centre Geesthacht, 38pp.

Hagen, S.C., J.J. Westerink, R.L. Kolar and O. Horstmann, 2001: Two dimensional unstructured mesh generation for tidal models. *Int. J. Num. Meth. Fluids*, 35, 669-686.

Hartley, S., R. Pace, III, J.B. Johnston, M. Swann, C. O'Neil, L. Handley, and L. Smith, 2000: A GAP Analysis of Louisiana: Final Report and Data. Lafayette, Louisiana, U.S. Department of the Interior, U.S. Geological Survey.

Hasselmann, K., T.P. Barnett, E. Bouws, H. Carlson, D.E. Cartwright and K. Enke, 1973: Measurements of wind-wave growth and swell decay during the Joint North Sea Wave Project (JONSWAP). *Dtsch. Hydrogr. Z., Suppl.*, 12(A8).

Hasselmann, K., 1974: On the spectral dissipation of ocean waves due to white-capping. *Bound.-layer Meteor.*, 6, 107-127.

Hasselmann, S., K. Hasselmann, J.H. Allender and T.P. Barnett, 1985: Computations and parameterizations of the nonlinear energy transfer in a gravity wave spectrum. Part II: parameterizations of the nonlinear transfer for application in wave models. *J. Phys. Oceanogr.*, 15(11), 1378-1391.

Hendershott, M.C., 1981: Long waves and ocean tides. *Evolution of Physical Oceanography*. B.A. Warren and C. Wunsch, ed., MIT Press, Cambridge, MA, 292-341.

Hill, C., C. DeLuca, V. Balaji, M. Suarez and A. da Silva, 2004: Architecture of the Earth System Modeling Framework. *Computing in Science and Engineering*, 6(1).

Holland, G., 1980: An analytic model of the wind and pressure profiles in hurricanes. *Monthly Weather Review*, 108, 1212-1218.

Holthuijsen, L.H., A. Herman and N. Booij, 2003: Phase-decoupled refraction-diffraction for spectral wave models. *Coastal Engineering*, 49, 291-305.

Janssen, P.A.E.M., 1991: Quasi-linear theory of wind-wave generation applied to wave forecasting. *Journal of Physical Oceanography*, 21, 1631-1642.

Janssen, P., 2004: *The Interaction of Ocean Waves and Wind*. Cambridge: Cambridge University Press.

Kalnay, E., M. Kanamitsu, R. Kistler, W. Collins, D. Deaven, L. Gandin, M. Iredell, S. Saha, G. White, J. Woollen, Y. Zhu, M. Chelliah, W. Ebisuzaki, W. Higgins, J. Janowiak, K.C. Mo, C. Ropelewski, J. Wang, A. Leetmaa, R. Reynolds, R. Jenne, and D. Joseph., 1996: The NCEP/NCAR 40-year reanalysis project. *Bulletin of the American Meteorological Society*. American Meteorological Society, Boston, Massachusetts. Vol. 77, no. 3, pp. 437-471 (1 p.3/4).

Karypis, G. and V. Kumar, 1999: A fast and high quality multilevel scheme for partitioning irregular graphs. *SIAM Journal of Scientific Computing*, 20(1), 359-392.

Kennedy, A.B., U. Gravois, B. Zachry, R.A. Luettich, T. Whipple, R. Weaver, J. Fleming, Q.J. Chen, and R. Avissar, 2010a: Rapidly Installed Temporary Gauging for Waves and Surge during Hurricane Gustav. *Continental Shelf Research*, accepted for publication.

Kennedy, A.B., U. Gravois, B. Zachry, J.J. Westerink, M. Hope, J.C. Dietrich, M.D. Powell, A.T. Cox, R.L. Luettich, and R.G. Dean, 2010b: Hurricane Ike Forerunner Surge: Origin and Implications. *Bulletin of the American Meteorological Society*, in review.

Kim, SY, T. Yasuda and H. Mase, 2008: Numerical analysis of effects of tidal variations on storm surges and waves. *Applied Ocean Research*, 30, 311-322.

Knabb, R. D., J. R. Rhome, and D. P. Brown, 2005: Tropical Cyclone Report, Hurricane Katrina, 23-30 August 2005, National Hurricane Center, NOAA, Dec 2005.

Knabb, R. D., J. R. Rhome, and D. P. Brown, 2006: Tropical Cyclone Report, Hurricane Rita, 18-26 September 2005, National Hurricane Center, NOAA, March 2006.

Kolar, R.L., J.J. Westerink, M.E. Cantekin, C.A. Blain, 1994: Aspects of nonlinear simulations using shallow water models based on the wave continuity equations. *Computers and Fluids*, 23(3), 1-24.

Komen, G., L. Cavaleri, M. Donelan, K. Hasselmann, S. Hasselmann, and P.A.E.M. Janssen, 1994: *Dynamics and Modeling of Ocean Waves*. Cambridge University Press, Cambridge, UK, 560 pages.

Kubatko, E.J., S. Bunya, C. Dawson, J.J. Westerink, C. Mirabito, 2009: A Performance Comparison of Continuous and Discontinuous Finite Element Shallow Water Models. *Journal of Scientific Computing*, 40, 315-339.

Le Provost, C., F. Lyard, J. Molines, M. Genco and F. Rabilloud, 1998: A hydrodynamic ocean tide model improved by assimilating a satellite altimeter-derived data set. *J. Geophys. Res. [Oceans]*, 103, 5513-5529.

Longuet-Higgins, M.S. and R.W. Stewart, 1964: Radiation stresses in water waves; physical discussions, with applications. *Deep-Sea Res.*, 11, 529-562.

Louisiana State University, 2004: Louisiana Lidar. http://atlas.lsu.edu/lidar/.

Luettich, R.A. and J.J. Westerink, 2004: Formulation and Numerical Implementation of the 2D/3D ADCIRC Finite Element Model Version 44.XX; http://adcirc.org/adcirc_theory_2004_12_08.pdf.

Madsen, O.S., Y.-K. Poon and H.C. Graber, 1988: Spectral wave attenuation by bottom friction: Theory, *Proc. 21th Int. Conf. Coastal Engineering*, ASCE, 492-504.

Mississippi Automated Resource Information System, 2006: Mississippi Island 10 meter by 10 meter DEM. http://www.maris.state.ms.us/HTM/DownloadData/DEM.html.

McGee, B.D., B.B. Goree, R.W. Tollett, B.K. Woodward, and W.H. Kress, 2006: Hurricane Rita Surge Data, Southwestern Louisiana and Southeastern Texas, September to November 2005. *U.S. Geological Survey Data Series 220*.

Moore, R.V. and I. Tindall, 2005: An Overview of the Open Modelling Interface and Environment (the OpenMI). *Environmental Science and Policy*, 8, 279-286.

Mukai, A., J.J. Westerink, R. Luettich, Jr. and D. Mark, 2002: *Eastcoast 2001: A tidal constituent database for the Western North Atlantic, Gulf of Mexico, and Caribbean Sea*. Tech. Rep. ERDC/CHL TR-02-24, U.S. Army Corps of Engineers. Available at: ERDC Vicksburg (WES), U.S. Army Engineer Waterways Experiment Station (WES), ATTN: ERDC-ITL-K, 3909 Halls Ferry Road, Vicksburg, MS, 39180-6199.

National Geophysical Data Center, 1988: *ETOPO5 Technical report*. National Oceanic and Atmospheric Administration, http://edcsgs9.cr.usgs.gov/glis/hyper/guide/etopo5.

National Ocean Service Hydrographic Survey Division, 1997: *Hydrographic Survey Digital Database*, Vol. 1, 3rd ed., National Oceanic and Atmospheric Administration.

NOAA National Geophysical Data Center, NGDC Coastal Relief Model, Retrieved 01 December 2008, http://www.ngdc.noaa.gov/mgg/coastal/coastal.html.

Pandoe, W.W. and B.L. Edge, 2008: Case Study for a Cohesive Sediment Transport Model for Matagorda Bay, Texas, with Coupled ADCIRC 2D-Transport and SWAN Wave Models. *ASCE J. Hydraulic Engineering*, 134(3), 303-314.

Powell, M., S. Houston and T. Reinhold, 1996: Hurricane Andrew's landfall in South Florida. Part I: Standardizing measurements for documentation of surface windfields. *Wea. Forecasting*, 11, 304-328.

Powell, M., S. Houston, L. Amat and N. Morrisseau-Leroy, 1998: The HRD real-time hurricane wind analysis system. *J. Wind Engr. Indust. Aero.*, 77-78: 53-64.

Powell, M.D., P.J. Vickery, T.A. Reinhold, 2003: Reduced drag coefficient for high wind speeds in tropical cyclones. *Nature*, 422: 279-283.

Powell, M., 2006: Drag Coefficient Distribution and Wind Speed Dependence in Tropical Cyclones. *Final Report to the National Oceanic and Atmospheric Administration (NOAA) Joint Hurricane Testbed (JHT) Program.*

Powell, M. D. and T. A. Reinhold, 2007: Tropical cyclone destructive potential by integrated kinetic energy. *Bull. Amer. Meteor. Soc.*, 87, 513-526.

Powell, M. D., S. Murillo, P. Dodge, E. Uhlhorn, J. Gamache, V. Cardone, A. Cox, S. Otero, N. Carrasco, B. Annane and R. St. Fleur, 2008: Reconstruction of Hurricane Katrina's Wind field for Storm Surge and Wave Hindcasting. *Ocean Engineering*, 37, 26-36.

Resio, D.T., 2007: *White Paper on Estimating Hurricane Inundation Probabilities.* U.S. Army Engineering Research and Development Center, Vicksburg, MS.

Resio, D.T. and J.J. Westerink, 2008: Modeling the Physics of Storm Surges. *Physics Today*, 61, 9, 33-38.

Ris, R.C., N. Booij and L.H. Holthuijsen, 1999: A third-generation wave model for coastal regions, Part II, Verification. *J.Geoph.Research*, 104, 7667-7681.

Rogers, W.E., P.A. Hwang and D.W. Wang, 2003: Investigation of wave growth and decay in the SWAN model: three regional-scale applications. *J. Phys. Oceanogr.*, 33, 366-389.

Sheremet, A., A.J. Mehta, B. Liu, and G.W. Stone. 2005: Wave-sediment interaction on a muddy inner shelf during Hurricane Claudette. *Estuarine, Coastal and Shelf Science*, 63, 225-233.

SiadatMousavi, S.M., F. Jose, and G.W. Stone, 2009: Simulating Hurricane Gustav and Ike Wave Fields along the Louisiana Innershelf: Implementation of an Unstructured Third-Generation Wave Model, SWAN. *Proceedings of the Oceans 2009 Conference*, Biloxi, MS, 873-880.

Smith, J.M., 2000: Benchmark Tests of STWAVE. *Proceedings of the 6th International Workshop on Wave Hindcasting and Forecasting*, Environment Canada, 369-379.

Smith, J.M., A.R. Sherlock, and D.T. Resio, 2001: STWAVE: Steady-State Spectral Wave Model User's Manual for STWAVE, Version 3.0. USACE, Engineer Research and Development Center, *Technical Report ERDC/CHL SR-01-1*, Vicksburg, MS 80 pp. `chl.erdc.usace.army.mil/Media/2/4/4/erdc-chl-sr-01-11.pdf`.

Smith, S.J., and J.M. Smith, 2001: Numerical Modeling of Waves at Ponce de Leon Inlet, Florida. *J. Waterway, Port, Coastal and Ocean Engineering*, 127(3), 176-184.

Smith, J.M., 2007. Full-plane STWAVE: II. Model overview. ERDC TN-SWWRP-07-5. Vicksburg, MS: U.S. Army Engineer Research and Development Center. `https://swwrp.usace.army.mil/`.

Snyder, R.L., F.W. Dobson, J.A. Elliott, R.B. Long, 1981: Array measurements of atmospheric pressure fluctuations above surface gravity waves. *J. Fluid Mech.*, 102, 1-59.

Stone, G.W., A. Sheremet, X. Zhang, Q. He, B. Liu, and B. Strong, 2003: Landfall of two tropical systems seven days apart along southcentral Louisiana, USA. *Proceedings of Coastal Sediments '03*, Clearwater Beach, Florida, USA, 333-334.

Tanaka, S., S. Bunya, J.J. Westerink, C. Dawson, and R.A. Luettich Jr., 2010: Scalability of an Unstructured Grid Continuous Galerkin Based Hurricane Storm Surge Model. *Journal of Scientific Computing*, in press.

Thompson, E.F. and V.J. Cardone, 1996: Practical modeling of hurricane surface wind fields. *J. Waterways Port, Coastal Eng.*, 122, 195-205.

Thompson, E.F., J.M. Smith, and H.C. Miller, 2004: Wave Transformation Modeling at Cape Fear River Entrance, North Carolina. *J. Coastal Research*, 20 (4), 1135-1154.

Tolman, HL, 2009: User manual and system documentation of WAVEWATCH III version 3.14. NOAA / NWS / NCEP / MMAB Technical Note 276.

Uhlhorn, E. W., P. G. Black, J. L. Franklin, M. Goodberlet, J. Carswell, and A. S. Goldstein, 2007: Hurricane surface wind measurements from an operational stepped frequency microwave radiometer. *Mon. Wea. Rev.*, 135, 3070-3085.

URS, 2006a: *HMTAP Task Order 18*, Mississippi Coastal Analysis Project, Geospatial Technology Task Report (Task 3).

URS, 2006b: *Final coastal and riverine high-water marks collection for Hurricane Katrina in Louisiana*. Final Report for the Federal Emergency Management Agency.

URS, 2006c: *Final coastal and riverine high-water marks collection for Hurricane Rita in Texas*. Final Report for the Federal Emergency Management Agency.
U.S. Army Corps of Engineers, 1963: *Interim Survey Report, Morgan City, Louisiana and Vicinity*, serial no. 63, US Army Engineer District, New Orleans, LA.

U.S. Army Corps of Engineers, 2006: Performance Evaluation of the New Orleans and Southeast Louisiana Hurricane Protection System, Report of the Interagency Performance Evaluation Task Force, USACE, Volume 4, Appendix 3.

U.S. Army Corps of Engineers, 2009: Hydraulics and Hydrology Appendix, *Louisiana Coastal Protection and Restoration: Final Technical Report*, US Army Engineer District, New Orleans, LA, 389 pp.

U.S. Army Engineer District New Orleans, 2005: Water Data Collection Unit, Coastal Engineering Section, Hydraulic and Hydrologic Branch, Private Communication; New Orleans, LA, 70160-0267.

U.S. Department of Defense, 1999: National Imagery Mapping Agency, Digital Nautical Chart, Washington, DC.

U.S. Geological Survey, 2004: National Elevation Dataset. `http://gisdata.usgs.net/ned/`.

U.S. Geological Survey, 2002: USGS topo data., National Elevation Dataset, EROS Data Center, Sioux Falls, SD: `http://ned.usgs.gov`.

Vickery, P. J., Wadhera, D., Powell, M. D., and Y. Chen, 2009: A hurricane boundary layer and wind field model for use in engineering applications. *J. Appl. Meteor. Climate*, 48, 381-405.

Villea, F.J., 2005: *Mississippi GAP Analysis Project*. GAP Analysis Bulletin No. 13, U.S. Department of the Interior, U.S. Geological Survey, `http://www.gap.uidaho.edu/bulletins/13/Mississippi.htm`.

Vogelmann, J.E., S.M. Howard, L. Yang, C.R. Larson, B.K. Wylie, N. Van Driel, 2001: Completion of the 1990s National Land Cover Data Set for the Conterminous United States from Landsat Thematic Mapper Data and Ancillary Data Sources. *Photogrammetric Engineering and Remote Sensing*, 67:650-652.

Walters, D.J., 2009: Personal communication.

WAMDI Group, 1988: The WAM model - a third generation ocean wave prediction model. *J. Phys. Oceanogr.*, 18, 1775-1810.

Wang, D.P. and L.Y. Oey, 2008: Hindcast of Waves and Currents in Hurricane Katrina. *Bulletin of the American Meteorological Society*, 89(4), 487-495.

Warner, J.C., N. Perlin and E.D. Skyllingstad, 2008: Using the model coupling toolkit to couple earth system models. *Environ. Modell. Softw.*, 23, 1240-1249.

Weaver, RJ and D.N. Slinn, 2004: Effect of wave forcing on storm surge. *Proceedings of Coastal Engineering '04*, Lisbon, Portugal, 1532-1538.

Westerink, J.J., R.A. Luettich and J.C. Muccino, 1994: Modeling tides in the Western North Atlantic using unstructured graded grids. *Tellus*, 46A, 178-199.

Westerink, J.J., R.A. Luettich , J.C. Feyen, J.H. Atkinson, C. Dawson, H.J. Roberts, M.D. Powell, J.P. Dunion, E.J. Kubatko, H. Pourtaheri, 2008: A Basin to Channel Scale Unstructured Grid Hurricane Storm Surge Model Applied to Southern Louisiana, *Monthly Weather Review*, 136, 3, 833-864.

Wu, J., 1982: Wind-stress coefficients over sea surface from breeze to hurricane. *J. Geophys. Res.*, 87, 9704-9706.

Zijlema, M., 2010: Computation of wind-wave spectra in coastal waters with SWAN on unstructured grids. *Coastal Engineering*, 57, 267-277.